

**University of Alberta**

**A DISLOCATION BASED APPROACH TO ROCK DAMAGE BY  
BLASTING IN UNDERGROUND MINES**

by  
Amir Karami



A thesis submitted to the Faculty of Graduate Studies and Research in partial fulfillment  
of the requirements for the degree of Doctor of Philosophy

in

Mining Engineering

Department of Civil and Environmental Engineering

Edmonton Alberta

Fall 2002



National Library  
of Canada

Acquisitions and  
Bibliographic Services

395 Wellington Street  
Ottawa ON K1A 0N4  
Canada

Bibliothèque nationale  
du Canada

Acquisitions et  
services bibliographiques

395, rue Wellington  
Ottawa ON K1A 0N4  
Canada

*Your file Votre référence*

*Our file Notre référence*

The author has granted a non-exclusive licence allowing the National Library of Canada to reproduce, loan, distribute or sell copies of this thesis in microform, paper or electronic formats.

L'auteur a accordé une licence non exclusive permettant à la Bibliothèque nationale du Canada de reproduire, prêter, distribuer ou vendre des copies de cette thèse sous la forme de microfiche/film, de reproduction sur papier ou sur format électronique.

The author retains ownership of the copyright in this thesis. Neither the thesis nor substantial extracts from it may be printed or otherwise reproduced without the author's permission.

L'auteur conserve la propriété du droit d'auteur qui protège cette thèse. Ni la thèse ni des extraits substantiels de celle-ci ne doivent être imprimés ou autrement reproduits sans son autorisation.

0-612-81209-X

**Canada**

**University of Alberta**

**Library Release Form**

Name of Author : **Amir Karami**

Title of Thesis: A Dislocation Based Approach to Rock Damage by Blasting in  
Underground Mines

**Degree:** Doctor of Philosophy

**Year this Degree Granted:** 2002

Permission is hereby granted to the University of Alberta Library to reproduce single copies of this thesis and lend or sell such copies for private, scholarly, or scientific research purposes only.

The author reserves all other publication and other rights in association with the copyright in the thesis, and except as here in before provided, neither the thesis nor any substantial portion thereof may be printed or otherwise reproduced in any material form whatever without the author's prior written permission.



430 Michener Park

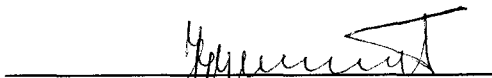
Edmonton AB T6H 4M5 Canada


Dated: October 1, 2002

# University of Alberta

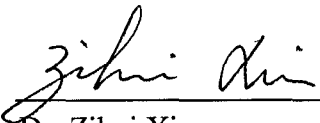
## Faculty of Graduate Studies and Research

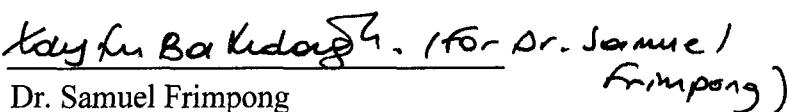
The undersigned certify that they have read, and recommended to the Faculty of Graduate Studies and Research for acceptance, a thesis entitled "*A Dislocation Based Approach to Rock Damage by Blasting in Underground Mines*" submitted by Amir Karami in partial fulfillment of the requirements for the degree of Doctor of Philosophy in Mining Engineering.

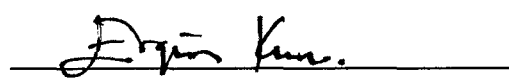
  
\_\_\_\_\_  
Dr. Jozef Szymanski

  
\_\_\_\_\_  
Dr. Fernand Ellyin

  
\_\_\_\_\_  
Dr. Stefan Planeta

  
\_\_\_\_\_  
Dr. Zihui Xia

  
\_\_\_\_\_  
Dr. Samuel Frimpong

  
\_\_\_\_\_  
Dr. Ergun Kuru

Date: September 25, 2002.

# **Dedication**

**To my mother  
who waited so long for this**

**And to the memory of my father**

## ABSTRACT

Mine blast damage problems in near-field have received considerable attention in the past two decades, in contrast rock damage by cyclic loading in mid- to far-field regions has not been fully investigated. The effect of blast vibration on stability of underground excavations has only been considered empirically by peak particle velocity criterion.

This study is concerned with the rock damage problem by vibration through the theoretical and experimental investigation into rock cyclic loading. A new method to assess damage by cyclic loading to the rock in shear mode is proposed. In this study, the theory of dislocations is used to model rock plastic response ahead of a crack. Plastic displacement is determined within the crack plastic zone for a rock with a Ramberg-Osgood type representation of the mechanical behavior. In this work rock damage is investigated for one cycle of loading and unloading.

Monotonic and fatigue tests were carried out on granite specimens using a new single shear apparatus based on the Iosipescu method. These tests resulted in attainment of fatigue life (S-N) curve of granite.

The main outcome of this study is the development of a new numerical tool to assess rock damage by blast vibration. This tool provides a novel way to quantify vibration damage and predicts rock damage due to cyclic loading.

The model is capable of assessing damage in rock during cyclic loading with satisfactory accuracy. Results show that rocks containing large cracks are more susceptible to damage

under vibration than those with small cracks. Moreover, while increase in the stress range increases damage to the rock, the rock response to such an increase is highly dependent on rock plastic behavior, and inherent crack size.

This research work is the first attempt to investigate rock damage by cyclic loading. The results are to be viewed as a first approximation to rock damage problem in mid- to far-field regions. Despite this, the results indicate that dislocation model can effectively be used to analyze blast damage in these regions. Once fully developed, the model can be integrated into the mine support design/selection processes for underground excavations.

## ACKNOWLEDGEMENT

I wish to express my deepest gratitude and appreciation to my advisors, Dr. Jozef Szymanski and Dr. Fernand Ellyin, for their academic support and guidance and their strong support and encouragement throughout the period of this study. My gratitude is also extended to the members of my committee, namely Dr. Samuel Frimpong, Dr. Stefan Planeta (External Examiner, Université Laval), Dr. Zihui Xia, Dr. Ergun Kuru, and Dr. Tayfun Babadagli for their valuable suggestions, comments, time and effort.

My special thanks are due to Mr. Sean Watts for his help in designing the experimental setup and running the experiments. I would like to thank Mr. Doug Booth for his logistic support during the entire period of this study.

I am also grateful to my sponsors for their financial support without which this work may not have been completed. Finally I reserve the rest of my acknowledgements for my wife, Razieh Mortazavi, whose patience and encouragement at some critical moments were instrumental to successful completion of this work and also to my children, Narges Karami and Negar Karami, who had to endure many dull nights.



## TABLE OF CONTENTS

ABSTRACT

ACKNOWLEDGEMENTS

LIST OF FIGURES

LIST OF TABLES

LIST OF NOMENCLATURE

<b>Chapter 1: Introduction to Rock Blast Damage .....</b>	<b>1</b>
1.1. Statement of Problem .....	2
1.2. Scope and Objectives of Research .....	7
1.3. Research Methodology.....	8
1.4. Assumptions and Limitations of the Model .....	9
1.5. Scientific and Industrial Contribution of Research .....	10
1.6. Outline of the Thesis .....	10
<b>Chapter 2: Literature Review .....</b>	<b>12</b>
2.1. Description of Rock Mass Damage and its Consequences .....	12
2.2. Mine Blast Damage Mechanisms.....	20

2.2.1. Near-Field Blast Damage .....	20
2.2.2. Mid- to Far-Field Blast Damage .....	22
2.3. Blast Damage Estimation .....	23
2.3.1. Determination of Critical Vibration Levels .....	27
2.3.2. Prediction of Peak Particle Velocity .....	27
2.3.2.1. Square Root Scaling Approach to PPV Prediction .....	30
2.3.2.2. Geometrical Prediction of Blast Vibration – Persson’s Approach.....	35
2.3.2.3. Geometrical Prediction of Blast Vibration – Lilley’s Approach.....	38
2.4. An Energy-Based Blast Damage Prediction Model.....	43

**Chapter 3: Theory of Dislocations and Its Application to Rock Damage**

<b>by Cyclic Loading .....</b>	<b>45</b>
3.1. Discrete Distribution of Finite Dislocations versus Continuous Distribution of Infinitesimal Dislocations.....	46
3.2. Application of Dislocation Theory to Crack Problem .....	47

3.2.1. Monotonic Loading Model for Elastic-Perfectly Plastic Materials .....	48
3.2.2. Unloading Model for Elastic-Perfectly Plastic Materials .....	55
3.2.3. Dislocation Model for Nonlinear Work Hardening Materials .....	59
3.3. Application of Dislocation Theory to Rock Deformation .....	60
3.4. Rock Damage Model by Dislocation Arrays .....	64
3.4.1. Monotonic Loading Stage.....	65
3.4.2. Unloading Stage.....	78
3.4.3. Monotonic and Cyclic J-Integral .....	89
3.4.3.1. Monotonic Loading Stage.....	90
3.4.3.2. Unloading Stage.....	91
3.5. Numerical Solution of Dislocation Model.....	93
3.5.1. Levenberg-Marquardt Algorithm.....	95
3.5.2.. Mathematical Model Singularities.....	98

**Chapter 4: Monotonic and Fatigue Shear Testing of Granite ..... 101**

4.1. ASTM D 5379/D 5379M - 1993: Iosipescu Shear Testing Method . 102

4.1.1. Experimental Program: Special Considerations..... 106

4.1.2. Specimen Preparation, Instrumentation, Loading and  
Data Acquisition Systems ..... 111

4.1.2.1. Monotonic Loading Tests..... 111

4.1.2.2. Fatigue Cyclic Shear Loading Tests..... 115

4.2. Monotonic Loading Tests Results..... 118

4.3. Cyclic Loading Tests Results..... 125

**Chapter 5: Analysis and Results ..... 131**

5.1. Numerical Results Using Data from Literature..... 132

5.1.1. Monotonic Loading Stage – Numerical Results ..... 132

5.1.2. Unloading Stage – Numerical Results: ..... 144

5.2. Numerical Results Using Data from Monotonic Loading Tests ..... 171

5.3. Verification of Model Results with Literature Data..... 177

<b>Chapter 6: Conclusions and Recommendations .....</b>	<b>189</b>
6.1. Findings and Observations .....	190
6.2. Further Work Recommendations .....	193
<b>References .....</b>	<b>194</b>
<b>Appendix A: Mine Blasting: an overview.....</b>	<b>209</b>
A.1. Blasting Theories.....	211
A.1.1. Reflection Theory.....	212
A.1.2. Gas Expansion Theory .....	212
A.1.3. Flexural Rupture.....	214
A.1.4. Compressional Stress Wave Theory .....	215
A.1.5. Combined Theory.....	216
A.1.6. Nuclei or Stress Wave/Flaw Theory .....	217
A.1.7. Torque Theory.....	219
A.2. Conventional approach to blast design and related damage .....	222
A.2.1. Surface and Underground Blast Design Methods .....	223

A.2.1.1. Spacing/Burden (S/B) ratio .....	226
A.2.1.2. Powder Factor .....	227
A.2.1.3. Blastability index.....	228
A.2.2. Limitations of the Conventional Blast Design Approaches ..	230
A.3. Engineering Models of Rock Fragmentation .....	232
A.4. Design Stability Charts.....	242
<b>Appendix B: Inversion of Cauchy Integral Equation .....</b>	<b>249</b>
<b>Appendix C: Monotonic Loading Solution .....</b>	<b>257</b>
<b>Appendix D: Loading Solution.....</b>	<b>262</b>

## LIST OF FIGURES

Figure 2-1: Schematic diagram of the regression line of the measured particle velocity in a log-log diagram and the determination of the lowest scaled distance, $R/W^{1/2}$ to be used .....	32
Figure 2-2: Confidence lines for US Bureau of Mines (Nicholls et al., 1971).....	34
Figure 2-3: Schematic diagram of blasthole configuration and geometric representation of point of observation with respect to blasthole .....	36
Figure 2-4: Geometry of blasthole and ore-filling material interface (Lilley, 1994) .....	39
Figure 3-1: Array of dislocations at the tips of a crack in a medium subject to far field shear stress.....	49
Figure 3-2: Dislocation density distribution under monotonic loading condition.....	52
Figure 3-3: Dislocation density distribution under monotonic loading and unloading conditions (Lardner, 1968).....	56
Figure 3-4: Schematic diagram of a block of rock formed by the intersecting cracks in the rock. ....	66
Figure 3-5: Schematic diagram of the crack at the bottom of the block under blast cyclic shear load	67
Figure 3-6: Shear stress within the crack tip plastic zone.....	70

Figure 3-7: Loading and unloading dislocation density distributions ahead of the crack tip (adopted from Ellyin et al. (1987)) .....	79
Figure 3-8: Schematic diagram of shear stress-strain relationship for monotonic loading and unloading (adopted from Ellyin et al. (1987)) .....	81
Figure 3-9: The sequence of loading used to calculate cyclic J-integral (Tanaka, 1983) .....	92
Figure 4-1: Specimen configuration used in the Iosipescu shear test.....	104
Figure 4-2: Iosipescu shear testing apparatus, original configuration .....	105
Figure 4-3: Schematic diagram of Iosipescu after the final modifications.....	108
Figure 4-4: Shear testing apparatus after the proposed modifications during a monotonic loading test.....	109
Figure 4-5: A 45° Strain gage rosette with three stacked gages .....	112
Figure 4-6: A granite specimen with a strain gage rosette installed on each side .....	112
Figure 4-7: Instronet Data Acquisition System and six channel Wheatstone quarter bridge circuit built for the monotonic loading tests.....	114
Figure 4-8: A crack propagation gage with twenty strands .....	117
Figure 4-9: Labview model capable of monitoring four channels (gages) at the same time with identical triggering mechanism .....	119



Figure 4-10: Granite shear stress – shear strain diagram as it was calculated from strain gage readings. Test 11 and test 12 indicate the shear strain as it was calculated from the two rosettes on specimen number 1. Test 21 and test 22 also show similarly shear strains as measured by rosettes on specimen 2 and Test 3 shows the only reading available from specimen 3. ....	121
Figure 4-11: Average shear stress – shear strain diagram for granite specimens.....	123
Figure 4-12: Fatigue stress life curve (S-N Curve) of granite and the fitted model .....	127
Figure 4-13: Sequence of breakage of individual strands of crack propagation gage, clearly at final stages of crack growth several strands of crack gage is broken at the same time. ....	129
Figure 5-1: Shear stress-shear displacement diagram of the gneiss (Bertacchi et al., 1974) .....	134
Figure 5-2: Non-dimensionalized plastic displacement versus distance from the crack tip for given applied stresses in MPa ahead of a crack of $2c = 10$ mm length .....	135
Figure 5-3: Shear stress distribution ahead of the crack tip versus distance from the crack tip for given applied stresses in MPa - $2c = 10$ mm.....	136

Figure 5-4: Non-dimensionalized plastic displacement versus distance from the crack tip for given applied stresses in MPa ahead of a crack of $2c = 400$ mm length .....	137
Figure 5-5: Shear stress distribution ahead of the crack tip versus distance from the crack tip for given applied stresses in MPa - $2c = 400$ mm.....	138
Figure 5-6: Non-dimensionalized plastic displacement versus distance from the crack tip for various crack sizes and an applied load of $\tau = 9$ MPa.....	140
Figure 5-7: Non-dimensionalized crack tip stress distribution versus distance from the crack tip for various crack sizes and an applied load of $\tau = 9$ MPa.....	141
Figure 5-8: Non-dimensionalized crack tip plastic displacement versus applied stress ratio for various crack sizes .....	142
Figure 5-9: Non-dimensionalized Crack tip stress ratio versus applied stress ratio for various crack sizes .....	143
Figure 5-10: Non-dimensionalized diagram of the change in the plastic displacement versus distance from the crack tip for an applied load of $\tau = 11$ MPa and unloading stresses proportionate to $\tau$ for initial crack length of $2c = 10$ mm under kinematic hardening rule .....	146
Figure 5-11: Non-dimensionalized diagram of the reversed shear stress ratio versus distance from the crack tip for an applied load of $\tau = 11$ MPa and	

unloading stresses proportionate to  $\tau$  for initial crack length of  $2c = 10$  mm under kinematic hardening rule .....147

Figure 5-12: Comparison of the monotonic loading results with the unloading results in terms of non-dimensionalized plastic displacement versus distance from the crack tip for an applied load of  $\tau = 11$  MPa and unloading stresses proportionate to  $\tau$  for initial crack length of  $2c = 10$  mm under kinematic hardening rule .....148

Figure 5-13: Comparison of the monotonic loading results with the unloading results in terms of non-dimensionalized shear stress distribution versus distance from the crack tip for an applied load of  $\tau = 11$  MPa and unloading stresses proportionate to  $\tau$  for initial crack length of  $2c = 10$  mm under kinematic hardening rule .....149

Figure 5-14: Non-dimensionalized diagram of the change in the plastic displacement versus distance from the crack tip for an applied load of  $\tau = 11$  MPa and unloading stresses proportionate to  $\tau$  for initial crack length of  $2c = 10$  mm under isotropic hardening rule .....150

Figure 5-15: Non-dimensionalized diagram of the reversed shear stress ratio versus distance from the crack tip for an applied load of  $\tau = 11$  MPa and unloading stresses proportionate to  $\tau$  for initial crack length of  $2c = 10$  mm under isotropic hardening rule .....151

Figure 5-16: Comparison of the monotonic loading results with the unloading results in terms of non-dimensionalized plastic displacement versus distance from the crack tip for an applied load of  $\tau = 11$  MPa and unloading stresses proportionate to  $\tau$  for initial crack length of  $2c = 10$  mm under isotropic hardening rule .....152

Figure 5-17: Comparison of the monotonic loading results with the unloading results in terms of non-dimensionalized shear stress distribution versus distance from the crack tip for an applied load of  $\tau = 11$  MPa and unloading stresses proportionate to  $\tau$  for initial crack length of  $2c = 10$  mm under isotropic hardening rule .....153

Figure 5-18: Non-dimensionalized diagram of the change in the plastic displacement versus distance from the crack tip for an applied load of  $\tau = 11$  MPa and unloading stresses proportionate to  $\tau$  for initial crack length of  $2c = 400$  mm under kinematic hardening rule .....154

Figure 5-19: Non-dimensionalized diagram of the reversed shear stress ratio versus distance from the crack tip for an applied load of  $\tau = 11$  MPa and unloading stresses proportionate to  $\tau$  for initial crack length of  $2c = 400$  mm under kinematic hardening rule .....155

Figure 5-20: Comparison of the monotonic loading results with the unloading results in terms of non-dimensionalized plastic displacement versus distance from the crack tip for an applied load of  $\tau = 11$  MPa and unloading

stresses proportionate to  $\tau$  for initial crack length of  $2c = 400$  mm under kinematic hardening rule .....156

Figure 5-21: Comparison of the monotonic loading results with the unloading results in terms of non-dimensionalized shear stress distribution versus distance from the crack tip for an applied load of  $\tau = 11$  MPa and unloading stresses proportionate to  $\tau$  for initial crack length of  $2c = 400$  mm under kinematic hardening rule .....158

Figure 5-22: Non-dimensionalized diagram of the change in the plastic displacement versus distance from the crack tip for an applied load of  $\tau = 11$  MPa and unloading stresses proportionate to  $\tau$  for initial crack length of  $2c = 400$  mm under isotropic hardening rule .....159

Figure 5-23: Non-dimensionalized diagram of the reversed shear stress ratio versus distance from the crack tip for an applied load of  $\tau = 11$  MPa and unloading stresses proportionate to  $\tau$  for initial crack length of  $2c = 400$  mm under isotropic hardening rule .....160

Figure 5-24: Comparison of the monotonic loading results with the unloading results in terms of non-dimensionalized plastic displacement versus distance from the crack tip for an applied load of  $\tau = 11$  MPa and unloading stresses proportionate to  $\tau$  for initial crack length of  $2c = 400$  mm under isotropic hardening rule .....161

Figure 5-25: Comparison of the monotonic loading results with the unloading results in terms of non-dimensionalized shear stress distribution versus distance from the crack tip for an applied load of $\tau = 11$ MPa and unloading stresses proportionate to $\tau$ for initial crack length of $2c = 400$ mm under isotropic hardening rule .....	162
Figure 5-26: Comparison of material behavior while unloading under kinematic and isotropic hardening rules with reference to the equivalent stress-strain diagram .....	163
Figure 5-27: Non-dimensionalized diagram of the plastic displacement at the crack tip versus unloading stress ratio ahead of a 10 and a 1000 mm crack - comparison of kinematic and isotropic hardening rules .....	165
Figure 5-28: Non-dimensionalized diagram of the plastic displacement at the crack tip versus the ratio of unloading stress over the applied load ahead of a crack of $2c=100$ mm long .....	167
Figure 5-29: Non-dimensionalized diagram of the change in the plastic displacement at the crack tip versus the ratio of unloading stress over yield stress of the rock ahead of a 100 mm long crack under kinematic hardening rule...	168
Figure 5-30: Non-dimensionalized diagram of the change in the plastic displacement at the crack tip for various crack sizes versus the ratio of unloading stress over the yield stress for an applied load of 11 MPa under kinematic hardening conditions.....	169

Figure 5-31: Non-dimensionalized diagram of the change in the plastic displacement at the crack tip for various crack sizes versus the ratio of unloading stress over the yield stress for an applied load of 11 MPa under isotropic hardening conditions.....170

Figure 5-32: Non-dimensionalized diagram of the plastic displacement versus distance from the crack tip for given applied stresses in MPa ahead of a crack of  $2c = 100$  mm length in granite .....173

Figure 5-33: Shear stress distribution ahead of the crack tip versus distance from the crack tip for given applied stresses in MPa -  $2c = 100$  mm in granite.....174

Figure 5-34: Non-dimensionalized diagram of the change in the plastic displacement versus distance from the crack tip for an applied load of  $\tau = 9$  MPa and unloading stresses proportionate to  $\tau$  for initial crack length of  $2c = 100$  mm under kinematic hardening rule in granite .....175

Figure 5-35: Non-dimensionalized diagram of the reversed shear stress ratio versus distance from the crack tip for an applied load of  $\tau = 9$  MPa and unloading stresses proportionate to  $\tau$  for initial crack length of  $2c = 100$  mm under kinematic hardening rule in granite .....176

Figure 5-36: Comparison of the monotonic loading results with the unloading results in terms of non-dimensionalized plastic displacement versus distance from the crack tip for an applied load of  $\tau = 9$  MPa and unloading

stresses proportionate to  $\tau$  for initial crack length of  $2c = 100$  mm under kinematic hardening rule in granite .....178

Figure 5-37: Comparison of the monotonic loading results with the unloading results in terms of non-dimensionalized shear stress distribution versus distance from the crack tip for an applied load of  $\tau = 9$  MPa and unloading stresses proportionate to  $\tau$  for initial crack length of  $2c = 100$  mm under kinematic hardening rule in granite .....179

Figure 5-38: Non-dimensionalized diagram of the change in the plastic displacement versus distance from the crack tip for an applied load of  $\tau = 9$  MPa and unloading stresses proportionate to  $\tau$  for initial crack length of  $2c = 100$  mm under isotropic hardening rule in granite.....180

Figure 5-39: Non-dimensionalized diagram of the reversed shear stress ratio versus distance from the crack tip for an applied load of  $\tau = 9$  MPa and unloading stresses proportionate to  $\tau$  for initial crack length of  $2c = 100$  mm under isotropic hardening rule in granite.....181

Figure 5-40: Comparison of the monotonic loading results with the unloading results in terms of non-dimensionalized plastic displacement versus distance from the crack tip for an applied load of  $\tau = 9$  MPa and unloading stresses proportionate to  $\tau$  for initial crack length of  $2c = 100$  mm under isotropic hardening rule in granite .....182



Figure 5-41: Comparison of the monotonic loading results with the unloading results in terms of non-dimensionalized shear stress distribution versus distance from the crack tip for an applied load of $\tau = 9$ MPa and unloading stresses proportionate to $\tau$ for initial crack length of $2c = 100$ mm under isotropic hardening rule in granite .....	183
Figure 5-42: Comparison of the plastic zone size (a/c) ahead of a crack in rock using dislocation model and that ahead of a crack in steel as given by Bilby et al. (1963) for elastic perfectly plastic material behavior .....	185
Figure 5-43: Comparison of the plastic displacement at the tip of a 25 mm crack in granite and in steel (Ellyin et al., 1986) subject to various applied loads ..	186
Figure 5-44: Comparison of the shear stress at the tip of a 25 mm crack in granite and in steel (Ellyin et al., 1986) subject to various applied loads .....	187
Figure A-1: Rock breakage mechanism according to nuclei theory (Morhard et al., 1987) .....	218
Figure A-2: Rock breakage mechanism based on Torque theory.....	221
Figure A-3: Blasthole section view (A) showing terminology used in design and (B) pattern array for layout of holes.....	224
Figure A-4: Lilly's blastability index vs. Powder factor and Energy Factor (Lilly, 1986) .....	229
Figure A-5: Two typical Rosin-Rammler curves for blasting (Barron, 1997) .....	237

Figure A-6: Gravity adjustment factor C for (a) sliding failure mode, (b) gravity falls and slabbing (Potvin, 1988).....	245
Figure A-7: Stability graph showing zones of stable ground, caving ground and ground requiring support (Potvin, 1988; Nickson, 1992).....	247
Figure C-1: Non-dimensionalized plastic displacement ahead of crack tip of a 20 mm crack subject to given monotonic loads as given.....	258
Figure C-2: Non-dimensionalized shear stress field ahead of crack tip of a 20 mm crack subject to given monotonic loads as given.....	258
Figure C-3: Non-dimensionalized plastic displacement ahead of crack tip of a 50 mm crack subject to given monotonic loads as given.....	259
Figure C-4: Non-dimensionalized shear stress field ahead of crack tip of a 50 mm crack subject to given monotonic loads as given.....	259
Figure C-5: Non-dimensionalized plastic displacement ahead of crack tip of a 100 mm crack subject to given monotonic loads as given.....	260
Figure C-6: Non-dimensionalized shear stress field ahead of crack tip of a 100 mm crack subject to given monotonic loads as given.....	260
Figure C-7: Non-dimensionalized plastic displacement ahead of crack tip of a 200 mm crack subject to given monotonic loads as given.....	261
Figure C-8: Non-dimensionalized shear stress field ahead of crack tip of a 200 mm crack subject to given monotonic loads as given.....	261

Figure D-1: Reversed plastic displacement versus distance from the crack tip for a loading stress of 11 MPa and unloading stress ratios as shown ahead of a 20 mm crack under kinematic hardening rule.....263

Figure D-2: Reversed crack tip stress field versus distance from the crack tip for a loading stress of 11 MPa and unloading stress ratios as shown ahead of a 20 mm crack under kinematic hardening rule.....263

Figure D-3: Reversed plastic displacement versus distance from the crack tip for a loading stress of 11 MPa and unloading stress ratios as shown ahead of a 20 mm crack under isotropic hardening rule .....264

Figure D-4: Reversed crack tip stress field versus distance from the crack tip for a loading stress of 11 MPa and unloading stress ratios as shown ahead of a 20 mm crack under isotropic hardening rule .....264

Figure D-5: Reversed plastic displacement versus distance from the crack tip for a loading stress of 11 MPa and unloading stress ratios as shown ahead of a 50 mm crack under kinematic hardening rule.....265

Figure D-6: Reversed crack tip stress field versus distance from the crack tip for a loading stress of 11 MPa and unloading stress ratios as shown ahead of a 50 mm crack under kinematic hardening rule.....265

Figure D-7: Reversed plastic displacement versus distance from the crack tip for a loading stress of 11 MPa and unloading stress ratios as shown ahead of a 50 mm crack under isotropic hardening rule .....266

Figure D-8: Reversed crack tip stress field versus distance from the crack tip for a loading stress of 11 MPa and unloading stress ratios as shown ahead of a 50 mm crack under isotropic hardening rule .....266

Figure D-9: Reversed plastic displacement versus distance from the crack tip for a loading stress of 11 MPa and unloading stress ratios as shown ahead of a 100 mm crack under kinematic hardening rule.....267

Figure D-10: Reversed crack tip stress field versus distance from the crack tip for a loading stress of 11 MPa and unloading stress ratios as shown ahead of a 100 mm crack under kinematic hardening rule.....267

Figure D-11: Reversed plastic displacement versus distance from the crack tip for a loading stress of 11 MPa and unloading stress ratios as shown ahead of a 100 mm crack under isotropic hardening rule .....268

Figure D-12: Reversed crack tip stress field versus distance from the crack tip for a loading stress of 11 MPa and unloading stress ratios as shown ahead of a 100 mm crack under isotropic hardening rule .....268

Figure D-13: Reversed plastic displacement versus distance from the crack tip for a loading stress of 11 MPa and unloading stress ratios as shown ahead of a 200 mm crack under kinematic hardening rule.....269

Figure D-14: Reversed crack tip stress field versus distance from the crack tip for a loading stress of 11 MPa and unloading stress ratios as shown ahead of a 200 mm crack under kinematic hardening rule.....269

Figure D-15:Reversed plastic displacement versus distance from the crack tip for a loading stress of 11 MPa and unloading stress ratios as shown ahead of a 200 mm crack under isotropic hardening rule .....	270
Figure D-16:Reversed crack tip stress field versus distance from the crack tip for a loading stress of 11 MPa and unloading stress ratios as shown ahead of a 200 mm crack under isotropic hardening rule .....	270
Figure D-17:Reversed plastic displacement versus distance from the crack tip for a loading stress of 11 MPa and unloading stress ratios as shown ahead of a 1000 mm crack under kinematic hardening rule.....	271
Figure D-18:Reversed crack tip stress field versus distance from the crack tip for a loading stress of 11 MPa and unloading stress ratios as shown ahead of a 1000 mm crack under kinematic hardening rule.....	271
Figure D-19:Reversed plastic displacement versus distance from the crack tip for a loading stress of 11 MPa and unloading stress ratios as shown ahead of a 1000 mm crack under isotropic hardening rule .....	272
Figure D-20:Reversed crack tip stress field versus distance from the crack tip for a loading stress of 11 MPa and unloading stress ratios as shown ahead of a 1000 mm crack under isotropic hardening rule .....	272

## LIST OF TABLES

Table 2-1: Damage criteria developed by Bauer et al. (1978) based on the particle velocity.....	29
Table 4-1: Summary of fatigue life data for all fatigue tests .....	126
Table A-1: Rock breakage theories – a historical review (Morhard et al., 1987) .....	213
Table A-2: Selected factors for first approximation surface blast designs.....	227
Table A-3: Ratings for blastability index parameters (Lilly, 1986) .....	229
Table A-4: Parameter values used to evaluate Factor A (Cunningham, 1987) .....	240
Table A-5: Blasting adjustment developed by Laubscher (1984) .....	248

## LIST OF NOMENCLATURE

- $a$  = particle acceleration
- $a$  = length of the plastic zone under monotonic loading
- $a_i$  = coefficients of the known approximating function for the Fredholm integral equation of the second kind
- $a', b'$  = limits of integration in the Fredholm integral equation of the second kind
- $A$  = area of the cross section between notches in granite specimens
- $A_I$  = amplitude of ground vibration
- $A'$  = rock factor, i.e. 7 for medium rocks, 10 for hard rocks, 13 for very hard, weakly fissured rocks
- $A_0$  = vibration amplitudes (mm/sec) in the blasthole
- $A_{(x,y)}$  = vibration amplitudes (mm/sec) in the filling material
- $A_{ore}$  = vibration amplitudes (mm/sec) in the ore body
- $A_{ore/filling}$  = vibration amplitudes (mm/sec) in the ore-filling material interface
- $b$  = Burger's vector
- $B$  = burden (m)
- $B'$  = joint orientation adjustment factor
- $BCL$  = bottom charge length (m)
- $c$  = half of the length of the crack
- $C$  = charge quantity
- $C'$  = design surface orientation factor
- $CCL$  = column charge length (m)
- $d$  = length of the reversed plastic zone (m) under unloading

$d'$  = distance (m) between the shot and the point of observation  
 $dw$  = vibration intensity  
 $E$  = relative weight strength of explosive  
 $ER$  = Energy Ratio  
 $f$  = frequency  
 $f(x)$  = dislocation density function under monotonic loading  
 $f_1(x)$  = unknown function in the Fredholm integral equation of the second kind  
 $g(x)$  = dislocation density function under unloading  
 $g_1(x)$  = known function in the Fredholm integral equation of the second kind  
 $h$  = height of the granite specimen between the notches  
 $H$  = length of charge column (m)  
 $H'$  = hardness  
 $H^k$  = Hessian matrix, i.e. the second derivative of the objective function in the  
Levenberg-Marquardt algorithm  
 $HF$  = hardness factor  
 $I$  = identity matrix  
 $J$  = J integral for monotonic loading  
 $J'$  = sub-grade drilling depth (m)  
 $JPA$  = joint plane angle  
 $JPO$  = joint plane orientation  
 $JPS$  = joint plane spacing  
 $K$  = site factor for peak particle velocity - scaled distance relationship  
 $K'$  = rock constant



- $K_{50}$  = the mesh size through which 50% of the material will pass
- $K_B$  = rock constant for estimating burden in surface blast design
- $K_S$  = constant relating spacing to burden in surface blast design
- $K_J$  = constant relating sub-grade to burden in surface blast design
- $K_T$  = constant relating stemming to burden in surface blast design
- $l$  = linear charge concentration (kg/m)
- $L$  = blasthole length (m)
- $m$  = dimensionless constant depending on material behavior
- $m'$  = site factor for peak particle velocity - scaled distance relationship
- $m_1$  = number of points within the plastic zone (for integration purposes)
- $n$  = work-hardening exponent
- $n'$  = ratio of characteristic impedance of materials (ore and filling materials)
- $n_1$  = number of coefficients in the known approximating function for the Fredholm  
integral equation of the second kind
- $n_2$  = Rosin-Rammler exponent of uniformity
- $N$  = number of cycle achieved at a given maximum applied stress
- $N'$  = stability number
- $N(x)$  = number of dislocations at  $x$
- $P_0$  = effective stress (Pa) in  $|x| < c$
- $P_1$  = effective stress (Pa) in  $c < |x| < a$
- $P_f$  = powder factor
- $P_i$  = blasthole pressure
- $P(x)$  = monotonic loading function

- $P'(x)$  = shear stresses due to dislocation at  $x$
- $PV$  = particle velocity
- $PPV$  = peak particle velocity (m/sec)
- $Q$  = mass of explosive charge equivalent in energy to TNT in one blasthole
- $Q'$  = modified Q Tunneling Quality Index
- $Q(x)$  = unloading dislocation density function
- $Q_{ore}$  = dimensionless rock quality factors in ore body
- $Q_{filling}$  = dimensionless rock quality factors in filling material
- $r_{ore}$  = distance (m) from blasthole along the path of propagation to the point of observation in ore body
- $r_{filling}$  = distance (m) from blasthole along the path of propagation to the point of observation in filling material
- $R$  = stress ratio, i.e.  $\tau_{min} / \tau_{max}$
- $R'$  = mass fraction larger than  $x$ , i.e. diameter of the fragment
- $RMD$  = rock mass description
- $R_u$  = unloading stress range (Pa)
- $s^{(k)}$  = search direction for the Levenberg-Marquardt algorithm
- $S$  = spacing (m)
- $S'$  = shape factor
- $S_d$  = standard deviation of drilling accuracy (m)
- $SGI$  = specific gravity influence
- $SRF$  = stress reduction factor
- $t$  = optimal delay time between blastholes

- $T$  = top-hole stemming length (m)
- $T(x)$  = resultant loading function after unloading for nonlinear work-hardening material behavior ( $T(x) = T_1(x) + T_2(x) + T_3(x)$ )
- $T_m$  = surface traction
- $u(x)$  = plastic displacement (m) as a function of  $x$
- $u_m$  = displacement vector
- $V_0$  = volume of rock defined by burden times spacing times bench height
- $w$  = width of the granite specimen
- $w'$  = vibration density function ( $\text{kg/m}^2$ )
- $W$  = strain energy density
- $W'$  = total weight (kg) of explosives per a minimum of 8 msec delay
- $W_l$  = unit weight explosive
- $x$  = arbitrary points within crack plastic zone
- $x'$  = diameter of the fragment (m)
- $\bar{x}$  = mean fragment size or  $K_{50}$
- $x_0$  = arbitrary points within crack plastic zone
- $x^*$  = exact solution
- $x_c$  = characteristic size
- $x^k$  =  $k^{\text{th}}$  estimate of exact solution  $x^*$
- $x^{k+1}$  =  $(k+1)^{\text{th}}$  estimate of exact solution  $x^*$
- $x_l, y_l$  = coordinate system of observation point
- $y_d$  = vertical distance (m) from the bottom of charge to the stress wave front along the charge

- $y_s$  = stemming length (m)
- $\alpha, \beta'$  = general form scaling factor indices
- $\alpha^*, \beta^*$  = angles of propagating wave with horizontal axis
- $\alpha^{(k)}$  = step length parameter to find exact solution  $x^*$  by Levenberg-Marquardt algorithm
- $\alpha$  = coefficients of the plastic displacement function under monotonic loading for nonlinear work-hardening material behavior
- $\beta$  = parameter indicating work hardening rule applied, i.e.  $\beta = +1$ : kinematic hardening rule,  $\beta = -1$ : isotropic hardening rule
- $\varepsilon_{+45}$  = longitudinal strain as measured by gage one staked at  $+45^\circ$  angle on the strain gage rosette.
- $\varepsilon_{-45}$  = longitudinal strain as measured by gage two staked at  $-45^\circ$  angle (perpendicular to the gage one) on the strain gage rosette.
- $\gamma$  = shear strain
- $\gamma_0$  = elastic yield intercept
- $\gamma_p(x)$  = plastic strain
- $\eta_A$  = strain energy absorption factor at the interface on the transmitted amplitude
- $\eta_j$  = nonlinear regression function for monotonic loading function for nonlinear work-hardening material behavior
- $\omega'$  = chosen function approximating unknown function in the Fredholm integral equation of the second kind
- $\varphi(x)$  = total plastic displacement (m)
- $\varphi_0$  = displacement at yield intercept (m)

$\varphi_l(x)$  = plastic displacement under monotonic loading for elastic-perfectly plastic material behavior

$\varphi_p(x)$  = plastic displacement as a function of  $x$  (m)

$\kappa$  = amplitude reduction factor for transmitted p-wave

$\lambda^{(k)}$  = parameter that controls both the direction and the length of the step in the Levenberg-Marquardt algorithm

$\lambda_{ore}$  = pulse wavelength (m) in ore

$\lambda_{filling}$  = pulse wavelength (m) in filling material

$\lambda$  = constant parameter relating burden to optimal delay time between blastholes

$\mu$  = shear modulus of rock

$\nu$  = Poisson's ratio of rock

$\theta$  = angle of line connecting bottom of blasthole to the point of observation with the horizontal axis

$\sigma_c$  = unconfined compressive strength of the intact rock

$\tau$  = far field stress

$\tau_0$  = yield stress (Pa)

$\tau_u$  = the reduction in applied far field stress during unloading

$\tau - \tau_u$  = stress level after unloading (Pa)

$\tau_{min}$  = minimum applied stress

$\tau_{max}$  = maximum applied stress

$\tau_h(x)$  = stress level required to achieve a plastic strain of  $\gamma_p$ .

$\tau_r(x)$  = shear stress ahead of the crack tip within the plastic zone under monotonic loading (Pa)

$\tau_{rr}(x)$  = shear stress ahead of the crack tip within the reversed plastic zone under unloading (Pa)

$\omega$  = coefficients of the change in the plastic displacement function under unloading for nonlinear work-hardening material behavior

$\xi_j$  = nonlinear regression function for unloading function for nonlinear work-hardening material behavior

$\Delta f(x)$  = change in dislocation density function after unloading

$\Delta J$  = path independent cyclic J integral

$\Delta T_m$  = change in surface traction

$\Delta u_m$  = change in displacement vector

$\Delta W$  = change in strain energy density

$\Delta \phi$  = reversed plastic displacement (m) under monotonic loading for elastic-perfectly plastic material behavior

$\Delta \phi_l(x)$  = change in the plastic displacement function under unloading for elastic-perfectly plastic material behavior

$\Delta \phi_p(x)$  = reversed plastic displacement under unloading for nonlinear work-hardening material behavior

$\Gamma$  = integration path for calculating J integral

$\nabla f(x)$  = gradient (first derivative) of the objective function in the Levenberg-Marquardt algorithm

## **Chapter 1: Introduction to Rock Blast Damage**

Mine blast damage is categorized into two distinct types; (i) a near-field rock damage that occurs in the immediate vicinity of the blasthole and (ii) a mid- to far-field damage to the rock that occurs in areas within the mine site far from the blasthole. Near-field blast damage is due to high stress wave propagation and high-pressure gases expanding into the rock mass adjacent to the blasthole. Damage in the near-field is basically in the form of shattering and crushing the blasthole wall and severe cracking beyond this region. Mid- to far-field rock damage is solely due to ground vibration resulting from production blasting in nearby stopes. Damage here is by the preconditioning and dislodging of the blocks of rocks leading to the sliding of these blocks on the pre-existing or newly generated weakness planes. Naturally created shear planes such as joints, bedding planes, faults and other types of discontinuities that already exist can accommodate the rock shear movements. In the absence of natural shear plane, shearing and slip could happen through the intact rock if the applied load is high enough to overcome the rock shear strength considering the normal stresses already in effect.

In this study, only the blast-induced damage to the rock in mid- to far-field region is investigated. In this region, rock damage by shear caused by the blast-generated waves traveling through the rock mass is studied. Depending on the orientation of inherent defects with respect to traveling blast waves, shear stresses are generated acting on the local defects and cracks causing rock to slip along the weakest direction. Damage is related to the deterioration of rock strength due to the generation of new cracks or the

extension of existing ones or by opening and shearing along these cracks. It is notable that rock may sustain considerable damage and still be able to perform structurally for the period required by the mine. Therefore, rock damage does not necessarily mean failure but requires continuous monitoring of the rock structure with the purpose of practicing a safe and economically viable mining environment.

### ***1.1. Statement of Problem***

In the last twenty years there has been a large amount of research reported in the mining literature on blasting, excavation design and modeling (Appendix A). However, there is a continuing gap between published research and its effective application to the problems facing mining operations.

Frequently, all underground mines encounter problems associated with poor fragmentation, ore dilution or the stability of excavations. These problems are generally addressed by separate departments within the mine office – e.g. drilling and blasting group and geotechnical group. The problems of blasting performance and geotechnical stability are usually closely related at both operational and engineering levels and this artificial separation into different functional departments is seldom productive.

This situation arises because the mechanisms behind these processes are not well understood and because of inconsistencies in the description of rock mass from the perspective of either blasting or geotechnical engineering. In addition, there are no effective tools that enable mine engineers to predict how each process affects the other.



The current empirical design approaches, for example, do not explicitly consider the rock damage or blast effects in determining the stability of a stope or the stable spans that can be achieved in a given geological environment.

There is a need for tools that provide engineers with simple design guidelines and practical methods for the design and optimization of blasts and to systematically address blast related problems. It is also important to be able to quantify the impact of blasting on excavation performance and the general mine stability. With such tools the engineer should be able to design blasts to meet the mine's fragmentation requirements with minimum dilution from waste rock or fill and without affecting the local or general stability of the mining area.

Blast-related problems in mining operations include blast damage to rock structures in mid- to far-field regions, selection of appropriate stope span, rock fragmentation control, sequence of mining, blast design standards, timing of detonations and the economics of mining operations.

Operators of mines are concerned with the effects of mid- to far-field vibration on rock structures. Typical situations include underground operations directly below or adjacent to open pit mines using large-hole blasting practices or stopes that are in close proximity to shaft pillars. In both situations, it is necessary to be able to predict the effects of vibrations in mid- to far-field regions on underground structures and be able to alter blast designs to minimize impact of blasting on stability in these regions.

Blast damage is often tolerated when it only results in isolated and minor hangingwall or pillar slabbing and rock fall off. It cannot be tolerated when it affects the stability of a stoping area or when it causes excessive ore dilution from waste rock or adjacent backfill. The impact of blast damage on excavation stability is generally not well understood and therefore not incorporated into current excavation design methods. Arbitrary and empirical adjustment factors are applied in the current empirical design methods to roughly account for blast effects.

In conventional mining operations, empirical methods, methods based on trial and error and one's own experience, are used to determine the stable spans or the size of hangingwall exposures that can be achieved under different mining and geological conditions. This is particularly true in sub-level stopes with steeply dipping and/or weak hangingwalls. Blast effects can prevent achievement of the spans or exposures designed and deemed stable using static analyses. The blasting effects are not well understood and therefore are not incorporated into existing design methods.

Rock fragmentation problems (large boulders) in large stopes can often be dealt with by the mining system and the effects of poor fragmentation on daily production may be minimal. In small stopes where a single blast produces only 1500 tones, for instance, fragmentation is more critical to the daily production cycle. Such small-scale stopes can not afford delays or disruptions due to poor fragmentation. Many operations are now beginning to specify fragmentation requirements in order to maximize productivity in downstream processes such as transport, crushing and grinding. If this optimization

between mining processes is to be achieved, methods to enable greater control over fragmentation are required.

In narrow ore bodies, situations often arise where parallel stopes separated by a narrow pillar need to be extracted simultaneously (Szymanski et al., 1997). A conservative approach is often adopted where a stope is fully mined and filled before its neighboring stope can be worked. There are usually significant economies if the second stope can be worked while the adjacent stope is still open. This is not routinely practiced because the impact of blasting on exposed hangingwalls or narrow pillars is not well understood to allow the design of simultaneous operations with sufficient confidence and safety.

Practicing mine engineers continue to apply trial and error methods to establish optimum designs for a given geological environment, excavation size and geometry. Standards are sought that include blasthole diameter, explosive characteristics and timing required to achieve a desired result. The existing “rules-of-thumb” or published formulae do not provide the engineer with consistent procedures to derive initial blast design parameters as a systematic means to optimize a standard design.

An ordered sequencing of charge initiations with controlled time delays between shots is an important design consideration, which affects blasting performance. Fragmentation and muck distributions also depend upon the time delays between shots. In a typical blast pattern, proper sequencing is crucial since charge loading and spacing are selected on the assumptions that new free faces are opened and that each row of loaded blastholes removes a share of the burden (Dowding et al., 1985). Just as importantly, delay times

must be set in a way to prevent damage in the neighboring areas (Wilson et al., 1987; Medaris, 1977). Theoretical investigations (Hagan, 1986; Morhard et al., 1987) have shown that use of delay detonators in mine blasting enhances overall efficiency of the blast by providing a better distribution of load and a destructive interaction of blast waves in the rock mass resulting in lower amplitude blast vibrations. The latter is a complex process involving wave interaction phenomena, and the effect of wave frequency and the resonant frequency of the structure in question has to be considered as well.

Much greater attention is being focused on the effect of blasting on mining economics. It is evident from prior work that measurement techniques are not ideal or well established. Geology is seldom accounted for in characterizing and understanding the damage and its genesis, and few mines practice routine damage monitoring and quality control. If practical control over these operations is to be improved, it is necessary to develop a suitable engineering environment for the design and implementation of blasts at mines. This must incorporate effective tools for excavation design, rock fragmentation and dilution control, near-field as well as mid- to far-field damage control, and optimization of the mine production sequence.

The problems described above clearly demonstrate the need for a better understanding of the impact of blast designs and practices on excavation design, performance and integrity, particularly in mid- to far-field regions from the blasthole. A better understanding is also required of blasting effects on the local and global stability of a given excavation. Effective tools and a structured approach are required to derive an optimum blasting standard for any given mine geology, mining method and excavation geometry.

## ***1.2. Scope and Objectives of Research***

The most significantly used parameter in predicting rock damage in mid- to far-field region is peak particle velocity. The particle velocity criterion is empirical, site specific and dependent on the explosive type and material properties. This criterion and its application to blast damage control in mid- to far-field region will be elaborated in Chapter 2 of this thesis. In short, there are several techniques proposed by rock mechanics researchers to determine this parameter and to generalize its usage in various mining and geological environments. However, all these methods are geometrical and/or empirical and based on limited data from specific mine sites. Therefore, their application to mining environments other than what they were originally designed for could lead to errors in blast design with potentially serious consequences.

The objectives of this research are two fold: i) to adapt a theoretical model to investigate blast-induced rock damage in mid- to far-field regions from the blasthole; ii) to carry out an experimental program to measure monotonic and fatigue life properties of the granite specimens subject to shear loading.

The numerical model quantifies the cycling effect of blast vibration on rock behavior by taking into account the plastic response of rock to cyclic loading. The model is based on a sound theoretical basis and the material response to vibration is predicted based on its mechanical properties.

Through an experimental program, monotonic shear testing of rock specimens provides the required material properties that are the necessary input data for the numerical model. Fatigue shear tests are also performed to determine fatigue life curve of the rock under investigation.

### ***1.3. Research Methodology***

Blast-induced rock damage is modeled from the point of view of ground control and stability. The emphasis being on minimizing blast damage leading to failure of rock blocks in underground mines subject to blast cyclic loading. Blast-induced rock damage is assessed through the study of damage ahead of the shear cracks in rocks using the theory of dislocations. This would be a first step toward solving blast-induced shear crack growth problem in rocks; however the crack growth problem will not be studied here. The dislocation model was initially developed by Bilby et. al, (1963; and 1964) for elastic-perfectly plastic materials and was later extended to include linear work hardening materials (Bilby et al., 1965), as well. It was further developed for non-linear work hardening materials by Ellyin et al., (1986; 1987; and 1989). The plastic behavior of rock is modeled through the fundamentals of dislocation movements. In modeling plastic behavior of rock, following Ellyin and Fakinlede's non-linear work hardening approach (Ellyin et al., 1986; 1987; and 1989), both kinematic and isotropic hardening rules are examined. Rock mechanical behavior is modeled by a non-linear Ramberg-Osgood type behavior (Ellyin et al., 1986). Plastic displacement at the crack tip and within the plastic zone, defined by the dislocation migration mechanism, is calculated under both monotonic loading and unloading stages of a vibration cycle.

A series of monotonic and fatigue shear experiments are conducted based on the modified ASTM D 5379/D 5379M standard to measure shear properties of granite specimens and to obtain fatigue stress life (S-N) curve of the granite under shear cyclic loading conditions, with no confining pressure present.

#### ***1.4. Assumptions and Limitations of the Model***

In investigating rock damage by vibration, a number of assumptions are considered and the proposed dislocation model is developed with certain limitations. The assumptions and limitations of the model are:

- Only damage by far field shear stresses is investigated and damage due to other stress modes is not considered.
- The effects of confining stresses are not directly considered.
- It is assumed that only a single dominant shear crack is present in the rock. The interaction of shear cracks with one another thus, is not investigated.
- In analyzing rock stability, it is assumed that rock shears along the crack plane and by the assumption of infinite half-plane, other sides virtually create no resistance to rock movement.
- Monotonic and fatigue shear tests are performed in laboratory conditions without confining stresses effect. The temperature effect is disregarded as well.

### ***1.5. Scientific and Industrial Contribution of Research***

The scientific contribution of this research is the design of a shear test apparatus to test rock specimens under monotonic and cyclic shear loading. This design allows rock specimens to be tested under pure shear conditions.

In addition, a numerical model based on dislocation theory is used to estimate blast-induced damage to the rock. It is the first attempt to model rock cyclic loading with the aim of finding an alternative, yet practical, criterion to previously used peak particle velocity. This application of dislocation theory to rock damage problem contributes significantly to the solution of rock damage problem.

The industrial contribution of this research is the introduction of a non-empirical approach to analyze rock damage by vibration that takes into account both blast vibration energy content and mechanical properties of the rock. It is to be noted that the proposed approach provides a first approximation to the rock damage by vibration.

### ***1.6. Outline of the Thesis***

Following this introduction, in Chapter 2, mechanisms of blast damage, its implications, and conventional blast damage prediction methods and their limitations are discussed. Chapter 3 introduces the theory of dislocations and its development toward its application to model damage ahead of cracks in materials in the last three decades. The application of dislocation theory to rocks and rock mechanics problems is also introduced in this



chapter and the mathematical formulation of blast damage model is presented to determine rock plastic behavior during monotonic loading stage and unloading stage of the blast vibration cycles. Chapter 4 details an experimental program carried out to determine shear properties of the granite specimens under monotonic loading conditions. Fatigue tests were also performed on the same type rock specimens to find fatigue life properties of the rock under investigation. This chapter ends with discussions on the experimental observations and findings. In Chapter 5, the numerical results of the dislocation model using data from literature and also data obtained from the results of the monotonic tests on granite specimens are presented. And, finally Chapter 6 ends the thesis with summary, conclusions and further recommendations. A brief description of various theories of blasting, surface and underground mine blast design, and rock fragmentation is given in Appendix A. The Muskhelishvili's (1953) solution to Cauchy integral equation is re-derived in Appendix B. Further numerical results for various crack sizes and applied loads under monotonic loading and unloading are also given in Appendices C, and D, respectively.

## **Chapter 2: Literature Review**

Despite the fact that the significance of the costs of blast-induced rock mass damage in terms of mine stability, mine operations efficiency and safety is becoming increasingly recognized, there is still no straightforward and systematic method of adequately measuring blast damage in on-going mining operations. Blast damage measurement must account for the natural in-situ state of the rock mass, as well as the damage subsequently caused by blasting or mechanical excavation, and the redistribution of ground stresses (Lizotte et al., 1996). Rock mass damage has received relatively little attention compared to that related to residential and industrial structures. Assessment and control of rock damage in mid- to far-field regions from blast location has not been studied extensively and the conventional rock mass damage criteria are solely based on ground motion characteristics and are developed empirically. They are only suitable for similar geological and blasting conditions.

### ***2.1. Description of Rock Mass Damage and its Consequences***

It is important to discriminate between damage to the rock mass and failure of the rock mass. A rock mass is said to have failed when it is no longer able to support the loads applied to it, leading to its collapse. Damage, on the other hand, is any deterioration of rock mass strength due to the presence of newly generated or extended fractures or opening and shearing along existing rock joints. A rock mass may sustain considerable damage and yet be able to perform structurally for the period required by the mine. Some damage is inevitable after blasting operations but it is important to control the extent of

damage and its ramifications with regard to ore loss, dilution and support. If the extent of damage and its effect on excavation performance is predicted, potential instability, excessive dilution, or safety hazards may be prevented by modifying blast, excavation or support designs.

Rock mass damage is defined in a number of ways by rock mechanics researchers depending on the approach taken to tackle rock damage problem induced by the blasting and non-blasting processes. In following, the most notable definitions of rock damage due to blasting found in the literature are summarized.

Damage can be defined in terms of the proportion of the original rock mass that is able to carry load (Chitombo et al., 1990). Cracks and joints can carry normal compressive loads but can only carry a proportion of shear and no tensile loads. Based on this definition, the relative change in rock mass structure (i.e., fracture density) can then be related to its mechanical behavior by deriving a suitable relationship to relate rock mass behavior to changes in the rock mass structure. Oriard (1982) defines damage as the breaking and rupturing of the rock beyond the desired limits of excavation, applicable mainly to underground mines and also as unwanted loosening, displacement, and disturbance of the rock mass, the integrity of which needs to be preserved. Forsyth (1993) defines damage by over-break as the breakage or significant reduction in rock quality beyond the design perimeter of the excavation. McKown (1986) states that over-break and damage to the surrounding rock mass may lead to safety problems due to rockfalls, and additional costs. The additional costs could be due to additional mucking of extra rock; extra backfill material to fill over-break; additional rock reinforcement, i.e. rock anchors, steel sets,

wire mesh, etc., which may be required due to damage to rock walls. Additional pumping or grouting may also be required if it is below the ground-water table or if the joints or other discontinuities are opened by explosive gases. To determine the relative cost benefit of reducing over-break, these additional costs have to be determined. The reduction of over-break must be based upon a real increase in cost efficiency when both the benefits from over-break reduction and the decreased cost of the excavation are considered. Forsyth (1993) further reported on changes in blast design that reduced over-break in tunneling from 25% to less than 5% with a decrease in both the time for shotcrete application and the total volume of shotcrete required. Singh (1994) reported that over-break can be reduced by changing the explosives used and the initiation techniques. Doing so, he was able to reduce over-break from 13.6% to 4.2%.

In underground mines, Lizotte et al. (1996) stated that it is important to distinguish between damage related to blasting by vibrations and high pressure gases and damage caused by ground stress redistribution, before making any attempt to control the blast damage. According to Chitombo et al. (1990), gross damage to mine structures from either cause is observed as visible alteration to the appearance of the rock structure in the form of cracking, slabbing, over-break and visible displacement, this is while a reduction in the strength of a rock mass can occur well before the onset of these obvious signs of damage. Although the impact of damage is perhaps more evident underground, the causes of the overall rock mass damage, such as inherent damage caused by tectonic forces prior to mining or damage from stress redistribution in deep openings, are sometimes harder to distinguish.

Lizotte et al. (1996), also reported that underground mining efficiency is strongly affected by ore loss and dilution as well as by the need for additional ground support and restricted access for safety reasons. Rock damage may require the design of larger pillars, reduced stope sizes, and causes ore loss. Damaged ground presents hazards to both personnel and equipment. In fact, rockfalls and ground failure remains a leading cause of fatalities and injuries in underground mines. Plis et al. (1991) found that the detrimental economic effects of over-break arise from the fact that over-broken ground must usually be handled from the mined area, resulting in higher production costs. Liu et al. (1996) added that for economic and safety reasons, blast damage must be controlled to help reduce dilution of waste and filling material from the peripheral stopewalls into ore. Ricketts (1988) quantified the amount of blast damage for a large-scale blasting operation in oil shale in terms of manshifts of effort required to reclaim underground working areas after blasting.

In surface mining, one significant impact of blast damage is on the slope stability and the consequences for the working and final pit slopes. Bauer (1982) noted that if back-break is not controlled, a decrease in the overall pit slope angle will ultimately be necessary, and that would result to such consequences as reduced ore recovery and increased stripping (waste to ore) ratios. Also, greater amounts of loose face rock will be produced and planned safety berms will be less effective creating hazardous working conditions. Remedial measures, such as scaling large areas and using wire mesh or other artificial support, are very expensive and difficult to implement. The benefits of reduced rock mass damage include: the stripping ratio can be increased, mechanical support, scaling and secondary blasting costs can be reduced; the berm interval can be increased because the

pit walls and rock berms are more sound; costly damage to buildings or tunnels can be prevented or minimized by controlling vibrations from blasting; rockfall hazards to miners and equipment can be reduced since pit walls are smoother and less fractured; safety berms will be more effective in catching rockfalls because they have not been degraded by over-break or crest fracture from production blasting; and additional rock support requirement can be avoided. (Calder, 1977; Mohanty et al., 1986; Persson et al., 1993; Stachura et al., 1989).

In the close vicinity of the blasthole, damage is defined by the crushing of the rock mass that is shattered by the explosion. A few blasthole diameters away from the blasthole where intense fracturing and cracking occurs, the strength of the rock mass is severely weakened, causing reduction in load bearing capacity of the rock. In tunnel blasting, this type of damage will lead to over-break beyond the excavation boundary and may require additional clean up and scaling costs. In addition, in underground stopes, this could cause partial failure of the hangingwall leading to more dilution and less mine and mill efficiencies. In open pits, this would lead to slope stability problems, excessive movement of rock blocks and possible local failures endangering the mine equipment and safety of the work force.

In addition to blasting, Oriard (1982) reports a number of non-blasting sources of rock damage, which are more difficult to account for in the design process, and are often overlooked. These sources are i) the over-break due to poor drilling control, ii) displacement of the rock mass due to venting of explosive gases, and iii) loosening of rock blocks due to ground vibrations. Rossmann et al. (1997) also assessed the stability

of rock blocks subject to a non-blasting rock damage mechanism, i.e. rock block weight and thermo-vibration-fatigue loads using fracture mechanics and damage mechanics approach and estimated the fatigue life of the rock block.

In last few decades, there have been a number of attempts to assess rock mass damage due to blasting. In earlier studies, attempt was mainly to correlate damage to one or more parameters that can be measured in practice, i.e. peak particle velocity, and/or dominant blast vibration frequency. Later blastability indices were developed to account for the blast damage. More recent studies involve the modeling of rock mass damage by blasting using the-state-of-the-art numerical techniques such as discrete element modeling (DEM), finite element modeling (FEM), and discontinuous deformation analysis (DDA) technique. These techniques enable ground control engineer to simulate mine blasting and assess the stress field in the rock mass and the influence of blasting on ground behavior. The advantage of these methods over the single parameter damage models and empirical methods is their ability to model explosive energy knowing the thermodynamic properties of the explosives and the rock mass and their interaction with one another as the high stress waves and high-pressure gases spread outward from the blasthole toward the free surface. These methods have mainly been used to measure blast damage in the areas close to blasthole. In following, a review of the well known blast damage models and damage criteria is presented.

Rock damage studies by the Swedish Detonic Foundation in the 1970's resulted in a damage model (Holmberg et al., 1980). The damage model was based on the difference between pre- and post-blast fractures in core drilling. Damage was considered to occur

when the number of cracks after the blast was measurably greater than before the blast. Holmberg (1993) reported that damage was observed mainly in the rock discontinuities and joints, cracks, or other weakness planes in the rock mass. Rock mass integrity and continuity is disturbed through blast damage by different mechanisms. The main disturbing mechanisms causing damage to the rock mass include: crushing near the blasthole from the generation of high amplitude shock waves; generating new cracks and extending of these and existing ones in the rock due to the penetration of high pressure gaseous products; fracturing induced through spalling effects, slip of the blocks of rock along the weakness planes due to reduction of joint (fracture) shear strength which is caused by blast cyclic loading.

Villaescusa et al. (1990) developed a fully three-dimensional rock joint model to provide a quantitative representation of rock mass structure as an input to blast design and geotechnical models. Conventional line mapping or photogrammetric techniques could then be used to gather field data, and the most likely distributions of joint extension, location and orientation are calculated using geostatistical methods (Chitombo et al., 1990). In this method, knowledge of the joint distribution allows calculation of the size of the intact rock blocks that make up the rock mass. The size distribution of the intact blocks is used as a measure of the in-situ degree of fracturing and when compared to the final block size distribution, provides a quantitative measure of the change in rock structure caused by damage. This method mainly relies on the macroscopic changes (change in joint density, whether open or closed, size of the rock blocks, etc.) in the rock structure after the blast in nearby regions. It falls short of investigating how rock mechanically responds to the applied load; what changes takes place in the mechanical



behavior of the rock, and what causes those changes. This whole process here will be referred to as 'damage' incurred by the rock mass due to blast loading.

In another study carried out by Paventi (1995), two major causes for rock damage were distinguished, i.e. stress induced damage and blast-induced damage. In this study, which is basically from a geological point of view, the inherent damage arises from natural processes during certain geological processes. The state of stress in the rock mass prior to mining is the determinant factor in this type of rock damage and can be characterized by scan line mapping (Paventi et al., 1996). An inherent rock damage index was derived from the product of five damage components including intact rock strength component, Meso-structure component relating to joint sets and nominal spacing between them, fabric component referring to the geological nature of the rock mass, joint condition component relating to dominant discontinuity sets and the condition of discontinuity surfaces and macro-structure component referring to shears and faults existing in the rock mass. Mining induced damage index, which refers to blast-induced damage, is also derived from the product of these five parameters. This method empirically showed that blast-induced damage is directly related to inherent damage of the rock mass prior to blasting (Paventi et al., 1996). This blast damage criterion is similar to the blastability index proposed by Lilly (1986). Similar to Lilly's blastability index, this damage index also does not take into account the impact of blasting process, i.e. blast pattern, initiation sequence and explosive type, on the induced damage on the rock mass. The rock damage is predicted by considering the changes in the mechanical and structural properties of the rock mass with the use of aforementioned parameters for both inherent and blast-induced

sources. The form of the blastability index developed by Paventi (1995) can be found in Paventi et al. (1996).

It is notable that applying these techniques may reduce the blast damage, however, these techniques are purely empirical and only applicable to certain operations. They do not provide a general procedure for blast damage control since the blast energy generated by the explosives is not directly taken into consideration. This means for every operation, field or experimental observations have to be made and new empirical relationships are to be fitted to that particular case study.

## ***2.2. Mine Blast Damage Mechanisms***

An adequate understanding of blasting process will assist in selection of the most suitable blast design and explosive type. This would help optimize primary fragmentation and limit unwanted damage. Blast damage and the mechanism causing them can be categorized as i) near-field blast damage, and ii) mid- to far-field blast damage. These damage mechanisms will further be explained in following sections.

### **2.2.1. Near-Field Blast Damage**

Near field blast damage is caused by two major blast components, the high-energy stress waves and the high-pressure gases penetrating into weakness planes in the rock mass. In the following, each process will be described briefly with main focus on damage mechanism imposed on the rock mass.

High stress waves initiate new fractures and extend them along with the existing ones in the surrounding rock mass adjacent to the blasthole. Immediately following the detonation phase, stress waves propagate throughout the rock mass. As the stress wave front proceeds outward, it tends to compress the rock material at the wave front through a volume change. At right angles to this compressive front, there exists a tangential component that if it is large enough it can cause tensile failures at right angles to the direction of propagation. The largest tensile failures are expected to occur close to the borehole where the tangential stress is high enough for failure to occur. A tangential stress-induced failure in the rock mass creates new radial cracks in immediate vicinity of the blasthole. When the compressive wave front encounters a discontinuity or interface, some of the energy is transferred across the discontinuity and some is reflected back toward its point of origin, causing more damage to the already damaged region.

In the second stage of the blasting process immediately following high stress wave propagation, high-pressure gases penetrate into the newly generated and existing rock fractures. As the stress waves quickly attenuate, the high-pressure, high temperature gases impart a stress field around the blasthole. The gas pressure takes the path with the least resistance meaning that they will expand the original blasthole, and migrate into the existing and/or newly created cracks, joints, faults and discontinuities in addition to seams of materials that exhibit low cohesion or bonding at interfaces. High-pressure gases intensify rock damage by opening and extending already existing rock fractures.

As for the primary cause of the rock damage, there is a debate as to which of the two mechanisms described here dominate the blast damage process and causes more damage.

The difference in opinion about the main mechanism of rock breakage is rooted in the blasting theory used to explain the process of blasting and fragmentation. Various rock-blasting theories are briefly introduced in Appendix A.

### **2.2.2. Mid- to Far-Field Blast Damage**

In the mid- to far-field regions, the dominant mechanism of rock damage or failure is the shaking of wedges, key blocks or pre-conditioned volumes of rock due to cyclic loading of the bench walls and hangingwalls from subsequent nearby mine blasts. Repetitive blasting along the ore body has been known to severely weaken the stope surfaces by decreasing the joints shear strength and accumulation of shear displacements along the joints. Joughin et al. (1983) have suggested that large magnitude seismic events that occur away from excavations are due to shear failures on major fracture planes. Joughin et al. have added that these events are triggered by regional stress redistributions. It has also been reported by Holmberg et al. (1993) that most of the mine failures happen by slip along the rock fractures, joints, bedding planes, faults, etc. Urbancic et al. (1993) have shown that most microseismic events occurring at 10 meter from the excavation face fail by shearing under the influence of local variations in stress. As the blast wave propagates throughout the rock mass, it shakes the partially formed rock blocks along its path causing rock fractures to initiate and grow; it also opens the closed fractures and extends them along with newly generated cracks. Stress waves generated from the blast may create shear stresses that, if properly oriented with respect to the plane of the existing dominant crack, could generate slip. Dislocation theory can effectively be used,

in this case, to describe plastic behavior of the rock under applied far field shear stresses and assess rock damage by shear cyclic loading.

Of the two types of blast damage, the latter (mid- to far-field blast damage) is the focus of this study and will be further investigated. The plastic behavior of rock at the crack tip is assessed on the basis of the theory of dislocations using a non-linear work hardening material behavior (Ellyin et al., 1986; 1987; and 1989). The mechanism of rock damage by cyclic loading is investigated on the basis of the dislocation migration process at the crack tip. A numerical model based on the Fakinlede's (1985) dislocation model is developed to investigate shear crack plasticity in the rock with application into the blast-induced instability problem in hangingwall in production stopes.

### ***2.3. Blast Damage Estimation***

In assessing the performance of underground excavations subject to blast vibration loading, the issues of concern are the modes of rock mass response and the types of structural damage to the rock mass under cyclic loading and the design criteria for prevention or mitigation of damage. The response of an excavation to an episode of cyclic loading depends on the static condition of the excavation, as well as the transient effects associated with cyclic loading. In assessment of cyclic loading of excavations, Stevens (1977) and Owen et al. (1981) identified three modes of damage: fault slip, rock mass failure, and shaking. Excavation damage due to shaking appears to be the most prevalent, and is expressed as slip along fractures with displacement of joint-defined blocks, and local cracking and spalling of the rock surface (Brady et al., 1993).

Blast loading of the rock mass would result in a dynamic state of stress near the blasthole and a quasi-static state of stress is observed in mid- to far-field regions from the blasthole. As noted by Labreche (1983), the state of stress in underground excavations depends on the ratio of  $\lambda/D$ , where  $\lambda$  is the wavelength of the vibration waveform and  $D$  is the excavation diameter. Accordingly, when the duration of load is short, corresponding to a small  $\lambda/D$  ratio, excavation response is dynamic. A large  $\lambda/D$  ratio is said to correspond to a relatively prolonged loading, and the response is effectively static. Field experience that damage by shaking is predominantly due to movement along the joint, is consistent with the experimental observation that a joint shear strength decreases under shear cyclic loading (Brown et al., 1974). Model studies of excavations in jointed rock under cyclic loading by Barton et al. (1974) confirmed that excavation failure occurred by accumulation of shear displacements at joints. This is the basis of the conclusion by St. John et al. (1987) that it is the number of excursions of joint motion into the plastic range that determines dynamically induced damage to an excavation.

Despite the fact that a number of factors affect ground behavior and contribute to rock damage during blasting, conventional mining practices employ a single parameter to estimate blast-induced damage. They correlate damage during a sequence of cyclic loading to peak ground motion or the so called, peak particle velocity (PPV). Peak particle velocity is the most commonly used parameter to quantify and estimate damage in the rock mass. Peak particle velocity has been used to predict and/or control blast damage in various surface and underground mine operations. This damage criterion is purely empirical and site specific. To apply this technique to new geological conditions, field experiments must be performed to determine correlation parameters that

appropriately fit to the case under investigation. Peak particle velocity criteria were mainly developed in 1970's and 1980's. A number of weaknesses associated with this technique have been reported and more and more its sole application as a criterion to rock mass damage is questioned during the last decade. Recent studies have shown that in addition to particle velocity, there are other blast parameters that need to be considered when a general damage criterion is to be determined. These parameters include blast vibration frequency, rock mass properties, blast pattern, initiation sequencing, and delayed and non-delayed detonations (Vuolio, 1991, Morhard et al., 1987, Singh, 1992, Bawden et al., 1993, Yu et al., 1996, Bieniawski, 1974, Bieniawski, 1984).

McGarr (1981) suggested that peak particle velocity is the most appropriate parameter with which to correlate damage, since it can be related directly to peak transient stress in the ground wave. Finnish blast monitoring practices (Vuolio, 1991) have also reported that based on 900,000 vibration data recording from 52,971 blasts, the vertical component of peak particle velocity is the most practical description of damage in rocks. Vuolio (1991), however, stated that vibration frequency is of significance if a proper estimate of damage is desired, since the level of damage to the rock structure is directly related to the nominal frequency of the rock structure and the peak particle velocity. According to Vuolio (1991), dominant frequency is always obtained from the highest particle velocity in a single blast recording. This frequency is lower when the distance is greater and higher in hard rocks than in soft rocks. Observations by Morhard et al. (1987), Singh (1992), and Bawden et al. (1993) have also shown that damage to underground workings varies from one location to another, depending on site characteristics, within the same perimeter from the blast source.

In a study to assess rock damage solely due to shock wave energy (disregarding explosive gas infiltration), Yu et al. (1996) introduced a new damage index based on vibration level, rock properties, site characteristics and the effects of ground support system. In this approach, blast damage index is defined as a function of dynamic tensile strength of the rock, the compressive strength of the rock, rock density, compressional wave velocity and particle velocity. Bieniawski's CSIR classification system (1974; 1984) is also used to determine a spatial site constant. This constant is a dimensionless parameter, which quantifies the characteristics applied in the blast damage index. It incorporates effects of existing geological features on the extent of blast damage at a given site, which weaken the integrity of the rock mass and make it more susceptible to damage. It also takes into account the effect of ground support system that may increase the resistance of the rock mass to blast damage.

Although the significance of vibration frequency, among other parameters, has been realized theoretically, it has not been implemented in rock blasting practices. Mine blasters and ground control engineers still rely on the peak particle velocity readings alone to assess rock mass quality after the blast. To assess the blastability of the rock mass and predict the possible damage to rock structure from blasting, one must take into account the effects of several factors mentioned earlier. A proper damage criterion should be related to all parameters involved in carrying out a successful mine blast.



### **2.3.1. Determination of Critical Vibration Levels**

During stope production, one of the most critical issues is the determination of the critical blast vibration levels that will induce excessive damage to the surrounding rock mass. In conventional blast monitoring practices, trial and error is used to assess rock damage after each blasting for given rock types and explosives. Morhard et al. (1987) reported that blast damage criteria for tunnel stability is somewhat more characteristic and tailored to each specific area and only empirical relationships have been established to assess blast-induced rock mass damage. In these methods, based on the macroscopic changes in the rock mass structure after the blast, a set of trivial rules is adopted for a particular mine site. The structural changes are mainly the number of joint sets in the rock mass and the density of rock fractures, the static and dynamic mechanical properties of the rock mass, explosive type, blast pattern, and the initiation timing and sequencing. In addition to these methods, other empirical models have been developed to predict blast damage. These methods mainly rely on predicting peak particle velocity using various forms of scaling laws (Morhard et al., 1987). Other researchers (Lilley et al., 1998; Lilley, 1994; Persson et al., 1993), have derived empirical relationships based on the geometry of the blastholes with respect to point of observation to predict peak particle velocity. These methods are briefly described in following section.

### **2.3.2. Prediction of Peak Particle Velocity (PPV)**

During the past several decades, many damage criteria have been established and implemented with varying degrees of success. Rockwell's (1934) vibration energy

formula was the first attempt to develop a damage criterion against blast vibration. The damage criteria developments continue in today's government regulation regarding blast vibration control. Rockwell (1934) indicated that vibration energy caused by blasting was proportional to  $f^2 A_1^2$ , where  $f$  is frequency and  $A_1$  is vibration amplitude. The US Bureau of Mines (1942), incorporated the effects of charge quantity, ground character, and distance in this formula as:

$$A_1 = \frac{C^{\frac{2}{3}}}{100} (0.07e^{-0.00143d'} + 0.001)$$

where,  $A_1$  is the amplitude of ground vibration,  $C$  is the charge quantity, and  $d'$  is the distance. According to Morhard et al. (1987), the person monitoring a blast with this formula needed to estimate a suitable frequency for the vibration expected and a ground factor depending on the depth of overburden. The formula provided a conservative measure of structural damage through amplitude calculation and was frequency dependent. According to this formula, an acceleration of less than 0.1g was considered safe, 0.1-1.0g was caution, and greater than 1.0g was damage (USBM, 1942).

Crandell (1949) developed the concept of Energy Ratio, ER, defined as the ratio of the square of the acceleration to the square of the frequency, or  $ER = a^2/f^2$ . He proposed that damage caused by vibration be related to the energy in the disturbance. Designed to control blast damage to residential structures, Crandell's damage criteria were based on pre- and post-blast investigations of over 1,000 residential structures and suggested that damage occur at Energy Ratios above 6.0. Between 1949 and 1960 other damage criteria were established based on displacement, velocity, and acceleration. However, due to their

Table 2-1: damage criteria developed by Bauer et al. (1978) based on the particle velocity

<i>Peak Particle Velocity, in./sec (mm/sec)</i>	<i>Effects on rock mass</i>
Less than 10 (250)	No fracturing of intact rock
10-25 (250-625)	Minor tensile slabbing will occur
25-100 (625-2500)	Strong tensile and some radial cracking
Greater than 100 (2500)	Complete breakup of rock masses

incapability to address damage properly (Morhard et al., 1987), particle velocity was chosen as the best to represent damage to the residential and rock mass structures. Selected particle velocity damage criteria introduced after 1960 are as follows.

There are several empirical rules available in the literature to assess rock mass damage based on the magnitude of particle velocity in a given blasting. Langefors et al. (1948) predicted rock-falls in underground excavations at peak particle velocities exceeding 12 in/sec (300 mm/sec) and rock fracturing to occur at 24 in/sec (600 mm/sec). Oriard (1970) suggested that most rock masses suffer some damage at peak particle velocities above 25 in/sec (625 mm/sec). Bauer et al. (1978) developed a damage criterion for rock masses based on the stresses generated by ground motion due to blasting. This damage criterion is given in Table 2-1.

According to Morhard (1987), at some of the Sudbury basin mines in Ontario, damage is reported as being visible in the form of tensile slabbing when peak particle velocities approach 14 in./sec (350 mm/sec). In an underground haulage tunnel underneath Iron Ore Company of Canada's open pit mine in Labrador, the peak particle velocity is contained below 10 in./sec (250 mm/sec) at all costs since, the haulage tunnel is a very important part of the operation.

Dowding et al. (1978) following observations of excavations performance, proposed a lower and upper threshold particle velocities that were correlated with minor and substantial rock mass damage, correspondingly. These threshold values were 200 mm/sec and 400 mm/sec for minor and substantial damage, respectively. However, according to St. John et al. (1987), these threshold values are very conservative and are practically well below major underground explosion test programs. In these tests, damage associated with intermittent spalling was observed at 900 mm/sec, and continuous damage at 1800 mm/sec. However, according to Brady et al. (1993), these observations were made for single explosions with the purpose of establishing design criteria, and therefore are of limited relevance to the performance of permanent mine excavations which may be subject to many episodes of explosive loading during their operating lives.

#### ***2.3.2.1. Square Root Scaling Approach to PPV Prediction***

Another method of estimating peak particle velocity is by using empirical scaling formulas. Scaling is the designation of relationships correlating ground motion levels at various distances from blasts (Morhard et al., 1987). It is the normalization of the particle

velocity with respect to distance from the blasthole containing a given amount of explosive per 8 msec delay. In this method, a scaling factor that is based on the parameter distance that is normalized by the explosive weight, scaled distance, is used. The scaled distance is derived as a combination of distance and charge weight influencing the generation of seismic energy. The total energy of the ground wave generated in the rock around a blast varies directly with the weight of the charge detonated. As the ground motion wave propagates outward from a blast, the volume of rock subject to the compression wave increases. Since the energy in the ground shock is distributed over successively greater volumes of rock, the peak ground vibration levels would decrease. The empirical scaling formula relating peak particle velocity to scaled distance has been developed based on the vibration data obtained in the field using vibration-monitoring equipment. Scaled distance,  $d'/W'^{1/2}$ , combines the effects of total charge weight per delay,  $W'$ , on the initial ground shock level with increasing distance,  $d'$ , from a blast. This empirical formula as given below contains site-specific factors,  $K$  and  $m'$ , which allow for the influence of local rock characteristics on the rate of peak particle velocity attenuation. Geometric spreading is included in the slope exponential ( $m$ ) in the following equation (Persson et al., 1993):

$$PPV = K \left( \frac{d'}{W'^{1/2}} \right)^{-m'} \quad (2-1)$$

where,  $PPV$  is the peak particle velocity (m/sec),  $d'$  is the distance (m) between the blasthole and the point of investigation,  $W'$  is the total weight (kg) of explosives per a minimum of 8 msec delay, and  $K$  and  $m'$  are site factors. The term  $d'/W'^{1/2}$  is scaled

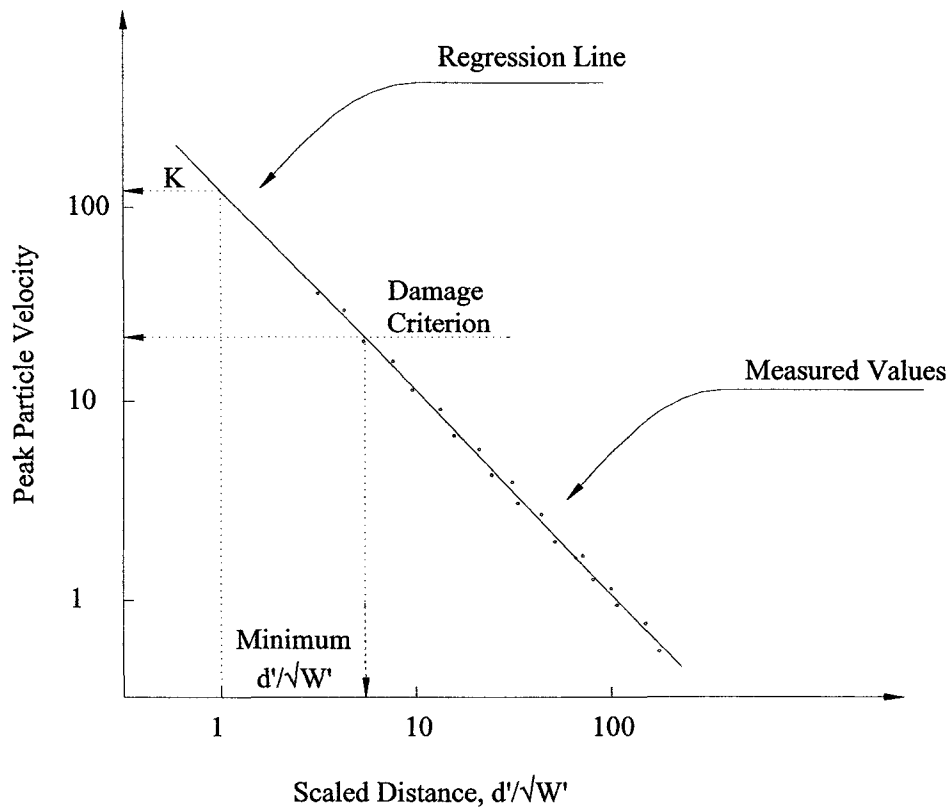


Figure 2-1: Schematic diagram of the regression line of the measured particle velocity in a log-log diagram and the determination of the lowest scaled distance,  $d'/W^{1/2}$  to be used.

distance for a cylindrical charge ( $m/Kg^{1/2}$ ). In this method, the peak particle velocity is correlated with scaled distance through  $K$  and  $m'$  indices.

The site factors  $K$  and  $m'$  are determined from logarithmic plot of particle velocity versus scaled distance.  $K$  is the intercept of the best straight line fitted to the data at the scaled distance of 1 and  $m'$  is the slope of the straight line found by regression analysis. The data is gathered by performing a number of tests in the area where the particle velocity prediction is to be made. Due to inhomogeneous nature of the rock mass, blast performance of the different explosive types, different blast patterns, etc. a large scatter is

normally found in between the fitted data and the regression line. A schematic log-log diagram of particle velocity and scaled distance is shown Figure 2-1. Before the diagram can be used to predict particle velocity, a maximum particle velocity characteristic of the rock structure and equipment in the area nearby the blasting has to be found. This level of particle velocity will act as the damage criterion beyond which damage occurs in the rock structure or equipment house. Knowing the particle velocity criterion, the minimum scaled distance corresponding to the maximum allowed particle velocity is determined from the diagram. The intersection between the damage criterion and the regression line gives the lowest  $d'/W^{1/2}$  value allowed to be used (Figure 2-1). Blasting has to be designed such that scaled distance for given blasting condition not to fall short of minimum allowed scaled distance. In other words, for each distance, a unique weight of charge is determined which must not be exceeded.

It is notable that regression line is not an upper limit for measured particle velocity. Therefore, it is probable that the damage criterion will be exceeded if the intersection point between the damage criterion and the regression line is used to determine maximum weight of charge. As a safety measure, one should shift the regression line so that all the points or a majority of points with a reasonably high correlation remain below the regression line. This is equivalent to decreasing the maximum allowed particle velocity or increasing the minimum scaled factor acceptable for given rock structure. Figure 2-2 shows a set of particle velocity diagrams versus scaled distance for four different line of confidence (Nicholls et al., 1971). In Figure 2-2, line 1 is the regression line and lines 2, 3, 4, and 5 are shifted regression lines for degrees of confidence shown in the Figure.

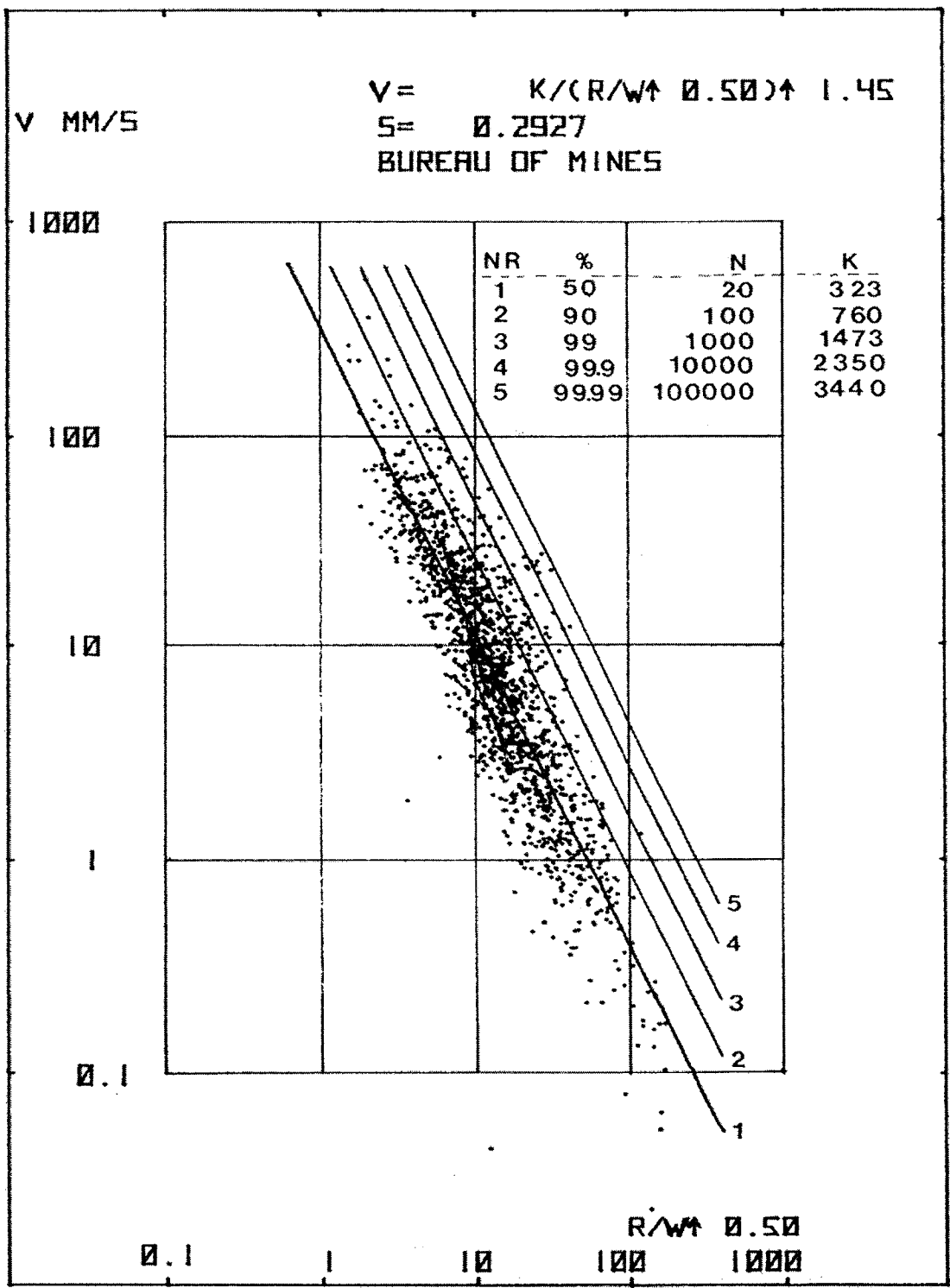


Figure 2-2: Confidence lines for US Bureau of Mines (Nicholls et al., 1971)



### 2.3.2.2. Geometrical Prediction of Blast Vibration – Persson’s Approach

Persson et al. (1993) proposed a geometrical method to estimate particle velocity in the region around the blasthole containing an extended charge. Figure 2-3 shows a schematic diagram of blasthole configuration and geometric representation of point of observation with respect to blasthole. In this method, an extended charge of length  $H$  with linear charge density  $\ell$  is placed in a blasthole in the rock mass. It is assumed that at any point away from the charge, the vibrations resulting from the detonation of each part of the extended charge are numerically additive. In addition, it is assumed that small differences in arrival times of shock front from the elements of an extended charge to the point of observation are negligible since the peak particle velocity occurs when the entire mass of rock is set to motion.

From the scaling law, the particle velocity resulting from a unit charge  $W_1$  at a distance  $d'$ , in general form, is given by:

$$PV = K' \frac{W_1^{\alpha'}}{d'^{\beta'}} \quad (2-2)$$

Persson et al. (1993) defined vibration intensity function,  $w'$ , as  $d'^{1.7}$  and 1.5 respectively. Persson et al. (1993) defined vibration intensity function,  $w'$ , as  $w' = \left( \frac{PV}{K'} \right)^{1/\alpha'}$ , and showed that

Equation (2-2) can be re-arranged and is shown by:

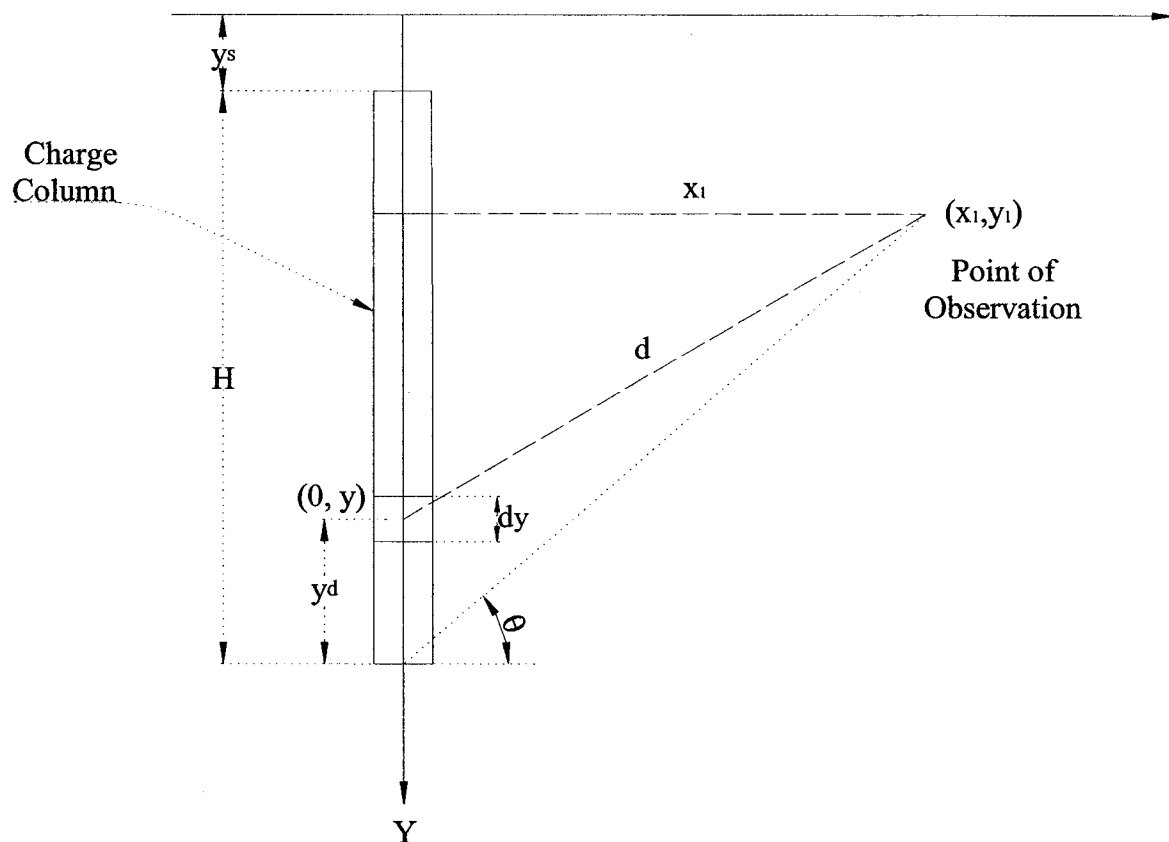


Figure 2-3: Schematic diagram of blasthole configuration and geometric representation of point of observation with respect to blasthole

$$w' = \left( \frac{PV}{K'} \right)^{1/\alpha'} = \frac{W_1}{d'^{\beta'/\alpha'}} \quad (2-3)$$

For very small charge  $dW_1$ , the vibration intensity,  $dw'$  is given by:

$$dw' = \frac{1}{d'^{\beta'/\alpha'}} dW_1 \quad (2-4)$$

Knowing  $dW_1 = \ell dy$ ,  $d = [x_1^2 + (x_1 \tan \theta - y_d)^2]^{1/2}$ ,  $x_1 \tan \theta = y_s + H - y_1$ , and  $y = y_s + H - y_d$ , Equation (2-4) is rearranged to get (Persson et al., 1993):

$$dw' = \frac{\ell dy}{[x_1^2 + (x_1 \tan \theta - y_d)^2]^{\beta'/2\alpha'}} = \frac{\ell dy}{[x_1^2 + (y - y_1)^2]^{\beta'/2\alpha'}}$$

By integration, the vibration intensity function,  $w'$ , is found:

$$w' = \ell \int_{y_s}^{y_s+H} \frac{dy}{[x_1^2 + (y - y_1)^2]^{\beta'/2\alpha'}}$$

Applying a simple change of variables, one can readily find the exact solution of this integral for the special case of  $\beta' = 2\alpha'$  (Persson et al., 1993):

$$w' = \frac{\ell}{x_1} \left[ \tan^{-1} \left( \frac{H + y_s - y_1}{x_1} \right) - \tan^{-1} \left( \frac{y_s - y_1}{x_1} \right) \right]$$

If combined with Equation (2-3), particle velocity is then given by (Persson et al., 1993):

$$PV = K \left( \frac{\ell}{x_1} \right)^{\alpha'} \left[ \tan^{-1} \left( \frac{H + y_s - y_1}{x_1} \right) - \tan^{-1} \left( \frac{y_s - y_1}{x_1} \right) \right]^{\alpha'} \quad (2-5)$$

Equation (2-5) shows the resulting particle velocity  $PV$  for a given linear charge concentrations  $\ell$  as a function of distance  $x_1$  ( $d'$ ) to the charge axis (Persson et al., 1993).

This method is a pure geometrical investigation into the blast vibration prediction and only considers blast configuration and the explosive type and the amount used. This ignores the effect of cyclic loading on the rock mechanical behavior and does not consider the dominant frequency of vibration.

### ***2.3.2.3. Geometrical Prediction of Blast Vibration – Lilley’s Approach***

In an attempt to control excessive dilution in the underground metalliferous mines in Australia, Lilley et al. (1998) proposed a vibration amplitude transfer function to quantify blast vibration-induced damage to the filling material. In this method, they estimated vibration amplitude of the blast in the ore and filling materials close to blast location, using transmissive properties of the ore and filling material, frequency spectrum of the blast vibration and the initial amplitude of the blast vibration. The quality of the ore and filling material were quantified using Q rock quality factor (Gladwin et al., 1974). The Q factor used in this study refers to attenuation characteristic of a stress wave traveling through a rock mass as described by Gladwin et al. (1974) and is not related to the rock mass classification scheme formulated by Barton et al. (1974). The blasthole configuration and observation points considered in this study are shown in Figure 2-4 (Lilley, 1994). The seismic attenuation properties of the geological materials, which

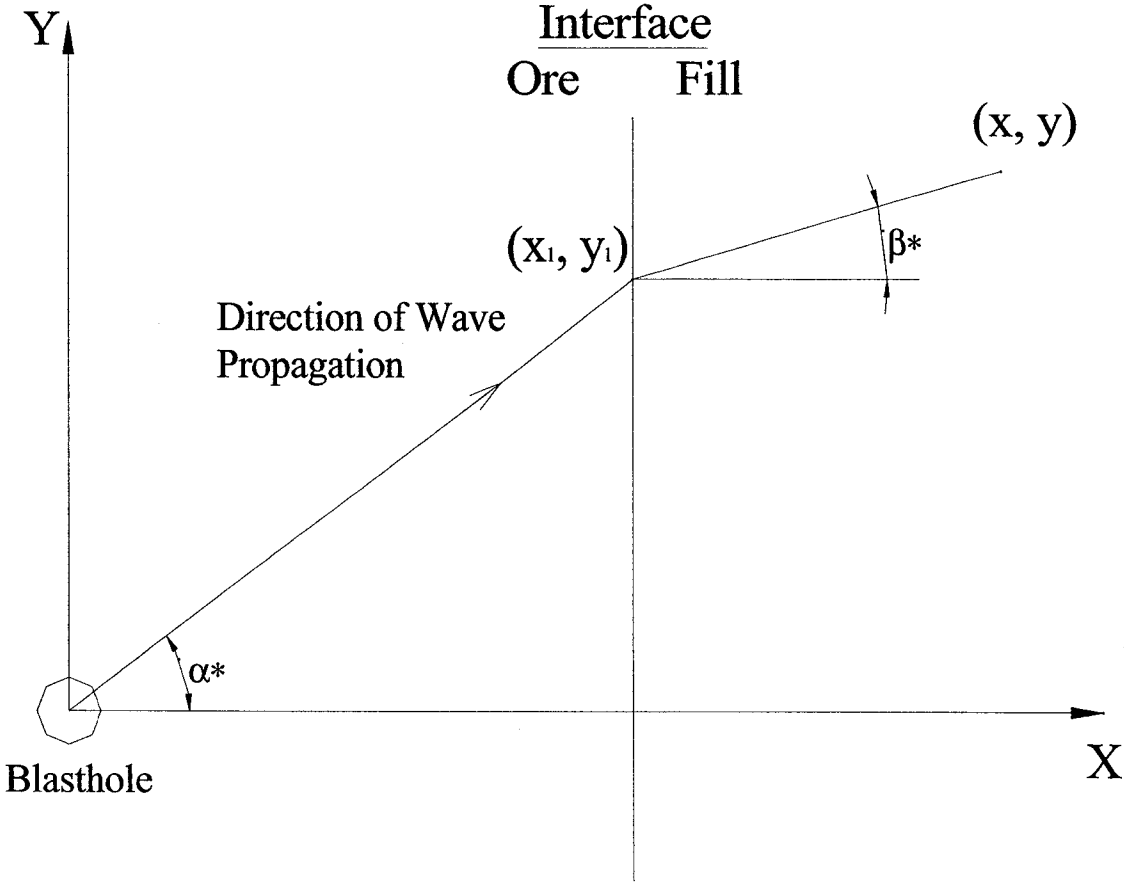


Figure 2-4: Geometry of blasthole and ore-filling material interface (Lilley, 1994)

consist of a geometric and a friction based phenomena (Lilley et al., 1998), were also considered in this study. They showed that vibration amplitude in the ore material could be shown as:

$$A_{ore} = \frac{A_0}{r_{ore}^{0.5}} \exp\left(\frac{-\pi r_{ore}}{Q_{ore} \lambda_{ore}}\right)$$

Similarly they obtained an expression for vibration amplitude at the interface of the ore and filling material:

$$A_{ore/filling} = \frac{2\kappa\eta_A}{n+1} \frac{A_0}{r_{ore}^{0.5}} \exp\left(\frac{-\pi r_{ore}}{Q_{ore} \lambda_{ore}}\right)$$

and in the filling material, they found the vibration amplitude as:

$$A_{(x,y)} = \frac{2\kappa\eta_A}{n+1} \frac{A_0}{(r_{ore} + r_{filling})^{0.5}} \cdot \exp\left(\frac{-\pi r_{ore}}{Q_{ore} \lambda_{ore}}\right) \exp\left(\frac{-\pi r_{filling}}{Q_{filling} \lambda_{filling}}\right)$$

where,  $A_0$ ,  $A_{ore}$ ,  $A_{ore/filling}$ , and  $A_{(x,y)}$  are the vibration amplitudes (mm/sec) in the blasthole, ore body, ore-filling material interface and filling material, respectively.  $r_{ore}$  and  $r_{filling}$  are distance (m) from blasthole along the path of propagation to the point of observation in ore body and filling material, respectively.  $Q_{ore}$  and  $Q_{filling}$  are dimensionless rock quality factors in ore body and filling material, respectively.  $\lambda_{ore}$  and  $\lambda_{filling}$  are pulse wavelength (m) in ore and filling material, respectively.  $\kappa$  is the amplitude reduction factor for transmitted p-wave,  $n$  is the ratio of characteristic

impedance of materials (ore and filling materials), and  $\eta_A$  is the strain energy absorption factor at the interface on the transmitted amplitude.

Lilley (1994) showed the vibration amplitude distribution between blasthole and the point of observation, in which the vibration amplitude attenuates farther from the blasthole. It also showed that vibration amplitude is magnified at the interface of the ore body and filling material. The reason for this behavior is believed to be due to change in transmissive and strength properties of the geo-media (ore versus filling material). In this method, a threshold vibration amplitude is obtained through an experimental study for every case study. Damage is defined to occur in the region where vibration amplitude is higher than the threshold value. Damage is defined by the plastic deformation of the filling material subject to dynamic loading. The extent of damage in this method is found by the vibration amplitude (particle velocity) in the ore and filling material. In other words, damage zone is defined by the entire area in which vibration amplitude is larger than threshold values. It is notable that the damage zone has been determined only by the amplitude of vibration and no account of how damage affects the material behavior is taken into consideration. Furthermore, filling damage (plastic deformation) does not necessarily mean failure and therefore more detailed study needs be undertaken. There are several assumptions made that need to be taken into consideration. These include: charge column is assumed to be parallel to interface of ore and filling material, only two dimensional space has been considered, effect of S-wave is assumed negligible, only the effect of blast shock wave and induced vibration is investigated and effect of gas pressurization is not included in this study (Lilley et al., 1998).

Despite their wide spread use in the mine operations to predict blast vibrations, peak particle velocity based approaches have several limitations and predictions made based on them may not be accurate enough for decision making on mine blast design, and ground support design/selection. The main limitations of these approaches are that:

- They do not explicitly take into account actual structural characteristics of the rock mass; i.e., whether the rock is massive or heavily jointed, the degree of fracturing, joint characteristics or the presence of key blocks. They relate damage to a critical level of vibration velocity alone without considering the total energy contained in the vibration, or the frequency of the disturbance.
- While approaches described may be applicable as a rough estimate to what is designated as preconditioning of the rock mass, they are certainly inaccurate and may not provide valid and reliable assessment of rock damage by blasting in mid- to far-field regions. In this case, damage is mainly due to the vibration and dislodging of wedges or key blocks by the cyclic loading generated by production blasts in adjacent stopes in underground mines.

To develop an appropriate rock damage criterion, a proper description of structure of the rock mass, indicating potential key rock blocks, its mechanical properties as well as the type and characteristics of the explosive used and the blasting mechanism, drill hole pattern, use of delayed detonation and sequence of blasting are required. The intended damage criterion has to be based on the mechanical response of the rock to cyclic loading which is related to the size of the blast and type of explosive used.



In the next section an energy-based blast damage model is introduced that is the main subject of this thesis. The energy-content of the vibration is incorporated into the model as input and the resulting damage to the rock is investigated.

#### ***2.4. An Energy-Based Blast Damage Prediction Model***

In this research program, a fracture mechanics approach is used to investigate blast vibration-induced damage in a rock of given type and mechanical properties. An energy-based model is introduced and damage in the rock is defined as the plastic displacement at the crack tip under given cyclic loading condition. A criterion is chosen for plastic displacement on the basis of the theory of dislocations. In this study, damage is considered to be resulted from plastic displacement at the tip of the newly generated or existing cracks in the rock.

The generation and extension of cracks in rock is the major mechanism of rock damage under blast loading conditions. The opening of a crack is induced by either shear displacement or a tensile force. In this study, only shear mechanism is considered as the major mechanism in opening the crack and causing damage. It is assumed that high confining pressures in underground excavations prevent opening of cracks under tensile stress conditions.

In this study, an approach, used in fracture initiation and propagation analysis in composite materials and metals, is applied to investigate crack tip plasticity in rocks under blast cyclic loading in mid- to far-field region. The application of this approach to cyclic loading analysis is unique in that it has not been applied to rock mechanics

problems before beyond the static analysis. In this method, rock damage is modeled by dislocation movements within the crack plastic zone while the rock is under loading and unloading stages of the vibration cycles.

In the current study, damage is defined as the mechanical state of the rock at which it behaves plastically subject to applied load. Damage starts as soon as rock reaches the plastic state, a state at which dislocation movement appears in the rock. The state of damage by dislocation movement will be elaborated in detail in the following chapter. The state of damage prevails until the state of the stressed rock reaches to the boundary of elastic-plastic region beyond which rock will behave elastically. Rock will be undamaged beyond the elastic-plastic boundary. Inside the boundary in the plastic zone, the rock is damaged by plastic displacement that is induced by the dislocation migration process.

In the next chapter, the theory of dislocations is introduced and its original application to crack plasticity problem by Bilby, Cottrel and Swinden (BCS) (Bilby et al., 1963) is reviewed. This chapter continues with the application of dislocation modeling to crack damage problem in rocks under cyclic loading.

## **Chapter 3: Theory of Dislocations and Its Application to Rock Damage by Cyclic Loading**

The mathematical theory of dislocations in elastic continuum was first systematically studied by Volterra (1907) and Weingarten (1901). The theory has been developed by many scientists for explanation of not only mechanical properties of crystals but also their optical and electromagnetic properties (Nabarro, 1967). Dislocations were applied to explain the plastic deformation of single crystals by Taylor (1934), Orowan (1934) and Polanyi (1934), independently. They considered dislocations as imperfections in crystals and explained why observed yield stresses of crystals are much lower than the theoretical values calculated from the atomic theory. They suggested that slip process occur via the operation of an edge dislocation (Lardner, 1974; Mura, 1969). An edge dislocation is one in which the direction of dislocation motion is perpendicular to the dislocation line.

When ductile materials are stressed beyond their yield limit it is observed that they undergo plastic deformation which is manifested as slip on a few suitably oriented planes. The planes on which plastic deformation occurs are known as slip planes. When a group of slip planes become active within the same neighborhood, they form a slip band.

After plastic straining, the dislocation density is observed to increase (Lardner, 1974). An important clue to the origin of the extra dislocations is provided by the observation that plastic flow tends to occur in concentrated amounts that is, the plastic strain is not spread uniformly throughout the material, but occurs as large amounts of slip on relatively few

planes. This may show up on the external surface in the form of slip-steps. In other words, as the shear load is applied, a large number of dislocations move on each active slip-plane increasing the density of dislocations at each point (Lardner, 1974).

Depending on the loading configurations, underlying material could experience various forms of deformations. Considering a material with a cut under given loading conditions, the relative displacement of the faces of the cut corresponds to rigid translations normal to the cut, in the plane of the cut, and in antiplane direction along the plane of the cut.

As a result, two different types of dislocations are created depending on the deformation configuration. Dislocations that are created by translation normal to the plane of the cut and those translated in the plane of the cut are called edge dislocations, in which the direction of dislocation motion is perpendicular to the dislocation line. Dislocations that are created by translation along the plane of the cut but in antiplane direction are called screw dislocations, in which dislocation motion is parallel to the dislocation line (Lardner, 1974). The vector indicating the direction and magnitude of dislocation advance is called Burgers vector,  $b$ .

### ***3.1. Discrete Distribution of Finite Dislocations versus Continuous Distribution of Infinitesimal Dislocations***

Because of the physical importance, a considerable amount of theoretical work has been carried out on dislocations in past decades. These analyses were based on two different approaches. In the first approach, the dislocations were treated as discrete singularities,

each with a finite Burgers vector (Mura, 1969). The original solution was given by Eshelby, Frank and Nabarro (1951), known as EFN solution, which is an exact solution. However, closed-form solutions are available for only a few simple cases. In this approach, the original equations are transformed analytically into a differential equation with a polynomial solution. The roots of the polynomial give the equilibrium positions of the free dislocations, and the properties of the polynomials provide relationships among the stress concentration, the number of dislocations, the density of dislocations and the applied stress. However, such a computation does not usually provide a general picture of the dislocation distribution in the material (Mura, 1969; Head et al., 1955). Furthermore, Olsson (1984) stated that due to singularities in both displacement and stress fields, as pointed out also by Weertman (1964), discrete dislocations approach is only appropriate in crystals because of their discrete atomic nature. In the second approach, introduced by Leibfried (1951) based on a powerful concept initiated by Eshelby (1949), the discrete dislocation arrangement is replaced by a continuous distribution of dislocations of infinitesimal Burgers vectors with the same total Burgers vector. This approach, although approximate for a finite number of discrete dislocations, is mathematically more tractable and provides solution for the limiting situation of a large number of discrete dislocations (Mura, 1969). Head et al. (1955) stated that little error is expected in this approximation when the distance between dislocations is of the same order as their width.

### ***3.2. Application of Dislocation Theory to Crack Problem***

In the last few decades, dislocation modeling has been extensively studied and developed to analyze crack tip plasticity in the materials subject to external loading and unloading.

In following, the development of this modeling technique is briefly reviewed for both monotonic loading and unloading for elastic-perfectly plastic materials (Bilby et al., 1963; Lardner, 1968). Its extension to nonlinear work hardening materials (Ellyin et al., 1986, and 1987) will then be described. The latter will be the basis of the modeling technique used to model shear crack damage in rocks subject to blast cyclic loading. This application will be explained in detail later in this chapter.

### 3.2.1. Monotonic Loading Model for Elastic-Perfectly Plastic Materials

Dislocation theory was initially applied to the analysis of plasticity at the notch roots by Bilby et al. (1963), known as BCS solution. In their solution, they represented the elastic-plastic strain (plastic relaxation) in the yielded region at the root of a notch in a steel specimen by a continuous distribution of infinitesimal dislocations in this region. They calculated the length of the plastic zone needed to accommodate a given plastic displacement at the root of a notch under a uniformly stressed condition. They solved this problem for a constant applied shear stress condition with no strain hardening i.e. for an elastic-perfectly plastic material, where no load reversal (unloading) considered.

Bilby et al. (1963) considered an infinite isotropic elastic medium subjected to a uniform applied shear stress at infinity, containing a plane crack of  $2c$  long and a distribution of straight dislocation lines lying in the plane of the crack (Figure 3-1). For applied shear stress  $\tau$  at infinity, the resistance to motion of the dislocations was taken to be  $\tau_0 (<\tau)$  in the region inside the crack ( $|x| < c$ ) and  $\tau_l (>\tau)$  in the region  $c < |x| < a$ . Therefore, the effective stresses in these regions would be (Bilby et al., 1963):

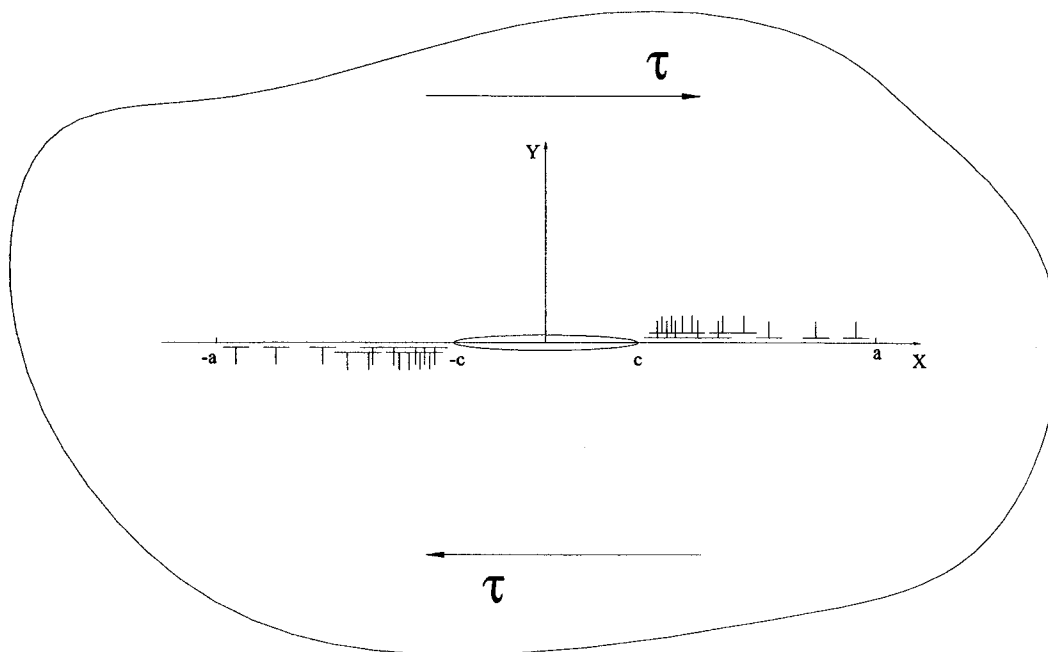


Figure 3-1: Array of dislocations at the tips of a crack in a medium subject to far field shear stress.

$$\begin{aligned} P_0 = \tau - \tau_0 &> 0 && |x| < c \\ P_1 = \tau - \tau_1 &> 0 && c < |x| < a \end{aligned} \quad (3-1)$$

Knowing the applied loading condition for this problem, Bilby et al., (1963) determined the dislocation density function,  $f(x)$ , for this problem as:

$$f(x) = \frac{P_0 + P_1}{\pi^2 A} \left\{ \cosh^{-1} \left| \frac{m}{c-x} + n \right| - \cosh^{-1} \left| \frac{m}{c+x} + n \right| \right\} \quad (3-2)$$

where  $A$ ,  $m$  and  $n$  are given by:

$$A = \frac{\mu b}{2\pi(1-\nu)}, \quad m = \frac{a^2 - c^2}{a}, \quad n = \frac{c}{a}$$

Applying the loading condition (3-1) to an appropriate crack boundary condition, they also found a relationship between the ratio of the crack size to the length of the plastic zone for the effective loading condition given in Equation (3-1) (Bilby et al., 1963):

$$\frac{c}{a} = \sin \left\{ \frac{\pi P_1}{2(P_0 + P_1)} \right\}$$

From this relationship it can be seen that  $a \rightarrow c$  if  $P_1/P_0 \rightarrow \infty$  that is  $P_1 \rightarrow \infty$  (infinite resistance to dislocation motion when  $|x| > c$ , meaning no dislocation movement and as a result no plastic zone is created) or  $P_0 \rightarrow 0$  so that  $\tau \rightarrow \tau_0$  (no resultant stress on dislocations when  $|x| < c$ ). Knowing the dislocation density function, the dislocation



density distribution can be plotted as a function of  $x$ , for elastic-perfectly plastic material behavior as given by Equation (3-2) and shown in Figure 3-2.

Bilby et al. (1963) also showed that the number of dislocations at any given point  $x$  in the plastic zone is given by:

$$\frac{\pi^2 A N(x)}{P_0 + P_1} = (x - c) \cosh^{-1} \left| \frac{m}{c - x} + n \right| - (x + c) \cosh^{-1} \left| \frac{m}{c + x} + n \right| + 2c \cosh^{-1} \left( \frac{a}{c} \right)$$

Accordingly, knowing that (Bilby et al., 1963):

$$\lim_{x \rightarrow c} \left\{ (x - c) \cosh^{-1} \left| \frac{m}{c - x} + n \right| \right\} = 0$$

the number of dislocations at the crack tip ( $x=c$ ) and at the end of the plastic zone ( $x=a$ ) are given by (Bilby et al., 1963):

$$\frac{\pi^2 A N(c)}{2c(P_0 + P_1)} = \cosh^{-1} \left( \frac{a}{c} \right) - \cosh^{-1} \left| \frac{c^2 + a^2}{2ac} \right|$$

$$\frac{\pi^2 A N(a)}{2c(P_0 + P_1)} = \cosh^{-1} \left( \frac{a}{c} \right)$$

The *relative* plastic displacement at any given point  $x$  in the plastic zone located in the positive side of the crack plane with respect to the negative side is given by (Bilby et al., 1963):

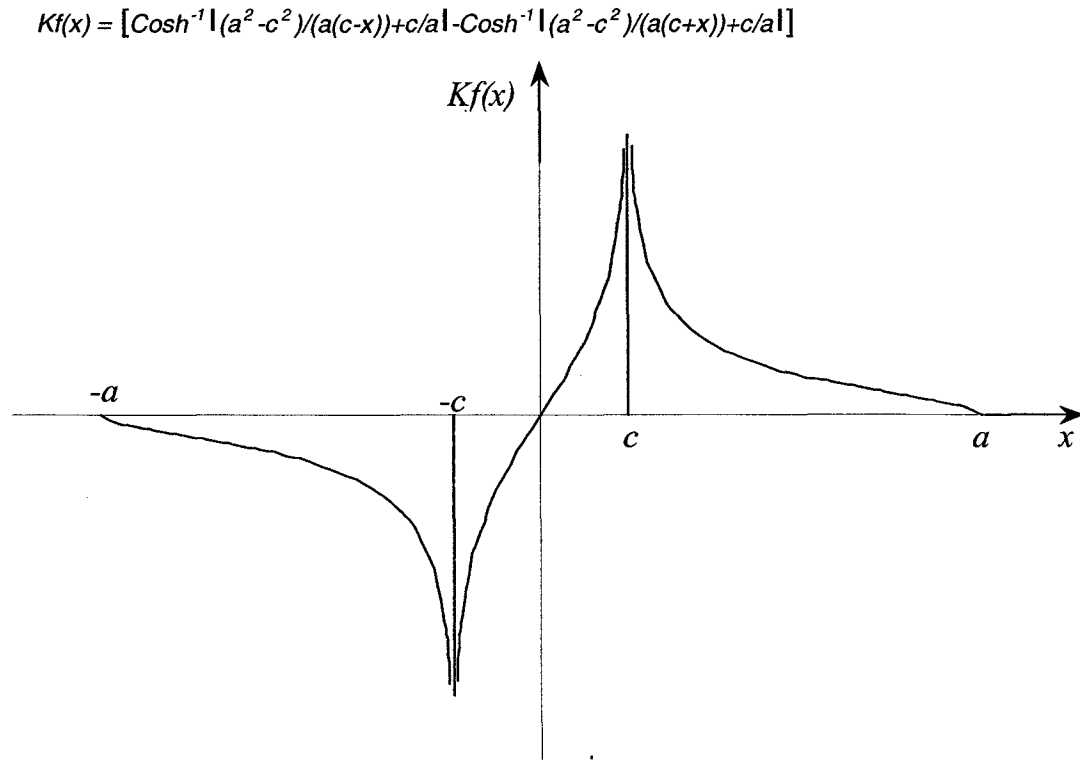


Figure 3-2: Dislocation density distribution under monotonic loading condition

$$u(x) = b\{N(c) - N(x)\}$$

Therefore (Bilby et al., 1963),

$$\frac{\pi^2 A u(x)}{b(P_0 + P_1)} = (x + c) \cosh^{-1} \left| \frac{m}{c + x} + n \right| - (x - c) \cosh^{-1} \left| \frac{m}{c - x} + n \right|$$

Bilby et al. (1963) showed that plastic displacement is maximum at the crack tip ( $x=c$ ) and drops to zero as it approaches the end of plastic zone ( $x=a$ ). They showed that their results are in good agreement with those of classical field plasticity by Hult et al. (1956).

Following their earlier work, Bilby et al. (1964) further developed their original model to investigate the spread of plasticity from one crack to another and how they influence one another. Bilby et al. (1964) reported that qualitatively, if conditions for catastrophic crack growth are satisfied before plasticity spreads fully between all the cracks, the body will appear brittle in the sense of failing at an applied stress below that for general yielding, even though large plastic strains may occur locally at the tips of individual cracks; whereas if the plasticity becomes general yielding before conditions for catastrophic fracture are satisfied, plastic deformation will continue and the body will appear slightly or fully ductile. It should be noted that the latter statement is only valid in the case of ductile materials where material could tolerate extensive plastic behavior before failing by a catastrophic fracture while the former statement is applicable to the behavior of the brittle materials such as rocks which show limited plastic behavior before catastrophic failure.

In this work, Bilby et al. (1964) investigated the spread of plasticity between a periodic sequence of cracks in an isotropic elastic medium subject to an externally applied shear stress  $\tau$ . According to Bilby et al. (1964), the loading condition in this case causes the material to deform in an anti-plane mode, which is represented by a continuous distribution of straight screw dislocations. The dislocation density function was determined based on their original solution (Bilby et al., 1963) by using a change of variables. They concluded that plastic relaxation spreads further in the presence of other cracks and the length of the relaxed zone required to accommodate a given plastic displacement at a crack tip is increased by 10%. Further details on this work are available in the original paper (Bilby et al., 1964).

Continuing their original work, Bilby et al. (1965) extended their original solution (Bilby et al., 1963) to account for linear work-hardening material behavior. Considering linear work-hardening material behavior, they related the material's resistance to dislocation motion to the relative displacement of the two crack surfaces (upper and lower surface of the slip plane). They studied the plasticity at notches by using an array of linear (edge) dislocations collinear with the crack itself using a critical displacement at the notch root as a criterion for plastic displacement to start. They further related the critical displacement to the applied stress, yield stress, notch size, size of the structure, and the extent of the plastic relaxation.

### 3.2.2. Unloading Model for Elastic-Perfectly Plastic Materials

As one of the many attempts to investigate fatigue crack growth under elastic-perfectly plastic conditions, Lardner (1968) used the theory of dislocations to investigate plastic displacement that takes place ahead of the crack tip under unloading conditions. He showed that, if the applied load is reduced to a lower level, a reversed shear loading on the dislocations is created. While the applied reversed stress is greater than the frictional resistance to dislocation movements, the reversed shear stress field forces some of the dislocations back into the crack tip. As a result, dislocation density ahead of the crack tip reduces and a reversed plastic displacement takes place as the material is unloaded. Figure 3-3 shows the dislocation density ahead of the crack under monotonic loading and unloading conditions (Lardner, 1968). The reversed plastic displacement vanishes, as the reversed shear stress becomes smaller than the frictional resistance of dislocations. The reversed plastic zone is bounded by the unloading dislocation density distribution at a distance ' $d$ ' from the crack tip (Figure 3-3), beyond which the dislocation density is the same for loading and unloading conditions.

Mathematical formulation of the dislocation model for unloading case for elastic-perfectly plastic materials is similar to the monotonic loading case given by Bilby et al. (1963) as shown in section 3.2.1. In this case, as material is loaded the BCS solution prevails. Once unloading is started, a reversed stress field is created in the plastic zone which causes some of the dislocations move back into the crack tip resulting in a reduction in dislocation density. The reduced dislocation density creates a reversed plastic zone inside the plastic zone generated by the dislocation movement under

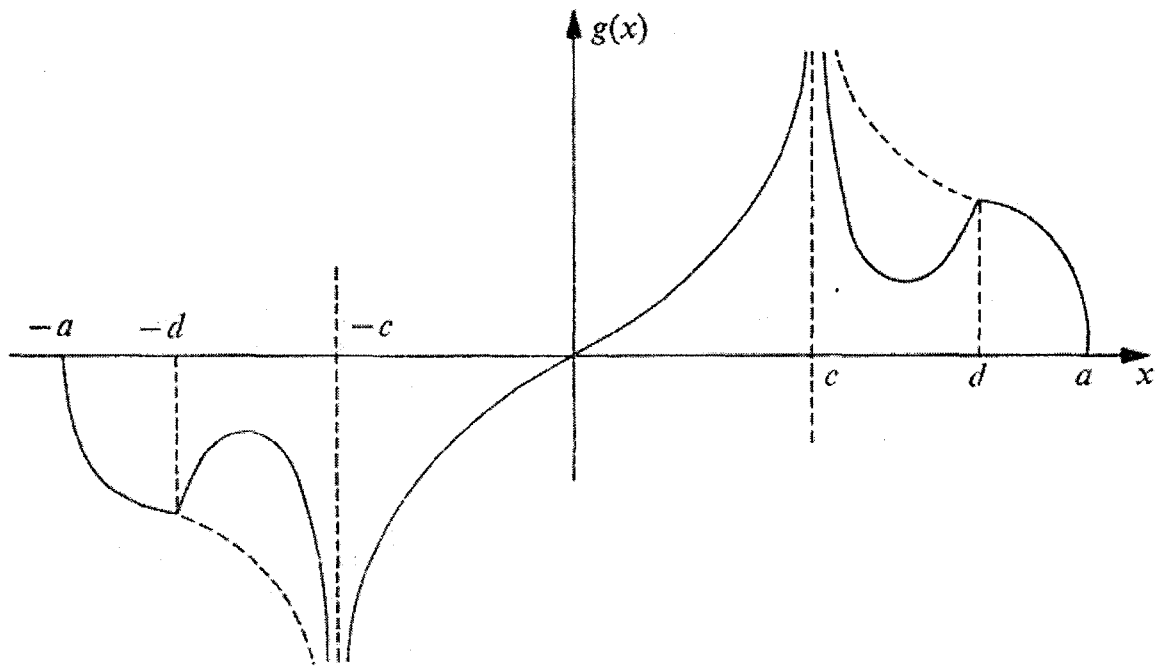


Figure 3-3: Dislocation density distribution under monotonic loading and unloading conditions (Lardner, 1968)

monotonic loading of the material. The reversed plastic zone size can be found in a similar way as it was found for the monotonic loading condition.

Lardner (1968) derived the mathematical formulation for the unloading problem for the elastic-perfectly plastic materials. If function  $g(x)$  represent the new dislocation density distribution after unloading has taken place as shown in Figure 3-3 and knowing that reversed plastic zone only extends to a limited part of the monotonic loading plastic zone i.e. ' $d$ ', the reversed plastic displacement in the reversed plastic zone can be determined numerically. If the applied load is reduced to  $\tau - \tau_u$ , a reduction in dislocation density takes place from  $f(x)$  to  $g(x)$ , where  $f(x) > g(x)$  (Figure 3-3). It is to be noted that reversed shear stress field has to be small enough (since material is not fully unloaded) so that not all dislocations move back into the crack tip. As a result, as soon as the acting reversed shear stress becomes less than the frictional resistance of the material to dislocation movement, reversed dislocation movement toward the crack tip is stopped. This would imply that beyond this point, dislocation density functions  $f(x)$  and  $g(x)$  will be equal. In the reversed plastic displacement region, the frictional resistance ( $\tau_f$ ) acts in the direction opposite to that it acted in monotonic loading case. Thus the reversed shear stress field loading function under unloading condition is given by (Lardner, 1968):

$$\begin{aligned} Q(x) &= \tau - \tau_u & |x| < c & \quad (a) \\ Q(x) &= \tau - \tau_u + \tau_f & c \leq |x| \leq d & \quad (b) \end{aligned} \tag{3-3}$$

The loading condition in the region between ' $d$ ' and ' $a$ ' is not known, however, it is not needed either since determination of reversed plastic zone does not require the loading

condition in this region. To solve the unloading problem, Lardner (1968; 1974) suggested subtracting cyclic loading equilibrium equation from the monotonic loading equilibrium equation, as well as the corresponding loading equations given by Equations (3-1) (considering  $\tau_0 = 0$ ) and (3-3). This would leave us with the change in the dislocation density function that is an indicator of the extent of the reversed plastic displacement ahead of the crack tip. Therefore,  $T(x)$ , the resultant loading function ( $P(x) - Q(x)$ ), is given by (Lardner, 1968):

$$\begin{aligned} T(x) &= \tau_u & |x| < c & \quad (a) \\ T(x) &= \tau_u - 2\tau_1 & c \leq |x| \leq d & \quad (b) \end{aligned} \quad (3-4)$$

It is important to notice the sign change because for the dislocations to move in monotonic loading condition, the applied shear stress  $\tau$  has to be greater than frictional resistance of the material,  $\tau_l$  ( $P_1 = \tau - \tau_1$ ,  $c < |x| < a$  in Equation (3-1)).

Using a technique similar to that of Bilby et al. (1963), Lardner (1968; 1974) solved the unloading problem for the elastic-perfectly plastic material behavior. He determined the extent of reversed plastic zone and the reversed plastic displacement ahead of the crack tip. Lardner (1974) showed that the ratio of crack length to the length of reversed plastic zone,  $c/d$ , and the amount of crack tip reversed plastic displacement,  $\Delta\phi$ , due to each unloading is given by:

$$\frac{c}{d} = \cos\left(\frac{\pi\tau_u}{4\tau_1}\right)$$



$$\Delta\phi = \frac{8(1-\nu)\tau_1 c}{\pi\mu} \ln \sec\left(\frac{\pi\tau}{4\tau_1}\right)$$

To find the effect of specimen size on his results, Lardner (1968) further modified his solution by using the original solution of the Bilby et al. (1963; 1964) of the effect of a series of cracks on one another. Further details about this work are available in the original paper (Lardner, 1968) or the contributor's book (Lardner, 1974).

### 3.2.3. Dislocation Model for Nonlinear Work Hardening Materials

Ellyin et al. (1986) further developed the original dislocation model by Bilby et al. (1963 - 1965) to account for the case of nonlinear work-hardening behavior of the material. This work provides a general model that can replicate the earlier BCS models in which the material behavior was considered elastic-perfectly plastic (constant yield stress) and linear work-harden. In this study, Ellyin et al. (1986) represented the work-hardening behavior of the material by relating the material's resistance to dislocation motion to the relative plastic displacement in the plastic zone ahead of the crack tip by a power law function. This implies that the post yield stress-strain relationship of the material modeled was nonlinear of the Ramberg-Osgood type.

Ellyin et al. (1987; 1989) further modified Lardner's (1968) model to account for nonlinear work-hardening material behavior. In their work, a power law function is used to represent the material behavior beyond the yield limit. Frictional resistance of the material was related to plastic strain at the crack tip using a power law function. They

further incorporated the memory effect (Bauschinger effect) in their model. They also considered both isotropic and kinematic hardening rules.

Following this introduction to the theory of dislocations, the application of dislocation migration model to rock damage problem in rocks subject to blast cyclic loading is investigated in detail and presented in the next section. A similar mathematical model developed by Ellyin et al. (1986; 1987) for both monotonic and cyclic loading of crack problem in metals is used in this study to assess rock damage by cyclic loading.

### ***3.3. Application of Dislocation Theory to Rock Deformation***

Laboratory experiments have shown that rock behaves elastically so long as the applied stress is less than the yield stress of the rock (Kidybinski, 1964; Kidybinski, 1965), as reported by Gil (1991). If applied stress exceeds material's yield strength, it will start to deform plastically until the point at which it fails. As the applied load exceeds the yield strength of the rock, stress concentrations around small defects inherent in the rock initiate cracks. Upon continued loading, microcracks coalesce and form a failure plane along which the rock failure happens. Plastic behavior of rocks depends on a number of factors including homogeneity, porosity, inherent defects, etc. Hard rocks tend to fail in brittle manner with limited plastic behavior followed by a strain-softening behavior reaching a residual strength. While soft rocks behave more plastically and their plastic response is more significant than hard rocks in their behavior under varying loading conditions. Both hard and soft rocks, however, show a transition from brittle to ductile behavior under confinement (Olsson, 1984). This is due to confining pressure closing

microcracks, preventing dilatation and increasing the contact area as a result of which the friction strength of the rock increases. In other words, confining pressure increases resistance to slip along the fracture plane.

Rock behavior is significantly affected by the nature of the applied loading environment. All materials including rocks demonstrate high peak strength under static loading while the same material shows much less strength if it is subjected to cyclic loads at lower levels than the peak strength of the material. This is due to damage accumulation in the rock under cyclic loading. It has been reported (Eberhardt et al., 1999) that under cyclic loading failure occurs when the crack population reaches a state, both in density and size, through which smaller cracks coalesce into larger cracks, and large scale crack interactions takes place. These, in turn, coalesce until a critical plane of failure is formed along which failure will take place.

The mechanism of elastic-plastic deformation developed in rocks can be explained through the theory of dislocations (Gil, 1991). According to this theory, a defect is an irregularity in structure of the material. A dislocation can be defined as linear defects, which are oriented arrangements of point defects (Gil, 1991).

The important role that dislocations play in the plastic deformation of rocks has been extensively studied (Griggs et al., 1960; Weertman, 1964; Raleigh, 1965; 1968; Young, 1966a; 1966b; 1969; and 1976; McGarr, 1971a; 1971b; Mavko et al., 1978; and Olsson, 1984) but not effectively investigated and applied in the common ground control techniques used in mining practices. Theory of dislocations has been used in a number of

studies to investigate the non-linear (plastic) behavior of rocks including study of the slip process along the faults caused by earthquakes (Weertman, 1964), the deformation of non-elliptical thin cracks in a loaded elastic rock (Mavko et al., 1978) and to study the slippage process associated with non-uniform frictional resistance (Olsson, 1984). Weertman (1964) showed that slippage on the fault plane that is due to earthquake loading could be initiated by dislocations. In his study, Weertman (1964) used Bilby et al., (1963) method to determine dislocation density functions for loading case and further developed an unloading model based on the original Bilby et al., (1963) model for the elastic-perfectly plastic material behavior.

Detailed work by Young (1966a; 1966b) on dislocation behavior in olivine illustrated the effects of dislocation densities and dislocation movements in ductile rock behavior. It further related the yield point in rocks to the behavior of dislocations as well. Young (1966a) showed that the derivative of strain along a shear zone defines a strain gradient, which is physically and mathematically equivalent to a continuous distribution of infinitesimal dislocations. This strain gradient would give rise to a stress field that is identical to that caused by the dislocation distribution and can be calculated by applying dislocation theory. Young (1966a; 1969) found an empirical relationship between dislocation density and the shear strain. It showed that dislocation density increases with shear strain.

McGarr (1971a; 1971b) carried out an analysis based on the theory of dislocations to provide a quantitative description of the plastic deformation that occurs near the edges of underground excavations and stopes at deep levels in brittle rocks. In this work, McGarr

(1971a) modeled the plastic deformation in the surrounding rock by edge dislocations that move on the slip plane under the effect of in-situ stresses. McGarr (1971a) argued that the interaction of dislocations with the in-situ stresses (disturbed by the mining operations) would lead to migration of dislocations into the surrounding rock. The continuous migration of dislocations essentially leads to formation of a fractured zone in the surrounding rock. This process consumes much of the energy released by expanding the stope and also relaxes the intense stress field near the edge of the underground excavation and stope.

Olsson (1984) studied the slippage process associated with non-uniform frictional resistance in rocks in terms of continuous distribution of infinitesimal dislocations. Using a non-uniform frictional resistance, he showed that stress-plastic strain curves exhibit non-linear, history dependent characteristics such that the slope of the diagram at any stress depends strongly upon the previous stress path. Olsson also investigated the effect of normal stress variations on the stress-plastic strain behavior using dislocation approach and found that it mimics the same behavior found experimentally.

It is to be noted that, in the current investigation, the application of continuous distribution of infinitesimal dislocations as opposed to discrete dislocations to rock is adopted. It is assumed that rock is smeared out of (discrete) dislocations. It is also worthwhile to mention that, here, any reference to any type of dislocation is merely a physical device to aid visualization of plastic process in the rock.

### ***3.4. Rock Damage Model by Dislocation Arrays***

When rock is loaded in shear, plastic deformations (slip) occur. According to the weakest link criterion, a material subjected to shear loading fails (slips) at the point where it has the least resistance and that would be the dislocation lines. As the applied load increases, local stresses ahead of the crack tip exceed the resistance opposing the dislocation movements, causing dislocations to start to move (Figure 3-1). Under the application of an external shear load dislocations move out of the crack plane. Under sustained loading, dislocations move further into the rock due to which the dislocation density ahead of the crack tip increases. Due to high stress concentration at the crack tip, more dislocations move along the slip plane ahead of the tip of the crack, which causes higher plastic displacement (damage) in this region.

Here, a nonlinear work hardening stress-strain relationship is used to model rock behavior prior to ultimate failure. Knowing that rocks behave differently under loading and unloading cycles, a different constitutive relationship has to be used for each case. This is because under unloading rock plastic behavior is affected by the Bauschinger effect (memory effect) (Olsson, 1984). In following, a dislocation model based on the nonlinear work hardening model of Ellyin et al. (1986; 1987) is developed for the case of monotonic loading and unloading of the rock. Rock damage, defined as the plastic displacement under cyclic loading, is then determined.

### 3.4.1. Monotonic Loading Stage

Consider a partially formed block of rock located in a stope wall under equilibrium conditions. The block geometry is defined by the existing cracks that are known from previous geological and exploration studies. These cracks may intersect and form a partial block of rock of regular or irregular shape. Here, it is assumed that a rectangular shaped partial rock block is formed by the existing cracks as shown in Figure 3-4. It is also assumed that all block sides except the bottom are fractured and separated. The bottom of the block is partially fractured. The damage at the tip of the bottom crack of the block will then be assessed by the dislocation model. For the reason that is given below, the back of the block, shown by the shaded area, is assumed to be completely separated and has no resistance to loading. Figure 3-5 schematically shows the crack at the bottom of the rock block.

The block is subjected to two types of loads: i) a transient cyclic load that attenuates fast. This load is applied as a result of blasting in mid- to far-field regions with respect to the point of investigation; and ii) the gravity load, which is a static load and is negligible compared with the transient load. It is to be noted that, crack length may reach a critical length upon which the gravity load will be enough to cause block failure even in the absence of blast transient load. In this case one needs to take into account the gravity load, as it will be the significant factor in the stability of the rock block. Depending upon the orientation of the block and the stress wave approaching the block, the applied transient load could have shear and normal components acting upon the bottom crack. Applied shear stress components that act in parallel directions to the crack plane, cause

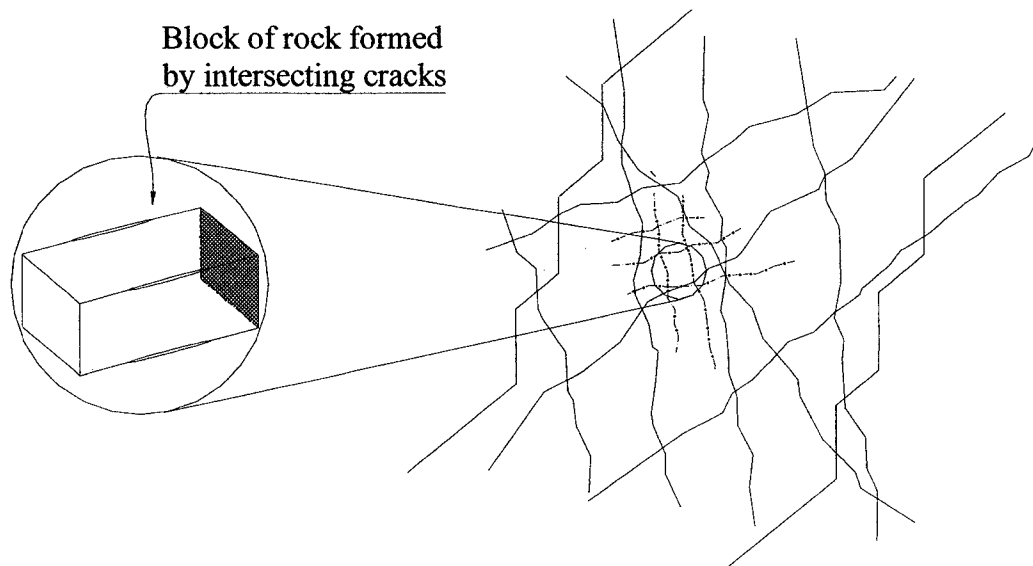


Figure 3-4: Schematic diagram of a block of rock formed by the intersecting cracks in the rock.



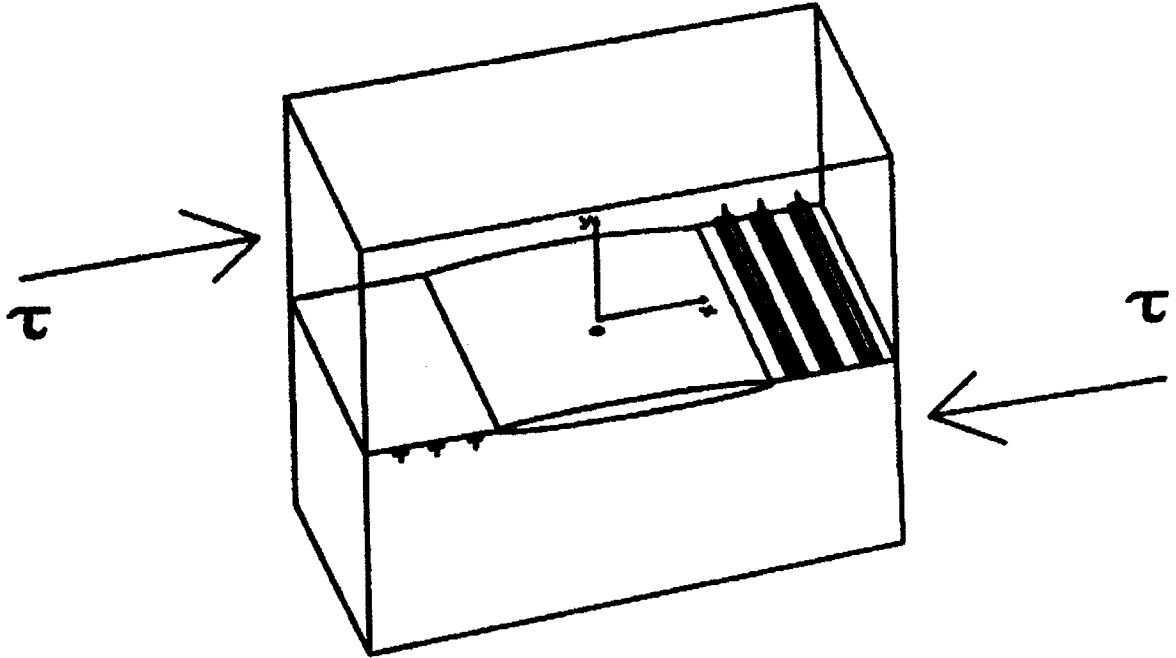


Figure 3-5: Schematic diagram of the crack at the bottom of the rock block under blast cyclic shear load (the condition of infinite half plane still applies).

mode II and/or mode III fractures, while applied normal stress component acts in the perpendicular direction to the crack plane and causes mode I fracture. However, due to confinement, the displacements caused by modes I and III are assumed to be negligible and only mode II fracture is considered significant and is studied here. An applied load, acting in shear on the bottom crack, acts as a tensile stress on the back and, if large enough, may cause a mode I opening fracture at the back of the block. This fracture mode will not be analyzed in this study and therefore, it is assumed that the back of the block is already separated and has no resistance to the applied load. Subjected to cyclic loading and unloading, rock experiences damage at the tip of the existing cracks in the form of plastic displacement. This may eventually lead to crack propagation and block instability. The frictional resistance here is the only resisting force against the applied load.

Consider a plane crack at the bottom of the rock block at  $y=0$ ,  $-c \leq x \leq c$ ,  $-\infty \leq z \leq \infty$  in an isotropic rock subjected to a far field shear stress ( $\tau$ ). The rock contains a distribution of long straight dislocation lines lying parallel to  $z$  direction in the  $xz$  plane (see Figure 3-1, Figure 3-4, and Figure 3-5). According to the principles of the fracture mechanics, there is no resistance to motion of the dislocations inside the crack i.e. crack faces can slip freely and the resistance to the motion ahead of the crack tip ( $c < |x| < a$ ) is governed by the frictional resistance,  $\tau_r(x)$ , only. In this region, dislocation movements caused by the applied shear stress,  $\tau$ , creates plastic displacement at the tip of the crack, which will extend throughout the plastic zone ahead of the crack tip. This is principally explainable in terms of a row of edge dislocations co-planar with the crack (Lardner, 1968). As the load is increased from zero to  $\tau$ , dislocations move out

from the crack tip into the rock, driven by the stress concentrations at the crack tip and opposed by the resisting shear strength,  $\tau_r(x)$ .

A general power law form of non-linear work-hardening material behavior similar to what was originally proposed by Ellyin et al. (1986), in which the frictional strength is the only resistance to the dislocation motion, is used to define rock behavior. A general power law form work-hardening rock behavior can only be applied to rocks prior to ultimate failure up to the peak strength of the rock. Therefore, this generalized model is represented by:

$$\tau_r(x) = m \tau_0 \left( \frac{\varphi(x)}{\varphi_0} \right)^n = F[\varphi(x)] \quad (3-5)$$

where  $\varphi(x)$  is the total shear displacement and  $n$  is the work-hardening exponent.  $m$  is a dimensionless constant depending on material properties. The total displacement consists of plastic displacement  $\varphi_p(x)$  and the elastic yield intercept,  $\varphi_0$ , i.e.  $\varphi(x) = \varphi_p(x) + \varphi_0$ .

Therefore, Equation (3-5) can be re-written as:

$$\tau_r(x) = m \tau_0 \left( \frac{\varphi_p(x)}{\varphi_0} + 1 \right)^n \quad (3-6)$$

The post-yield behavior of the material is non-linear of the type of Ramberg-Osgood (Ellyin et al., 1986). For continuously distributed dislocations with Burgers vector  $\mathbf{b}$  and a density function  $f(x)$  at each point, the equilibrium condition requires that the sum of all

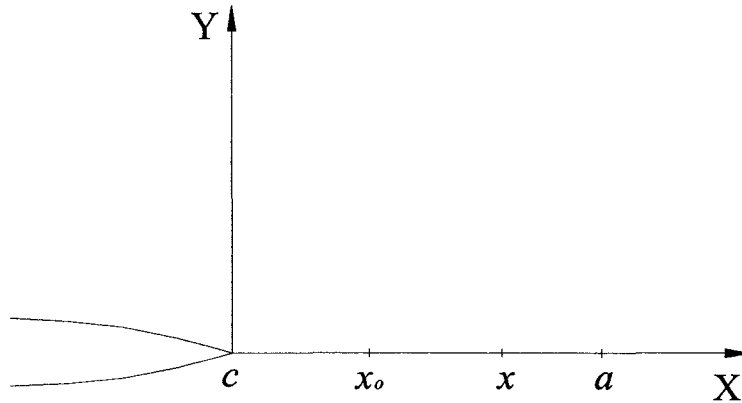


Figure 3-6: Shear stress within the crack tip plastic zone

forces, dislocations and external, at each point to be zero (Head et al., 1955). The shear stress at point  $x$  due to all dislocations at  $x_0$  (Figure 3-6) is given by (Bilby et al., 1963):

$$P'(x) = \frac{Af(x_0)dx_0}{x - x_0}$$

Hence, knowing shear stresses due to external sources given by  $P(x)$ , for equilibrium:

$$P'(x) + P(x) = 0,$$

thus,

$$\int_{-a}^a \frac{f(x_0)dx_0}{x - x_0} + \frac{P(x)}{A} = 0 \quad (3-7)$$

where  $A = \frac{\mu b}{2\pi(1-\nu)}$ ,  $\mu$  is the shear modulus,  $\nu$  is the Poisson's ratio and  $P(x)$  is the applied external stress, and is given by:

$$\begin{aligned} P(x) &= \tau & |x| < c & \quad (a) \\ P(x) &= \tau - \tau_r(x) & & \quad (3-8) \\ &= \tau_0 \left[ \frac{\tau}{\tau_0} - 1 \right] - \tau_0 \left[ \frac{\tau_r(x)}{\tau_0} - 1 \right] & c \leq |x| \leq a & \quad (b) \end{aligned}$$

It is notable that to avoid divergence at  $x = x_0$  the Cauchy principal value of the singular integral equation (Equation (3-7)) must be taken. According to Head et al., (1955), the self stress of dislocations is excluded from the equilibrium equation. This is the physical meaning of the principal value of the Cauchy integral.

As shown in Appendix B, the general solution of the Equation (3-7)) is given by Muskhelishvili (1953) as

$$f(x) = \frac{2(1-\nu)}{\pi\mu b} \int_{-a}^a R(x,y)P(y)dy \quad (3-9)$$

where

$$R(x,y) = \frac{1}{x-y} \sqrt{\frac{a^2-x^2}{a^2-y^2}}$$

provided that the  $P(x)$  satisfies the Hölder condition. Fakinlede (1985) and Ellyin et al., (1986) have shown that a power law work-hardening loading function satisfies Hölder

condition and therefore the solution given above is valid. If a plastic displacement  $d\phi$  is obtained as  $f(x)$  dislocations move from point  $x$  to  $x+dx$  under the applied stress, knowing that total Burgers vectors in this region ( $x \rightarrow x+dx$ ) is  $bf(x)dx$ , the total plastic displacement  $\phi_p(x)$  can be shown as

$$\phi_p(x) = b \int_x^a f(x') dx' \quad (3-10)$$

Substituting Equation (3-9) into Equation (3-10),

$$\phi_p(x) = \frac{2(1-\nu)}{\pi\mu} \int_x^a \int_{-a}^a R(x', y) P(y) dy dx' \quad (3-11)$$

To distinguish between the non-hardening and hardening parts of the solution in the region  $c \leq |x| \leq a$ , while factoring out yield stress  $\tau_0$ , the functions  $P'(x)$  and  $P''(x)$  are introduced respectively, as:

$$P'(x) = \frac{\tau}{\tau_0} - 1$$

$$P''(x) = \frac{\tau_r(x)}{\tau_0} - 1 = m \left( \frac{\phi_p(x)}{\phi_0} + 1 \right)^n - 1$$

Therefore, the Equation (3-8b) can be re-written as

$$P(x) = \tau_0 P'(x) - \tau_0 \left[ m \left( \frac{\phi_p(x)}{\phi_0} + 1 \right)^n - 1 \right] \quad c \leq |x| \leq a \quad (3-12)$$

Substituting (3-12) into (3-11), the plastic displacement function,  $\varphi_p(x)$  will be:

$$\varphi_p(x) = B\tau_0 \left[ \int_x^a \int_{-a}^a R(x', y) P'(y) dy dx' - \int_x^a \int_{-a}^a R(x', y) P''(y) dy dx' \right] \quad (3-13)$$

where  $B = \frac{2(1-\nu)}{\pi\mu}$ . Equation (3-13) is the governing equation for the plastic displacement function for a nonlinear work-hardening material in monotonic loading condition, only. To solve this equation, a boundary condition must be identified and satisfied. The dislocation density function has to be zero at the end of the plastic zone, meaning that the general solution of the Muskhelishvili should be bounded at the end of this zone,  $x = \pm a$  i.e. this solution, as shown in Appendix B, at the boundary reduces to:

$$f(x) = -\frac{[R_1(x)]^{1/2}}{\pi^2 A} \int_{-a}^a \frac{P(x') dx'}{(x'-x)[R_1(x')]^{1/2}}$$

where  $R_1(x) = (x+a)(x-a)$ .

And, for  $f(x)$  to be zero at the boundary requires that (Ellyin et al., 1986):

$$\int_{-a}^a \frac{P(x') dx'}{[R_1(x')]^{1/2}} = 0 \quad (3-14)$$

In these equations also the Cauchy principal value of the singular integral is to be taken. Substituting Equation (3-8) for  $P(x)$  in Equation (3-14), knowing  $\tau_r(x) = 0$  inside the crack ( $|x| < c$ ), we get:

$$\int_{-a}^a \frac{\tau - \tau_r(x')}{(a^2 - x'^2)^{1/2}} dx' = 0$$

or

$$\int_{-c}^c \frac{\tau dx'}{(a^2 - x'^2)^{1/2}} + \left( \int_{-a}^{-c} + \int_c^a \right) \frac{\tau - m\tau_0 \left( \frac{\phi_p(x')}{\phi_0} + 1 \right)^n}{(a^2 - x'^2)^{1/2}} dx' = 0 \quad (3-15)$$

Equation (3-15) is the boundary condition for the Equation (3-13), the governing equation of the plastic displacement function. Equation (3-13) can only be solved numerically. The solution of Equation (3-13) under boundary condition (3-15) yields the plastic displacement function for monotonic loading.

The first term in Equation (3-13) is known as the *BCS* solution (Bilby et al., 1963) for the elastic-perfectly plastic problem. The *BCS* solution was modified by Falkinlede (1985) and is given by,  $\phi_1(x)$ :

$$\phi_1(x) = (x+c) \cosh^{-1} \left| \frac{a^2 - x^2}{a(x+c)} + \frac{x}{a} \right| - (x-c) \cosh^{-1} \left| \frac{a^2 - x^2}{a(c-x)} + \frac{x}{a} \right|$$

Equation (3-13) can then be rearranged as follows (Fakinlede, 1985):

$$\phi_p(x) = B\tau_0\phi_1(x) - B\tau_0 \int_x^a \int_{-a}^a R(x',y)P''(y)dydx' \quad (3-16)$$

By expanding the second term in Equation (3-16), we get:



$$\varphi_p(x) = B\tau_0\phi_1(x) - B\tau_0 \int_x^a \left[ \int_{-a}^c R(x', y)P''(y)dy + \int_c^a R(x', y)P''(y)dy \right] dx' \quad (3-17)$$

The second term in the bracket in Equation (3-17) is zero since crack surfaces are already separated and can slip freely with no resistance inside the crack; therefore, plastic displacement is zero in this region. For the given function  $R(x, y)$ , Falkinlede (1985) has shown that:

$$\int_{-a}^c R(x', y)P''(y)dy = \int_c^a R(x', -y)P''(y)dy$$

Therefore,

$$\varphi_p(x) = B\tau_0\phi_1(x) - B\tau_0 \int_x^a \left[ \int_c^a \{R(x', y) + R(x', -y)\}P''(y)dy \right] dx'$$

After further rearrangements,

$$\varphi_p(x) = B\tau_0\phi_1(x) - B\tau_0 \int_c^a \left[ \int_x^a \{R(x', y) + R(x', -y)\}dx' \right] P''(y)dy \quad (3-18)$$

If we define the bracket in Equation (3-18) as the kernel,  $K(x, y)$ , by:

$$K(x, y) = \int_x^a \{R(x', y) + R(x', -y)\}dx' \quad (3-19)$$

Fakinlede (1985) showed that kernel is given by:

$$K(x, y) = \cosh^{-1} \left| \frac{a^2 - x^2}{a(x-y)} + \frac{x}{a} \right| + \cosh^{-1} \left| \frac{a^2 - x^2}{a(x+y)} + \frac{x}{a} \right| - 2 \sqrt{\frac{a^2 - x^2}{a^2 - y^2}} \quad (3-20)$$

Thus, Equation (3-18) can be re-written in this form:

$$\varphi_p(x) = B\tau_0\phi_1(x) - B\tau_0 \int_c^a K(x, y) \left[ m \left( \frac{\varphi_p(y)}{\varphi_0} + 1 \right)^n - 1 \right] dy \quad (3-21)$$

Equation (3-21) is a Fredholm Integral Equation of the Second Kind. To solve equation (3-21), using one of expansion methods (Delves et al., 1974), a perturbation of the elastic-perfectly plastic solution of the *BCS* is introduced and the plastic displacement function,  $\varphi_p(x)$ , is defined, as suggested by Fakinlede (1985), by

$$\begin{aligned} \varphi_p(x) = & \alpha_1(x+c) \cosh^{-1} \left[ \left( 1 + |\alpha_2| \right) \left| \frac{a^2 - x^2}{a(c+x)} + \frac{x}{a} \right| \right] - \\ & \alpha_3(x-c) \cosh^{-1} \left[ \left( 1 + |\alpha_4| \right) \left| \frac{a^2 - x^2}{a(c-x)} + \frac{x}{a} \right| \right] + \alpha_5 e^{-\alpha_6(x/a)} + \alpha_7 e^{-\alpha_8(x^2/a^2)} \end{aligned} \quad (3-22)$$

or simply

$$\varphi_p(x) = \sum_i \alpha_i \varphi_i(\alpha_i, x)$$

Substituting  $\varphi_p(x)$  into Equation (3-21) the problem will invert to solving a non-linear regression problem by minimizing:

$$\min. \sum_{j=1}^{m_1} \eta_j^2 \quad (3-23)$$

where  $m_1$  is the number of points taken within the plastic zone and  $\eta_j$  is given by:

$$\eta_j = \phi_p(x_j) - B\tau_0\phi_1(x_j) + B\tau_0 \int_c^a K(x_j, y) p''(y) dy$$

The problem now inverts to solving Equation (3-23) with boundary condition (3-15). There are eight unknown coefficients in Equation (3-22), therefore, at least 8 equations are needed to solve the system of equations with boundary condition (3-15). However, by choosing more points an over-determined system of equations is obtained (Ellyin et al., 1986). This system of equations can be solved using one of optimization techniques. Levenberg-Marquardt's (LM) algorithm (Scales, 1974) is used to find the optimum solution of the system of equations. One only needs an initial estimate in this algorithm to find the optimal solution for  $\alpha_i$ . For  $\alpha = (1, 0, 1, 0, 0, 1, 0, 1)^T$ , one would recover the BCS solution for elastic-perfectly plastic case and so it is used as the initial estimate for LM algorithm.

In Equations (3-23) and (3-15), the plastic displacement coefficients,  $\alpha_i$ , and the extent of the plastic zone,  $a$ , are unknown. The solution process is as follows: For two arbitrary values of plastic zone length,  $a$ , the nonlinear regression problem, Equation (3-23), is solved. Then knowing the coefficients,  $\alpha_i$ , the boundary condition (3-15) is tested for each case. Then, the extent of plastic zone is modified accordingly and Equation (3-23) is solved iteratively until the boundary condition (3-15) is satisfied with sufficient accuracy.

Knowing the plastic displacement coefficients,  $\alpha_i$ , the plastic displacement function,  $\varphi_p(x)$ , is obtained as a function of  $x$ , the position within the plastic zone, using Equation (3-22). Then, the stress field in front of crack tip is found using Equation (3-6).

### 3.4.2. Unloading Stage

Mathematical formulation of the rock behavior under monotonic shear loading condition was derived in previous section. Weertman (1964), and Lardner (1968) investigated the plastic displacement occurred ahead of the crack tip under unloading conditions using an elastic-perfectly plastic, and Ellyin et al. (1987) studied the same problem for a material with non-linear work-hardening behavior. They showed that, if the applied load is reduced to a lower level, a reversed shear loading on the dislocations is created. While the applied reversed stress is greater than the frictional resistance to the dislocation movement, the reversed shear stress field forces some of the dislocations to move back into the crack tip. As a result, the dislocation density at the crack tip reduces and a reversed plastic displacement takes place in the reversed plastic zone, as the block is unloaded.

Figure 3-7 shows the dislocation density distribution ahead of the crack under unloading conditions (Ellyin et al., 1987). The reversed plastic displacement vanishes, as the reversed shear stress field becomes smaller than the frictional resistance opposing the dislocation movement. The reversed plastic zone is bounded by the unloading dislocation density curve at distance  $d$  from the crack tip (Figure 3-7), beyond which dislocation

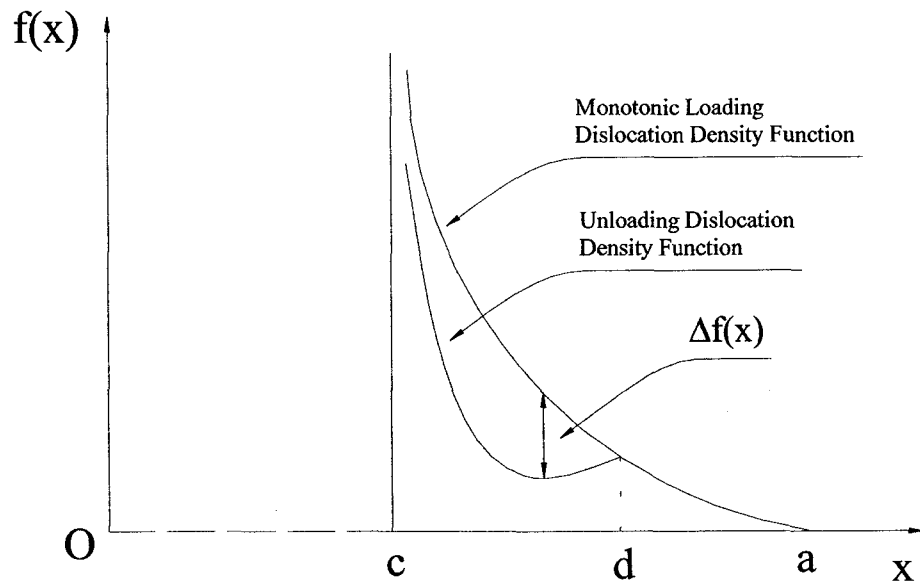


Figure 3-7: Loading and unloading dislocation density distributions ahead of the crack tip (adopted from Ellyin et al. (1987))

density is the same for both loading and unloading conditions. The plastic behavior of material under unloading depends on its characteristics whether or not it has a memory effect (Bauschinger effect). Bauschinger effect can be shown for a one-dimensional case as in Figure 3-8 (Ellyin et al., 1987). For  $\tau_r(x)$ , the maximum shear stress under monotonic loading, if  $\tau_h(x)$  indicates the amount of stress required to reach to the  $\tau_r(x)$  from the yield stress,  $\tau_0$ , then  $\tau_h(x)$  is the stress level required to reach a plastic strain of  $\gamma_p$ . Combined with the parameter  $\beta$ , it may also be used to indicate the type of hardening rule to be used for a given material. As shown in the Figure 3-8 for different values of  $\beta\tau_h(x)$ , material would show a different hardening behavior. For  $\beta = +1$ , it reflects the kinematic hardening rule, at which Bauschinger effect is considered, i.e. material starts to yield under unloading sooner than it did under monotonic loading indicating the memory effect. For  $\beta = -1$ , it shows the isotropic hardening rule, which means material starts to harden at similar stress level under loading and unloading.

A distinguishing fact about the two hardening rules is that under isotropic hardening conditions, yield surface expands uniformly in all directions with the centre of yield surface at the centre of coordinate system while under kinematic hardening conditions, yield surface does not expand, it rather shifts in the direction of loading path while keeping its original size.

Considering the resultant dislocation density ahead of the crack tip and using the same technique that was used in the monotonic loading analysis, one can derive the governing equations of the reversed plastic displacement function under unloading conditions. In the

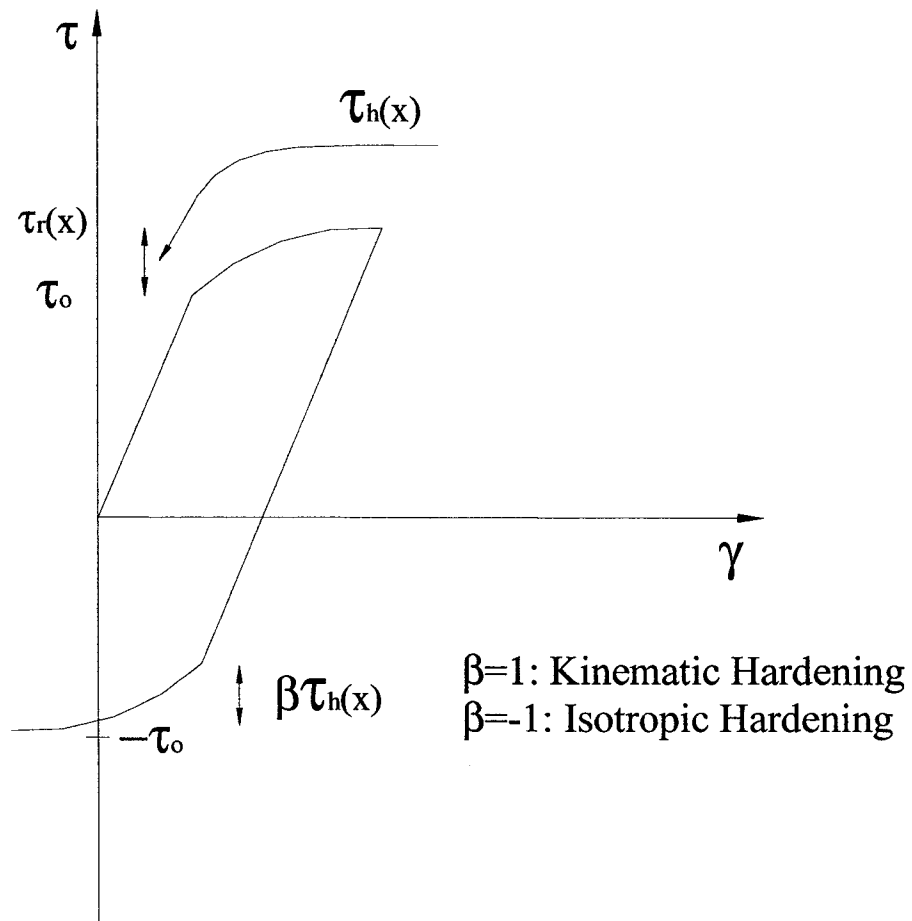


Figure 3-8: Schematic diagram of shear stress-strain relationship for monotonic loading and unloading (adopted from Ellyin et al. (1987))

following, the mathematical formulation of the material behavior under unloading using the theory of dislocations is derived in the same manner as Ellyin et al. (1987).

If the applied load on the rock block is reduced to  $\tau - \tau_u$ , the reduction in dislocation density from  $f(x)$  to  $g(x)$ , where  $f(x) > g(x)$  (Figure 3-7), results in a change in the plastic displacement. A functional form of the frictional stress similar to what was used in monotonic loading is used for unloading case in which plastic displacement function,  $\varphi_p(x)$ , is replaced by the change in the plastic displacement function,  $\Delta\varphi_p(x)$ . The change in the plastic displacement function is due to change in dislocation density distribution under unloading, therefore (Ellyin et al., 1987),

$$\tau_{rr}(x) = F[\Delta\varphi_p(x)] - \beta\tau_h(x) \quad (3-24)$$

where  $\Delta\varphi_p(x)$  is the change in plastic displacement due to unloading,  $\beta\tau_h$  accounts for the change in the yield surface due to hardening, parameter  $\beta$  is valid in the range  $[-1,1]$  and determines the plasticity hardening rule discussed earlier.  $\tau_h(x)$  is defined by:

$$\tau_h(x) = \tau_r(x) - \tau_0 \quad (3-25)$$

If  $g(x)$  indicates the dislocation density function after unloading, to satisfy the equilibrium requirement at the crack tip, the sum of all the applied forces, internal and external, must be zero. That is:



$$\int_{-d}^d \frac{g(x')dx'}{x-x'} + \frac{Q(x)}{A} = 0 \quad (3-26)$$

where the reduced applied load,  $Q(x)$  is given by

$$\begin{aligned} Q(x) &= \tau - \tau_u & |x| < c & \quad (a) \\ Q(x) &= \tau - \tau_u + \tau_{rr}(x) & c \leq |x| \leq d & \quad (b) \end{aligned} \quad (3-27)$$

The loading function between  $d$  and  $a$  is unknown, however, as the change in plastic displacement occurs between  $c$  and  $d$ , the load function between  $d$  and  $a$  is not important to the solution of unloading problem.

Since the change in plastic displacement is due to change in dislocation density, subtracting  $g(x)$  from  $f(x)$ , and following the same method as for monotonic loading part, we obtain an analytical form for the change in the plastic displacement under unloading. Therefore, subtracting Equation (3-26) from Equation (3-7), we get

$$\int_{-d}^d \frac{[f(x') - g(x')]dx'}{x-x'} + \frac{T(x)}{A} = 0 \quad (3-28)$$

where  $T(x)$ , using Equations (3-5), (3-8), (3-24), (3-25), and (3-27), is given by

$$\begin{aligned} T(x) &= \tau_u & |x| < c & \quad (a) \\ T(x) &= \tau_u - \tau_r(x) - \tau_{rr}(x) & & \quad (3-29) \\ &= (\tau_u - 2\tau_0) - (1 - \beta)[F(\varphi_p(x)) - \tau_0] - [F(\Delta\varphi_p(x)) - \tau_0] & c \leq |x| \leq d & \quad (b) \end{aligned}$$

Similar to Equation (3-10), the change in the plastic displacement due to unloading is given by:

$$\Delta\phi_p(x) = b \int_x^d (f(x') - g(x')) dx' \quad (3-30)$$

In a similar way to the solution of Equation (3-7), using the method of Muskhelishvili (1953), the solution of Equation (3-28) is found to be:

$$[f(x) - g(x)] = \frac{2(1-\nu)}{\pi\mu b} \int_{-d}^d R_u(x, y) T(y) dy$$

where  $R_u(x, y)$  is given by:

$$R_u(x, y) = \frac{1}{x-y} \sqrt{\frac{d^2 - x^2}{d^2 - y^2}}$$

When it is substituted into Equation (3-30), one obtains the change in the plastic displacement function,  $\Delta\phi_p(x)$  as given by:

$$\Delta\phi_p(x) = \frac{2(1-\nu)}{\pi\mu} \int_x^d \int_{-d}^d R_u(x, y) T(y) dy dx' \quad (3-31)$$

The loading function  $T(y)$  in the region  $c \leq |x| \leq d$ , (Equation (3-29)b) can be divided into three parts as follows:

$$\begin{aligned}
T_1(x) &= 2\tau_0 \left( \frac{\tau_u}{2\tau_0} - 1 \right) \\
T_2(x) &= -\tau_0(1-\beta) \left[ \frac{F(\varphi_p(x))}{\tau_0} - 1 \right] \\
T_3(x) &= -\tau_0 \left[ \frac{F(\Delta\varphi_p(x))}{\tau_0} - 1 \right]
\end{aligned} \tag{3-32}$$

After substituting loading functions  $T_1$ ,  $T_2$  and  $T_3$  into Equation (3-31), we get:

$$\begin{aligned}
\Delta\varphi_p(x) &= B \int_x^d \int_{-d}^d R_u(x,y) (T_1(y) + T_2(y) + T_3(y)) dy dx' \\
&= B \int_x^d \int_{-d}^d R_u(x,y) T_1(y) dy dx' + B \int_x^d \int_{-d}^d R_u(x,y) (T_2(y) + T_3(y)) dy dx'
\end{aligned} \tag{3-33}$$

The first term on the RHS of Equation (3-33) corresponds to the Lardner's (1968; 1974) solution for elastic-perfectly plastic material behavior and is denoted by  $\Delta\varphi_1(x)$ . The second term on the RHS of Equation (3-33), can also be expanded such that (Fakinlede, 1985):

$$\begin{aligned}
\Delta\varphi_p(x) &= 2\tau_0 B \Delta\varphi_1(x) + B \int_x^d \int_{-d}^d R_u(x,y) (T_2(y) + T_3(y)) dy dx' \\
&= 2\tau_0 B \Delta\varphi_1(x) + B \int_x^d \left[ \int_{-d}^c R_u(x,y) (T_2(y) + T_3(y)) dy + \int_c^d R_u(x,y) (T_2(y) + T_3(y)) dy \right] dx'
\end{aligned} \tag{3-34}$$

The second term  $\left( \int_{-c}^c R_u(x,y) \dots \right)$  in the second expression of the Equation (3-34) is zero since there is no plastic displacement inside the crack (freely slipping crack surfaces). Also, similar to monotonic loading case (Fakinlede, 1985):

$$\int_{-d}^{-c} R_u(x', y)(T_2(y) + T_3(y))dy = \int_c^d R_u(x', -y)(T_2(y) + T_3(y))dy$$

therefore,

$$\Delta\varphi_p(x) = 2\tau_0 B \Delta\varphi_1(x) + B \int_x^d \left[ \int_c^d [R_u(x, y) + R_u(x, -y)] [T_2(y) + T_3(y)] dy \right] dx'$$

After further re-arrangements, we get:

$$\Delta\varphi_p(x) = 2\tau_0 B \Delta\varphi_1(x) + B \int_c^d \left[ \int_x^d [R_u(x, y) + R_u(x, -y)] dx' \right] [T_2(y) + T_3(y)] dy \quad (3-35)$$

The term in the curly bracket on the RHS of Equation (3-35) is defined as the kernel and is given by (Fakinlede, 1985):

$$K_u(x, y) = \int_x^d \{R_u(x', y) + R_u(x', -y)\} dx'$$

After substituting  $T_2$  and  $T_3$  from Equation (3-32) into Equation (3-35) above, the change in the plastic displacement function is obtained as:

$$\begin{aligned} \Delta\varphi_p(x) = & 2B\tau_0 \Delta\varphi_1(x) - B\tau_0(1-\beta) \int_c^d \left[ m \left( \frac{\varphi_p(y)}{\varphi_0} + 1 \right)^n - 1 \right] K_u(x, y) dy \\ & - B\tau_0 \int_c^d \left[ m \left( \frac{\Delta\varphi_p(y)}{\varphi_0} + 1 \right)^n - 1 \right] K_u(x, y) dy \end{aligned} \quad (3-36)$$

where  $B = \frac{2(1-\nu)}{\pi\mu}$ , and  $\Delta\phi_1(x)$  is the change in plastic displacement under unloading

for an elastic-perfectly plastic material found by Lardner (1968),

$$\Delta\phi_1(x) = (x+c) \cosh^{-1} \left| \frac{d^2-x^2}{d(x+c)} + \frac{x}{d} \right| - (x-c) \cosh^{-1} \left| \frac{d^2-x^2}{d(c-x)} + \frac{x}{d} \right|$$

$K_u(x, y)$  is the kernel function for the unloading case and is given by (Fakinlede, 1985):

$$K_u(x, y) = \cosh^{-1} \left| \frac{d^2-x^2}{d(x-y)} + \frac{x}{d} \right| + \cosh^{-1} \left| \frac{d^2-x^2}{d(x+y)} + \frac{x}{d} \right| - 2 \sqrt{\frac{d^2-x^2}{d^2-y^2}} \quad (3-37)$$

Equation (3-36) is a Fredholm integral equation of the second kind. The second and third terms in this equation indicate that under the unloading conditions, the change in the plastic displacement in the reversed plastic zone ahead of the crack tip is related not only to the unloading function but the monotonic loading function as well.

The condition that dislocation density be bounded at point  $d$  where the change in plastic displacement reduces to zero, leads to:

$$\int_{-d}^d \frac{T(x') dx'}{[R_2(x')]^{1/2}} = 0$$

where  $R_2(x) = (x+d)(x-d)$ . Substituting for  $T(x)$  from Equation (3-29), after some simplification, we get:

$$\int_{-d}^d \frac{\tau_u - \tau_r(x') - \tau_{rr}(x')}{[R_2(x')]^{1/2}} dx' = 0 \quad (3-38)$$

$$\int_{-d}^d \frac{\tau_u dx'}{\sqrt{d^2 - x'^2}} + \left( \int_{-d}^{-c} + \int_c^d \right) \frac{-(1-\beta)m\tau_0 \left( \frac{\varphi_p(x')}{\varphi_0} + 1 \right)^n - m\tau_0 \left( \frac{\Delta\varphi_p(x')}{\varphi_0} + 1 \right)^n - \beta\tau_0}{\sqrt{d^2 - x'^2}} dx' = 0$$

To find the change in plastic displacement,  $\Delta\varphi_p(x)$ , the integral Equation (3-36) has to be solved. As the extent of reversed plastic zone  $d$  is also unknown, the integral equation (3-36) will be solved for two initial values of  $d$ . Then, iteratively the value of  $d$  is changed and this procedure continues until the boundary condition (3-38) is satisfied. The integral equation (3-36) can be solved by the same technique used to solve integral equation (3-21) for monotonic loading problem. To solve Equation (3-36), the perturbation of the elastic-perfectly plastic solution of the BCS introduced for monotonic loading is used again and the change in the plastic displacement function,  $\Delta\varphi_p(x)$ , is expressed as

$$\Delta\varphi_p(x) = \omega_1(x+c) \cosh^{-1} \left[ \left( 1 + |\omega_2| \right) \left| \frac{d^2 - x^2}{d(c+x)} + \frac{x}{d} \right| \right] - \omega_3(x-c) \cosh^{-1} \left[ \left( 1 + |\omega_4| \right) \left| \frac{d^2 - x^2}{d(c-x)} + \frac{x}{d} \right| \right] + \omega_5 e^{-\omega_6(x/d)} + \omega_7 e^{-\omega_8(x^2/d^2)} \quad (3-39)$$

where eight unknown coefficients ( $\omega_i, i = 1, \dots, 8$ ) have to be determined. By substituting Equation (3-39) into Equation (3-36), it will be inverted to a non-linear least square problem:

$$\min. \sum_{j=1}^{m_1} \xi_j^2 \quad (3-40)$$

where  $m_1$  is the number of points within the reversed plastic zone and  $\xi_j$  is given by:

$$\begin{aligned} \xi_j = & \Delta\varphi_p(x_j) - 2B\tau_0\Delta\varphi_1(x_j) + B\tau_0(1-\beta) \int_c^d \left[ m \left( \frac{\varphi_p(y)}{\varphi_0} + 1 \right)^n - 1 \right] K_u(x_j, y) dy \\ & + B\tau_0 \int_c^d \left[ m \left( \frac{\Delta\varphi_p(y)}{\varphi_0} + 1 \right)^n - 1 \right] K_u(x_j, y) dy \end{aligned}$$

Using a twenty-integration point scheme, an over-determined system of equations will be obtained. Using Levenberg-Marquardt algorithm the non-linear least square problem ( $\min. \sum \xi_j^2, j = 1, \dots, 20$ ) will be solved and the coefficients  $\omega_i$ , are found. As the change in plastic displacement is related to monotonic loading plastic displacement function,  $\varphi_p(x)$ , the monotonic loading problem has to be solved, first.

Knowing the plastic displacement function for both monotonic loading and unloading cases, the plastic displacement at any distance from the crack tip can be determined using Equations (3-22) and (3-39)). Also the stress field in that region can easily be calculated using Equations (3-6) and (3-24), respectively.

### 3.4.3. Monotonic and Cyclic J-Integral

Ellyin et al., (1987) showed that J-integral combines the effects of both stress field and plastic displacement at the crack tip and is an indicator of the driving forces causing

damage in the material. J-integral is an energy parameter indicating the amount of energy used to cause the damage, i.e. plastic displacement.

For monotonic loading, J-integral is used as it was initially introduced by Rice (1968). For unloading, Tanaka (1983) derived an expression for cyclic J-integral and proved that it also is path independent as is the original Rice's J-integral. Tanaka (1983) showed that cyclic J-integral remains constant during the reversal of loading under a constant stress range, if the first monotonic loading stage is excluded.

### 3.4.3.1. Monotonic Loading Stage

Rice (1968) defined the J-integral for two-dimensional problem as

$$J = \int_{\Gamma} (W dx_2 - T_m \partial u_m / \partial x_1 ds)$$

where  $\Gamma$  is the integration path around the crack tip plastic zone,  $W$  is the strain energy density,  $\left( \int_0^{\epsilon_{mn}} \sigma_{mn} d\epsilon_{mn} \right)$ ,  $T_m$  is the surface traction exerted on the material within the contour  $\Gamma$ ,  $u_m$  is the displacement, and  $x_i$  is the coordinate system. For the dislocation model, here, the surface traction is  $T_m = \tau_r(x)$ ,  $u_m = \varphi_p(x)$  and  $\Gamma$  is defined as the upper and lower surface of the plastic zone, therefore, as in the limiting case  $dx_2$  approaches zero ( $dx_2 = 0$ ) and the first term in the integral is eliminated. Therefore, for monotonic loading, J-integral is defined as (Ellyin et al., 1986):



$$J = \int_c^a \left( -\tau_r(x) \frac{\partial \varphi_p(x)}{\partial x} dx \right)$$

which after substituting for  $\tau_r(x)$  from Equation (3-6), we get:

$$J = \int_c^a -m\tau_0 \left( \frac{\varphi_p(x)}{\varphi_0} + 1 \right)^n \frac{\partial \varphi_p(x)}{\partial x} dx \quad (3-41)$$

where from monotonic loading stage the plastic displacement function  $\varphi_p(x)$  is known.

The Equation (3-41) can then easily be evaluated analytically and  $J$ -integral is obtained for this case by:

$$J = \frac{m\tau_0\varphi_0}{n+1} \left[ \left( \frac{\varphi_p(c)}{\varphi_0} + 1 \right)^{n+1} - 1 \right]$$

### 3.4.3.2. Unloading Stage

For the unloading stage of the load cycle, cyclic  $J$ -integral is obtained as follows. For the loading sequence shown in Figure 3-9, Tanaka (1983) defined the cyclic  $J$ -integral as:

$$\Delta J = \int_{\Gamma} (\Delta W dx_2 - \Delta T_m \partial \Delta u_m / \partial x_1) ds$$

where  $\Delta W = \int_{(\varepsilon_{mn})_i}^{(\varepsilon_{mn})_j} [\sigma_{mn} - (\sigma_{mn})_i] d\varepsilon_{mn}$  is the change in the strain energy density,

$\Delta T_m = (T_m)_j - (T_m)_i$  is the change in traction vector from  $i$  to  $j$  and  $\Delta u_m = (u_m)_j - (u_m)_i$  is

the change in displacement vector,  $u_m$ .

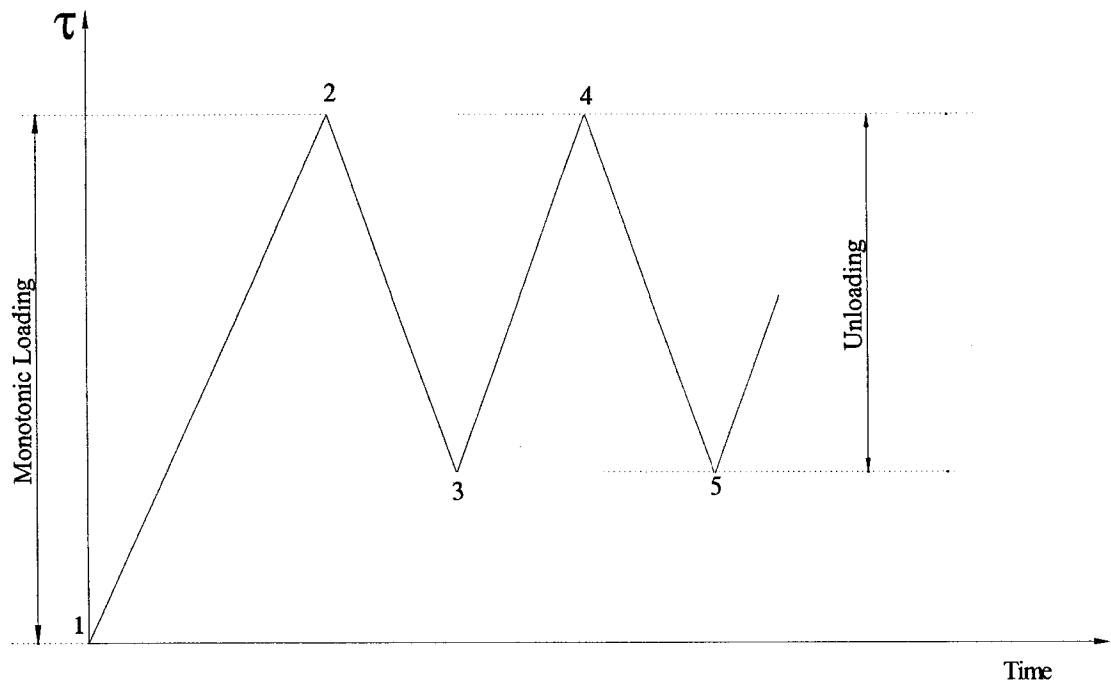


Figure 3-9: The sequence of loading used to calculate cyclic  $J$ -integral (Tanaka, 1983)

If we consider the unloading path from 2  $\rightarrow$  3 (Figure 3-9), again for the integration path,  $\Gamma$ , given by upper and lower surfaces of the reversed plastic zone, the cyclic  $J$ -integral for this problem is defined as (Ellyin et al., 1987):

$$\Delta J = \int_c^d -(\tau_{rr}(x) - \tau_r(x)) \frac{\partial \Delta \varphi_p(x)}{\partial x} dx$$

which after substituting for  $\tau_r(x)$  and  $\tau_{rr}(x)$  from Equations (3-6) and (3-24), respectively, we get:

$$\Delta J = \int_c^d -\tau_0 \left[ m \left( \frac{\Delta \varphi_p(x)}{\varphi_0} + 1 \right)^n + (1 - \beta) m \left( \frac{\varphi_p(x)}{\varphi_0} + 1 \right)^n + \beta \right] \frac{\partial \Delta \varphi_p(x)}{\partial x} dx \quad (3-42)$$

Knowing  $\varphi_p(x)$  and  $\Delta \varphi_p(x)$  from loading and unloading functions, the cyclic  $J$ -integral, Equation (3-42) can be evaluated.

### ***3.5. Numerical Solution of Dislocation Model***

The plastic displacement and the reversed plastic displacement functions derived in the previous sections can only be determined numerically, as there are no analytical solutions available to the non-linear Fredholm integral equations (3-21) and (3-36). The method to solve the integral equations is given by Barker (Delves et al., 1974, P. 80). Barker describes a method of approximating the solution of a general form Fredholm integral equation of the second kind given by:

$$f_1(x) - \lambda \int_a^{b'} K(x, y) f_1(y) dy = g_1(x) \quad (3-43)$$

through the expansions of the form

$$f_1(x) = \sum_{i=1}^n a_i \eta_i(x) \quad (3-44)$$

where  $\eta_i(x)$  are the chosen approximating functions. Applying approximating function (3-44) into Equation (3-43), we get:

$$\sum_{i=1}^n a_i \eta_i(x) - \lambda \int_a^{b'} K(x, y) \sum_{j=1}^n a_j \eta_j(y) dy = g_1(x) \quad (3-45)$$

The finite integral term in Equation (3-45) can be evaluated using quadrature formula. There are  $n$  unknown coefficients,  $a_i$ ,  $i = 1, \dots, n$ . To find the unknown coefficients a system of  $N$  equations at  $x_i$ ,  $i = 1, \dots, N$  is formed. If  $n = N$ , for the system of  $N$  equations there exists a unique solution if  $\det(A - \lambda B) \neq 0$  where  $A_{ij} = \eta_j(x_i)$  and  $B_{ij} = \int_a^{b'} K(x_i, y) \eta_j(y) dy$ . In this case, the error (residual) function should be zero. If no unique solution exists, then for  $N > n$ , there will be an over-determined system of equations and the unknown coefficients will be found by minimizing the square of the error function as given by:

$$\min. \sum_{j=1}^N \xi_j^2(x_j)$$

where

$$\xi_j(x_j) = \sum_{i=1}^n a_i \eta_i(x_j) - \lambda \int_a^{b'} K(x_j, y) \sum_{i=1}^n a_i \eta_i(y) dy - g_1(x_j) \quad (3-46)$$

Equation (3-46) is similar to the Equations (3-23) and (3-40), the cases of monotonic loading and unloading, respectively. In these cases, the chosen approximating functions, i.e. Equations (3-22) and (3-39), as suggested by Fakinlede (1985), are perturbation of the original BCS solution (Bilby et al., 1963) for the plastic displacement function for elastic-perfectly plastic materials as shown in previous sections. Using the proposed approximating functions and following the same scheme as above, the two non-linear regression problems are obtained for monotonic loading and unloading problems as given by Equations (3-23) and (3-40).

By setting up a system of equations for  $x_i$ ,  $i = 1, \dots, N$ , and  $N = 20$ , an over-determined system of equations is found. The system of equations will then be solved using an optimization technique. Among other methods, Levenberg-Marquardt algorithm is chosen to solve the non-linear regression problems. This method is briefly described in the next section.

### 3.5.1. Levenberg-Marquardt Algorithm

Levenberg-Marquardt algorithm is a gradient-based method for solving unconstrained multivariable functions. This solution scheme uses function evaluation as well as first and second derivative evaluations of the objective function to find the unknown variables.

Gradient-based methods are iterative since the elements of the gradient are in general nonlinear functions of the unknown variables (Reklaitis et al., 1983). The iteration procedure is as follows:

$$x^{(k+1)} = x^{(k)} + \alpha^{(k)} s(x^{(k)})$$

where  $x^{(k)}$  is the current estimate of  $x^*$ , the solution,  $\alpha^{(k)}$  is the step-length parameter,  $s(x^{(k)}) = s^{(k)}$  is the search direction in the space of the unknown variables,  $x_i$ ,  $i = 1, \dots, n$  and  $x^{(k+1)}$  is the next best estimate of the solution.  $s(x)$  and  $\alpha$  are determined differently in different gradient-based methods, however, usually  $\alpha^{(k)}$  is selected so as to minimize the objective function in the  $s(x^{(k)})$  direction. In Levenberg-Marquardt algorithm the search direction is defined by:

$$\begin{aligned} s(x^{(k)}) &= -[\mathbf{H}^{(k)} + \lambda^{(k)} \mathbf{I}]^{-1} \nabla f_1(x^{(k)}) \\ \alpha^{(k)} &= 1 \end{aligned} \tag{3-47}$$

where  $\nabla f_1(x^{(k)})$  is a column vector of the first derivative of the objective function,  $\mathbf{H}^{(k)}$  is a matrix of the second derivative of the objective function, called the *Hessian* matrix,  $\lambda^{(k)}$  is a parameter that controls both the direction and the length of the step and  $\mathbf{I}$  is the identity matrix. The Levenberg-Marquardt algorithm combines the two gradient-based methods known as steepest descent or Cauchy's Method and Newton's method. Cauchy's method uses first derivative information to find the unknown variables and is very effective way of finding solution when the starting point is far from the exact solution of the problem. Newton's method uses both first and second derivative information and is

very effective in finding the solution at locations close to the exact solution of the problem. By combining the two gradient-based methods, the Levenberg-Marquardt algorithm makes use of the advantages of both methods while avoids their disadvantages.  $\lambda$  is a key parameter upon which either of the Cauchy's method or Newton's method is chosen. For sufficiently large values of  $\lambda$ , the identity matrix  $I$  dominates the terms in the bracket in Equation (3-47) and  $s(x^{(k)}) \rightarrow -\nabla f_1(x^{(k)})$ , i.e. the Cauchy's method. As  $\lambda$  decreases to zero, the *Hessian* matrix,  $H^{(k)}$  will dominate the expression in the bracket in Equation (3-47) and  $s(x^{(k)}) \rightarrow -H^{(k)-1}\nabla f_1(x^{(k)})$ , i.e. the Newton's method. The Levenberg-Marquardt algorithm is set up such that at estimates of solution far from the exact solution  $\lambda$  is large therefore Cauchy's method is used. At estimates close to the exact solutions,  $\lambda$  is decreased and therefore, Newton's method is used which has a fast convergence rate as the estimated solution approaches the exact solution.

The main advantages of the method are its simplicity, fast descent property, and excellent convergence rate near the exact solution. The major disadvantage of the method is the need to calculate the second derivatives, i.e., the *Hessian* matrix,  $H^{(k)}$  (Reklaitis et al., 1983). The method was initially proposed by Marquardt (1963) to solve sum of square type of problems and has extensively been used with problems where objective function is of this form (Reklaitis et al., 1983). Powell (1972) and Bard (1974) have shown that the method is particularly attractive for sum of square type of applications.

To solve the nonlinear regression problems, i.e. Equations (3-23) and (3-40), using Levenberg-Marquardt algorithm, the *RNLIN/DRNLIN* routine of the *IMSL* library was

used. This routine is specially built for solving nonlinear regression problems using Levenberg-Marquardt algorithm.

### 3.5.2. Mathematical Model Singularities

As shown in Equations (3-21) and (3-36), plastic displacement function and the change in the plastic displacement function both have similar form of singularities. The kernel of both of the integral equations, i.e. Equations (3-20) and (3-37), have two forms of singularities. A singularity at  $x = y$  and a singularity at  $y = a$  for monotonic loading plastic displacement function and at  $y = d$  for the change in the plastic displacement function under unloading. According to Delves et al. (1974), singularity of kernel functions at  $x = y$  is *severe* meaning that at this point integral does not exist. Delves et al. (1974) have shown that a *severe* singularity of this form can be transformed to a *mild* singularity as follows.

A definite integral of the form  $\int_a^b K(x, y) f_1(y) dy$  where kernel,  $K(x, y)$  has a *severe* singularity at  $x = y$ , can be rewritten as:

$$\int_a^b K(x, y) f_1(y) dy = \int_a^b K(x, y) [f_1(y) - f_1(x)] dy + \int_a^b K(x, y) f_1(x) dy \quad (3-48)$$

Adding and subtracting the last expression from the original integral transform the severe singularity in the integral into a *mild* one. This is because at  $x = y$ , the first expression in the RHS of Equation (3-48) disappears since  $f_1(y) - f_1(x) = 0$  and the second expressions



is rearranged to  $f_1(x) \int_a^b K(x, y) dy$  in which the integral has a *mild* singularity at  $x = y$  and is assumed to be a known function (Delves et al., 1974) or it can be evaluated numerically. Therefore, for all numerical evaluation purposes, the original integral equation can be written as:

$$\int_a^{b'} K(x, y) f_1(y) dy \quad x \neq y$$

$$\int_a^{b'} K(x, y) [f_1(y) - f_1(x)] dy + f_1(x) \int_a^{b'} K(x, y) dy \quad x = y$$

The second type of singularity in the kernel functions (3-20) and (3-37) is of the type known as end point singularity and is fairly easy to evaluate. The end-point singularity in Equation (3-20) is at  $y = a$  and in Equation (3-37) is at  $y = d$ . The simplest way to handle end-point singularity is to avoid the end-point by approaching it numerically as close as possible but avoiding the exact end-point.

Also each of the approximating functions for the plastic displacement and the reversed plastic displacement functions have end-point singularity at  $x = c$ . However, the presence of the  $(x - c)$  term as a multiplier to the singular expression eliminates the need to deal with the end-point singularities in these cases. Boundary conditions (3-15) and (3-38) also each have an end-point singularity at  $x = a$  and  $x = d$ , respectively. These mild singularities can also be treated numerically by avoiding the end-points.

Following development of dislocation model, which was described in detail in this chapter, an experimental program was undertaken in which the mechanical behavior of

---

granite under static and fatigue shear loading conditions were investigated. The static shear tests results are then used in the dislocation model to assess damage in granite under given loading condition. The fatigue tests provide fatigue properties and fatigue stress life (S-N) curve of the granite. The shear testing method used is described in the next chapter followed by the presentation of the obtained results.

## **Chapter 4: Monotonic and Fatigue Shear Testing of Granite**

An experimental investigation was carried out on granite specimens to determine static and fatigue properties of granite subject to monotonic and cyclic shear loading conditions, respectively. The main objective of this experimental work was to obtain static shear mechanical properties of the granite and to use them as input into the dislocation model to analyze damage to rock due to loading and unloading. The fatigue tests results also provided fatigue properties of the granite and fatigue stress life curve (S-N curve) of granite was obtained.

The proposed experiments were performed on the hard rock specimens, i.e. granite. Brittle behavior of hard rocks made this effort more challenging since hard rocks are much weaker in tension than in shear. An appropriate testing method must be adopted such that while it accommodates shear loading of the specimen, it must prevent tensile failure of specimens.

A number of methods have been reported in literature that are used to test shear properties of rock specimens (Skempton, 1949; Protodyakonov, 1969; Kenty, 1970; Wernick, 1977; Matthews, 1988; Nagaraj, 1993). While none of these methods are approved as standard testing method to obtain shear properties of rocks, there are other standard shear testing methods that are prescribed for testing non-metallic materials. The D 5379/D 5379M is an ASTM standard test method to measure shear properties of composite materials by the V-notched beam method. This test method is one of the most commonly used methods to measure shear properties of composite materials (Adams et

al., 1987a; Pierron et al., 1994; Ho et al., 1993). This test method has successfully been used to determine shear properties of concrete as well (Adams, 2001; Walrath, 2001). There are similar characteristics of rocks and composite materials, e.g. both being brittle. This then somewhat justifies the use of this method to test rock specimens and to obtain shear properties of rock under monotonic loading as well as fatigue properties of rock under shear cyclic loading. However, one should bear in mind that the presence of high-modulus fibers, which reinforce the composite materials, increases the tensile strength of the composites compared to low tensile strength of rocks that lack reinforcing fiber structure. This fundamental difference between the two materials was later found to be a key differentiating factor in applying this test method to brittle hard rocks as opposed to composite materials. This fact will further be elaborated later in this chapter.

#### ***4.1. ASTM D 5379/D 5379M - 1993: Iosipescu Shear Testing Method***

Iosipescu (1967) originally introduced this test method primarily for shear testing of metals and other isotropic materials. For this reason, it is also called Iosipescu shear test. It was further developed by Walrath et al. (1983a; 1983b; 1984) and Adams et al. (1987b) with the fixture modified to its current configuration and was standardized as ASTM D 5379/D 5379M (American Society for Testing and Materials, 1993). According to Whitney (1996), the basis of the Iosipescu shear test is the utilization of a beam specimen loaded in such a manner as to produce a zero bending moment relative to at least one cross section. According to classic beam theory, pure shear will exist at this cross section. Iosipescu (1967) argued that the introduction of v-notches at the top and bottom of the beam would produce a uniform shear rather than the classic parabolic distribution

obtained from classic beam theory. Finite element studies have also confirmed this argument as well. The specimen and fixture configurations are set up such that the bending moment at the cross section where the v-notches are located would be zero and at this location there will be pure shear (Figure 4-1).

For this shear testing method, a special apparatus known as Iosipescu fixture must be built (Figure 4-2). A specimen in the form of a rectangular flat strip with symmetrical centrally located v-notches (Figure 4-1) is placed in the apparatus. To avoid normal stresses to be built at the v-notches, the apparatus is designed such that the load is applied symmetrically and along the line-of-action. The specimen is inserted into the fixture with the notches located along the line-of-action of loading by means of an alignment tool that references the fixture. The halves of the fixture are compressed by the loading machine while monitoring load. The applied load exerts a relative displacement between the two fixture halves. By placing a strain gage rosette on each side of the specimen, oriented at  $\pm 45^\circ$  to the loading axis, in the middle of the specimen away from the notches and along the line of loading, the shear response of the rock specimen can be measured. Two  $45^\circ$  strain gage rosettes installed on front and back of each specimen provides two readings at the desired angles ( $\pm 45^\circ$ ), from which shear response of the rock can be determined on each side.

V-notches influence shear strain along the loading direction, making the distribution more uniform than would be seen without the notches (American Society for Testing and Materials, 1993). The length of the gap between the edges of two contact zones on the left and right of the v-notch on both top and bottom of the specimen (Figure 4-2) is a

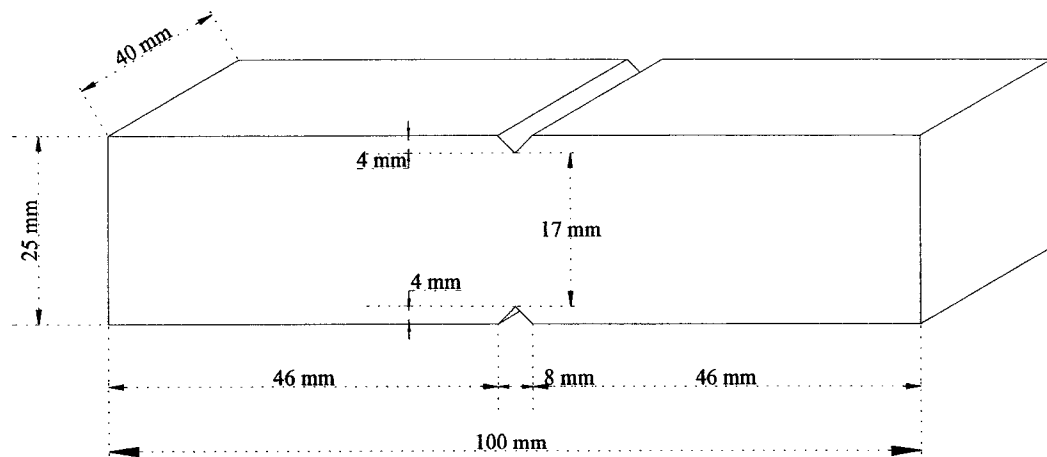


Figure 4-1: Specimen configuration used in the Iosipescu shear test

critical length factor and its effects depends on the material properties and isotropy. For materials with significant plastic behavior this gap is kept large to avoid interference of high stress concentration at the edge of the contact zones with the stress distribution along the line-of-action of loading and also at the notch roots. For brittle materials, on the contrary, the gap has to be as small as possible because as the movable half of the apparatus is displaced by the compressive load, high stress concentrations at the edge of the contact zones create a high bending moment at this location that would generate high tensile stresses and will cause the specimen to fail in tension in a location close to the contact zones, away from the notched zones. The smaller the gap, the smaller the bending moment will be. In ideal case where the gap is closed, no bending moment is generated and the applied load generates pure shear loading at the notched zone. This ideal case is equivalent to the single shear test method.

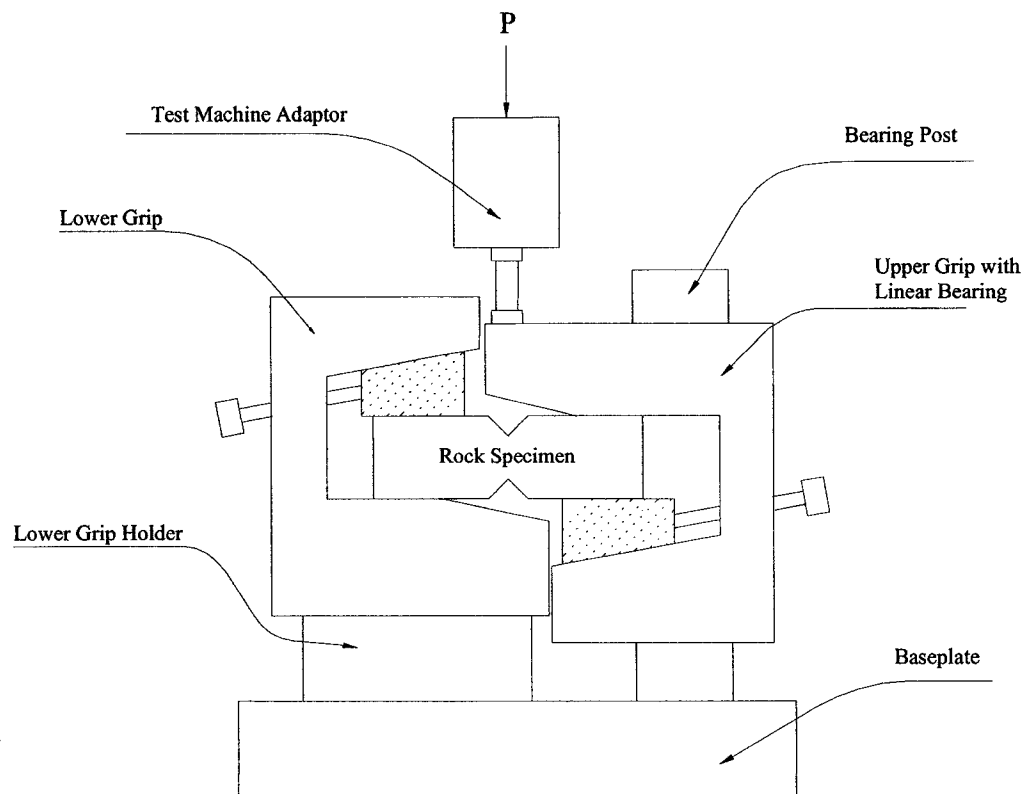


Figure 4-2: Iosipescu shear testing apparatus, original configuration

#### 4.1.1. Experimental Program: Special Considerations

In this experimental investigation, a series of monotonic shear and fatigue shear cyclic loading experiments were performed on the granite specimens. Due to relatively large grain size of the granite, specimens of larger size than the standard size specimen as noted in the ASTM D 5379/D 5379M were needed. The specimen height was therefore altered from its standard size such that the distance between the tip of the two notches at the top and bottom of the specimen would be at least ten times the grain size of the granite. This would guarantee that the strength properties obtained from the experiment would be indicators of the overall material behavior rather than the response of a single grain.

A larger specimen size would require a larger size apparatus to be built. For this reason, Iosipescu fixture is built twice as large as the standard size apparatus. Due to the high modulus of granite that is to be tested, a very stiff type of steel is chosen to build the apparatus. The new apparatus is built using tools steel and is then hardened to avoid surface damages while loading rock specimens and also during the tests. Since granite is a very hard rock a diamond grind wheel was required to cut the v-notches on the granite specimens.

It was observed in the early tests that bending moments do affect the granite response to monotonic and cyclic loading when tests were carried out using Iosipescu with original configuration. Therefore, to assure rock specimens fail in shear rather than in tension under monotonic and cyclic loads, it was concluded that the Iosipescu apparatus had to be



modified such that the bending moments generated in the specimen were eliminated or minimized.

It was suggested to cut the upper part of the right grip and lower part of the left grip such that it transformed the apparatus into a single shear testing system (Figure 4-3). To keep the applied load symmetric, an adaptor was built such that the line-of-action of the applied load was aligned with the line connecting the two notches on the specimen. It also required the use of smaller specimens. Figure 4-4 shows the apparatus after the proposed changes has been performed during a monotonic loading test.

In addition to specimen and apparatus configurations, a number of other factors affect the shear response of the rock specimens and should therefore be taken into consideration. These factors include material type, its homogeneity, and isotropy, specimen preparation, gripping and alignment, the rate of loading and the test environmental factors.

Any pre-existing defect or crack in the rock structure would result in pre-mature failure of specimen. Anisotropic materials whose mechanical response is dependent on the direction of applied load with respect to the orientation of the isotropy in the material, would also demonstrate differing shear properties when the orientation of the applied load is changed.

Specimen preparation is a crucial step of this shear testing method. To obtain a satisfactory result from the test, one needs to make sure that specimens are cut in parallel and that the top and bottom surfaces of specimens are perfectly flat with no deflections in any direction and are also free from surface roughness. Even smallest surface deflection

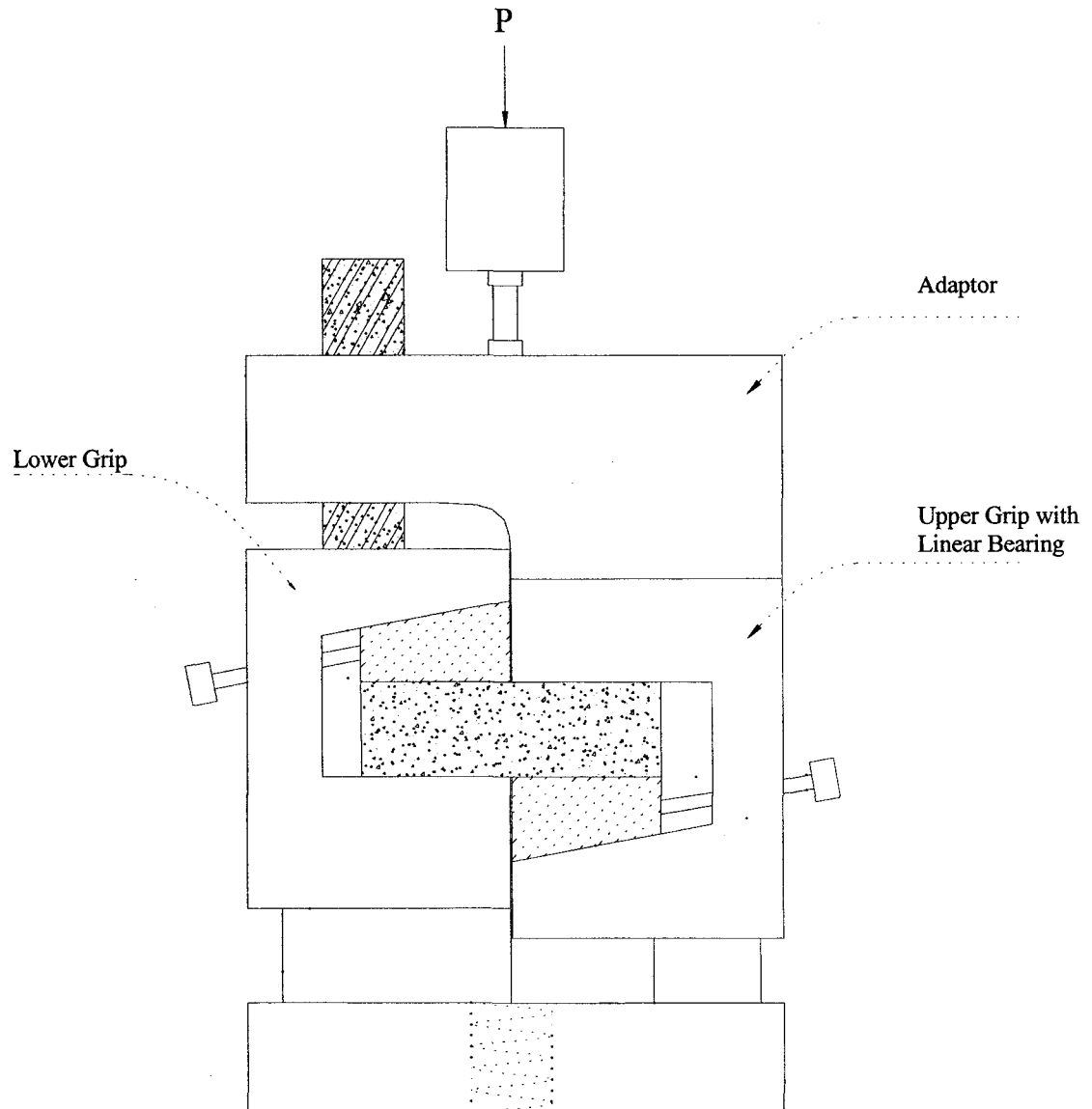


Figure 4-3: Schematic diagram of Iosipescu after the final modifications

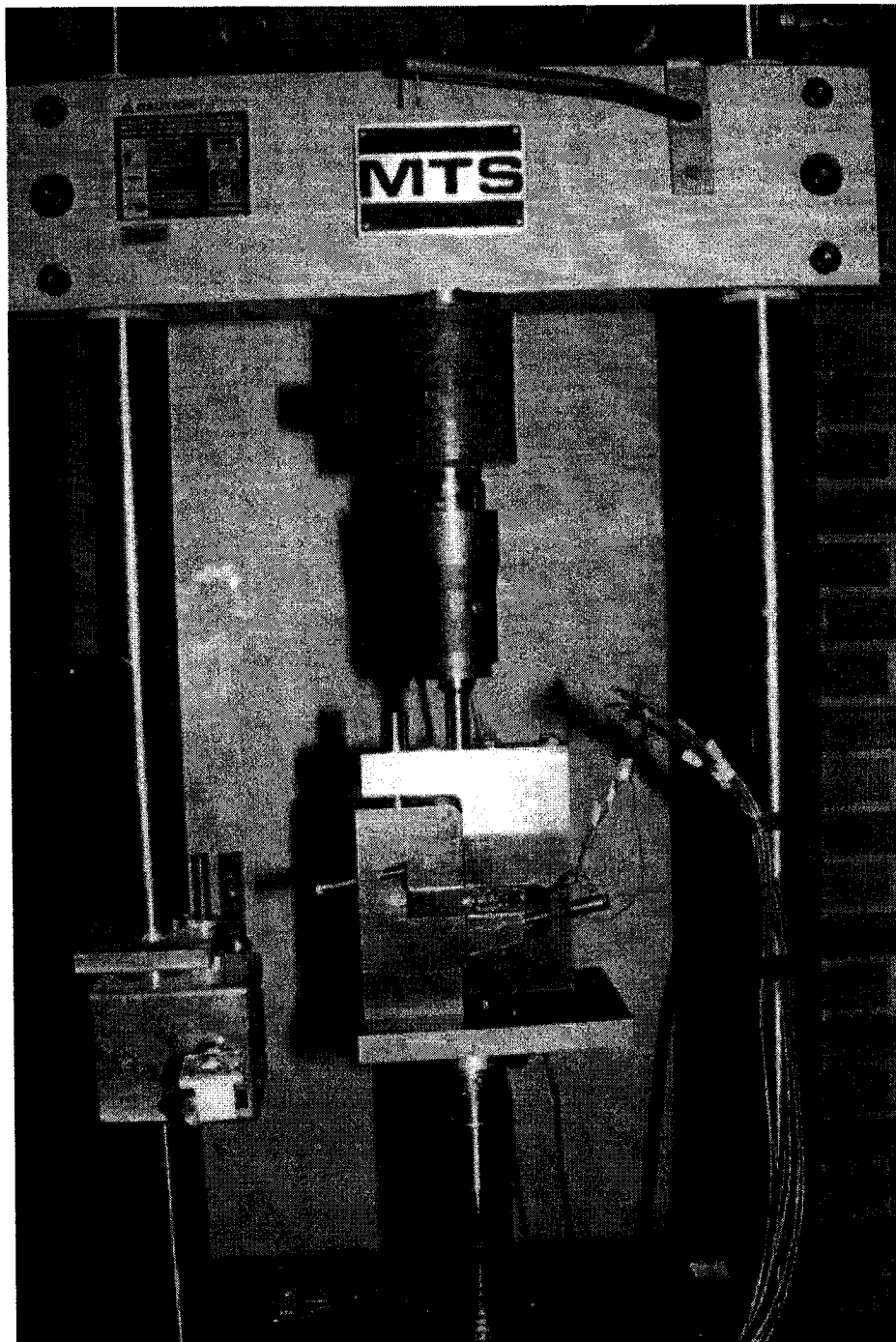


Figure 4-4: Shear testing apparatus after the proposed modifications during a monotonic loading test

would cause twisting and results in torsion in the specimen. Surface roughness may also cause high stress concentration on the surface at the given location. These would eventually lead to pre-mature failure of rock specimen in a mode other than shear. Care must also be taken when cutting v-notches, as they both should perfectly be in line with the line-of-action of the applying load. Slightest misalignment of the notches would result in failure of specimen at a location between the notched zone and the edges of the contact zones on either right or left side of the notches and may start from either the top or bottom of the specimen. In addition, in the process of cutting the notches, care must be taken to avoid damaging the specimen while v-notches are cut by the diamond grind wheel. Any small crack induced during this process could cause pre-mature failure of rock specimens resulting in incorrect measurements. Special care must be attended when inserting specimen into the apparatus. Specimen must be placed in the apparatus in a perfect flat (horizontal) configuration and must be tightened such that it will not move in the apparatus when loading starts and is increased. In case of under-tightening, any such movement will cause twisting of the specimen and invalidates the readings. Over-tightening must also be avoided to prevent pre-loading of the specimen which could cause failure of specimen by twisting or bending and/or errors in reading the applied load.

The rate of loading must be low enough so that the post-yield response of the rock specimen can be recorded with the desired accuracy. Of course, this would depend on the type and capabilities of the data acquisition system, i.e. the number of channels that can be traced and recorded simultaneously and how fast data can be recorded, as well.

Since each monotonic experiment does not take more than a few minutes to complete, the environmental factors are not significantly important provided that no dramatic change in such factors i.e., temperature, happen while test is running.

#### **4.1.2. Specimen Preparation, Instrumentation, Loading and Data**

##### **Acquisition Systems**

To avoid potential problems with specimen preparation in terms of non-flat, uneven surfaces, surface roughness and possible damage during the process of cutting and finishing the specimens, precision granite parallels were purchased from Geneva Gages. The granite parallels were produced from a quarry in California by Stanridge Granite Corp. Granite parallels were cut professionally and finished on four faces at the grade of  $\pm 0.000050$ " per 12". Granite parallels were 12" long and each was cut in 4" pieces to make three specimens. Following this stage, special set up was made to cut the notches on the top and bottom surfaces of the specimens using a diamond grind wheel. The notches were cut in the middle of the specimens. It is to be noted that care must be taken to perfectly align the top and bottom notches on each specimen to avoid misalignment and errors in readings.

##### ***4.1.2.1. Monotonic Loading Tests***

For the purpose of monotonic loading tests, once the specimen was cut, a 45° strain gage rosette (Figure 4-5) was installed on each side of the specimen (Figure 4-6). A 45° rosette has three stacked gages with two of them oriented at  $\pm 45^\circ$  angle with respect to the

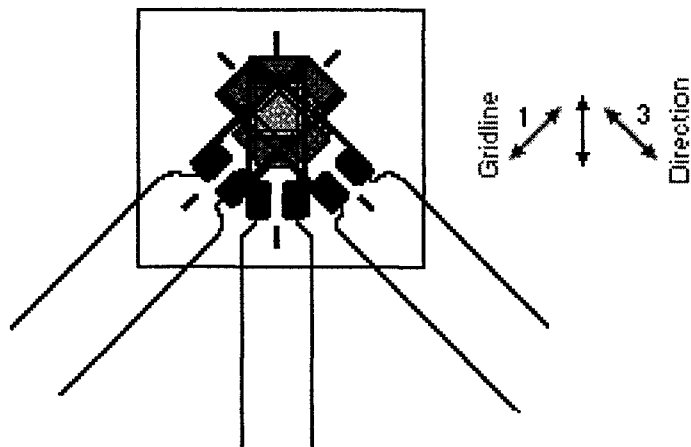


Figure 4-5: A 45° Strain gage rosette with three stacked gages

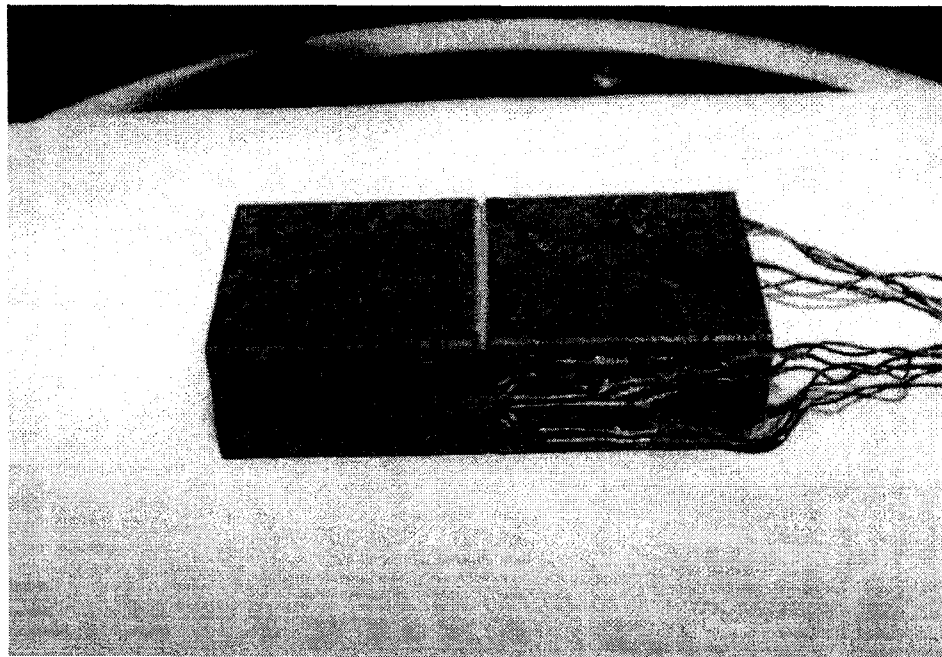


Figure 4-6: A granite specimen with a strain gage rosette installed on each side

direction of loading (or horizontal plane), i.e. gages 1 and 3 (Figure 4-5) and the third gage, i.e. gage 2, is oriented horizontally and measures lateral strain on the specimen. The gages 1 and 3 measure the strain in  $\pm 45^\circ$  angles with respect to horizontal axis, i.e. one measures tensile strain while the other measures the compressive strain in these orientations. The rosette used is 6 mm long with 120 ohms resistance and a gage factor of 2.11.

The monotonic load is applied by a MTS hydraulic loading system with a maximum loading capacity of 20000 lbs. The applied load and strains were recorded by a 12 bit, 160 kHz Instronet data acquisition system with a maximum 8 channel differential input and simultaneous reading at a maximum sampling rate of 3500 samples per second (3.5 kHz) per channel. In order to measure strains each gage is hooked up into a Wheatstone quarter bridge circuit. Each gage of the rosettes was connected to the Instronet data acquisition system through a Wheatstone quarter bridge circuit. Having two rosettes on each specimen, six Wheatstone quarter bridges were built to complete the circuit for recording strains on all gages at the same time. The seventh channel on the Instronet data logger was used to record the applying load as it increased from zero to peak load at which specimen failed. Figure 4-7 shows the Instronet data acquisition system during a monotonic loading test. The six channel Wheatstone quarter bridge circuit is also located beside the Instronet data acquisition system.

Total shear strain was then obtained from the readings of the two  $\pm 45^\circ$  (with respect to horizontal axis) gages, i.e. gages 1 and 3, on each side of the specimen by:

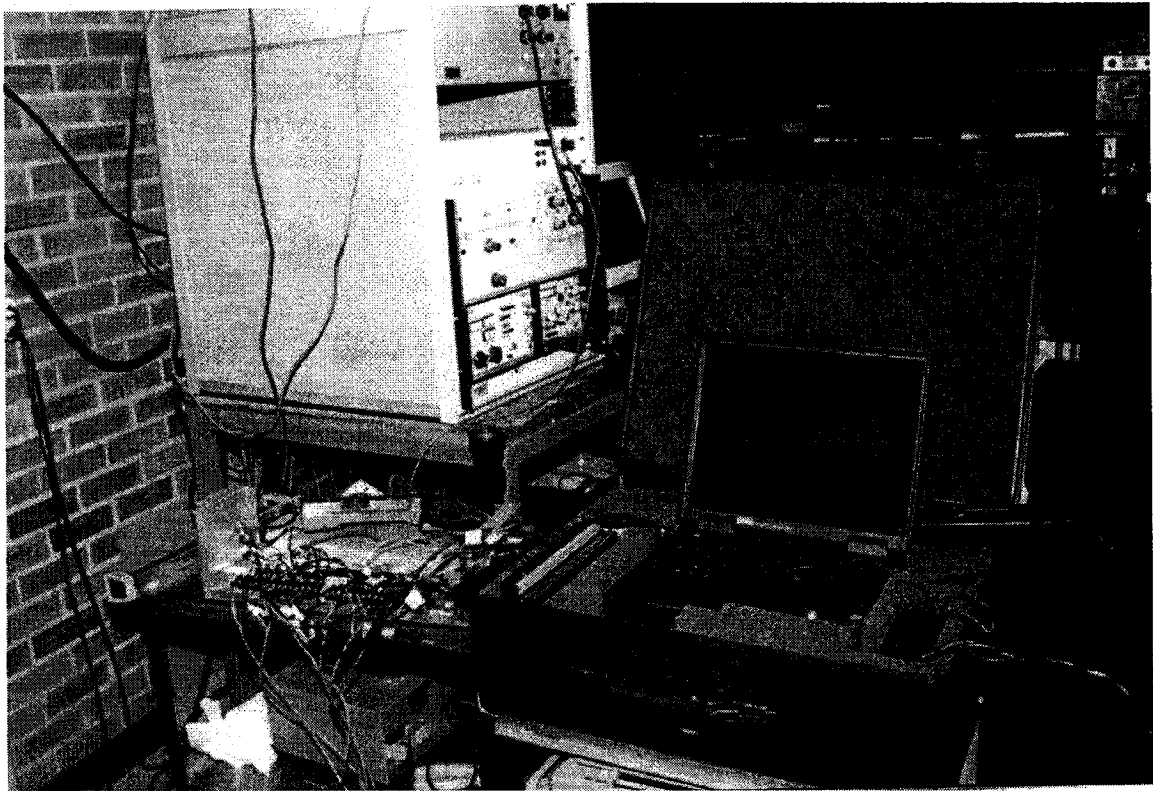


Figure 4-7: Instronet Data Acquisition System and six channel Wheatstone quarter bridge circuit built for the monotonic loading tests.



$$\gamma = |\varepsilon_{+45}| + |\varepsilon_{-45}|$$

To find the shear stress at the notched zone the applied load was divided by the area of the cross section of the specimen between the two notches as given by:

$$A = w * h$$

where  $A$  is the area of specimen at the cross section between the two notches,  $w$  is the width of the specimen and  $h$  is the distance between the tip of the two notches. This is the average shear stress along the line of action of the applying load.

The applied load was also monitored and recorded simultaneously as strains were recorded from which the shear stress-shear strain relationship was plotted. From this diagram, static mechanical properties of the granite were determined.

The shear mechanical properties of granite obtained from the monotonic tests were then inputted into the dislocation model and the rock damage was determined from the numerical model.

#### ***4.1.2.2. Fatigue Cyclic Shear Loading Tests***

In the second stage of experimental program, several sets of shear cyclic loading tests were performed on granite specimens. The objective of these tests was to determine fatigue life properties of the granite by establishing its fatigue life (S-N) curve.

The cyclic loading tests were carried out on the granite specimens with the same configuration as those of the specimens used in monotonic loading tests. In each test, specimen was loaded and unloaded for as many cycles as needed until it failed, i.e. a crack initiated and grew leading to specimen failure. The loading range was kept constant during each test. Several tests were carried out applying a different loading range in each test while the loading ratio ( $R = \tau_{\min} / \tau_{\max}$ ) was kept constant in all tests. The data collected from all tests were used to establish fatigue stress life (S-N) curve of the granite.

Granite is naturally very brittle; therefore the process of crack initiation and propagation in granite is expected to be very fast. For this reason, special crack propagation gages were selected as proper means of recording the rate of crack propagation in rocks. Special crack propagation gages should be bonded at the tip of both v-notches on each side of each specimen. Crack propagation gages (Figure 4-8) have provided a convenient way for measuring rate of crack propagation in the specimens prepared from other materials. In current effort, its application to measure rate of crack propagation in rock specimens were examined. Each crack propagation gage has a number of resistor strands connected in parallel. When bonded to the rock specimen, as the cyclic loads are applied a crack will initiate. Under subsequent cyclic loading the crack starts to grow and as it grows through the gage it causes successive open-circuiting (breaking) of the strands, resulting in an increase in total resistance in the circuit. As every strand of gage is broken, the change in total resistance in the circuit is picked up by the data acquisition system and is recorded sequentially. This data is used to find the number of cycles leading to a given



Figure 4-8: A crack propagation gage with twenty strands

crack growth and also to determine the number of cycles to ultimate failure of the specimen. In these tests, crack propagation gages with ten strands were used. The gages were built by Micro-Measurements Group Inc. and have a nominal resistance of 5 ohms. Each specimen was instrumented with four crack propagation gages bonded at the tip of the notches on the specimen. To record the rate of crack propagation a special circuit was built for each gage. Each fatigue test was expected to take from a few minutes to a few days depending on the applied loading range. Therefore, the data acquisition system had to be set up such that it monitored all the gages throughout the test and started the recording as soon as the first strand in one of the gages broke meaning that a crack had initiated and crack growth were to be followed.

Instronet data acquisition system is capable of monitoring only one channel (one gage) continuously and triggers recording based on the readings from that channel, therefore, to monitor all four channels a different data acquisition card was needed and the recording was set to start as soon as the first strand in any one of four gages broke triggering the recording system. For cyclic loading tests, then, a 12 bit, 8 channel single ended inputs, 16 kHz National Instrument data acquisition card was used. The data logging task was

performed by a Labview model (Figure 4-9) which was capable of monitoring all four channels simultaneously. Once the first strand of one of the gages broke, recording started and continued until all gages broke completely.

Due to brittleness of granite, it was not possible to pre-crack the specimens. All attempts to pre-crack the specimen failed since once the crack started in granite it was unstable and grew very fast resulting in failure of the specimen. It is important to note that the tests were carried out in laboratory conditions without confinement. In the field, high confining pressure affects the shear strength of the rock. In addition, it reduces the size of the process (plastic) zone, i.e. effectively reducing the crack growth rate (Schmidt et al., 1977; Lyakhovskiy, 2001) when compared with an specimen with no confining pressure applied.

#### ***4.2. Monotonic Loading Tests Results***

Three specimens were cut, prepared and instrumented for monotonic loading tests. In order to minimize bending moment on the specimen, the gap between the support zones on the top and bottom of the specimens had to be minimized. This would require the use of thicker specimens than was available. To cover for the extra thickness needed, thin steel shims were used on both top and bottom of the specimen. Use of thicker specimen or shims makes it possible to move the upper and lower jaws toward the centre of the specimen reducing the gap between the contact zones on top and bottom of the specimen. Therefore, steel shims of various thicknesses (1/32" to 3/32") were acquired for this purpose. The tests were performed using a MTS hydraulic loading system at a rate of

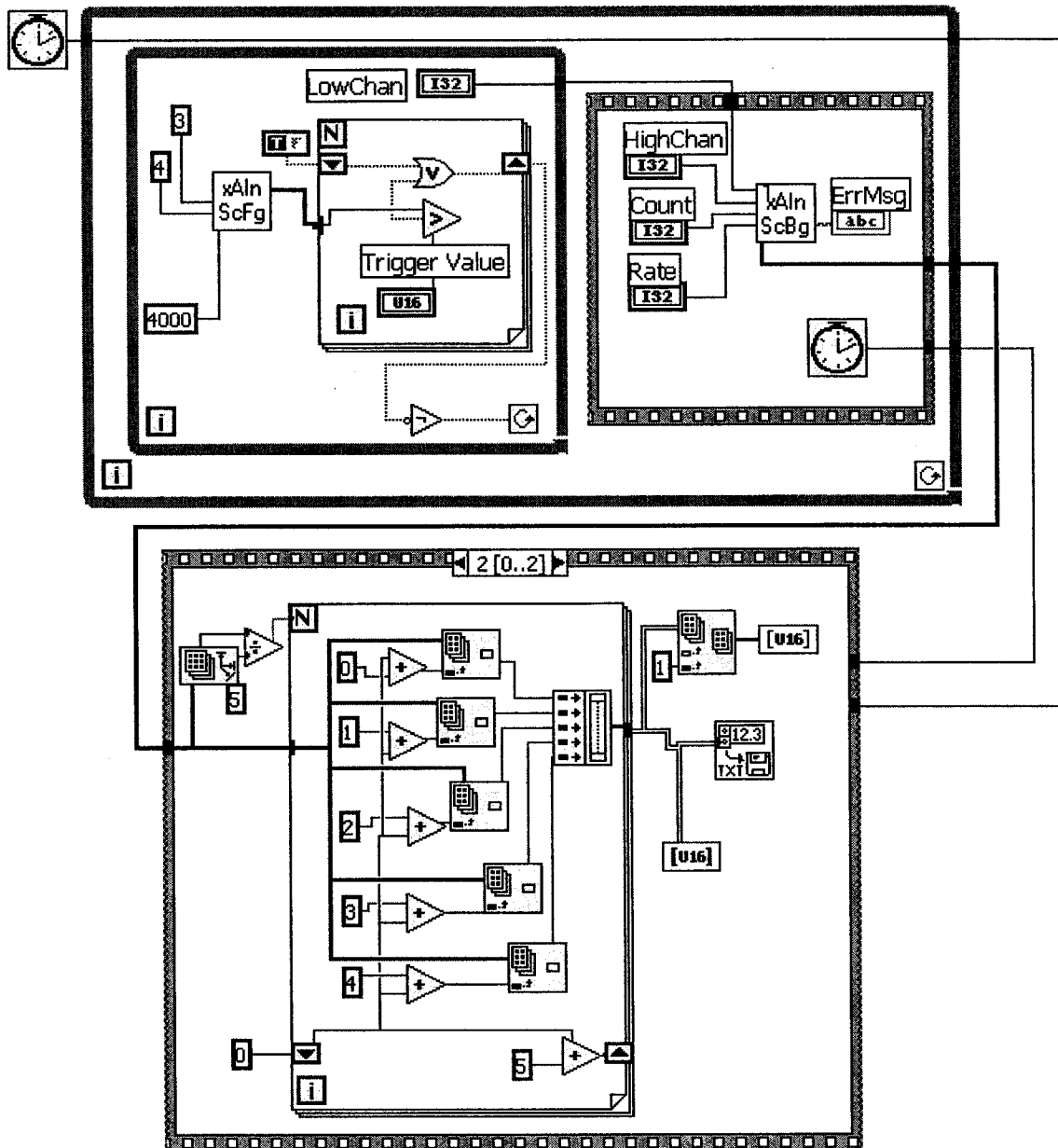


Figure 4-9: Labview model capable of monitoring four channels (gages) at the same time with identical triggering mechanism

2000 lbs/min and strain gage readings were recorded by a 12 bit, 160 kHz Instronet data acquisition system. Using the modified apparatus the monotonic loading tests were successfully performed. All three specimens failed along the line-of-action of load aligned with the notches. The three specimens failed at a maximum load in range of 5200 to 5700 lbs. Tensile and compressive strains were then calculated from the data collected by the data logger. Shear strain was then determined from tensile and compressive strains as shown in section 4.1.2.1.

Figure 4-10 shows the shear stress - shear strain diagram as it was measured and calculated from the monotonic tests. As shown, two measurements of shear strains were made from the readings on both sides of each specimen, except the specimen three in which one of the rosettes broke while inserting the specimen into the apparatus. Two of three tests showed consistently similar results. As seen, in test number 1, shear strain measurement on both sides were initially identical. At loads close to peak shear strength, one gage departed and showed more shear strain. Test 2 showed similar behavior with one gage showing higher shear strain at loads close to peak shear strength of the specimen. This behavior could be because at the instant of failure while crack starts at one side and is growing through the thickness of the specimen, the gage in the opposite side may still be intact and reads lower strains. Under these circumstances the specimen is unstable and therefore this behavior is not indicative of the granite mechanical properties. Therefore, for modeling purposes, this part of stress-strain curve is not taken into account. The peak shear strength as it is measured from each test differs from 19 to 21 MPa. Test 3 showed considerably higher shear strain but the maximum shear strength

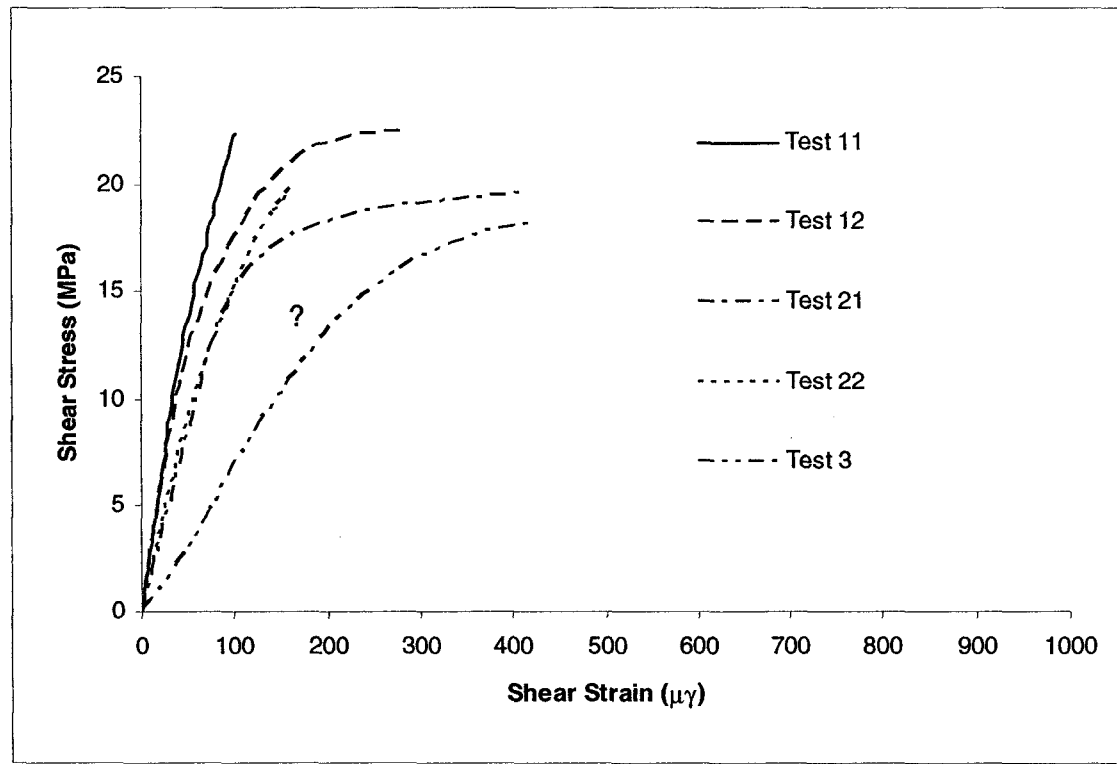


Figure 4-10: Granite shear stress – shear strain diagram as it was calculated from strain gage readings. Test 11 and test 12 indicate the shear strain as it was calculated from the two rosettes on specimen number 1. Test 21 and test 22 also show similarly shear strains as measured by rosettes on specimen 2 and Test 3 shows the only reading available from specimen 3.

of this specimen is in line with shear strength range as it was obtained from tests 1 and 2. The reason for demonstrating higher shear strains could be the presence of internal defects in the specimen. Have we had a second readings from this specimen, this fact could have been confirmed. The data obtained from the monotonic tests were used in the dislocation model to determine crack tip damage in the rock type under investigation, i.e. granite. An average of the shear strength properties of the granite specimen was obtained from the available test results. The average value was inputted into the numerical model. Figure 4-11 shows the average shear stress – shear strain diagram for the granite specimen under investigation.

It is to be noted that Equation (3-6) of Chapter 3 is derived for a shear stress – shear displacement diagram. It has to be modified in such a way that it can be used when shear stress – shear strain diagram is available. For this purpose, the method of Bilby et al. (1965) is adopted in which these investigators defined plastic strain in terms of plastic displacement by using a parameter  $\alpha$  with the dimension of length. The derivation of shear stresses within the plastic zone in this case is as follows. The nonlinear rock response according to the Ramberg-Osgood material model can be given by:

$$\tau_r(x) = m\tau_0 \left( \frac{\gamma(x)}{\gamma_0} \right)^n \quad (4-1)$$

where  $\gamma(x)$  is the total shear strain and  $\gamma_0$  is the shear strain at the yield intercept. The



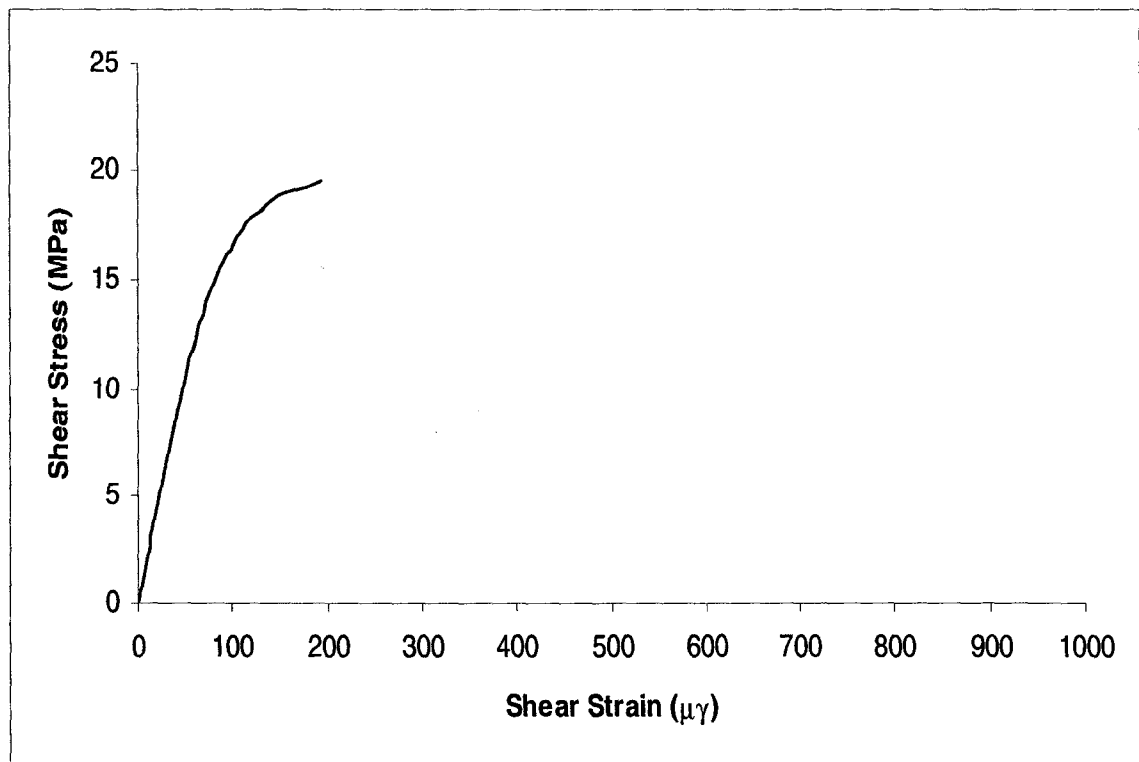


Figure 4-11: Average shear stress – shear strain diagram for granite specimens

total shear strains consist of plastic strains  $\gamma_p(x)$  and the elastic yield intercept,  $\gamma_0$ , i.e.,

$\gamma(x) = \gamma_p(x) + \gamma_0$ . Therefore, Equation (4-1) can be re-written as:

$$\tau_r(x) = m\tau_0 \left( \frac{\gamma_p(x)}{\gamma_0} + 1 \right)^n \quad (4-2)$$

According to Bilby et al., (1965), plastic strain can be defined by:

$$\gamma_p(x) = \frac{\varphi_p(x)}{\alpha}$$

where  $\varphi_p(x)$  is the plastic displacement and  $\alpha$  is a constant of the dimension length.

Using this relationship the Equation (4-2) can be rearranged such that:

$$\tau_r(x) = m\tau_0 \left( \frac{\varphi_p(x)}{\alpha\gamma_0} + 1 \right)^n \quad (4-3)$$

There will be little changes to the mathematical model and the assessment of damage through dislocation theory due to this modification. Similarly for the unloading case the reversed shear stress field within the reversed plastic zone is defined by:

$$\tau_{rr}(x) = m\tau_0 \left( \frac{\Delta\varphi_p(x)}{\alpha\gamma_0} + 1 \right)^n - \beta\tau_h(x) \quad (4-4)$$

This formulation will be used for assessment of rock damage when granite properties are used. The results of this simulation will be presented in Chapter 5.

### ***4.3. Cyclic Loading Tests Results***

Following monotonic loading tests, seven specimens were cut and prepared for fatigue cyclic loading tests. On each specimen four crack gages were attached, one at the tip of each notch.

Table 4-1 shows the applied loading range, frequency, applied load ratio ( $R$ ) and the number of cycles to failure for each specimen tested. Results suggest that at low maximum applied loads granite demonstrates a high variability in the number of cycles to failure. Specimens 4 to 7 were all loaded at the same loading range but while one could stand 65000 cycles, another one could barely stand 100 cycles. This could be due to internal defects, the presence of which plays an important role in rock behavior during fatigue tests. Therefore, it is expected that at low maximum applied loads, fatigue life data to be largely scattered. Figure 4-12 shows fatigue stress life ( $S-N$ ) curve of granite. A fitted semi-logarithmic model as given below can be used to predict fatigue life of granite for various maximum applied loads. The fitted model characterizes fatigue of granite by:

$$\tau = 19.638 - 1.5929 (\log N)$$

where  $\tau$  is the maximum applied stress in MPa and  $N$  is the number of cycles that the rock can stand at the given stress level. For  $N=1$ , the peak shear strength of granite is

Table 4-1: Summary of fatigue life data for all fatigue tests

Specimen Number	Load Range (lbs)		$R = \frac{P_{Min.}}{P_{Max.}}$	Frequency (Hz)	Number of Cycles to Failure (N)
	$P_{Min.}$	$P_{Max.}$			
1	470	4700	0.1	0.5	145
2	430	4300	0.1	1	809
3	390	3900	0.1	1	11405
4	355	3550	0.1	1	1100
5	355	3550	0.1	1	65000
6	355	3550	0.1	1	85
7	355	3550	0.1	1	4500

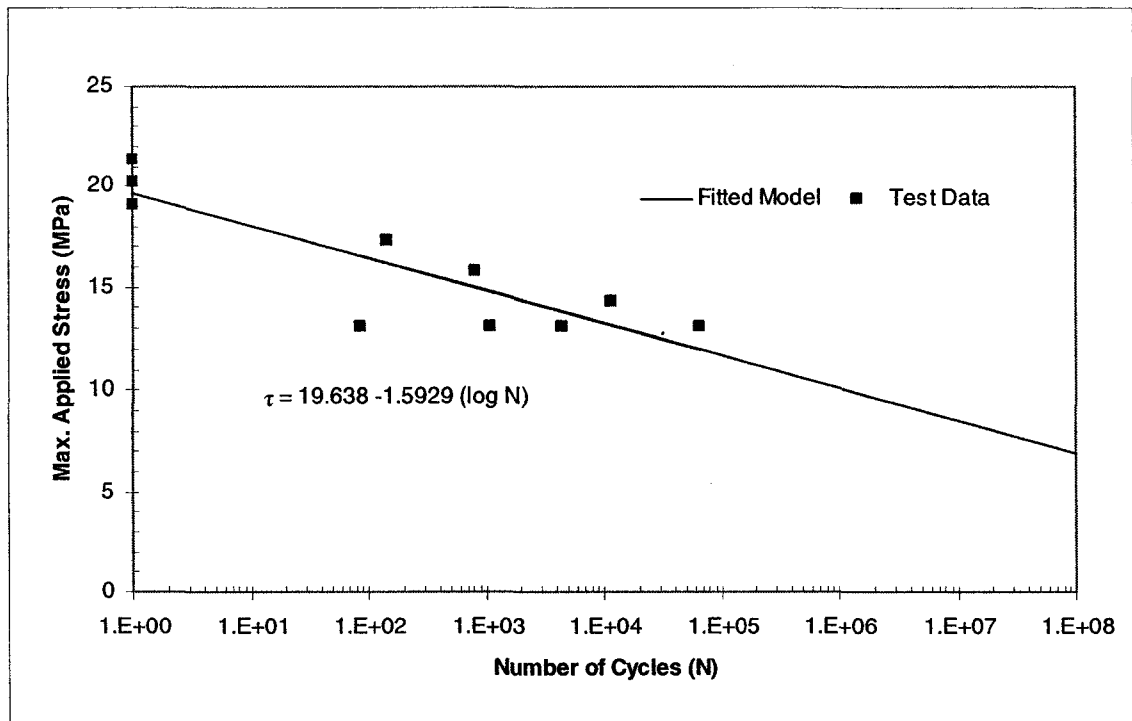


Figure 4-12: Fatigue stress life curve (S-N Curve) of granite and the fitted model

recovered. Similarly, the fatigue model can be rearranged to determine fatigue life of granite at a given maximum applied stress:

$$N = 10^{\left[ \frac{\tau_f - \tau}{m} \right]}, \quad \tau_f = 19.638, \quad \text{and } m = 1.5929$$

where  $\tau$  is the required maximum applied stress in MPa and  $\tau_f$  is the fatigue strength of granite. Using this relationship, we can see that for any applied stress less than 75% of the yield stress of the granite, the number of cycles increases exponentially to levels that practically means specimen will not break, i.e. infinite fatigue life.

During cyclic loading tests, the application of crack propagation gages was also examined. The use of crack propagation gages proved to be ineffective in measuring crack propagation rate since due to brittleness of granite once crack is initiated it propagates very fast. At this situation crack growth is unstable and uncontrollable (For this same reason, as mentioned before, pre-cracking was not possible either.). Therefore, after crack is initiated, the process of crack growth is so fast that breakage of the individual strands of the crack gages can not be distinguished with the available equipment. Out of seven fatigue tests performed only one produced an output in which breakage of the first few strands were visible (Figure 4-13). After this stage, crack growth sped up and the remaining strands broke simultaneously or at a very close time together. Data logger, although running at its maximum reading rate, could only pick up their signal in a distorted form as shown in Figure 4-13 between 6300 and 6400 readings. Another problem with crack propagation gages that was observed, was that as soon as the

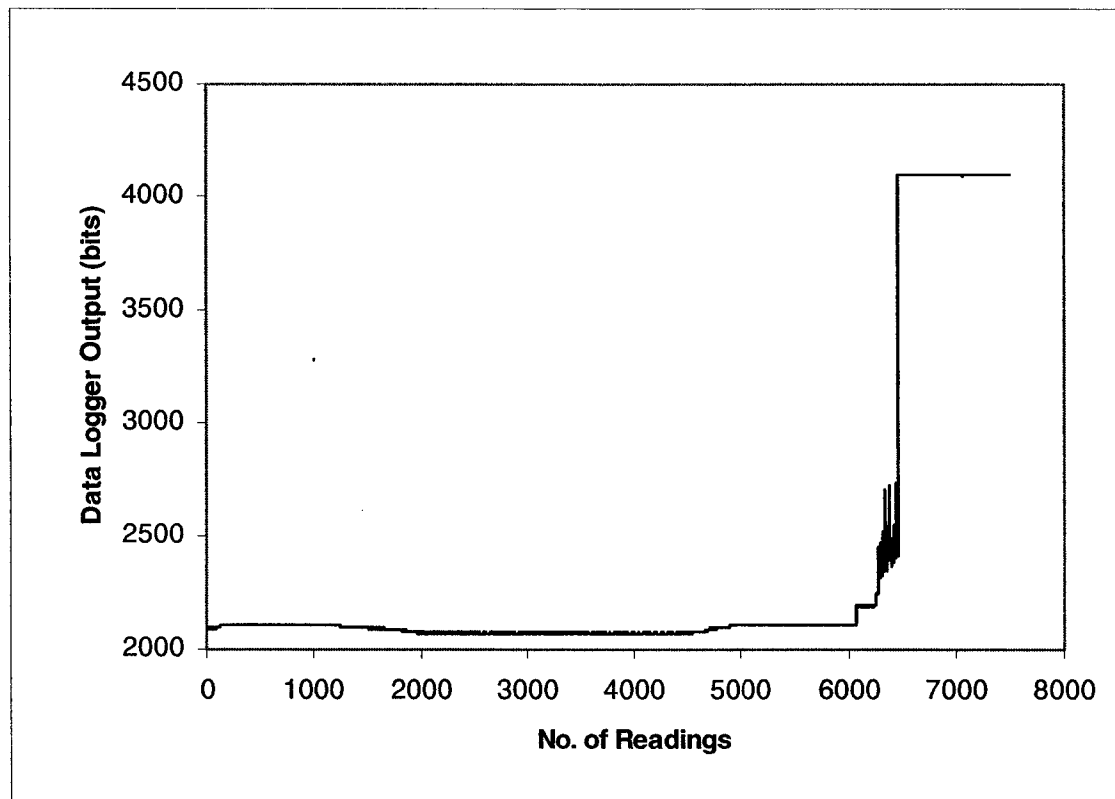


Figure 4-13: Sequence of breakage of individual strands of crack propagation gage, clearly at final stages of crack growth several strands of crack gage is broken at the same time.

strands of wire started to break one after another, movement of rock specimen caused the wires to reconnect and as a result the readings from the crack gages were distorted. This effect can be seen in Figure 4-13 between readings 2000 to 5000 where readings drop to 2071 bits after it has reached to 2105 bits in previous readings (readings 1000-2000).

As part of the research thesis an experimental program was undertaken to analyze monotonic and cyclic loading behavior of granite specimens. The testing method used along with special consideration with regard to shear testing of granite specimens were described in this chapter. This followed by the results of the monotonic and cyclic tests. In the next chapter, the results of the numerical model is presented and discussed. The granite shear properties obtained from the experiments will be used to analyze plastic displacement and stress field at the crack tip and to determine crack tip damage in granite subject to cyclic loading and unloading.



## **Chapter 5: Analysis and Results**

In this study, a numerical model based on the theory of dislocations was built to investigate the problem of post-blast rock damage in underground excavations. The problem is mainly due to blast cyclic loading of the rock that causes cracks to initiate from the already existing microcracks. The damage process is followed by the crack propagation due to sustained cycling of the rock by the blast vibration.

The development of dislocation model was explained in detail in Chapter 3. In Chapter 4 the experimental investigation by which the monotonic and cyclic mechanical properties of granite were obtained, was described. The mechanical properties of the granite specimens obtained from the shear tests are inputted into the dislocation model to simulate rock damage in terms of crack tip plastic displacement subject to cyclic loading.

The proposed dislocation model takes mechanical properties of rock into account and calculates the amount of damage in rock as it occurs by the blast-induced cyclic loading. Using this information, the fatigue damage of the rock can be predicted and used in ground control practices in designing a support system that is safe against both static and dynamic loads. The latter is the application of this model and is beyond the scope of this study and hence is not pursued here.

Numerical analysis is performed using the data obtained from the literature (Bertacchi et al., 1974) and the data obtained from the monotonic testing on granite. In the following, the results of the dislocation model using the data from the literature are presented

starting with the monotonic loading followed by the unloading results. The analysis is continued with the results of the dislocation model using the data from the monotonic loading tests. In each case, the analysis is performed for several crack sizes subject to various applied loads up to  $0.65\tau_0$ . The unloading analysis is also performed for five unloading stress ratios, i.e.  $\tau_u/\tau^\infty = 0.2, 0.4, 0.6, 0.8, 1.0$ .

### ***5.1. Numerical Results Using Data from Literature***

Numerical results are divided into two parts. In the first part, the results of the monotonic loading of rock are presented in terms of plastic displacement and stress distribution at the crack tip and within the plastic zone, and the extent of the plastic zone is also determined. In the second part, using the results of the monotonic loading part, the change in the plastic displacement at the crack tip and within the reversed plastic zone is calculated, and the extent of reversed plastic zone is determined as well.

#### **5.1.1. Monotonic Loading Stage – Numerical Results**

As shown in Figure 3-1 of Chapter 3, under monotonic loading a plastic displacement field is formed ahead of the crack tip that extends to point 'a' from the crack tip. Subject to applied load, dislocations move out of the crack tip and spread along the plastic zone. The proposed dislocation model calculates the length of the plastic zone 'a' and finds the unknown coefficients  $\alpha_i$  of the plastic displacement function,  $\varphi_p(x)$  ahead of the crack tip (Equation 3-22, Chapter 3). In the following, the monotonic loading model is applied to a case study where

plastic displacement function ahead of the crack in a rock of given type is determined. The length of the plastic zone ' $a$ ' is also numerically calculated. It is to be noted that this information is needed to find the change in the plastic displacement in the unloading stage.

The type of rock under consideration is gneiss with a shear stress - shear displacement diagram as shown in Figure 5-1 (Bertacchi et al., 1974). The diagram was digitized and fitted by a power law function of the form proposed by the Equation 3-6 in Chapter 3.

For this rock type, dislocation model was run for the initial crack sizes of 10, 20, 50, 100, 200, and 400 mm subject to the applied monotonic load of up to  $0.65\tau_0$  of the rock. The values of the plastic displacement function coefficients,  $(\alpha_i, i = 1, \dots, 8)$ , and the length of the plastic zone, ' $a$ ', were determined for different applied loads and crack sizes. Knowing  $\alpha_i$ , one can easily determine crack tip plastic displacement and crack tip stress distribution from Equation 3-22 and Equation 3-6 of Chapter 3, respectively. Figure 5-2 and Figure 5-4 show the non-dimensionalized plastic displacement versus distance from the crack tip for a 10 mm and a 400 mm crack, respectively, subject to the given applied loads. As shown in these figures, plastic displacement is maximum at the tip of the crack. It reduces to zero at the end of the plastic zone, i.e. point ' $a$ ' in Figure 3-1 of Chapter 3. The length of the plastic zone increases as the magnitude of the applied load and the initial length of the crack increases. It is to be noted that as initial crack size increases from 10 mm to 400 mm the crack tip plastic displacement is suggested to increase by two orders of magnitude indicating the effect of initial crack size on the extent of plastic displacement at the crack tip. Figure 5-3 and Figure 5-5 also show the non-dimensionalized shear stress distribution versus distance from the crack tip along the

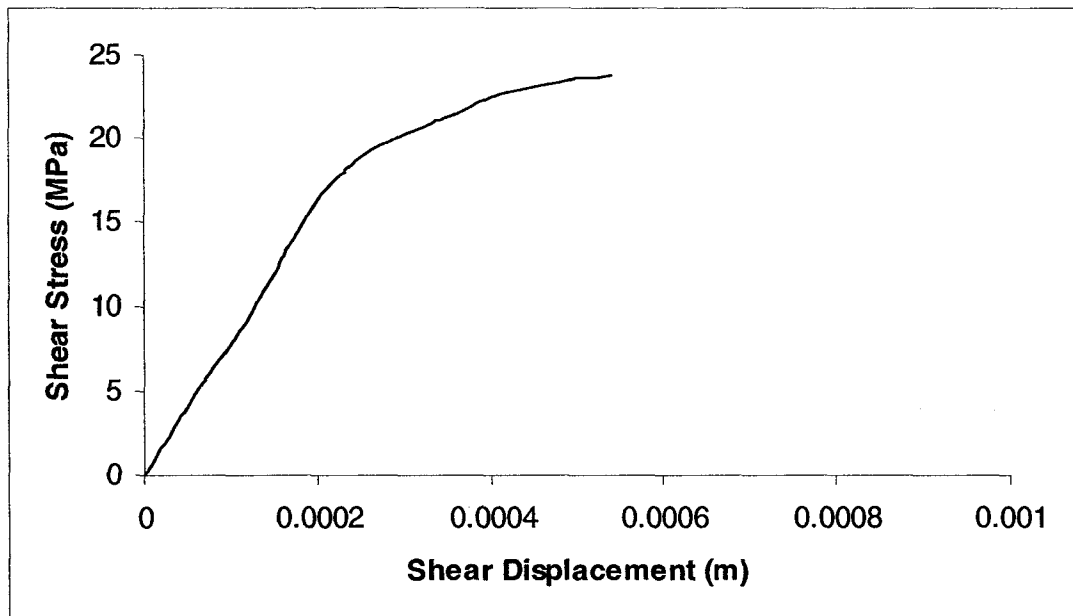


Figure 5-1: Shear stress-shear displacement diagram of the gneiss (Bertacchi et al., 1974)

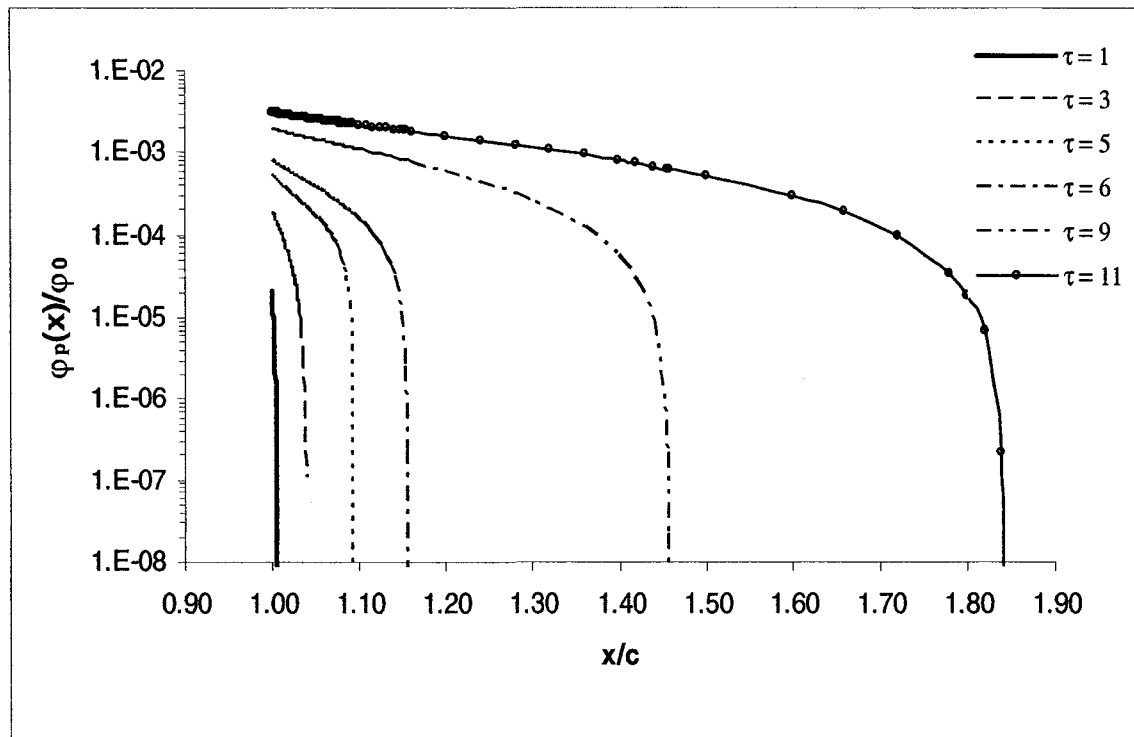


Figure 5-2: Non-dimensionalized plastic displacement versus distance from the crack tip for given applied stresses in MPa ahead of a crack of  $2c = 10$  mm length

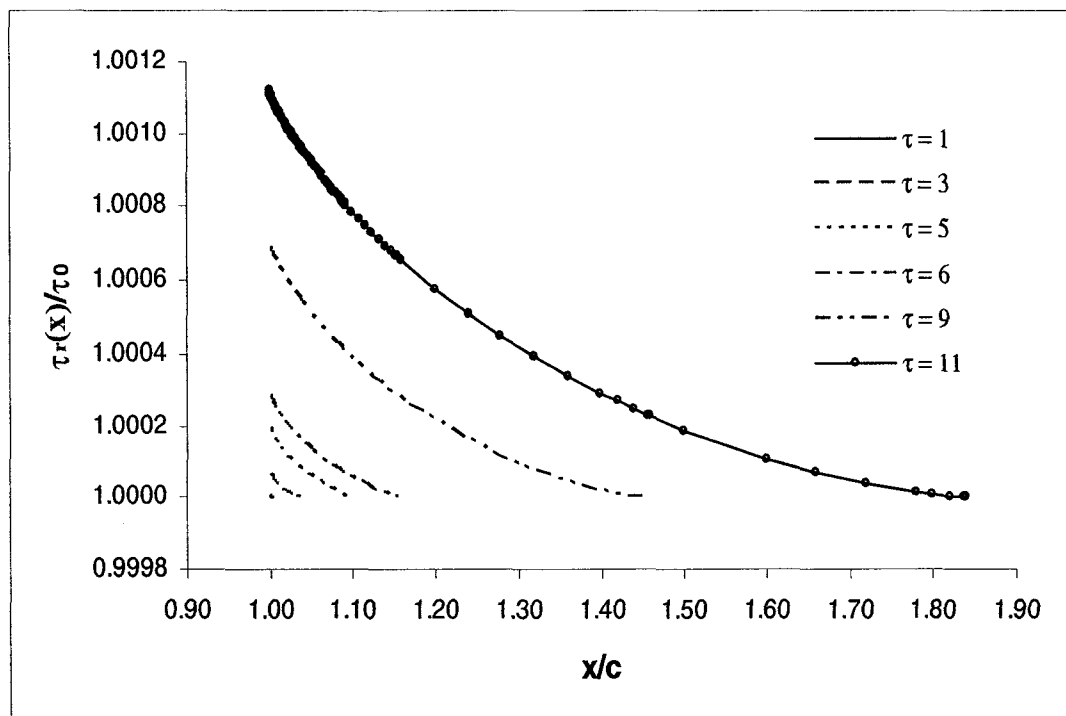


Figure 5-3: Shear stress distribution ahead of the crack tip versus distance from the crack tip for given applied stresses in MPa -  $2c = 10$  mm

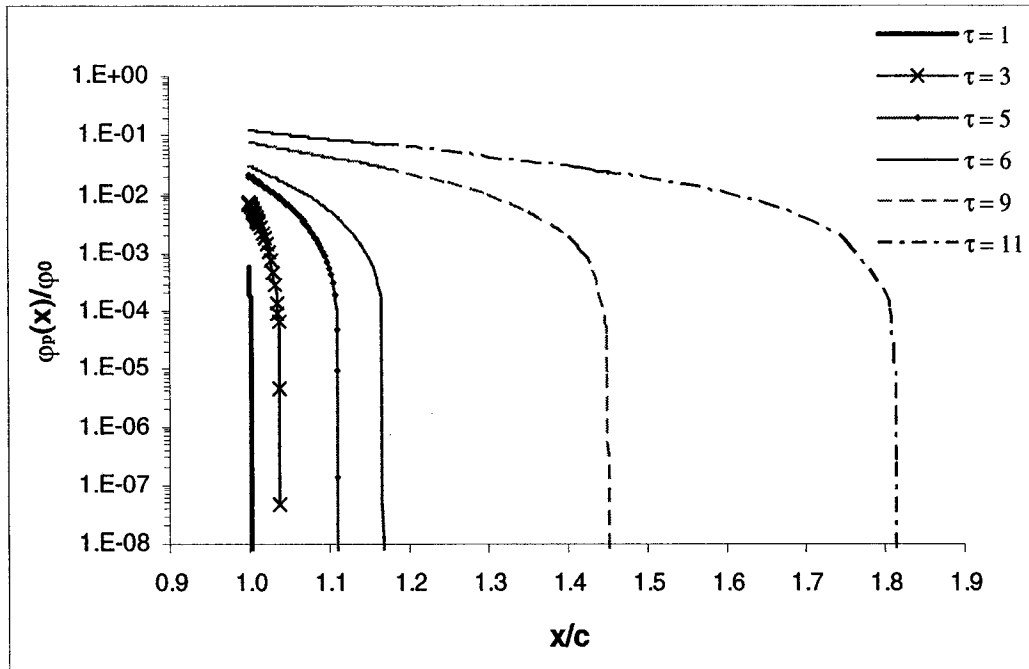


Figure 5-4: Non-dimensionalized plastic displacement versus distance from the crack tip for given applied stresses in MPa ahead of a crack of  $2c = 400$  mm length

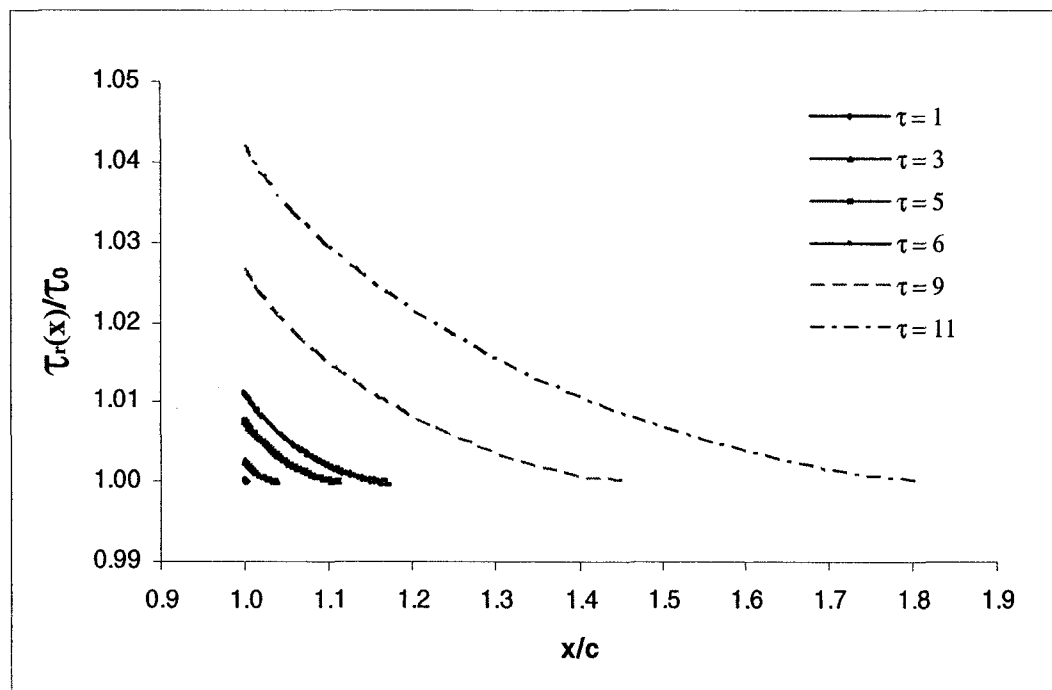


Figure 5-5: Shear stress distribution ahead of the crack tip versus distance from the crack tip for given applied stresses in MPa -  $2c = 400$  mm



plastic zone for a 10 mm and a 400 mm crack, respectively, subject to the given applied loads. Induced shear stress in the plastic zone is also maximum at the crack tip and decreases rapidly along the plastic zone. As expected, in the plastic zone shear stresses are higher than the resisting stresses that prevent dislocations to move away from the crack tip. Therefore, they cause dislocations to move out and spread along the plastic zone. Stresses drop to less than resistance stress of the rock beyond the point 'a' where rock response is elastic. Comparison of these figures reveals the effect of the initial crack size on the magnitude of the crack tip stresses. Plastic displacement field and shear stress distribution diagrams for the other crack sizes of 20, 50, 100 and 200 mm are also shown in Appendix C. In Figure 5-6 and Figure 5-7, the effect of initial crack size on plastic displacement distribution and shear stress distribution in the plastic zone is examined in non-dimensionalized form, for a given applied load of 9 MPa ( $0.53\tau_0$ ), respectively. As shown, although the length of the plastic zone is different for different crack sizes, for a given rock type and under the same applied load, all cracks of different sizes experience the same  $a/c$  ratio. The non-dimensionalized forms of crack tip plastic displacement,  $\varphi_p(c)$ , and crack tip shear stress,  $\tau_r(c)$ , diagrams are plotted against the ratio of the applied load for different crack sizes in Figure 5-8 and Figure 5-9, respectively. Figure 5-9 illustrates that large cracks experience larger shear stress at the crack tip than the small cracks. It also shows that for a given crack size higher applied loads cause higher shear stress at the crack tip. The effect of higher stress at the crack tip is reflected in Figure 5-8 in terms of larger plastic displacement at the crack tip.

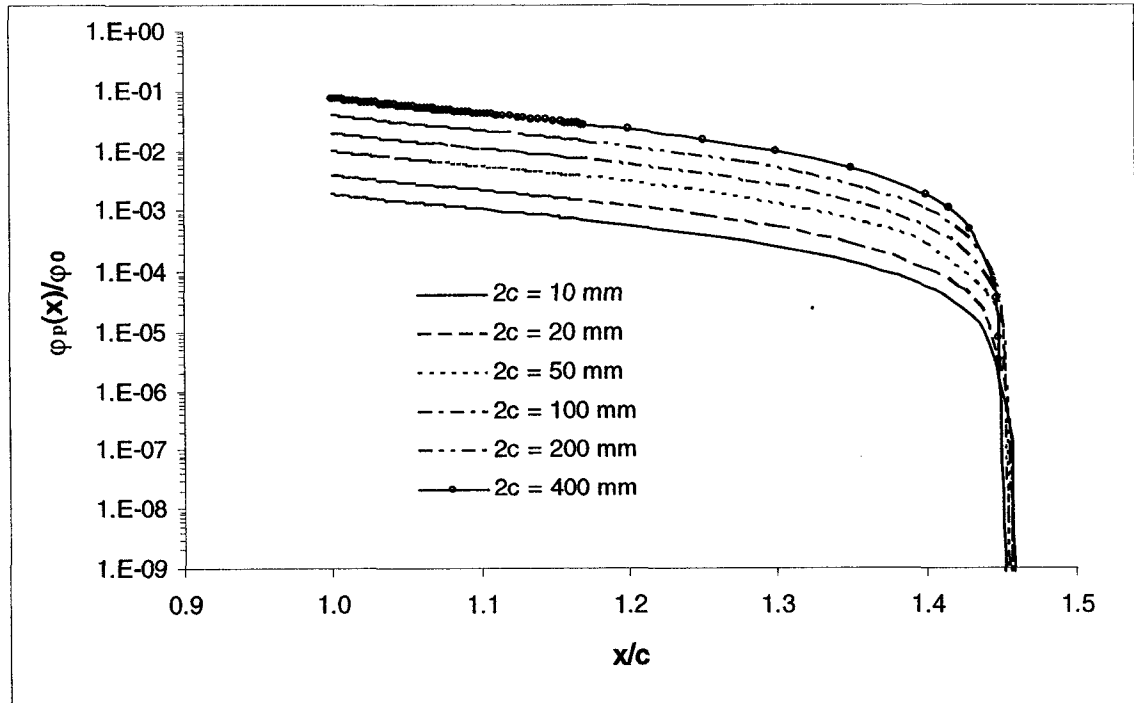


Figure 5-6 Non-dimensionalized plastic displacement versus distance from the crack tip for various crack sizes and an applied load of  $\tau = 9$  MPa

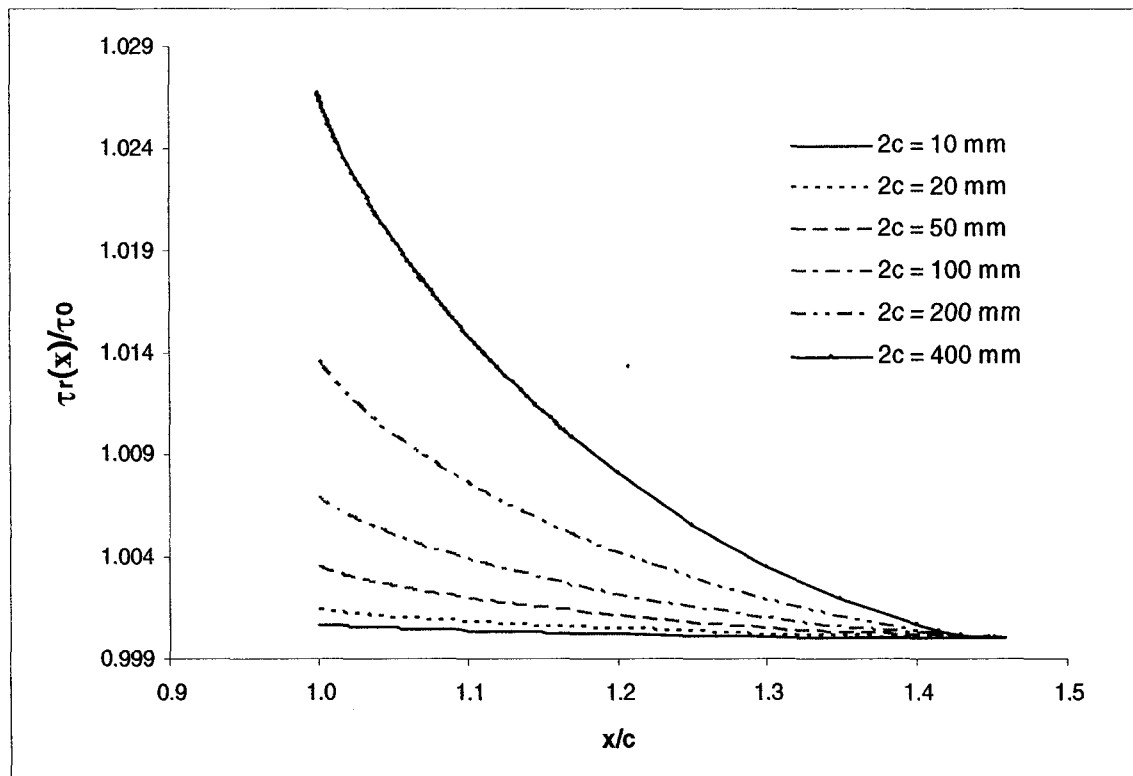


Figure 5-7: Non-dimensionalized crack tip stress distribution versus distance from the crack tip for various crack sizes and an applied load of  $\tau = 9$  MPa

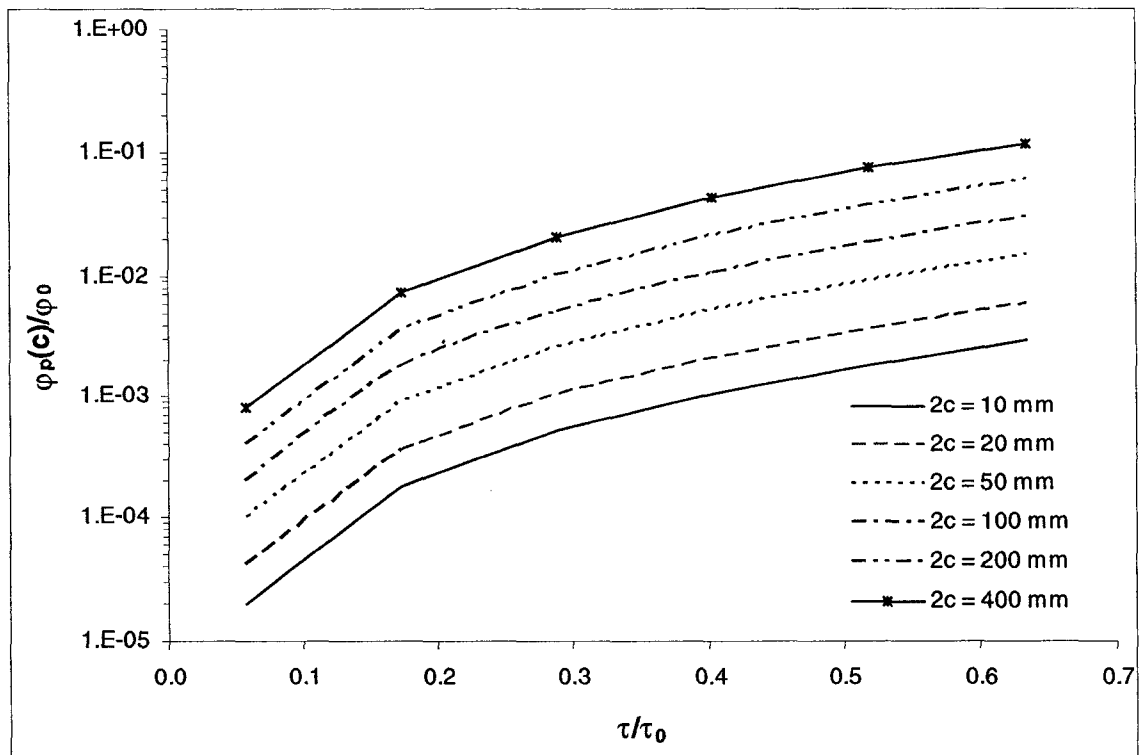


Figure 5-8: Non-dimensionalized crack tip plastic displacement versus applied stress ratio for various crack sizes

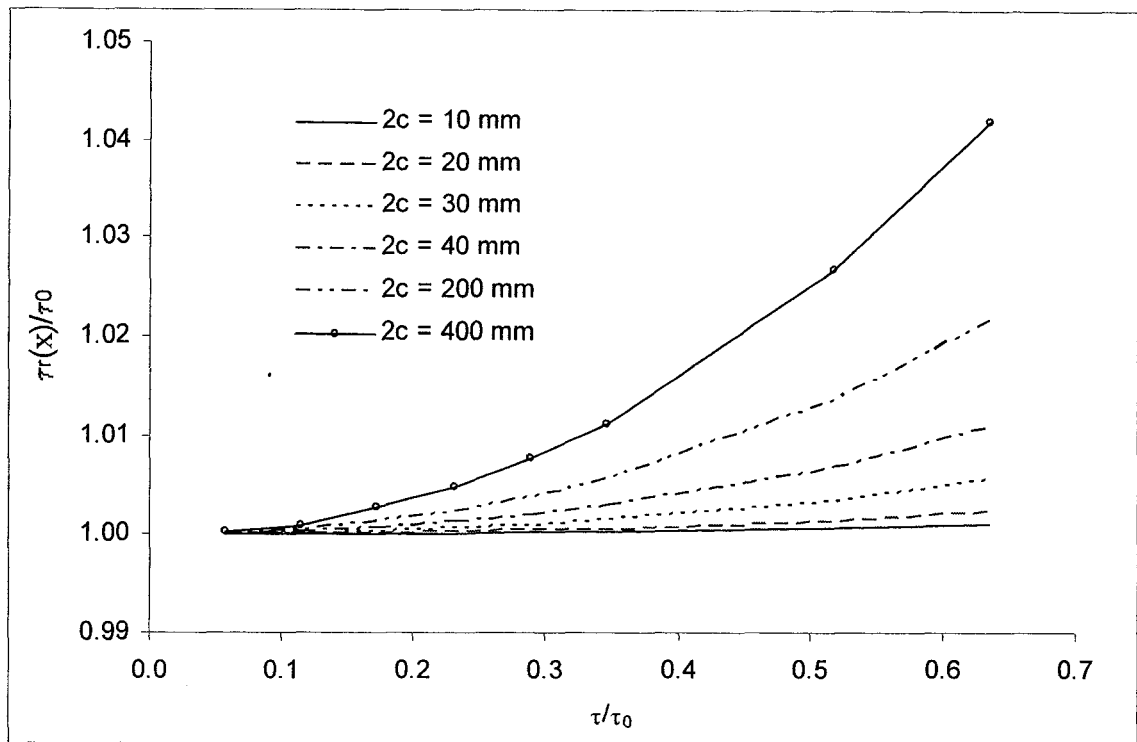


Figure 5-9: Non-dimensionalized Crack tip stress ratio versus applied stress ratio for various crack sizes

In the next section, the cyclic unloading results are presented. The monotonic loading solution presented above is used in the unloading problem to find the unloading solution.

### 5.1.2. Unloading Stage – Numerical Results

The monotonic loading solution is inputted into the dislocation model to find the unloading solution. The analysis is carried out for several different initial crack sizes of 10 mm to 1000 mm and for various applied loads of up to  $0.65\tau_0$  where  $\tau_0$  is the yield strength of the rock.

For each given crack size and applied load, the monotonic loading problem is first solved. Then, the unloading solution is found for five different unloading ratios ( $\tau_u/\tau$ ) of 0.2, 0.4, 0.6, 0.8 and 1.0 (fully unloaded) where  $\tau$  is the applied monotonic load. The unloading problem is solved for two commonly used plasticity rules, i.e. kinematic hardening and isotropic hardening. As explained earlier, according to kinematic hardening rule, at applied stresses above yield limit of the material, the yield surface only shifts in the stress space with no expansion in any direction while under isotropic hardening conditions the yield surface does not move rather it expands in all directions evenly in the stress space. In the following, the unloading solution for two cracks of initial sizes of 10 mm and 400 mm subject to an applied load of 11 MPa with unloading at five different ratios is illustrated. The unloading solution is given in terms of the change in the plastic displacement and the reversed shear stress distribution within the reversed plastic zone.

Figure 5-10 and Figure 5-11 show the change in the plastic displacement and the reversed shear stress distribution within the reversed plastic zone that are formed ahead of a 10 mm crack that is subjected to an 11 MPa ( $0.65\tau_0$ ) monotonic loading and subsequent unloading as given, considering kinematic hardening rule is applied. The results suggest a similar trend to monotonic loading solution except that the length of the reversed plastic zone is smaller by about one order of magnitude. However, the length of the reversed plastic zone increases as the magnitude of the unloading stress is increased, i.e. it increases up to ten times when it fully unloaded compared with when it is only unloaded by 20% (Figure 5-11). This fact has been shown in Figure 5-12 and Figure 5-13 where plastic displacement and shear stresses, respectively, under monotonic loading ( $\tau = 11$  MPa) are superimposed on the change in the plastic displacement diagram and the reversed shear stress distribution diagram, respectively, for given unloading ratios from the same monotonic load ( $\tau = 11$  MPa). This is because, as mentioned in Chapter 3, some of the dislocations under unloading move back inside the crack resulting in a reduced dislocation density in this region and as a result a shorter reversed plastic zone is formed. Similar results are obtained for the isotropic hardening rule as shown in Figure 5-14, Figure 5-15, Figure 5-16 and Figure 5-17 for a 10 mm crack subjected to an 11 MPa monotonic and subsequent cyclic loading.

Figure 5-18 and Figure 5-19 also show the change in the plastic displacement and the reversed shear stress distribution and the extent of the reversed plastic zone, formed ahead of a 400 mm crack and subjected to an 11 MPa ( $0.65\tau_0$ ) monotonic loading and subsequent unloading under kinematic hardening rule. Figure 5-20 compares the monotonic loading plastic displacement within the plastic zone with the unloading-induced changes in the plastic

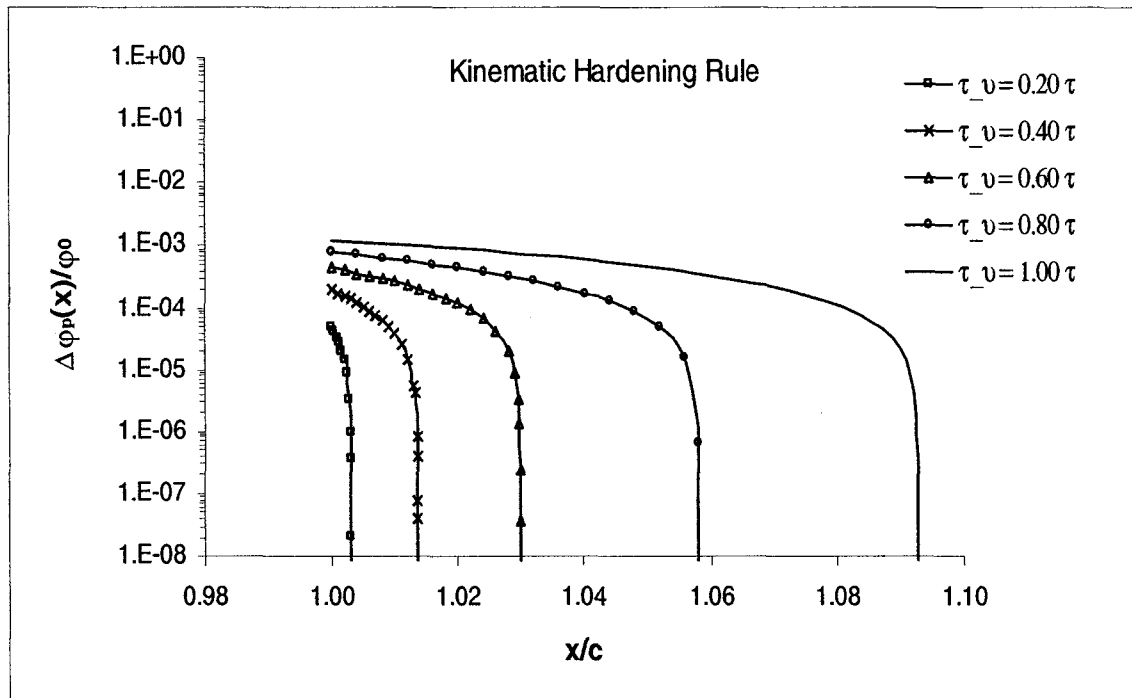


Figure 5-10: Non-dimensionalized diagram of the change in the plastic displacement versus distance from the crack tip for an applied load of  $\tau = 11$  MPa and unloading stresses proportionate to  $\tau$  for initial crack length of  $2c = 10$  mm under kinematic hardening rule



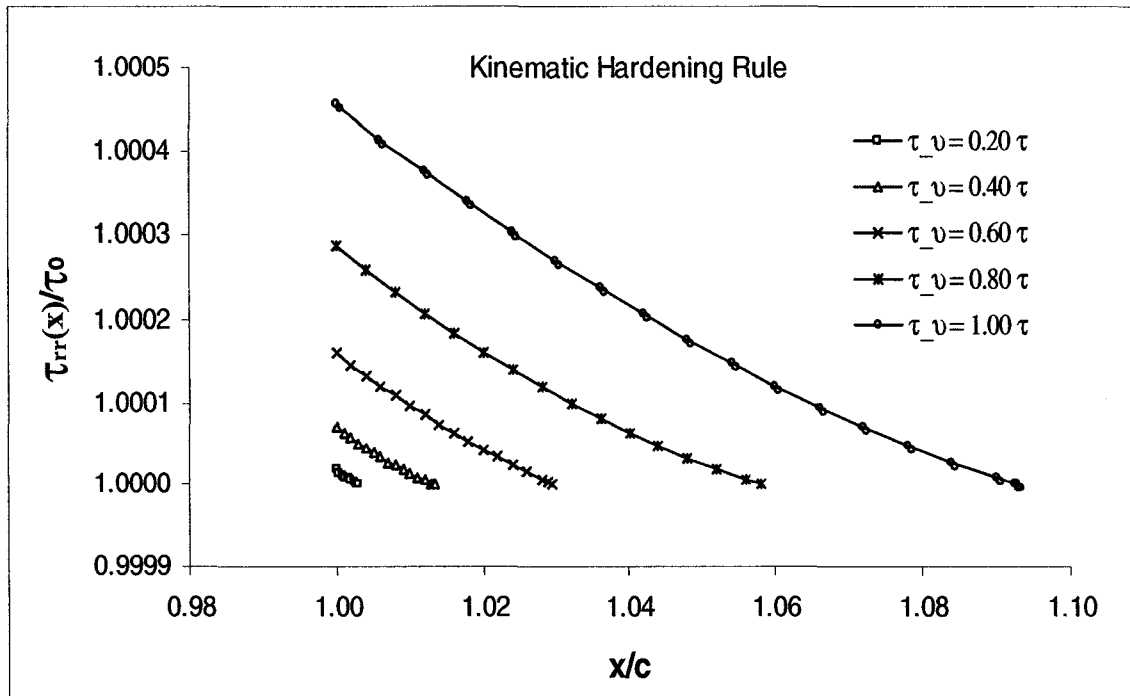


Figure 5-11: Non-dimensionalized diagram of the reversed stress distribution ratio versus distance from the crack tip for an applied load of  $\tau = 11$  MPa and unloading stresses proportionate to  $\tau$  for initial crack length of  $2c = 10$  mm under kinematic hardening rule

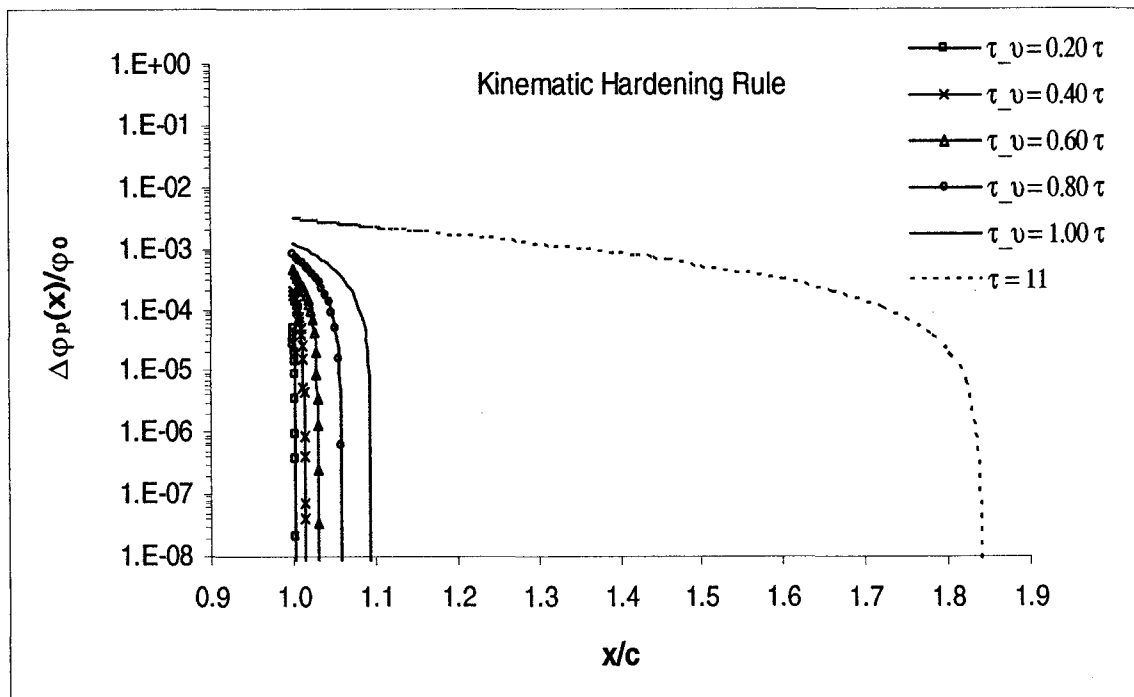


Figure 5-12: Comparison of the monotonic loading results with the unloading results in terms of non-dimensionalized plastic displacement versus distance from the crack tip for an applied load of  $\tau = 11$  MPa and unloading stresses proportionate to  $\tau$  for initial crack length of  $2c = 10$  mm under kinematic hardening rule

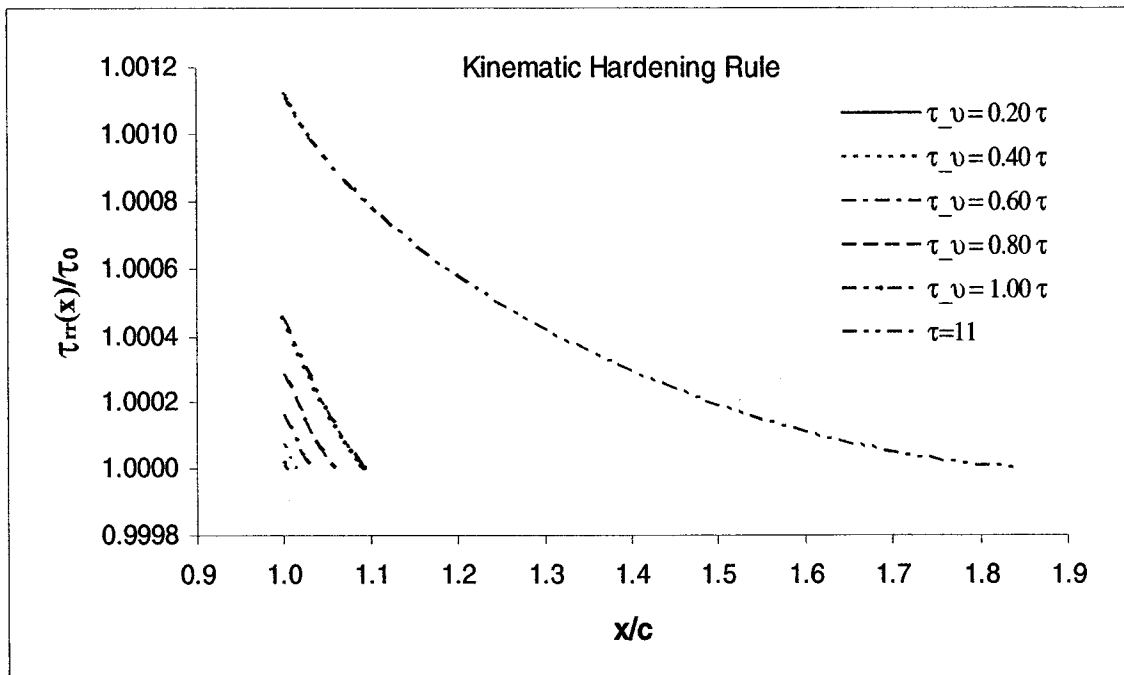


Figure 5-13: Comparison of the monotonic loading results with the unloading results in terms of non-dimensionalized shear stress distribution versus distance from the crack tip for an applied load of  $\tau = 11$  MPa and unloading stresses proportionate to  $\tau$  for initial crack length of  $2c = 10$  mm under kinematic hardening rule

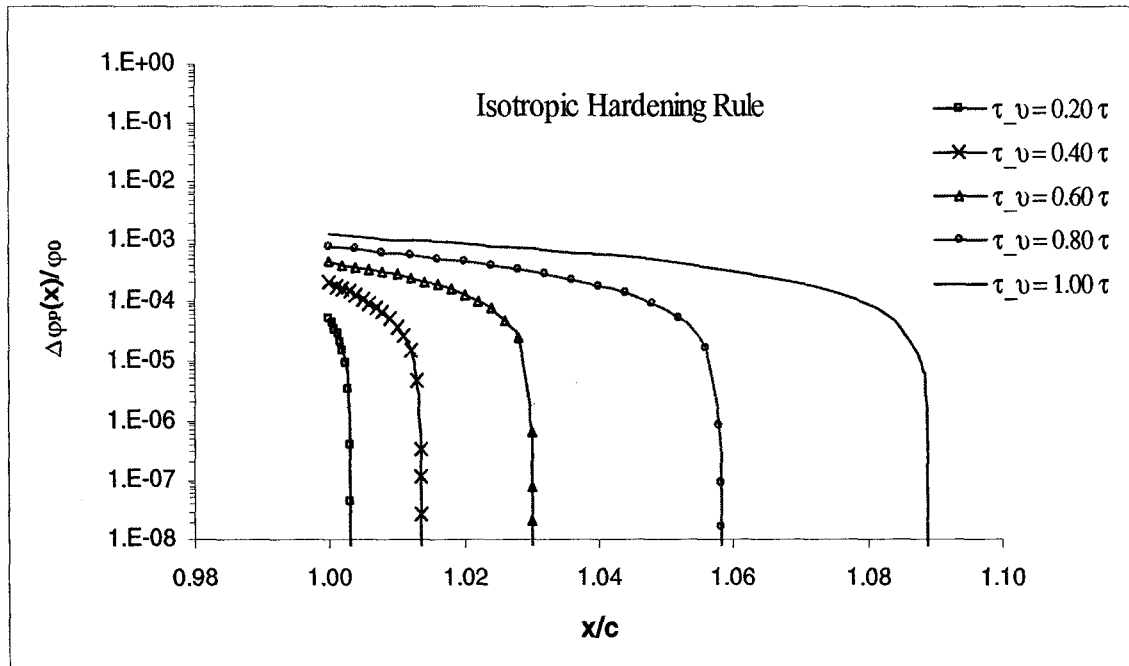


Figure 5-14: Non-dimensionalized diagram of the change in the plastic displacement versus distance from the crack tip for an applied load of  $\tau = 11$  MPa and unloading stresses proportionate to  $\tau$  for initial crack length of  $2c = 10$  mm under isotropic hardening rule

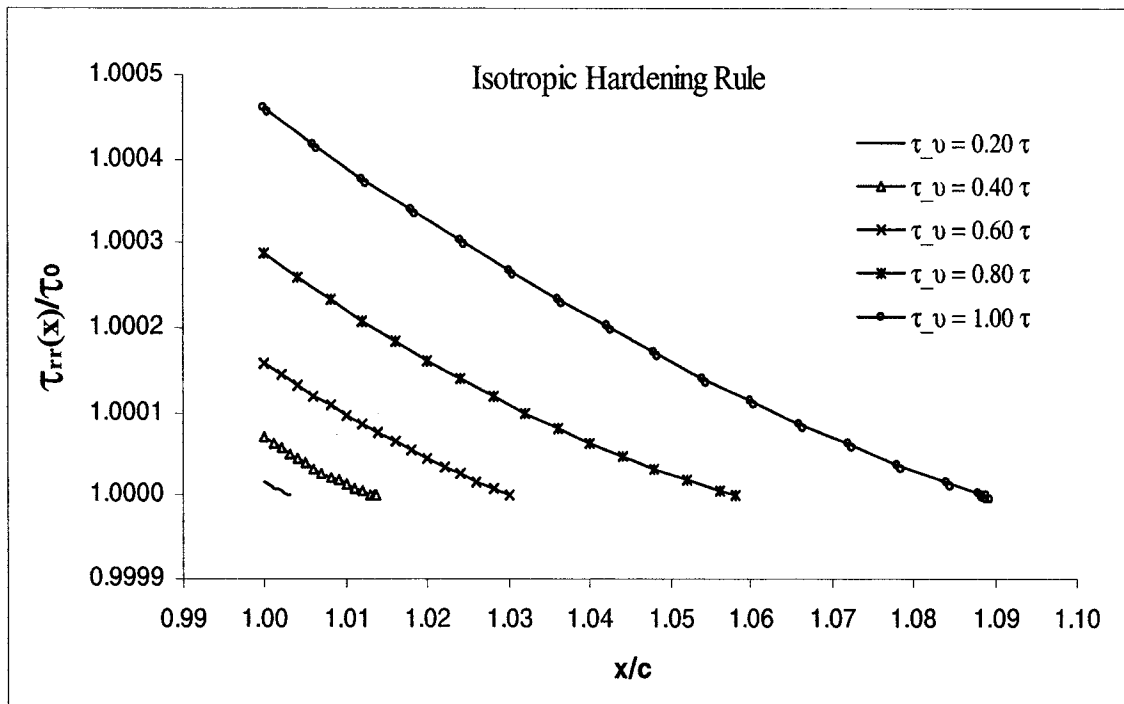


Figure 5-15: Non-dimensionalized diagram of the reversed shear stress distribution ratio versus distance from the crack tip for an applied load of  $\tau = 11$  MPa and unloading stresses proportionate to  $\tau$  for initial crack length of  $2c = 10$  mm under isotropic hardening rule

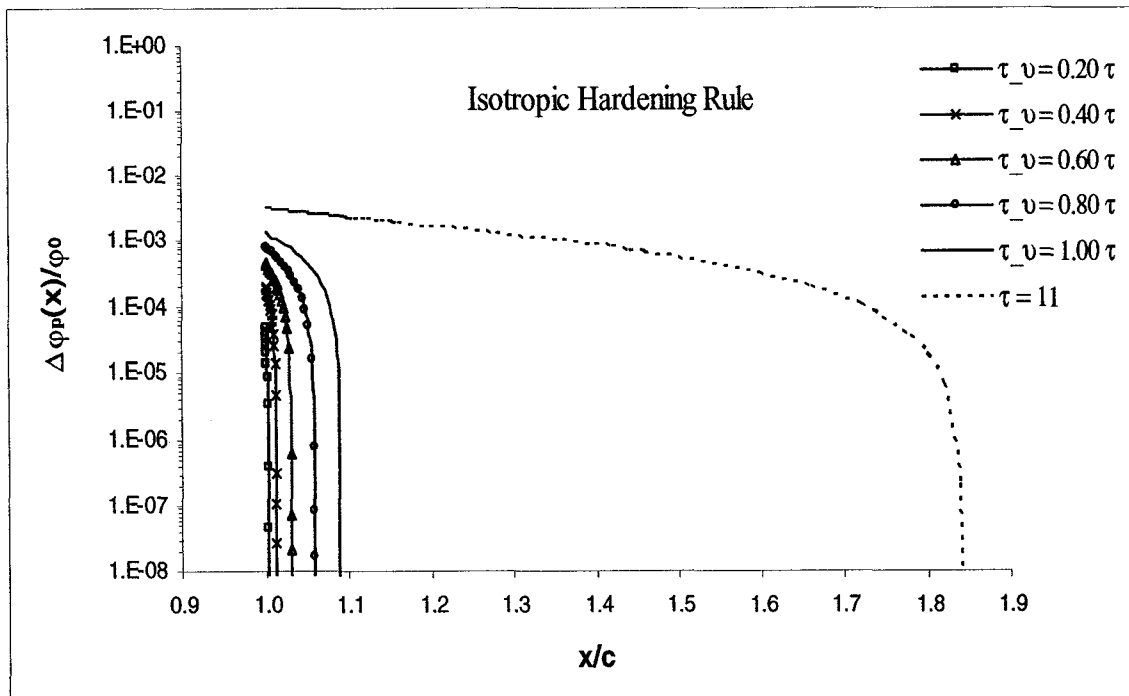


Figure 5-16: Comparison of the monotonic loading results with the unloading results in terms of non-dimensionalized plastic displacement versus distance from the crack tip for an applied load of  $\tau = 11$  MPa and unloading stresses proportionate to  $\tau$  for initial crack length of  $2c = 10$  mm under isotropic hardening rule

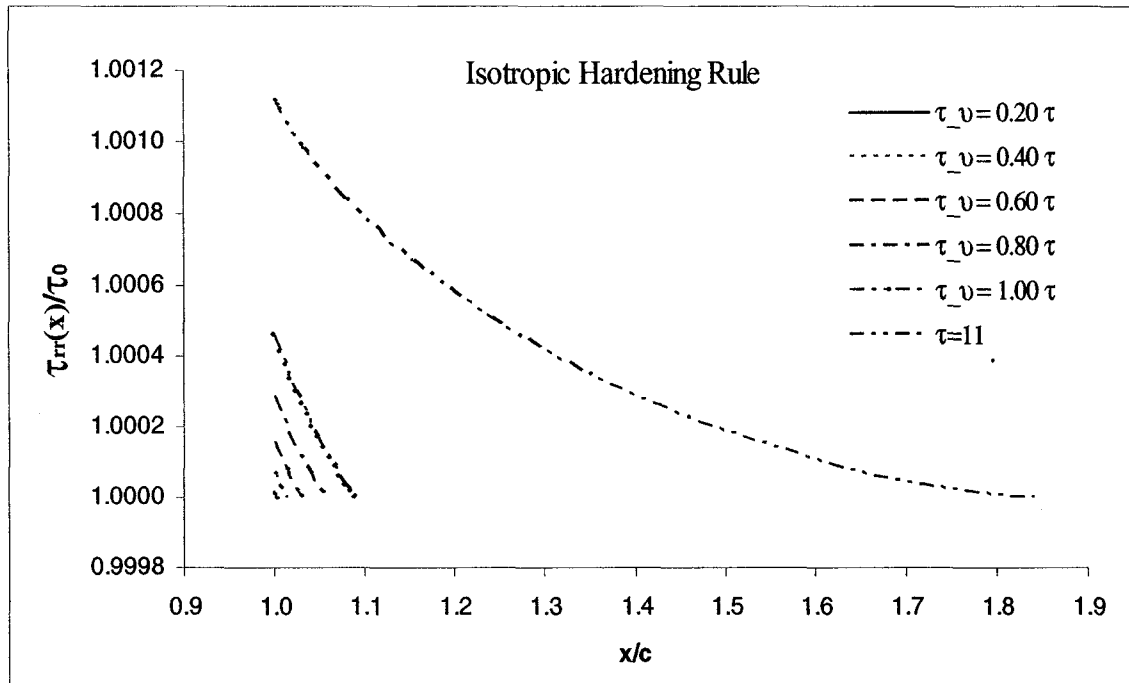


Figure 5-17: Comparison of the monotonic loading results with the unloading results in terms of non-dimensionalized shear stress distribution versus distance from the crack tip for an applied load of  $\tau = 11$  MPa and unloading stresses proportionate to  $\tau$  for initial crack length of  $2c = 10$  mm under isotropic hardening rule

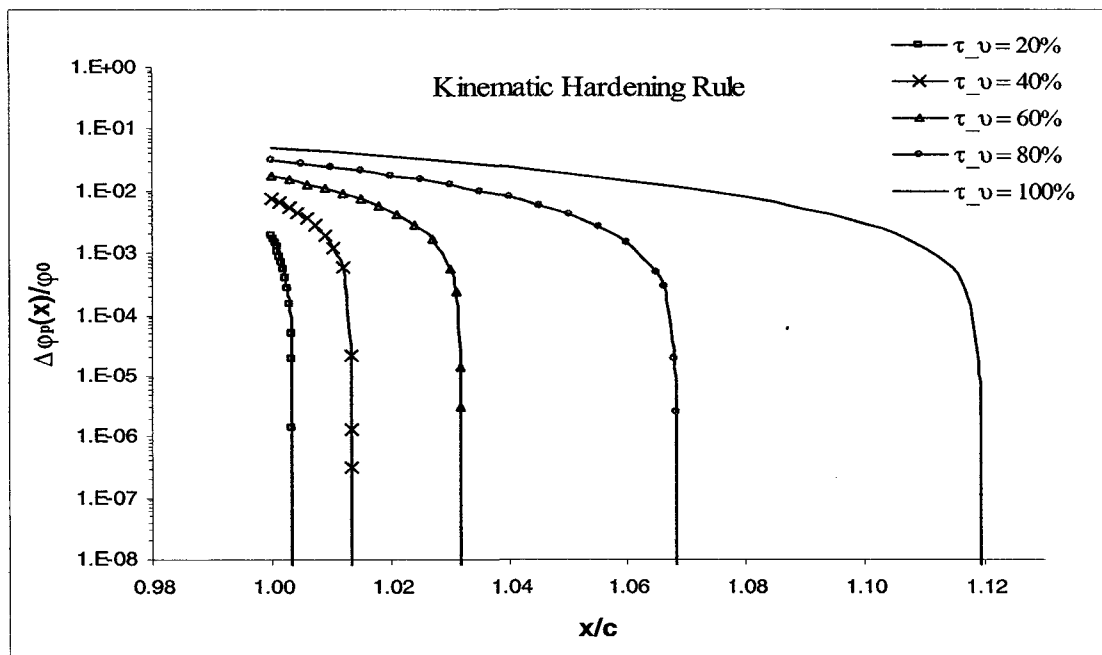


Figure 5-18: Non-dimensionalized diagram of the change in the plastic displacement versus distance from the crack tip for an applied load of  $\tau = 11$  MPa and unloading stresses proportionate to  $\tau$  for initial crack length of  $2c = 400$  mm under kinematic hardening rule



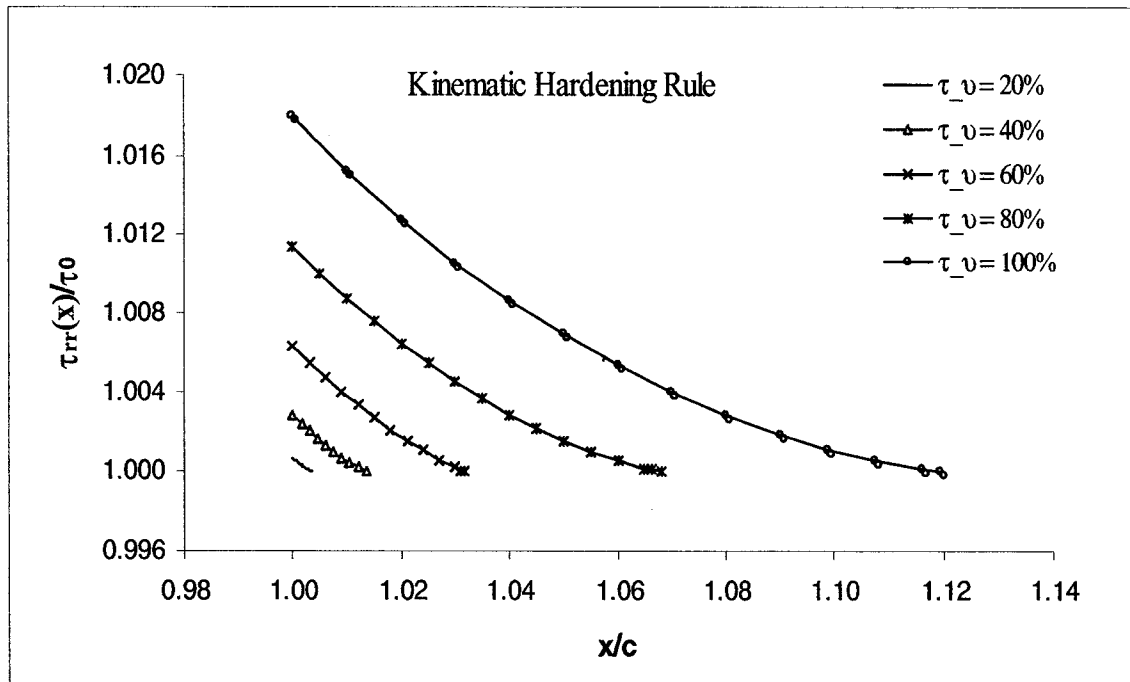


Figure 5-19: Non-dimensionalized diagram of the reversed shear stress distribution ratio versus distance from the crack tip for an applied load of  $\tau = 11$  MPa and unloading stresses proportionate to  $\tau$  for initial crack length of  $2c = 400$  mm under kinematic hardening rule

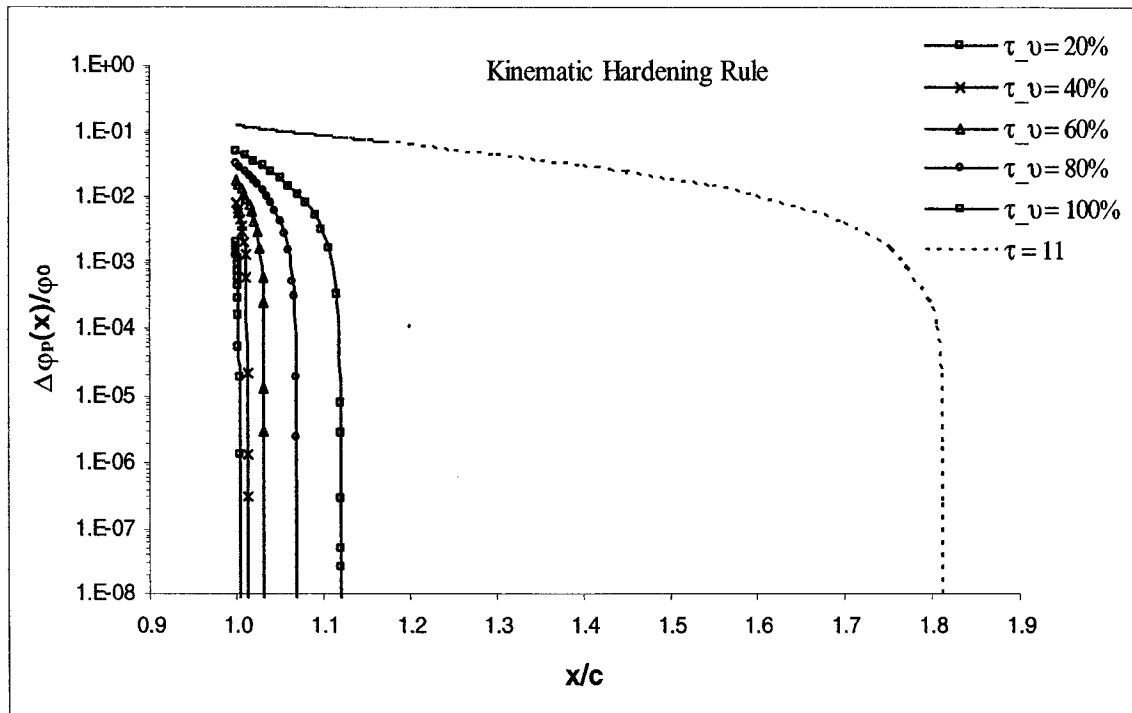


Figure 5-20: Comparison of the monotonic loading results with the unloading results in terms of non-dimensionalized plastic displacement versus distance from the crack tip for an applied load of  $\tau = 11$  MPa and unloading stresses proportionate to  $\tau$  for initial crack length of  $2c = 400$  mm under kinematic hardening rule

displacement within the reversed plastic zone. It compares plastic displacement when rock is subjected to a monotonic load of 11 MPa and then unloaded proportionately by 20%, 40%, 60%, 80% and 100%. The length of the reversed plastic zone is suggested also to reduce by about one order of magnitude under unloading. This behavior is similar to what was obtained when a 10 mm crack is subjected to the same loading and unloading condition. Figure 5-21 makes the same comparison based on the shear stress distribution under monotonic loading and unloading.

The response of a rock containing a 400 mm crack under the same loading condition as above was examined under isotropic hardening rule as well. The results of this analysis are also shown in Figure 5-22, Figure 5-23, Figure 5-24 and Figure 5-25.

Comparing the changes in the plastic displacement at the crack tip of two different cracks of 10 mm and 400 mm length (Figure 5-12 and Figure 5-20) suggests that the change in the plastic displacement at the crack tip increases by one order of magnitude when crack length increases by the same order of magnitude. Same suggestion can be made when the comparison is made for both cracks loaded under isotropic hardening rule (Figure 5-16 and Figure 5-24).

Comparing Figure 5-10 and Figure 5-14 for the case of a 10 mm crack (or Figure 5-18 and Figure 5-22 for the case of a 400 mm crack) with one another, it is found that for a given rock type and an initial crack size, rock suffers more plastic displacement under kinematic hardening rule than under isotropic hardening rule. This can be explained through the unloading process and by the use of equivalent stress-equivalent strain diagram (Figure 5-26). It is known that

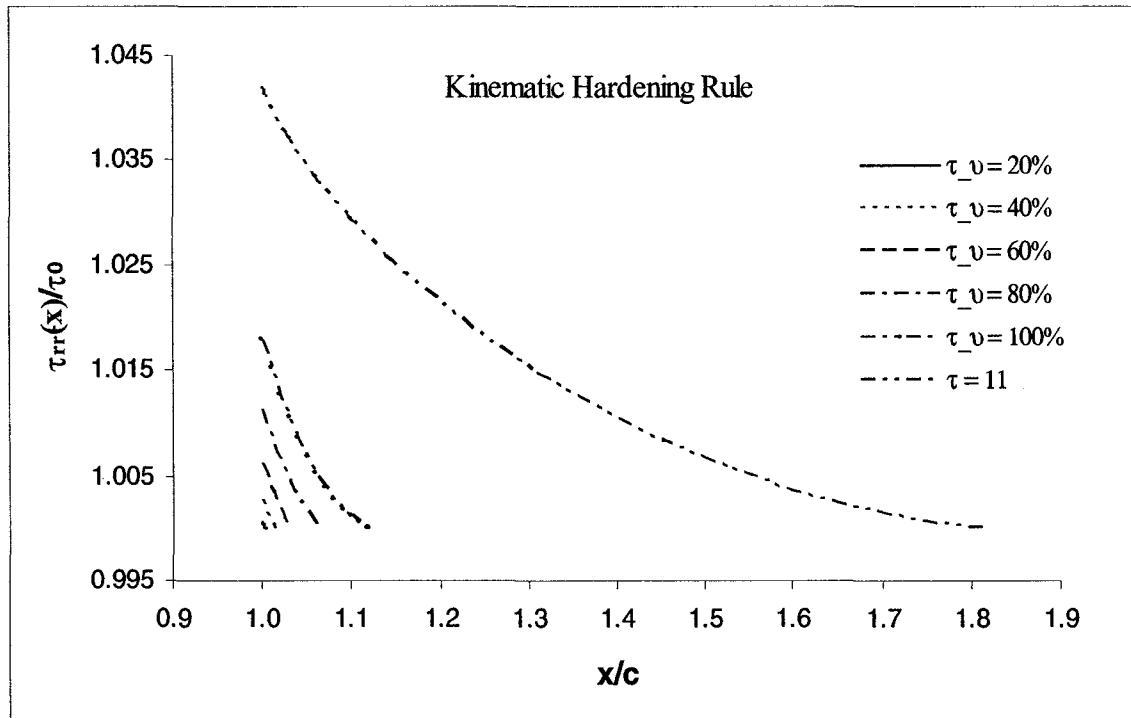


Figure 5-21: Comparison of the monotonic loading results with the unloading results in terms of non-dimensionalized shear stress distribution versus distance from the crack tip for an applied load of  $\tau = 11$  MPa and unloading stresses proportionate to  $\tau$  for initial crack length of  $2c = 400$  mm under kinematic hardening rule

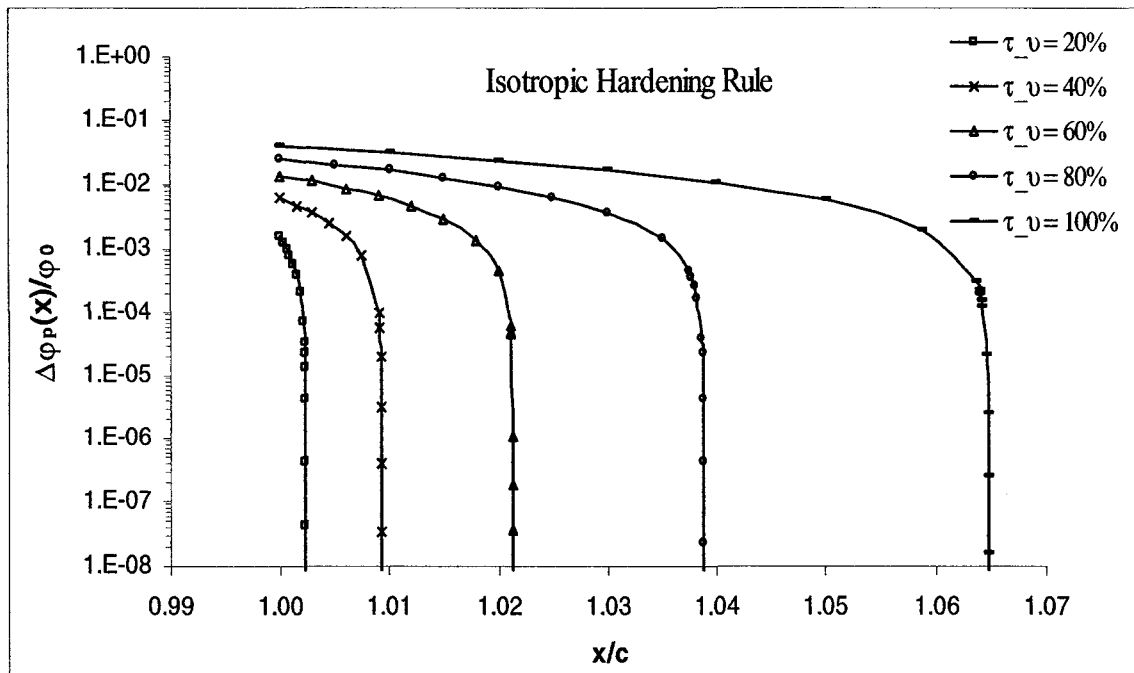


Figure 5-22: Non-dimensionalized diagram of the change in the plastic displacement versus distance from the crack tip for an applied load of  $\tau = 11$  MPa and unloading stresses proportionate to  $\tau$  for initial crack length of  $2c = 400$  mm under isotropic hardening rule

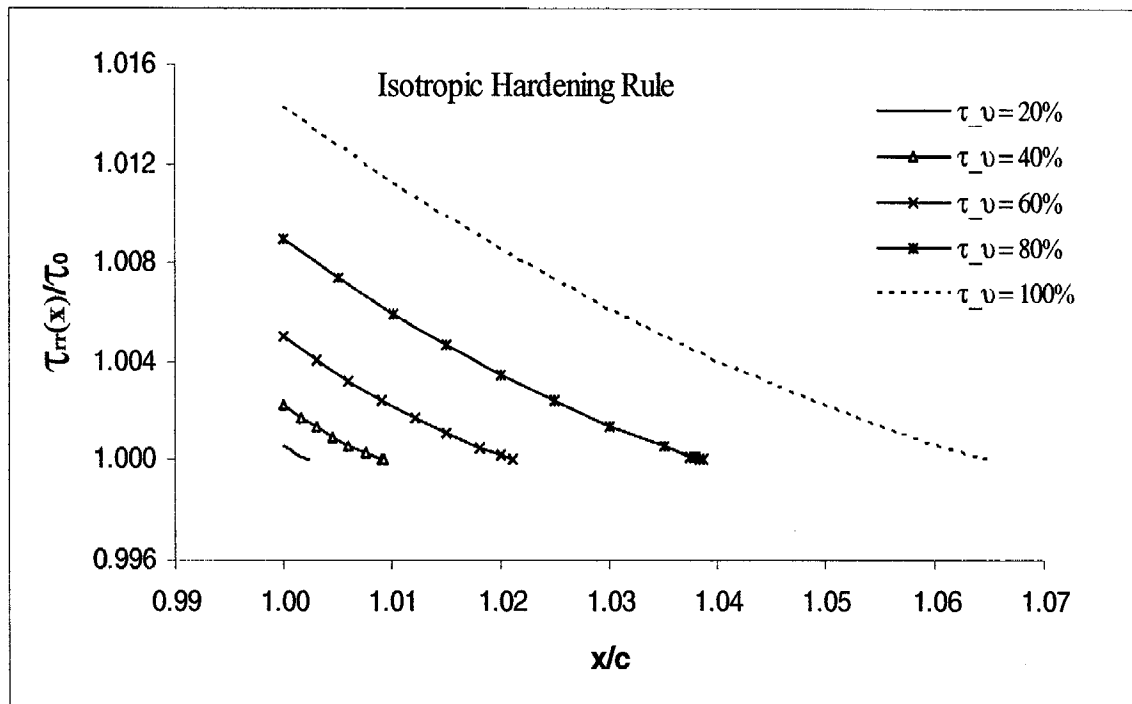


Figure 5-23: Non-dimensionalized diagram of the reversed shear stress distribution ratio versus distance from the crack tip for an applied load of  $\tau = 11$  MPa and unloading stresses proportionate to  $\tau$  for initial crack length of  $2c = 400$  mm under isotropic hardening rule

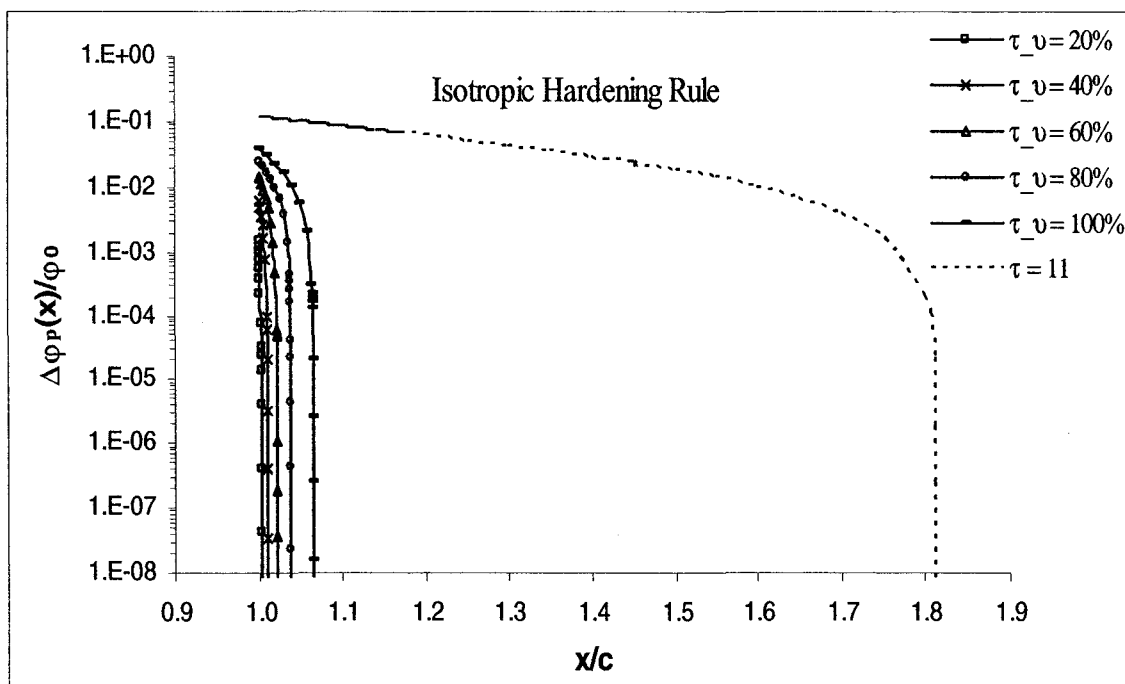


Figure 5-24: Comparison of the monotonic loading results with the unloading results in terms of non-dimensionalized plastic displacement versus distance from the crack tip for an applied load of  $\tau = 11$  MPa and unloading stresses proportionate to  $\tau$  for initial crack length of  $2c = 400$  mm under isotropic hardening rule

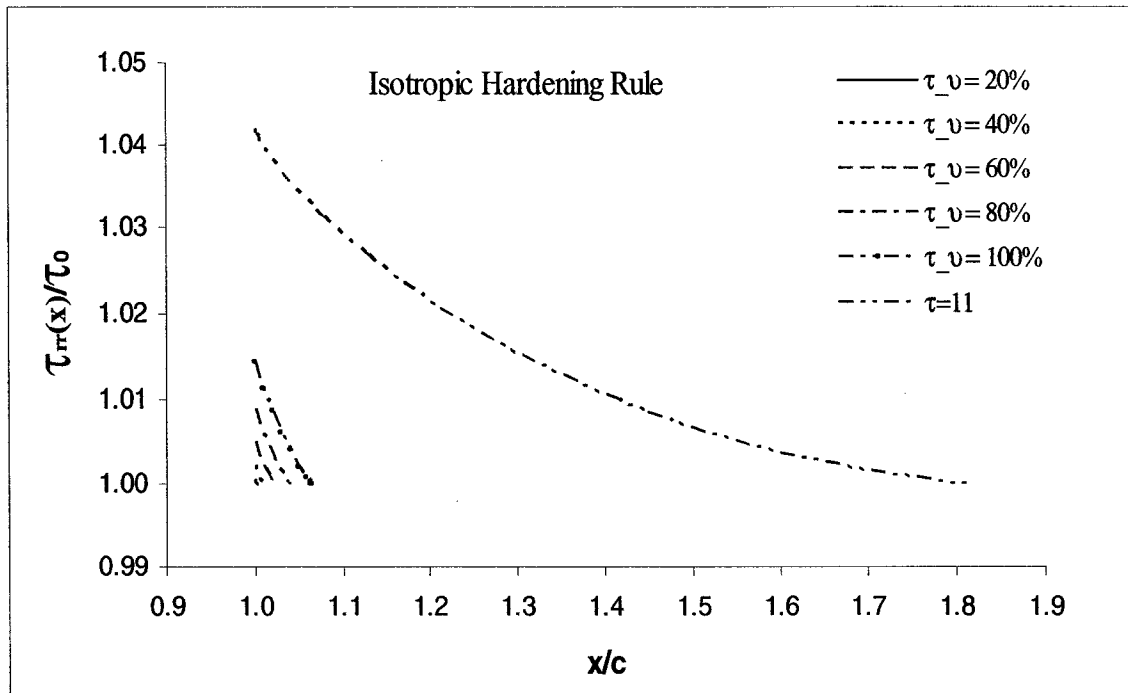


Figure 5-25: Comparison of the monotonic loading results with the unloading results in terms of non-dimensionalized shear stress distribution versus distance from the crack tip for an applied load of  $\tau = 11$  MPa and unloading stresses proportionate to  $\tau$  for initial crack length of  $2c = 400$  mm under isotropic hardening rule



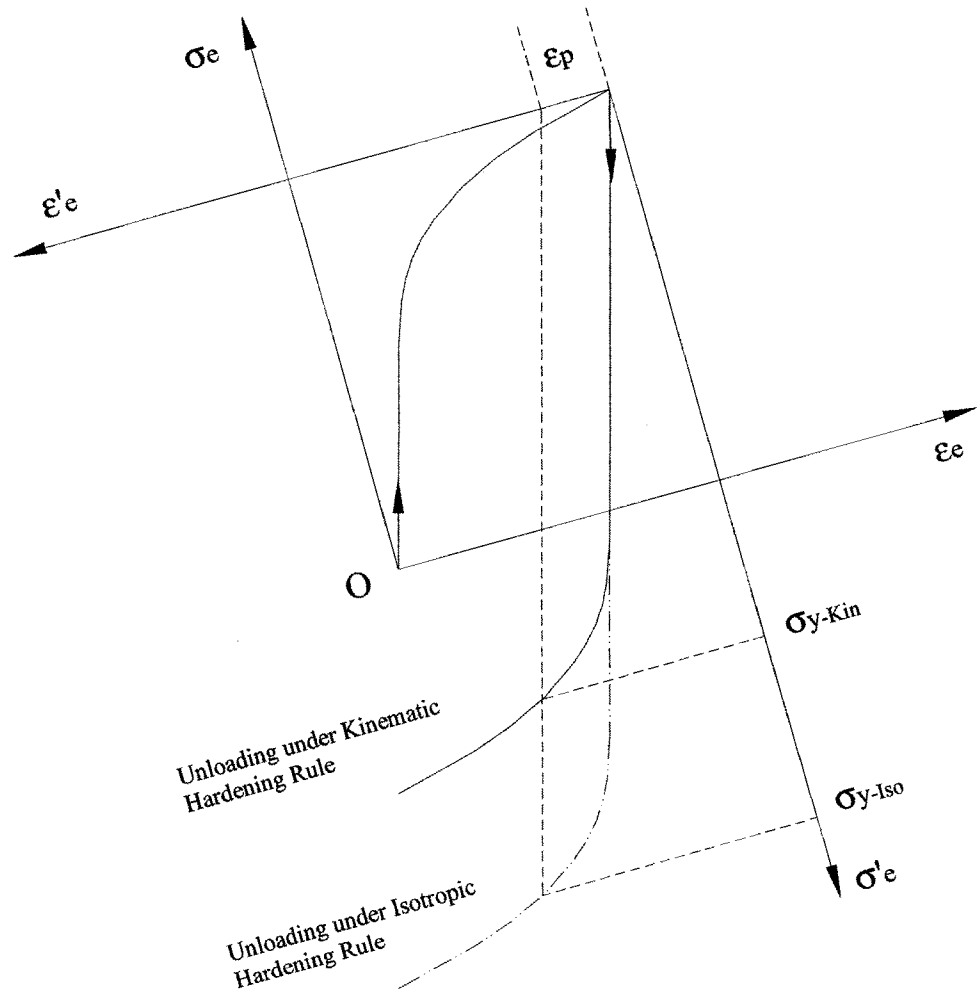


Figure 5-26: Comparison of material behavior while unloading under kinematic and isotropic hardening rules with reference to the equivalent stress-strain diagram.

material hardening is determined by the slope of the equivalent stress-equivalent strain diagram at stress levels above yield limit and it is the same for both hardening rules under monotonic loading. However, after unloading starts, under kinematic hardening rule, material will start to harden after unloading by  $2\tau_0$  while under isotropic hardening rule material will start to harden after unloading by  $2\tau(x)$ . Therefore, for a given unloading stress level material will experience higher strain under kinematic hardening rule as opposed to isotropic hardening rule. This is due to the kinematic hardening rule that stipulates the yield surface to shift with no expansion in the stress space, while under isotropic hardening rule yield surface expands uniformly in all directions, i.e. material hardens symmetrically under loading and unloading conditions. Therefore, in the case under consideration, after unloading to a certain stress level, rock will undergo more reversed plastic displacement under kinematic hardening than isotropic hardening. Therefore, the results shown in the aforementioned figures are in agreement with the plasticity theory.

Figure 5-27 compares the changes in the plastic displacement at the crack tip of a 10 mm and a 1000 mm crack for two different hardening rules for various unloading stress ratios. As shown, rock suffers more plastic displacement under kinematic hardening rule at the crack tip than under isotropic hardening condition. Furthermore, it shows the effect of crack size on the significance of the type of plasticity rule used. For smaller cracks, kinematic hardening and isotropic hardening rules generate identical solutions while for larger cracks, under kinematic hardening rule rock shows larger change in the plastic displacement than under isotropic hardening rule.

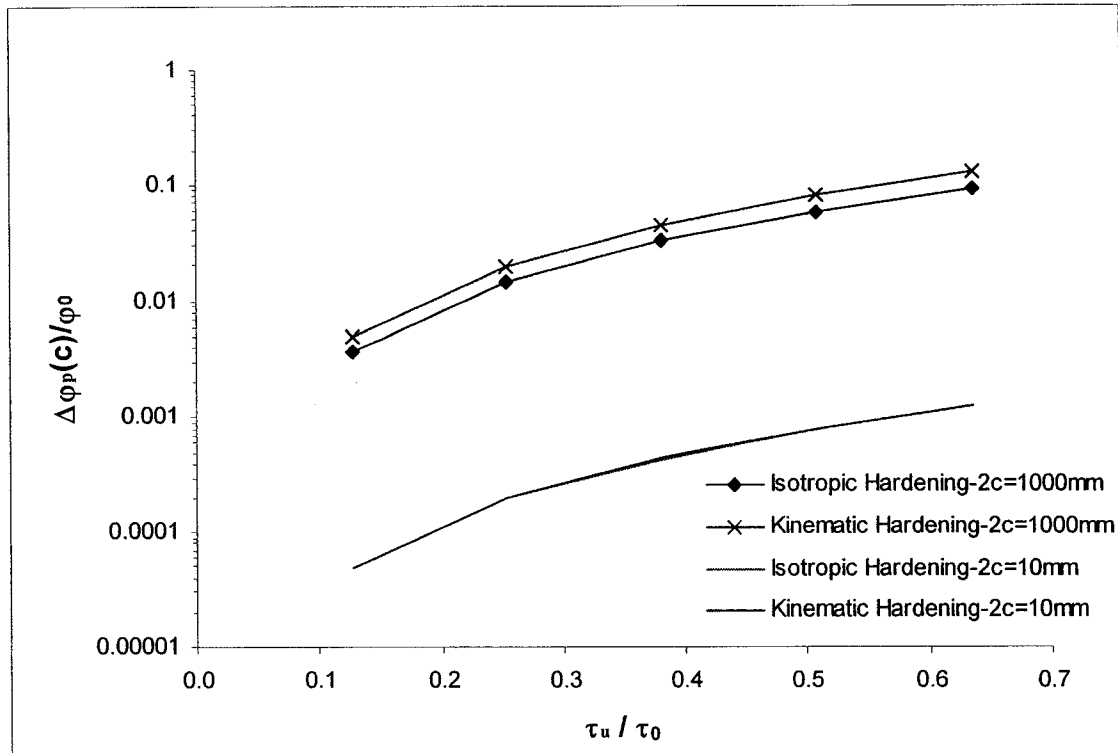


Figure 5-27: Non-dimensionalized diagram of the plastic displacement at the crack tip versus unloading stress ratio ahead of a 10 and a 1000 mm crack - comparison of kinematic and isotropic hardening rules

Figure 5-28 also shows the changes in the plastic displacement at the crack tip versus the ratio of unloading stress over the applied load for a 100 mm crack under various applied loads under kinematic hardening rule. As shown, the changes in the plastic displacement at the crack tip increases with the unloading stress ratio ( $\tau_u/\tau$ ). Furthermore, the results suggest that the extent of the change in the plastic displacement is also more significant if the rock is loaded initially to a higher stress level. Figure 5-29 similarly shows the change in the plastic displacement at the crack tip of a 100mm long crack against the unloading stress over yield stress ratio ( $\tau_u/\tau_0$ ). This diagram suggests that at the low unloading ratios below  $0.2\tau_u/\tau_0$ , the change in the plastic displacement increases at a linear rate. As the unloading ratio exceeds this limit, the change in the plastic displacement increases at an increasing rate as it approaches the limiting case of  $0.65\tau_0$ .

At stress level above  $0.65\tau_0$ , as the loading ratio approaches one i.e.  $\tau=\tau_0$ , the theory will break down, because for  $\tau=\tau_0$  it is general yielding across the cross section. Figure 5-29 is obtained under kinematic hardening rule. A similar diagram, however with a lower magnitude of the change in the plastic displacement at the crack tip, can also be obtained for unloading under isotropic hardening rule.

Figure 5-30 and Figure 5-31 show the change in the plastic displacement at the crack tip versus the ratio of unloading stress over the yield stress for different crack sizes under kinematic hardening and isotropic hardening rules, respectively. As shown, the change in the plastic displacement at the crack tip increases as the ratio of unloading stress over yield stress increases. Again, the amount of change in the plastic displacement is greater under kinematic

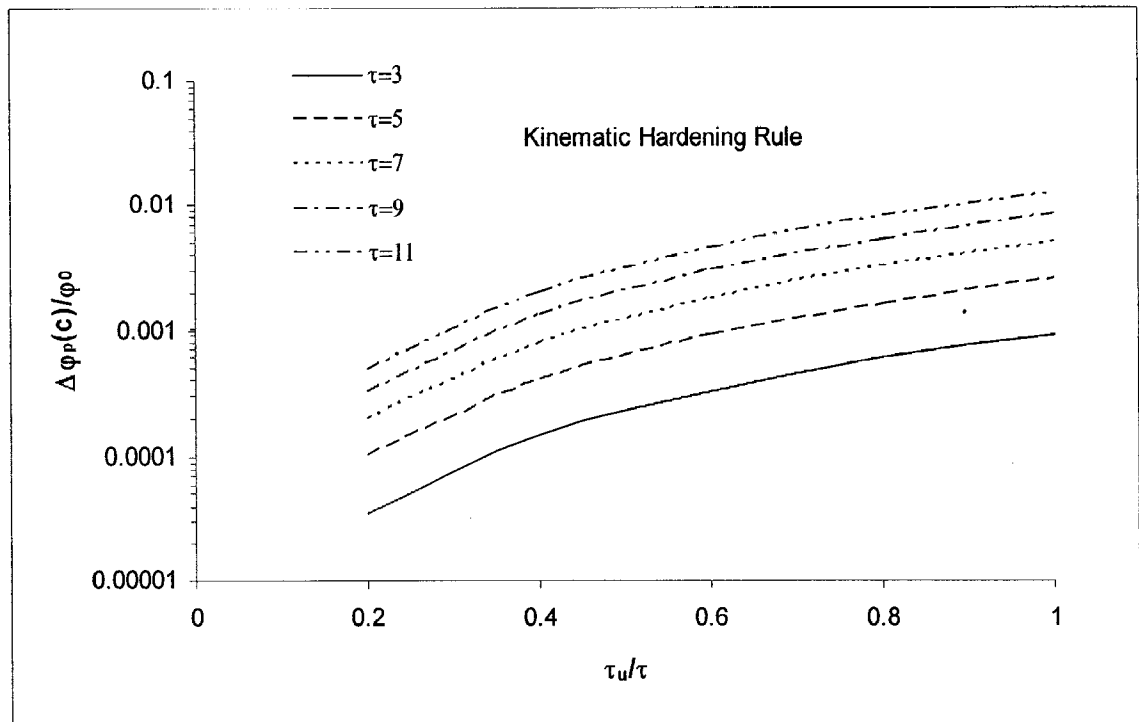


Figure 5-28: Non-dimensionalized diagram of the plastic displacement at the crack tip versus the ratio of unloading stress over the applied load ahead of a crack of  $2c=100$  mm long

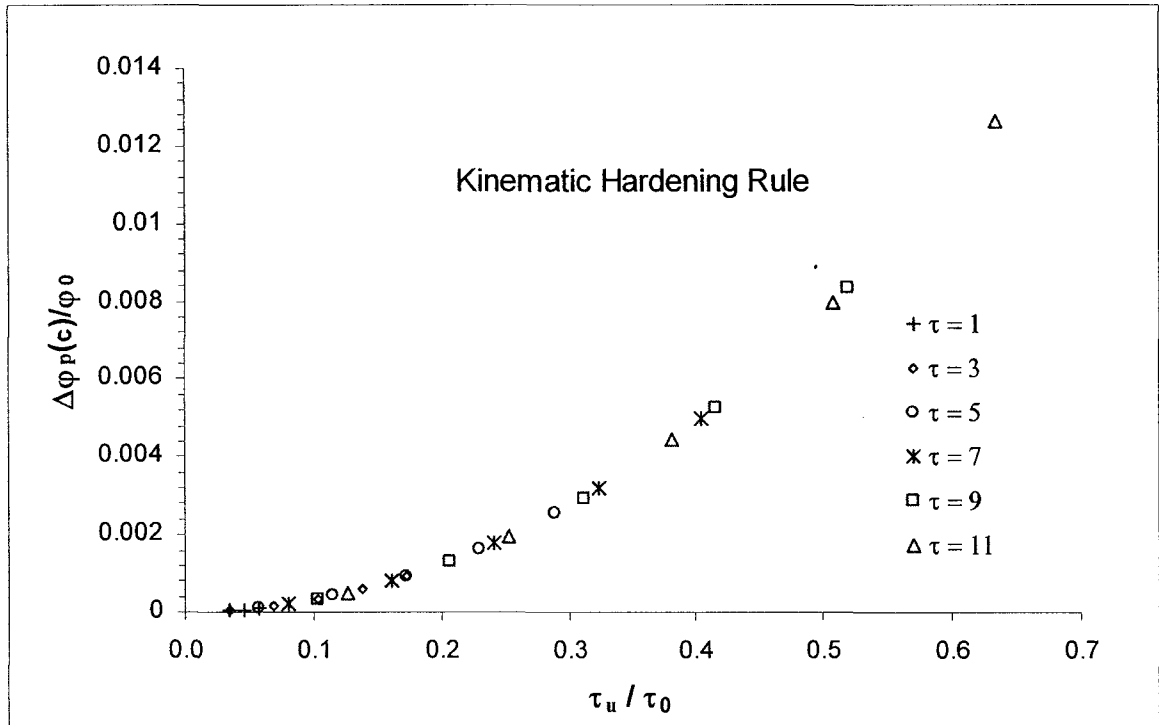


Figure 5-29: Non-dimensionalized diagram of the change in the plastic displacement at the crack tip versus the ratio of unloading stress over yield stress of the rock ahead of a 100 mm long crack under kinematic hardening rule

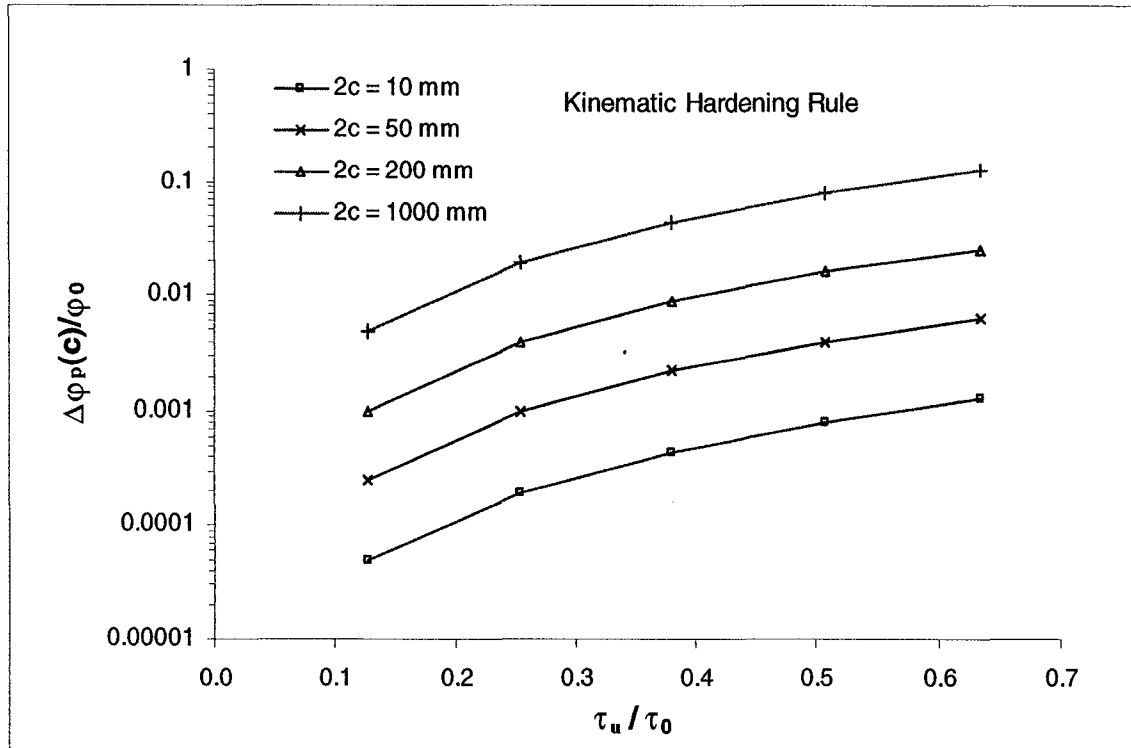


Figure 5-30: Non-dimensionalized diagram of the change in the plastic displacement at the crack tip for various crack sizes versus the ratio of unloading stress over the yield stress for an applied load of 11 MPa under kinematic hardening conditions.

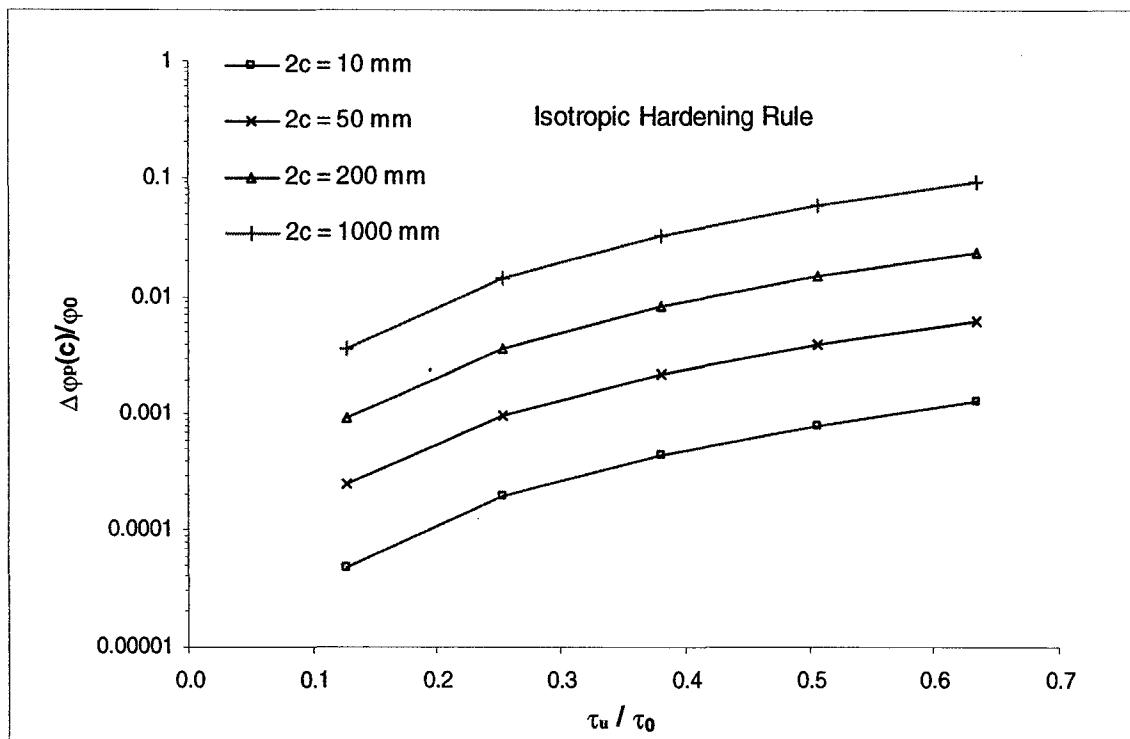


Figure 5-31: Non-dimensionalized diagram of the change in the plastic displacement at the crack tip for various crack sizes versus the ratio of unloading stress over the yield stress for an applied load of 11 MPa under isotropic hardening conditions.



hardening rule than under the isotropic hardening rule.

Appendix D contains diagrams showing the change in the plastic displacement and the reversed shear stress distributions ahead of the crack tip in the reversed plastic zone for various crack sizes (20 mm, 50 mm, 100 mm, 200 mm and 1000 mm) and applied loads that are not presented in this chapter.

## ***5.2. Numerical Results Using Data from Monotonic Loading Tests***

In this section the numerical results of the dislocation model using the data obtained from the monotonic loading tests on granite specimens (described in Chapter 4) are presented. The numerical results are presented in two parts, the monotonic loading and the unloading results. The results are shown in terms of plastic displacement and shear stress distribution at the crack tip and within the plastic zone for monotonic loading and unloading cases, and the extent of the plastic zone is also determined for both cases.

To carry out the analysis the data obtained from the shear testing on granite specimens were inputted into the dislocation model and rock damage ahead of a given crack was simulated. The shear properties of the granite specimens were determined from the monotonic tests. The shear stress – shear strain diagram of the granite as obtained from the tests is shown in Figure 4-11. It is to be noted that the dislocation model was modified to accommodate the new material model as given by Equations 4-3 for monotonic loading and Equation 4-4 for the unloading case. This modification was necessary to allow for the use of the model when shear stress – shear strain diagram is available. The model is initially set for a shear stress – shear displacement based

material model. In this analysis, as a first approximate,  $\alpha$  was assumed to equal to unity and damage was assessed based on the new material models given by Equations 4-3 and 4-4 of Chapter 4.

The damage ahead of a 100 mm crack in granite was simulated and the results of the monotonic loading stage of the blast cycle were obtained. Figure 5-32 shows the non-dimensionalized plastic displacement versus distance from the crack tip in granite subject to various applied loads up to  $0.65\tau_0$ . Figure 5-33 also shows the non-dimensionalized shear stress distribution versus distance from the crack tip along the plastic zone for the same crack, subject to the same loading conditions. Figure 5-32 and Figure 5-33 show that plastic displacement is maximum at the crack tip and drops to zero at the end of plastic zone. The size of the plastic zone depends on the rock strength properties. Stresses are also higher than yield stress within the plastic zone causing plastic displacement in this region. At and beyond the end of the plastic zone shear stresses drop to less than yield stress of the rock.

Following monotonic loading analysis, the dislocation model was used to simulate crack tip damage by the unloading stage of the blast cycle. For the same crack size and the applied load of 9 MPa ( $0.65 \tau_0$ ), the unloading solution was found for five different unloading ratios ( $\tau_u/\tau$ ) of 0.2, 0.4, 0.6, 0.8 and 1.0 (fully unloaded) where  $\tau$  is the applied monotonic load. The unloading problem was solved for the two commonly used plasticity rules, i.e. kinematic hardening and isotropic hardening. Figure 5-34 and Figure 5-35 show the non-dimensionalized diagrams of the change in the plastic displacement and the reversed shear stress distribution in the reversed plastic zone that are formed ahead of the given crack in granite under kinematic hardening rule.

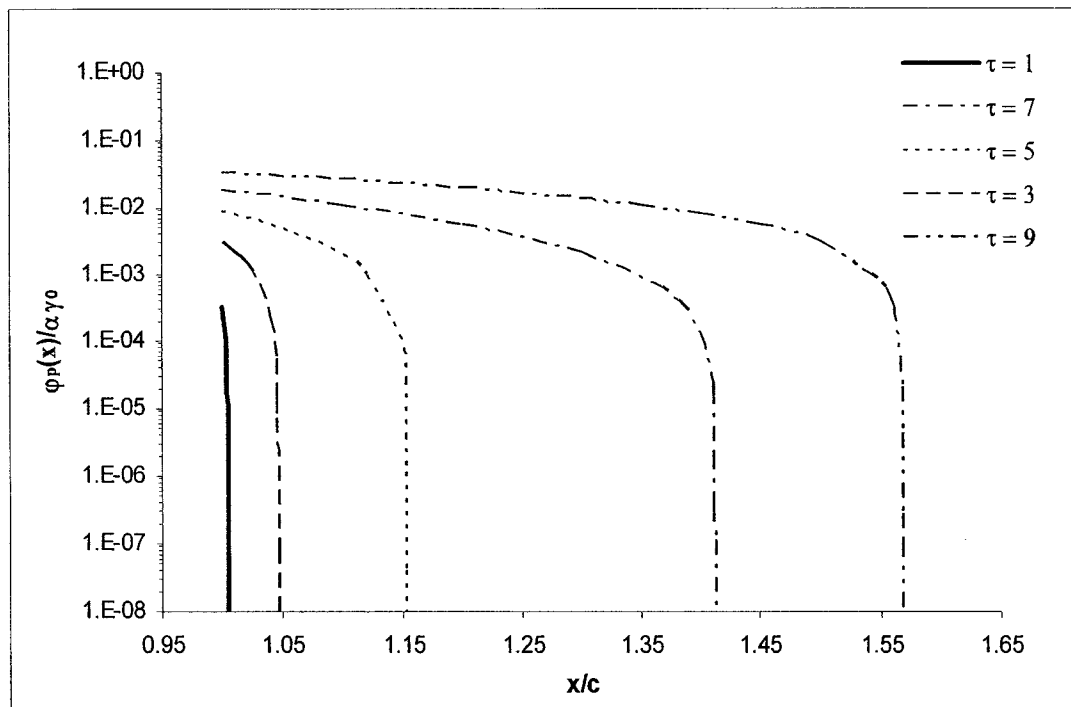


Figure 5-32: Non-dimensionalized diagram of the plastic displacement versus distance from the crack tip for given applied stresses in MPa ahead of a crack of  $2c = 100$  mm length in granite

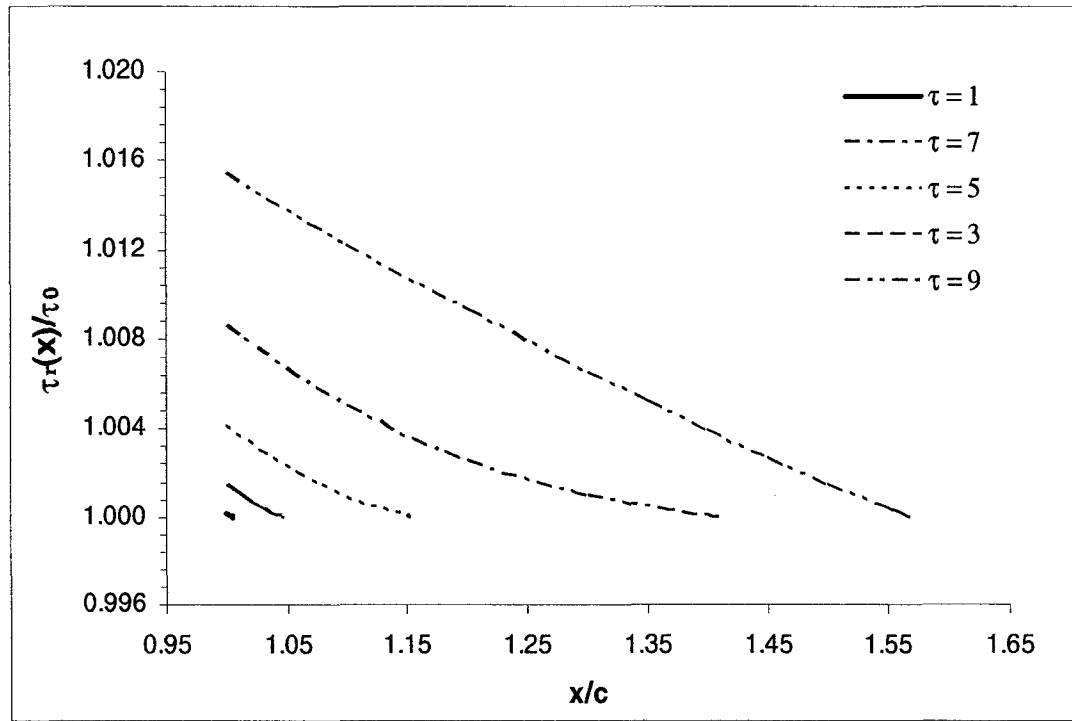


Figure 5-33: Shear stress distribution ahead of the crack tip versus distance from the crack tip for given applied stresses in MPa -  $2c = 100$  mm in granite

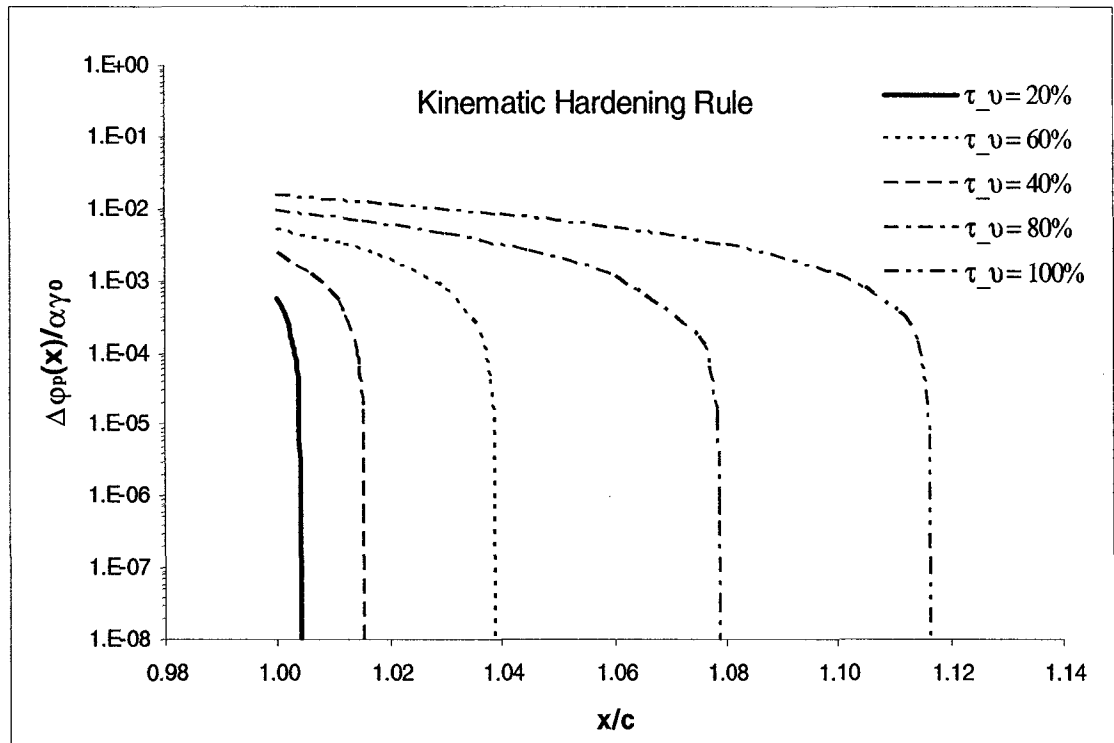


Figure 5-34: Non-dimensionalized diagram of the change in the plastic displacement versus distance from the crack tip for an applied load of  $\tau = 9$  MPa and unloading stresses proportionate to  $\tau$  for initial crack length of  $2c = 100$  mm under kinematic hardening rule in granite

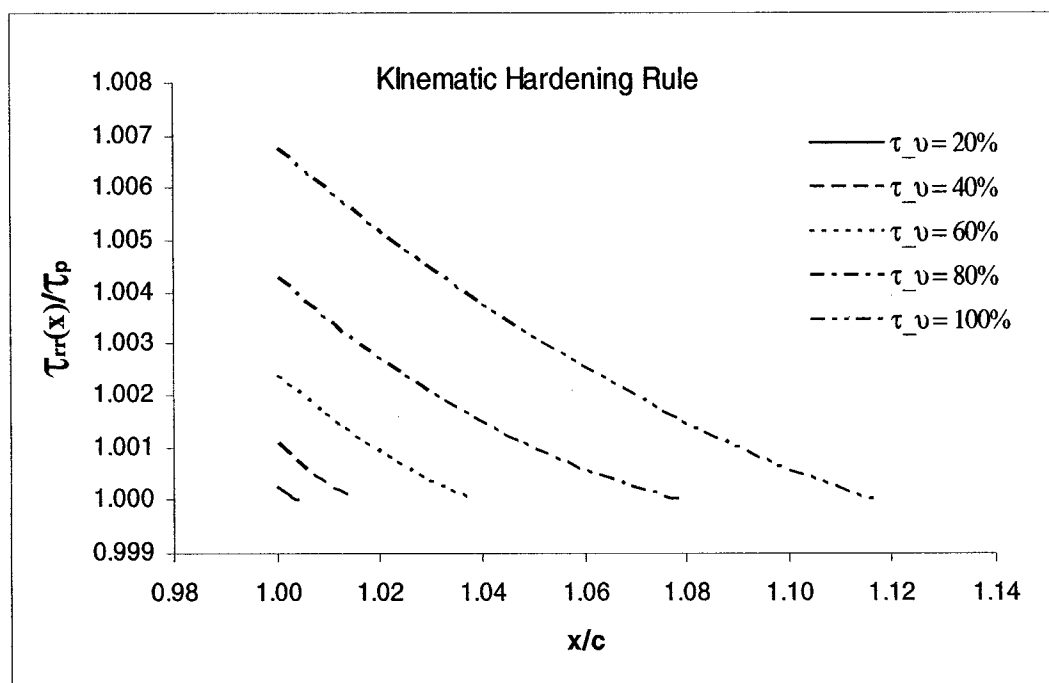


Figure 5-35: Non-dimensionalized diagram of the reversed shear stress distribution ratio versus distance from the crack tip for an applied load of  $\tau = 9$  MPa and unloading stresses proportionate to  $\tau$  for initial crack length of  $2c = 100$  mm under kinematic hardening rule in granite

Results suggest that the extent of the reversed plastic zone is significantly shorter than that under monotonic loading condition. This is due to the lower dislocation density within the reversed plastic zone that happens because of dislocations moving back into the crack tip. However, the length of the reversed plastic zone increases as the unloading ratio increases from 0.2 to 1.0 (fully reversed). Figure 5-36 compares the extent of plastic zone in rock under monotonic loading of 9 MPa and subsequent unloading ratios as shown. It also compares the extent of crack tip plastic displacement under monotonic loading and unloading as well. Figure 5-37 makes similar comparison based on the shear stress distribution ahead of the crack tip. Figure 5-38 and Figure 5-39 also show the non-dimensionalized diagrams of the change in the plastic displacement and the reversed shear stress distribution in the same rock subject to the same loading conditions under isotropic hardening rule. Results similar to those obtained under kinematic hardening rule were obtained. Figure 5-40 also compares the extent of plastic zone and plastic displacement in rock under monotonic loading of 9 MPa and subsequent unloading ratios as shown, assuming isotropic hardening rule is used. A similar comparison with respect to shear stress distribution ahead of the crack can also be made as shown in Figure 5-41.

### ***5.3. Verification of Model Results with Literature Data***

In this section, it will be shown that the model results compare favorably with the elastic perfectly plastic solution of Bilby et al., (1963) in terms of the size of the plastic zone under monotonic loading conditions. Also, a comparison will be made between the model results with that of Ellyin et al., (1986 and 1989) for nonlinear work hardening material behavior in terms of plastic displacements and shear stresses at the crack tip.

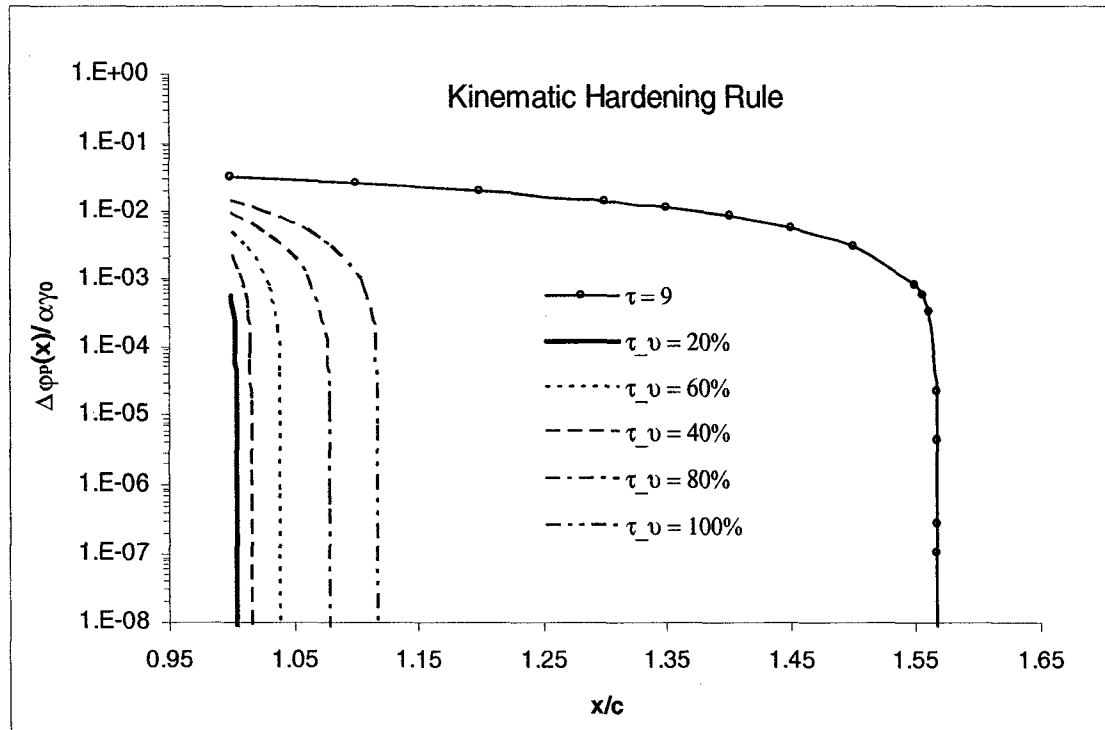


Figure 5-36: Comparison of the monotonic loading results with the unloading results in terms of non-dimensionalized plastic displacement versus distance from the crack tip for an applied load of  $\tau = 9$  MPa and unloading stresses proportionate to  $\tau$  for initial crack length of  $2c = 100$  mm under kinematic hardening rule in granite



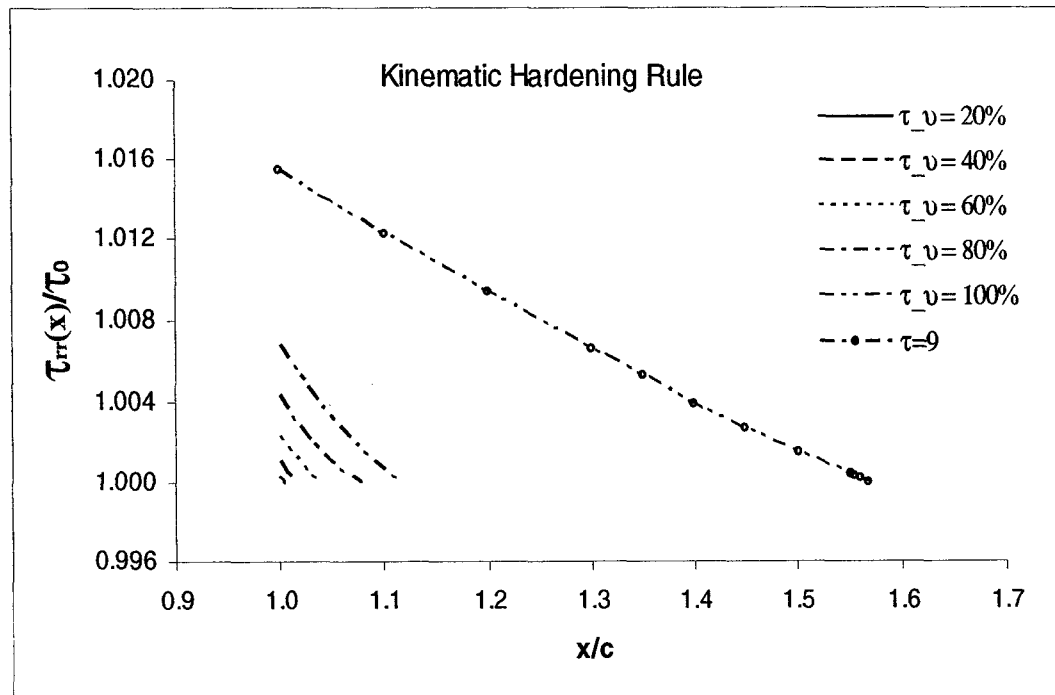


Figure 5-37: Comparison of the monotonic loading results with the unloading results in terms of non-dimensionalized shear stress distribution versus distance from the crack tip for an applied load of  $\tau = 9$  MPa and unloading stresses proportionate to  $\tau$  for initial crack length of  $2c = 100$  mm under kinematic hardening rule in granite

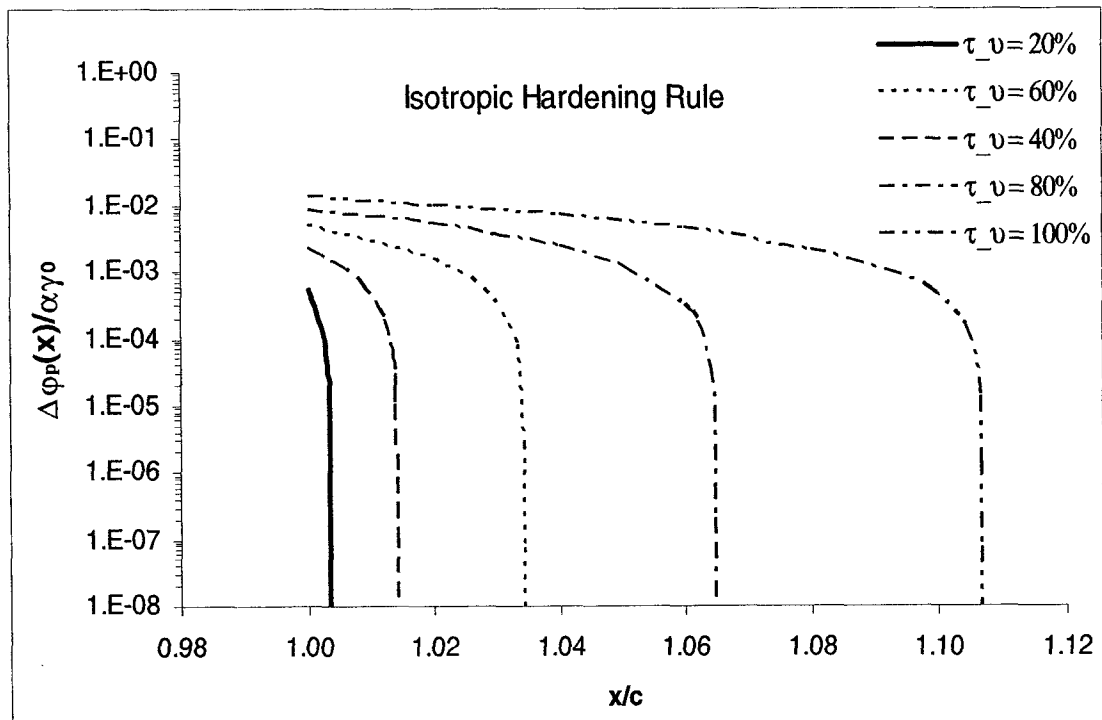


Figure 5-38: Non-dimensionalized diagram of the change in the plastic displacement versus distance from the crack tip for an applied load of  $\tau = 9$  MPa and unloading stresses proportionate to  $\tau$  for initial crack length of  $2c = 100$  mm under isotropic hardening rule in granite

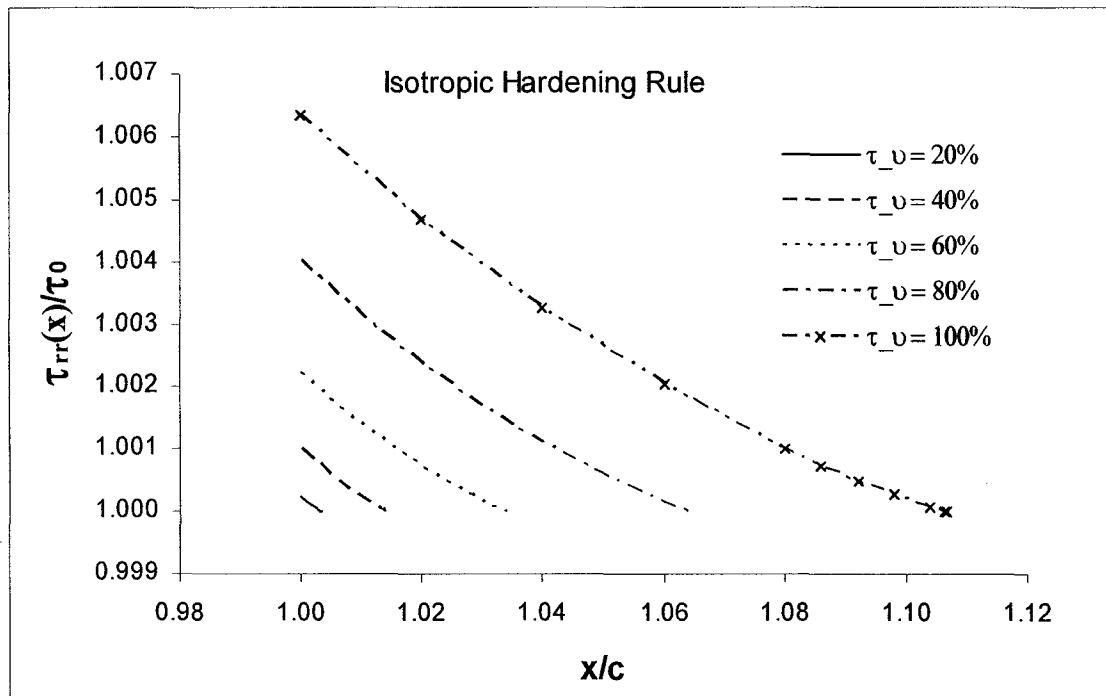


Figure 5-39: Non-dimensionalized diagram of the reversed shear stress ratio versus distance from the crack tip for an applied load of  $\tau = 9$  MPa and unloading stresses proportionate to  $\tau$  for initial crack length of  $2c = 100$  mm under isotropic hardening rule in granite

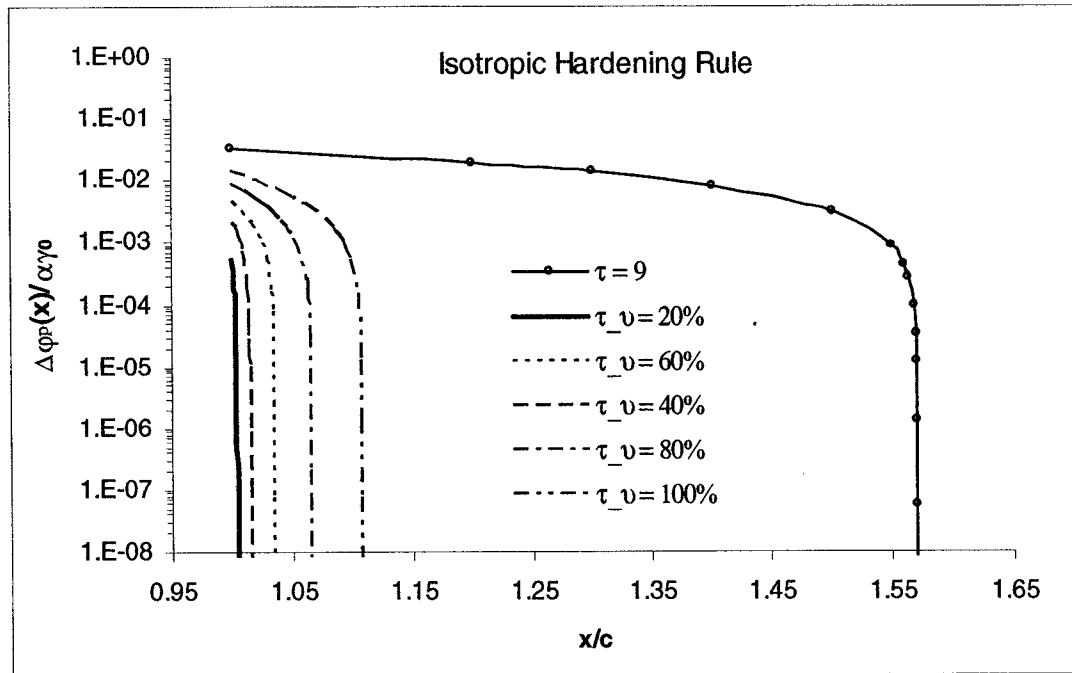


Figure 5-40: Comparison of the monotonic loading results with the unloading results in terms of non-dimensionalized plastic displacement versus distance from the crack tip for an applied load of  $\tau = 9$  MPa and unloading stresses proportionate to  $\tau$  for initial crack length of  $2c = 100$  mm under isotropic hardening rule in granite

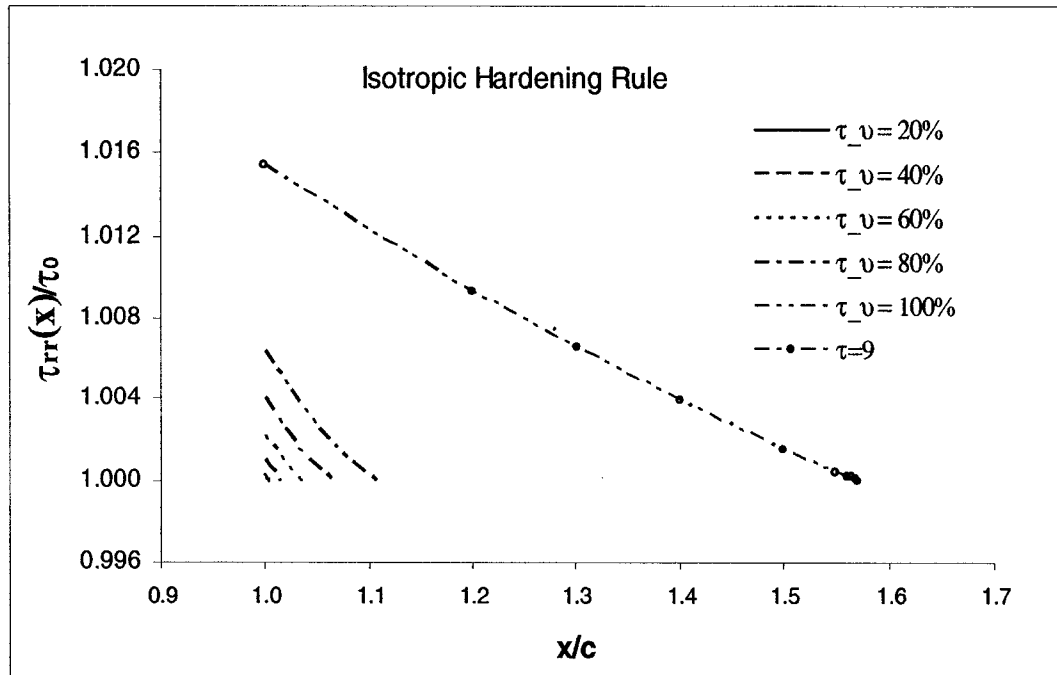


Figure 5-41: Comparison of the monotonic loading results with the unloading results in terms of non-dimensionalized shear stress distribution versus distance from the crack tip for an applied load of  $\tau = 9$  MPa and unloading stresses proportionate to  $\tau$  for initial crack length of  $2c = 100$  mm under isotropic hardening rule in granite

Figure 5-42 shows the comparison between the plastic zone size ahead of a crack in steel as determined by Bilby et al., (1963) and that obtained by dislocation model proposed in this study. The diagram shows that the plastic zone size estimate as obtained by dislocation model compares favorably with BCS solution for elastic perfectly plastic materials.

Figure 5-43 compares the results of the dislocation model as applied to rock damage assessment with that obtained by a similar model for steel (Ellyin et al., 1986) in terms of crack tip plastic displacement. The results suggest that crack tip plastic displacement in rocks with larger (than steel) work hardening index ( $n$ ) is smaller than that of steel. This is in line with the findings of the Ellyin et al. (1986 and 1989) that increasing hardening index would decrease the amount of plastic displacement at the crack tip. However, the results indicate a larger drop in plastic displacement in rocks than in steel. This is believed to be due to the differences between mechanical properties of rock and steel.

Figure 5-44 makes a similar comparison between dislocation model solution for rock damage assessment and the solution of Ellyin et al. (1986 and 1989) for steel in terms of crack tip shear stress. The results indicate that crack tip shear stresses are larger in rocks than in steel. This could be in part due to larger work hardening index of rock in comparison with steel. This finding is in agreement with Ellyin et al. (1986 and 1989) conclusion that the larger the hardening index the larger the resulting shear stress will be. It is to be noted that rock mechanical properties also affect the rock response to external loading and must be taken into account when comparing with steel and other materials.

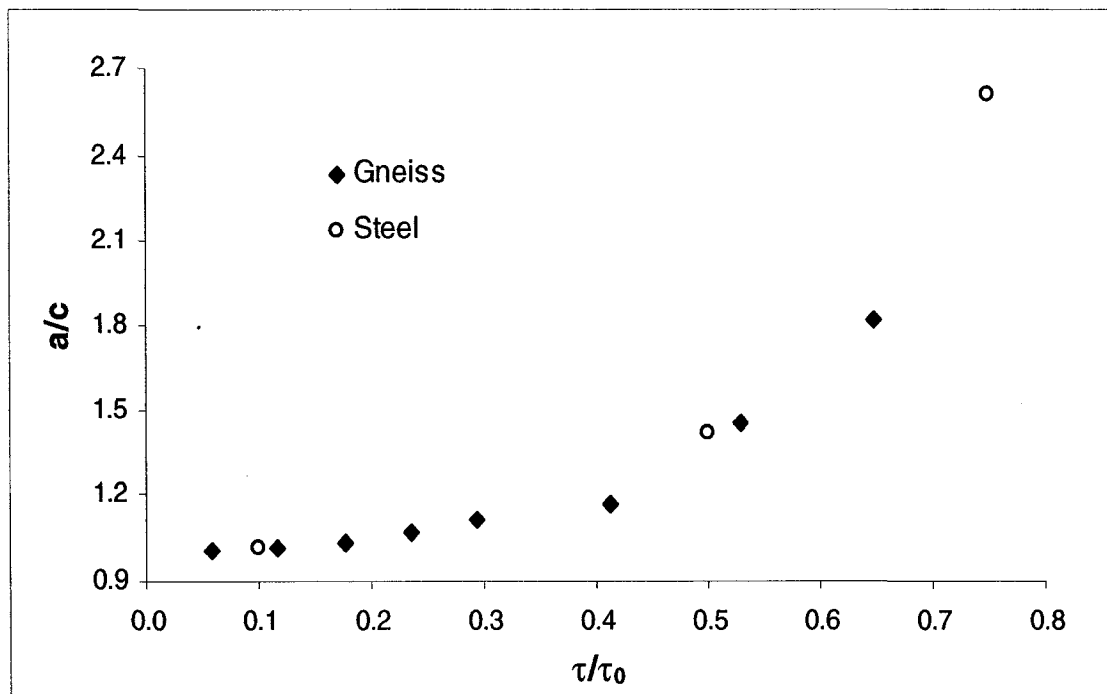


Figure 5-42: Comparison of the plastic zone size ( $a/c$ ) ahead of a crack in rock using dislocation model and that ahead of a crack in steel as given by Bilby et al. (1963) for elastic perfectly plastic material behavior

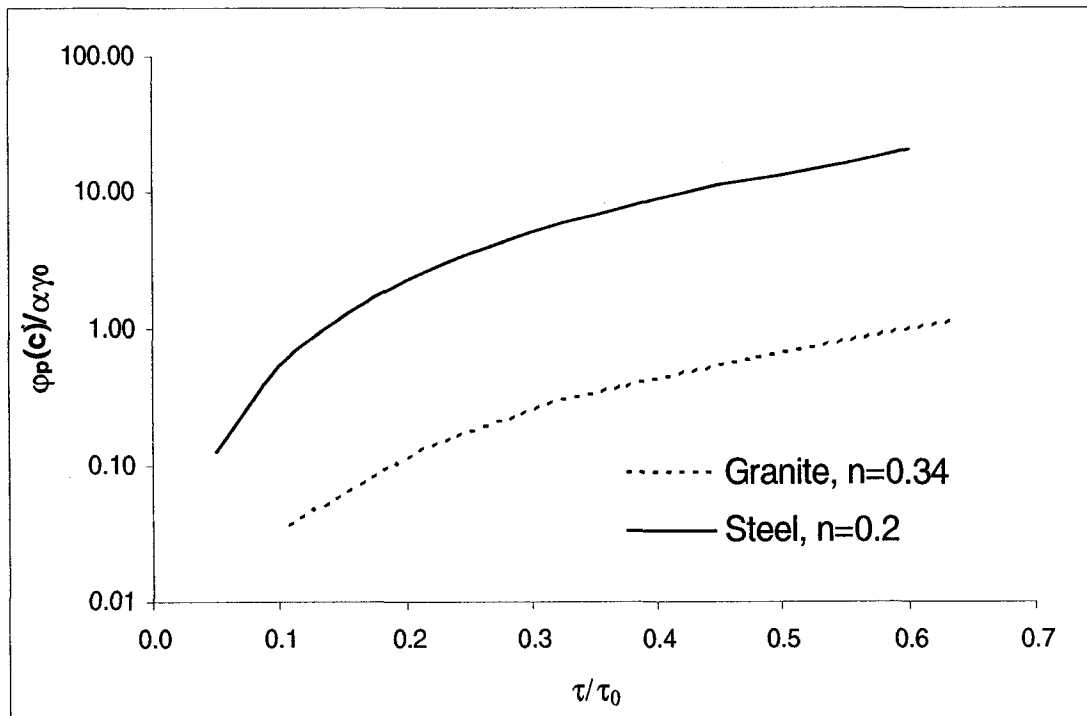


Figure 5-43: Comparison of the plastic displacement at the tip of a 25 mm crack in granite and in steel (Ellyin et al., 1986) subject to various applied loads.



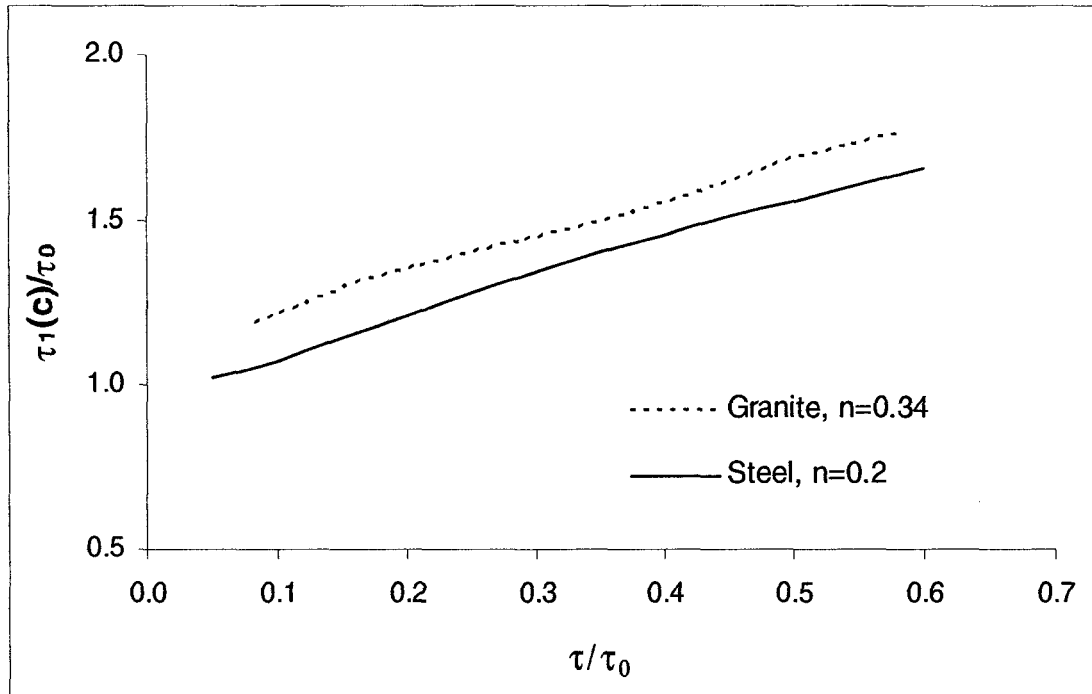


Figure 5-44: Comparison of the shear stress at the tip of a 25 mm crack in granite and in steel (Ellyin et al., 1986) subject to various applied loads.

The numerical results of the dislocation model were presented in this chapter in detail using data from both literature and the monotonic shear tests results. In addition several factors including Bauschinger effect and initial crack size affecting mechanical behavior of rock were analyzed and results were discussed. Also it was shown that the model results were compared favorably with the solution of the Bilby et al. (1963) model for elastic perfectly plastic materials in terms of the size of the plastic zone. Similar comparison were made with the solutions of the Ellyin et al. (1986 and 1989) for nonlinear work hardening materials in terms crack tip plastic displacement and crack tip shear stresses.

The next chapter summarizes the research undertaken in this study and the major findings and observations made are discussed. The application of model to practical problems is further discussed. The chapter will then be concluded by recommendations for further works in this area of research.

## **Chapter 6: Conclusions and Recommendations**

The mine blast damage problem has been investigated by numerous researchers in the last two decades. In recent years, many attempts have been made to model blast-induced rock damage by applying various numerical methods, i.e. finite element analysis, discrete element analysis and discontinuous deformation analysis. In almost all of these attempts the research was focused on the near-field blast damage analysis only and the mid- to far-field rock damage where the damage mechanism is solely by vibration was disregarded. The effect of blast vibration on the stability of underground excavations has only been considered by trial and errors through adoption of arbitrary parameters such as peak particle velocity. No attempt was made to study the blast vibration phenomenon from a blast energy point of view by taking into account the actual cyclic loading of the rock by vibration.

Adaptation of the nonlinear dislocation model was successfully applied to assess rock damage by cyclic loading. The model is based on the theory of dislocations and the fundamentals of fatigue and fracture mechanics in rocks. The model is capable of assessing damage by cyclic loading in rocks. Since slip is the main mechanism of damage in underground excavations subject to cyclic loading, therefore, in this research work damage is defined by the plastic displacement ahead of the cracks that will eventually lead to slip along crack planes. It is modeled by the process of dislocation movement along the slip planes under applied load for cyclic loading and unloading phases.

The size of the plastic zone ahead of an existing crack is determined under this loading and unloading. Plastic behavior of the rock is incorporated into the model and both

kinematic and isotropic hardening rules are examined. Then, plastic displacement function valid in the plastic zone ahead of the crack tip is determined for both monotonic loading and unloading.

An experimental program was carried out in which monotonic loading and fatigue tests were performed on granite specimens. The objective of monotonic tests was to measure static shear properties of granite to be used in the dislocation model. Fatigue tests were performed to determine fatigue life properties of granite and draw the fatigue stress life diagram (S-N curve) of the granite. The Iosipescu shear testing method (ASTM D 5379/D 5379M) was modified and up-scaled to perform the experiments. Three monotonic loading tests and seven fatigue loading tests were successfully performed and the results were reported in Chapter 4.

In following, the main findings obtained and observations made throughout this research program are summarized.

### ***6.1. Findings and Observations***

A new approach has been developed to quantify the rock damage in mid- to far-field region from the blast. A quantitative alternative to peak particle velocity criterion is introduced to assess rock damage by cyclic loading. The recommended rock damage assessment technique is related to the plastic displacement and the extent of damage within the crack plastic zone in rock.

The numerical results suggest that plastic displacement is maximized at the crack tip and is reduced to zero at the boundary of plastic zone beyond which stresses are elastic. They also indicate that the extent of plastic zone directly related to the applied load.

The Bauschinger effect was examined and it was shown numerically that the change in the plastic displacement at the crack tip is higher in the case of kinematic hardening rule, which is in agreement with the plasticity theory. The numerical results suggest that the difference between the solutions under kinematic and isotropic hardening rules are more substantial when initial crack size is large. This is due to for small cracks, plastic deformation is small and there is no significant difference as to which rule is used.

The dislocation model was used to simulate blast damage ahead of a crack in two different rock types, i.e., gneiss and granite. The data for the former was obtained from the literature (Bertacchi et al., 1974) and the data for the latter was obtained from the results of the monotonic loading tests. Both simulations suggest a similar trend in rock behavior subjected to a cycle of loading and unloading. The results of both simulations suggest that the higher the unloading range the higher the change in the plastic displacement ahead of the crack within the reversed plastic zone will be. The results of the monotonic loading and unloading simulations indicate that the extent of the plastic displacement under monotonic loading is much larger than the extent of the change in the plastic displacement under unloading, which is in agreement with the dislocation migration process as indicated by the dislocation theory.

It was shown that the model results were compared favorably with the solution of the Bilby et al. (1963) model for elastic perfectly plastic materials in terms of the size of the

plastic zone. Similar comparison were made with the solutions of the Ellyin et al. (1986 and 1989) for nonlinear work hardening materials in terms crack tip plastic displacement and crack tip shear stresses.

Experimental investigations of granite of its mechanical behavior when subjected to monotonic and cyclic loads were also performed. Static mechanical properties of the rock under shear loading are the minimum required data for damage assessment by dislocation model.

Fatigue tests on granite specimens resulted in a stress life curve (S - N) for granite. This curve indicates the number of cycles to initiate a crack in brittle rock specimen i.e. granite, followed by brittle failure of the specimen. A large scatter was observed in the stress life curve of granite. This was partly caused by the imperfections in specimen surface finish, notches, preloading etc. (ASME Professional Development, online document).

Brittle nature of granite prevented pre-cracking of the rock specimens. It is suggested that brittle behavior of granite caused the crack to grow at a very fast rate as soon as it was initiated. For the same reason, an attempt to measure crack growth rate during cyclic loading test was also unsuccessful. Specialty crack propagation gages were used to measure rate of crack growth as the crack was initiated and started to grow. However, the brittle failure of granite broke the crack propagation gage at once and disrupted the process of recording the growth of the crack by the data acquisition system.

Overall, the numerical results show that the dislocation model can effectively be used to predict shear crack growth in rock subject to cyclic loading. It is, however, to be noted that the results obtained from this study are a first approximation to the solution of the rock damage problem by cyclic loading. The results obtained numerically need to be verified by experiment and as such they are to be seen as suggestions to rock behavior under cyclic loading as opposed to definite conclusions which can only be made after experimental observations and verifications. Therefore, more future research should be carried out to verify these results.

## ***6.2. Recommendations for Further Work***

This is the first study of the quantification of the rock damage numerically in mid- to far-field region where vibration is the main cause of rock damage. An alternative approach to peak particle velocity criterion is suggested and the model results provide a first approximation to the solution of a complex slope wall stability problem. In continuation of this work, the following recommendations for the future work are made.

- Further development of the model to investigate damage by several cycles of loading and unloading and select a proper crack growth criterion.
- In this model, the extension of only one crack was investigated. In other words, rock damage is only estimated at the tip of one crack. It is recommended to further develop the model to consider two or more intersecting cracks and assess rock damage accordingly.

- Proper means of measuring shear crack growth in rock must be adopted in the process of data collection. Crack growth measurement is a difficult and costly task;
- One method to measure rock movement (slide) is by Time Domain Reflectometry (TDR). The method has extensively been used for deformation measurement in rocks in underground and open pit mines (Aimone-Martin et al., 1994; Aimone-Martin et al., 1997; Francke et al., 1994; and Francke et al., 1996). The assessment of the applicability of this method and its possible application to measure rock slide due to cyclic loading is recommended.
- An extensive field study has to be performed to collect data from various mine sites and different rock types and be used against the dislocation model results to verify the model;
- It is recommended to perform similar analysis (numerical and experimental) on soft rocks to investigate the plastic behavior of these rocks under cyclic loading and to compare them against hard rocks.



### List of References

1. Adams, Donald F., 2001, "Personal Communications".
2. Adams, Donald F. and Walrath, David E., 1987a, "Current Status of the Iosipescu Shear Test Method", *Journal of Composite Materials*, 21, June, p. 494-507.
3. Adams, Donald F. and Walrath, David E., 1987b, "Further Development of the Iosipescu Test Method", *Experimental Mechanics*, 27, 2, p. 113-119.
4. Aimone-Martin, C. T. and Francke, J. L., 1997, "Time Domain Reflectometry (TDR): A Comparison of Field Data to Laboratory Shear Tests", *NYRocks '97: 36th U S Rock Mechanics Symposium*, p. Paper No. 084.
5. Aimone-Martin, Catherine T., Oravecz, Calman I., and Nytra, Timothy K., 1994, "TDR Calibration for Quantifying Rock Mass Deformation at the Wipp Site, Carlsbad, NM", *Time Domain Reflectometry in Environmental, Infrastructure, and Mining Applications*, p. 507-517.
6. American Society for Testing and Materials, 1993, "ASTM D 5379/D 5379M - 93: Standard Test Method for Shear Properties of Composite Materials by the V-Notched Beam Method", p. 235-247.
7. Bard, Y., 1974, "Nonlinear Parameter Estimation", Academic Press, New York.
8. Barton, N., Lien, R., and Lunde, J., 1974, "Engineering Classification of Rock Masses for the Design of Tunnel Support", *Rock Mechanics*, 6, 4, p. 183-236.
9. Bauer, A., 1982, "Wall Control Blasting in Open Pits", *Proceedings of 14th Canadian Rock Mechanics Symposium*, CIM Special Volume 30, p. 3-10.
10. Bauer, A. and Calder, P. N., 1978, "Open Pit and Blast Seminar", Course # 63-321, Mining Engineering Department, Queen's University.

11. Bawden, W. F., Katsabanis, P., and Yang, R. L., 1993, "Blast Damage Study by Measurement and Numerical Modeling of Blast Damage and Vibration in the Area Adjacent to Blasthole", Proceedings of the International Congress on Mine Design, p. 853-861.
12. Bertacchi, P. and Sampaolo, A., 1974, "Some Critical Considerations on the Deformation and Failure of Rock Samples in the Laboratory", Third International Congress on Rock Mechanics, Vol. 2 Part A, p. 21-26.
13. Bieniawski, Z. T., 1974, "Geomechanics Classification of Rock Masses and Its Application in Tunneling", Proceedings of the 3rd International Society for Rock Mechanics Congress, 2A, p. 27.
14. Bieniawski, Z. T., 1984, "Rock Mechanics Design in Mining and Tunneling", Balkema, Rotterdam.
15. Bilby, B. A., Cottrell, A. H., Smith, E., and Swinden, K. H., 1964, "Plastic Yielding From Sharp Notches", Proceedings Of The Royal Society Of London Series A-Mathematical And Physical Sciences, A279, p. 1-9.
16. Bilby, B. A., Cottrell, A. H., and Swinden, K. H., 1963, "The Spread of Plastic Yield From a Notch", Proceedings Of The Royal Society Of London Series A-Mathematical And Physical Sciences, A272, p. 304-314.
17. Bilby, B. A. and Eshelby, J. D., 1968, "Dislocations and the Theory of Fracture", In *Fracture: An Advanced Treatise*, Editor: H. Liebowitz, Academic Press, Chapter 2, p. 99-182.
18. Bilby, B. A. and Swinden, K. H., 1965, "Representation of Plasticity at Notches by Linear Dislocation Arrays", Proceedings of the Royal Society of London Series A-Mathematical and Physical Sciences, A285, p. 22-33.
19. Brady, B. H. G. and Brown, E. T., 1993, "Rock Mechanics for Underground Mining", CHAPMAN & HALL, Second Edition.

20. Brown, E. T. and Hudson, J. A., 1974, "Fatigue Failure Characteristics of Some Models of Jointed Rock", *Earthquake Engineering and Structural Dynamics*, 2, p. 379-386.
21. Calder, P., 1977, "Pit Slope Manual, Chapter: Perimeter Blasting", CANMET, Canada Centre for Mineral and Energy Technology, Energy, Mines and Resources Canada, Vol. 7, p. 82.
22. Chitombo, Gideon and Scott, A., 1990, "An Approach to the Evaluation and Control of Blast Induced Damage", *Fragblast '90, Third International Symposium for Rock Fragmentation and Blasting*, p. 239-244.
23. Crandell, F. J., 1949, "Ground Vibration Due to Blasting and Its Effect upon Structures", *Journal of Boston Society of Civil Engineers*.
24. Delves, L. M. and Walsh, J., 1974, "Numerical Solution of Integral Equations", 1<sup>st</sup> edition, Oxford University Press, Oxford, p. 1-339.
25. Dowding, C. H. and Rozen, A., 1978, "Damage to Rock Tunnels from Earthquake Loading", *Journal of Geotechnical Engineering Division, ASCE, American Society of Civil Engineers*, 104, GT2, p. 175-191.
26. Eberhardt, E., Stead, D., and Stimpson, B., 1999, "Quantifying Progressive Pre-Peak Brittle Fracture Damage in Rock During Uniaxial Compression", *International Journal of Rock Mechanics and Mining Sciences*, 36, p. 361-380.
27. Ellyin, F. and Fakinlede, C. O. A., 1986, "Nonlinear Dislocation Model of the Work-Hardening Crack-Tip Field", *International Journal of Fracture*, 32, p. 3-20.

28. Ellyin, F. and Fakinlede, C. O. A., 1987, "A Dislocation Model for Work-Hardening Material and Cyclic J-Integral", *International Journal of Fracture*, 33, p. 95-110.
29. Ellyin, F. and Fakinlede, C. O. A., 1989, "Nonlinear Work-Hardening Crack-Tip Fields by Dislocation Modeling", *Special Technical Publication 995 (STP 995)*, p. 107-119.
30. Eshelby, J. D., 1949, "Edge Dislocations in Anisotropic Materials", *Philosophical Magazine*, 40, p. 903-912.
31. Eshelby, J. D., Frank, F. C., and Nabarro, F. R. N., 1951, "The Equilibrium of Linear Arrays of Dislocations", *Philosophical Magazine*, 42, p. 351-364.
32. Fakinlede, Omotayo Abayomi, 1985, "Some Factors Affecting Fatigue Crack Propagation", PhD. Thesis, Department of Mechanical Engineering, University of Alberta, Edmonton, Canada.
33. Feng, H. and Wnuk, M. P., 1991, "Cohesive Models for Quasi-Static Cracking in Inelastic Solids", *International Journal of Fracture*, 48, p. 115-138.
34. Forsyth, W. W., 1993, "A Discussion of Blast-Induced Over-break Around Underground Excavations", *4th International Symposium on Rock Fragmentation by Blasting - Fragblast '4*, p. 161-166.
35. Francke, J. L., Terrill, L. J., and Allen, W. W., 1996, "Time Domain Reflectometry as a Rock Mass Monitoring Technique", *PREPRINTS- SOCIETY FOR MINING ENGINEERS OF AIME*, 189.
36. Francke, J. L., Terrill, L. J., and Francke, C. T., 1994, "Time Domain Reflectometry Study at the Waste Isolation Pilot Plant", *Time Domain Reflectometry in Environmental, Infrastructure, and Mining Applications*, p. 555-568.

37. Gil, Henryk, 1991, "The Theory of Strata Mechanics", Developments in Geotechnical Engineering, Polish Scientific Publishers, Warsaw, 1<sup>st</sup> edition, 63, p. 1-276.
38. Gladwin, M. T. and Stacey, F. D., 1974, "Anelastic Degradation of Acoustic Pulses in Rock", Physics of the Earth and Planetary Interiors, 8, p. 332-336.
39. Griggs, D. T., Turner, F. J., and Heard, H. C., 1960, "Deformation of Rocks at 500° to 800°", In *Rock Deformation*, Editors: Griggs, D.T; Handin, J., Geological Society of America, p. 39-104.
40. Head, A. K. and Louat, N., 1955, "The Distribution of Dislocations in Linear Arrays", Australian Journal of Physics, 8, p. 1-7.
41. Ho, Henjen, Budiman, Haryanto T., Tsai, Ming-Yi, Morton, John, and Farley, Gary L., 1993, "Composite Material Shear Property Measurement Using the Iosipescu Specimen", ASTM STP 1206, p. 70-89.
42. Holmberg, R., 1993, "Recent Development to Control Rock Damage", 4th International Symposium on Rock Fragmentation by Blasting - Fragblast '4, p. 197-198.
43. Holmberg, Roger and Perrson, Per Anders, 1980, "Design Of Tunnel Perimeter Blasthole Patterns To Prevent Rock Damage", Trans Inst Min Metall. Sect A., 89 Jan 1980, p 37-40, p. 37-40.
44. Hult, J. A. and McClintock, F. A., 1956, "Elastic-Plastic Stress and Strain Distribution Around Sharp Notches Under Repeated Shear", 9th International Congress of Applied Mechanics, 8.
45. Iosipescu, N., 1967, "New Accurate Procedure for Single Shear Testing of Metals", Journal of Materials, 2, 3, p. 537-566.

46. Kenty, J. D., 1970, "Suggested Method of Test for Direct Shear Strength of Rock Core Specimens.", Special Procedures for Testing Soil and Rock for Engineering Purposes: Suggested Methods, Standard and Tentative Methods, Definitions and Nomenclature, ASTM special technical publication 479.
47. Kidybinski, A., 1964, "Modele Reologiczne Skal Karbonskich", Prace GIG, 360.
48. Kidybinski, A., 1965, "Badania Nad Reologicznymi Wlasnosciami Skal Prowadzone WG IG-u", Zesz. Probl. PAN.
49. Labreche, Duane A., 1983, "Damage Mechanisms in Tunnels Subjected To Explosive Loads", Seismic Design of Embankments and Caverns. Proceedings of Symposium, p. 128-141.
50. Langefors, Ulf, Kihlstrom, B., and Westerberg, H., 1948, "Ground Vibrations in Blasting", Water Power, 1, Feb. 1948.
51. Laird, C and Smith, G. C., 1963, "Initial Stages of Damage in High Stress Fatigue in Some Pure Metals", Philosophical Magazine, 8, p. 1945-1963.
52. Lardner, R. W., 1968, "A Dislocation Model for Fatigue Crack Growth in Metals", Philosophical Magazine, 17, p. 71-82.
53. Lardner, R. W., 1974, "Mathematical Theory of Dislocations and Fracture", University of Toronto Press, p. 363.
54. Leibfried, G., 1951, "Verteilung Von Versetzungen Im Statischen Gleichgewicht", Z. Physik, 130, p. 214-226.
55. Lilley, C. R., 1994, "The Likelihood of Blast Induced Near Field Damage in Cemented Hydraulic Fill", Ph.D. Thesis, Department of Mining and Metallurgical Engineering, The University of Queensland, Brisbane, Australia.

56. Lilley, C. R. and Chitombo, G. P. F., 1998, "Development of a Near Field Damage Model for Cemented Hydraulic Fill", *Minefill '98*, p. 191-196.
57. Lilly, Peter A., 1986, "Empirical Method Of Assessing Rock Mass Blastability", *Symposia Series Australasian Institute of Mining and Metallurgy*. Published by the Australasian Inst of Mining & Metallurgy, Parkville, Australia, 48, p. 89-92.
58. Liu, Q. and Proulx, R., 1996, "The Mechanisms of Rock Damage in Blasthole Open Stopping: Blast Induced Versus Stress Induced", *6th High-Tech Seminar: State-of-the-Art Blasting Technology, Instrumentation and Explosives Applications*, p. 599-608.
59. Lizotte, Yves C., Mohanty, Bibhu, Paventi, Mario, and Scoble, Malcolm, 1996, "The Measurement and Control of Blast Damage: Measurement and Audit", *Proceedings of SME/AIME Annual Meeting and Exhibit, March 11-14, 1996*
60. Lyakhovsky, Vladimir, 2001, "Theoretical and Numerical Study of the Electro-seismic Effect for Various Fluid Containing Media", *Project INTAS 99-064*.
61. Marquardt, D. W., 1963, "An Algorithm for Least Squares Estimation of Non-Linear Parameters", *Journal of the Society for Industrial and Applied Mathematics (SIAM Journal)*, 11, p. 431-441.
62. Matthews, M. C., 1988, "The Engineering Application of Direct and Simple Shear Testing", *Ground Engineering*, 21, 2, p. 13-21.
63. Mavko, Gerald M. and Nur, Amos, 1978, "The Effect of Non-Elliptical Cracks on the Compressibility of Rocks", *Journal of Geophysical Research*, 83, B9, p. 4459-4468.
64. McGarr, A., 1971a, "Stable Deformation of Rock near Deep-Level Tabular Excavations", *Journal of Geophysical Research*, 76, 29, p. 7088-7106.

65. McGarr, A., 1971b, "Violent Deformation of Rock Near Deep-Level Tabular Excavations - Seismic Events", Bulletin of the Seismological Society of America, 61, 5, p. 1453-1466.
66. McGarr, A., 1981, "Strong Ground Motion of Mine Tremors: Some Implications for Near-Source Ground Motion Parameters", Bulletin of the Seismological Society of America, 71, 1, p. 295-319.
67. Mckown, Andrew F., 1986, "Perimeter Control Blasting For Underground Excavations In Fractured And Weathered Rock", Bull Assoc Eng Geol., 23, 4, p. 461-478.
68. Medaris, K., 1977, "The Development of Rational Damage Criteria for Low-Rise Structures Subjected to Blasting Vibrations", Proceedings of 18th U. S. Symposium on Rock Mechanics, p. 1-16.
69. Mohanty, B. and Chung, S. H., 1986, "Production Blasts in Open Pit Mines and Their Effect on Slope Stability", Geotechnical Stability in Surface Mining, Proceedings of the International Symposium, p. 133-140.
70. Morhard, R. C., Chiappetta, R. F., Borg, D. G., Sterner, and V.A., 1987, "Explosives and Rock Blasting", Atlas Powder Company.
70. Mura, Toshio, 1969, "Mathematical Theory of Dislocations", Proceedings of the Joint Applied Mechanics and Fluid Engineering Conference, Northwestern University, Evanston, Illinois, June 16-18, 1969, p. 1-209.
71. Muskhelishvili, N. I., 1953, "Singular Integral Equations", NOORDHOFF LTD GRONINGEN, HOLLAND.
72. Nabarro, F. R. N., 1967, "Theory of Crystal Dislocations", Clarenton Press, Oxford.
73. Nagaraj, T. S., 1993, "Principles of Testing Soils, Rocks and Concrete", 1st, 66.



74. Neumann, P., 1974, "New Experiments Concerning the Slip Processes at Propagating Fatigue Cracks - I", *Acta Metallurgica*, 22, p. 1155-1165.
75. Nicholls, H. R., Johnson, C. F., and Duvall, W. I., 1971, "Blasting Vibrations and Their Effects on Structures", US Bureau of Mines, Bulletin 656.
76. Olsson, William A., 1984, "A Dislocation Model of the Stress History Dependence of Frictional Slip", *Journal of Geophysical Research*, 89, B11, p. 9271-9280.
77. Oriard, L. L., 1970, "Dynamic Effect on Rock Masses From Blasting Operations", Slope Stability Seminar.
78. Oriard, L. L., 1982, "Blasting Effect and Their Control", In *Underground Mining Methods Handbook*, first edition, p. 1590-1603.
79. Orowan, E., 1934, "Zur Kristallplastizität", *Z. Physik*, 89, p. 605-659.
80. Owen, G. N. and Scholl, R. E., 1981, "Earthquake Engineering of Large Underground Structures", FHWA/RD-80-195, p. 171-174.
81. Paventi, M., 1995, "Rock Mass Characteristics and Damage at the Birchtree Mine", Ph.D. Thesis, Department of Mining and Metallurgical Engineering, McGill University.
82. Paventi, M., Lizotte, Yves C., and Scoble, M., 1996, "An Assessment of Inherent and Mining-Induced Rock Mass Damage in Development Drifting", Proceedings of the CIM Annual General Meeting.
83. Persson, Per-Anders, Holmberg, Roger, and Lee, Jaimin, 1993, "Rock Blasting and Explosive Engineering", CRC Press.
84. Pierron, Fabrice and Vautrin, Alain, 1994, "Accurate Comparative Determination of the In-Plane Shear Modulus of T300/914 by the Iosipescu and 45° Off-Axis Tests", *Composites Science and Technology*, 52, p. 61-72.

85. Plis, Matthew N., Fletcher, Larry R., Stachura, Virgil J., and Sterk, Paul, V, 1991, "Over-break Control in VCR Stopes at the Homestake Mine", Proceedings of the Conference on Explosives and Blasting Technique., 1, p. 1-9.
86. Polanyi, M., 1934, "Über Eine Art Gitterstörung, Die Einen Kristall Plastiach Machen Könnte", Z. Physik, 89, p. 660-664.
87. Powell, M. J. D., 1972, "Problems Related to Unconstrained Optimization", 3, p. 29.
88. Protodyakonov, M. M., 1969, "Methods of Determining Shearing Strength of Rocks", In: Mechanical Properties of Rocks, p. 15-27.
89. Raleigh, C. B., 1965, "Glide Mechanisms in Experimentally Deformed Mineral", Science, 150, 3697, p. 339-341.
90. Raleigh, C. B., 1968, "Mechanisms of Plastic Deformation of Olivine", Journal of Geophysical Research, 73, p. 5391-5406.
91. Reklaitis, G. V., Ravindran, A., and Ragsdell, K. M., 1983, "Engineering Optimization, Methods and Applications", John Wiley & Sons, p. 1-684.
92. Rice, J. R., 1968, "A Path Independent Integral and Approximate Analysis of Strain Concentration by Notches and Cracks", Journal of Applied Mechanics, 35, p. 379-386.
93. Ricketts, T. E., 1988, "Estimating Underground Mine Damage Produced by Blasting", 4th Mini-Symposium on Explosives and Blasting Research, p. 1-5.
94. Rockwell, E. H., 1934, "Vibrations Caused by Blasting and Their Effect on Structures", Hercules Powder Company.

95. Rossmannith, H. P. and Uenishi, K., 1997, "Post-Blast Bench Block Stability Assessment", Proceedings of the 36th US Rock Mechanics Symposium, NYRocks '97 ISRM International Symposium.
96. Scales, L. E., 1974, "Introduction to Non-Linear Optimization", Springer-Verlag, New York, p. 1-115.
97. Schmidt, A. and Huddle, C. W., 1977, "Effect of Confining Pressure on Fracture Toughness of Indiana Limestone", International Journal of Rock Mechanics and Mining Sciences, 14, p. 289.
98. Singh, S. P., 1992, "Investigation of Blast Damage Mechanism In underground Mines. Report to MRD Mining Research Directorate", Sudbury, Ontario, p. 50.
99. Singh, S. P., 1994, "Blast Damage Control during Underground Mining", 20th Conference on Explosives and Blasting Technique, p. 341.
100. Skempton, A. W., 1949, "Alexandre Collin, a Note on His Pioneer Work in Soil Mechanics", Geotechnique, 1, 4, p. 216-221.
101. St John, C. M. and Zahrah, T. F., 1987, "A Seismic Design of Underground Structures", Tunneling and Underground Space Technology, 2, 2, p. 165-197.
102. Stachura, V. J. and Cumerlato, C. L., 1989, "Changing Powder Distribution in the Highwall Holes Reduces Over-break and Rockfall Hazards", 5th Conference on Explosives and Blasting Research, p. 11-24.
103. Stevens, P. R., 1977, "Review of Effects of Earthquakes on Underground Mines", Open File Report 77-313.

104. Szymanski, J., Karami, A., Frimpong, S., and Sudak, L., 1997, "The Total Open Stope Design Approach - Part I", Mine Planning and Equipment Selection Conference, Calgary, Alberta, Canada, p. 575-583.
105. Tanaka, K., 1983, "The Cyclic J-Integral as a Criterion for Fatigue Crack Growth", International Journal of Fracture, 22, p. 91-104.
106. Taylor, G. I., 1934, "The Mechanism of Plastic Deformation of Crystals", Proceedings of the Royal Society of London Series A-Mathematical and Physical Sciences, 145, p. 362-415.
107. Thoenen, J. R. and Windes, S. L., 1942, "Seismic Effects of Quarry Blasting", Bulletin 442.
108. Volterra, V., 1907, "L'Équilibre Des Corps Élastiques Multiplement Connexes", Annls. Scient. Écol. Norm. Sup., series 24, p. 401-517.
109. Villaescusa, E. and Brown, E. T., 1990, "Characterizing Joint Spatial Correlation Using Geotechnical Methods.", ISRM Conference on Rock Joints, 4-6 June, 1990.
110. Vuolio, Raimo, 1991, "Estimating Damage Caused by Rock Vibrations", Proceedings of the Conference on Explosives and Blasting Technique, 2. Publ by Soc of Explosives Engineers, Solon, OH, USA, p 131-142, p. 131-142.
111. Walrath, David E., 2001, "Personal Communications".
112. Walrath, David E. and Adams, Donald F., 1983a, "Analysis of The Stress State in an Iosipescu Test Specimen", UWME-DR-301-102-1 (June 1983).
113. Walrath, David E. and Adams, Donald F., 1983b, "The Iosipescu Shear Test As Applied to Composite Materials", Experimental Mechanics, 23, 1 (March), p. 105-110.

114. Walrath, David E. and Adams, Donald F., 1984, "Verification and Application of the Iosipescu Shear Test Method", UWME-DR-401-103-1 (June 1984).
115. Weertman, J., 1964, "Continuum Distribution of Dislocations on Faults With Finite Friction", *Bulletin of the Seismological Society of America*, 54, 4, p. 1035-1058.
116. Weingarten, G., 1901, "Sulle Superficie Di Discontinuitá Nella Teoria Della Elasticitá Dei Corpi Solidi", *Atti. Accad. Nax. Lincei, Rend, Cl. Sci. Fis. Mat. Natur. V, Series 10/1*, p. 57-60.
117. Wernick, E., 1977, "Stresses and Strains on the Surface of Anchors", *Proceedings of 9th International Conference on Soil Mechanics and Foundation Engineering*, Tokyo, Japan.
118. Whitney, James M., 1996, "Effect of Load Distribution and Placement in the Iosipescu Shear Test", *Journal of Reinforced Plastics and Composites*, 17, 1, p. 26-38.
119. Wilson, W. H., Wilson, W. B., and Holloway, D. C., 1987, "Self-Contained Electronic Delay Detonator", *Proceedings of the 2nd International Symposium on Rock Fragmentation by Blasting*, p. 541-549.
120. Young, Chapman, 1966a, "Application of Dislocation Theory to Upper-Mantle Deformation", Ph.D. Thesis, Stanford University.
121. Young, Chapman, 1966b, "Applications of Dislocation Theory to Rock Deformation", *Transactions: American Geophysical Union*, 47, 1, p. 189-189.
122. Young, Chapman, 1976, "A Dislocation Model for Rock Deformation in an Arbitrary Loaded Half Space", *Proceedings Symposium on Rock Mechanics*, 17, p. 5C2.1-5C2.7.

- 
123. Young, Chapman III, 1969, "Dislocations in the Deformation of Olivine", American Journal of Science, 267, Summer Issue, p. 841-852.
  124. Yu, T. R. and Vongpaisal, S., 1996, "New Blast Damage Criteria for Underground Blasting", CIM Bulletin, 89, 998, p. 139-145.

## **Appendix A: Mine Blasting: an overview**

An explosion is a rapid thermo-chemical reaction, which converts the ingredients of the explosive into gases. The detonation process creates a wave front traveling at a speed which exceeds the velocity of sound in the material, producing temperatures ranging from 1650°C to 3870°C and pressures just behind the detonation front in the order of 1000 MPa to 27000 MPa (Morhard et al., 1987). According to Mohanty et al. (1986), the detonation wave is transmitted into the adjacent rock mass at characteristic velocities of 3 km/s to 6 km/s. The pressure transmitted to the rock in the vicinity of a cylindrical charge can be computed to be in the range of 2000 MPa to 8000 MPa, exceeding the compressive strength of the rock by several orders of magnitude (Lizotte et al., 1994).

Fragmentation is a complex process and depends on many factors including rock mass and explosive characteristics. The main characteristics of the explosives, with regard to rock fragmentation, are velocity of detonation, detonation pressure, sensitivity, water resistance, temperature stability, etc. (Morhard et al., 1987), none of which provides a direct indication of how effective a particular explosive will be to fragment a particular rock mass. The propagation geometry of the stress wave also affect the blast performance and depends on a number of factors such as the initiation point, detonation velocity and shock wave velocity in the rock. In the near field, in close vicinity of the blasthole, it only takes a few microseconds for the high stress waves to form at the blasthole wall which would shatter and crush the surrounding rock medium. As the stress wave proceeds outward in every direction at the speed of sound characteristic of the particular rock

medium, it decays rapidly while still high enough to compress the rock material at the wave front. At right angles to this compressive wave front, another wave component referred to as the tangential wave stress is formed. If the tangential stress is large enough it can cause tensile failures at right angles to the direction of propagation causing radial cracks to form and extend along with existing cracks and joints inherent in the rock mass. According to Morhard et al. (1987), radial cracks develop at the speed of 25 to 50% of the P wave velocity in the rock mass. The largest tensile failures are expected to occur close to blasthole where the tangential stress is high enough for failure to occur. For this reason, the largest number of cracks is formed close to the blasthole.

When a compressive stress wave strikes a free surface, it is immediately converted to a tensile wave that starts at the free surface and travels back through the rock mass toward the blasthole. If the intensity of the reflected tensile wave is large enough it could cause spalling at the free face although no significant mass movement will occur. This is seen more often in open pit mines causing slope stability problem.

During and/or after stress wave propagation, the high pressure, high temperature gases impart a stress field around the blasthole that can expand the original blasthole, extend original cracks and penetrate into rock mass discontinuities. The travel path of the gases are not known but are expected to follow the path with the least resistance. This means that gases will first migrate into existing cracks, joints, faults, and discontinuities, and also in the layers of materials that exhibit low cohesion or bonding at interfaces. The length of time the explosion gases are confined within the rock mass vary significantly depending on the amount and type of explosive, blast pattern (spacing and burden) and



initiation sequence, effect of detonation timing, rock type and its structure, fracture network, and the amount and type of stemming in the blasthole. It is notable that a lengthy confinement of explosive gases within the rock mass may cause more damage to surrounding rock structure while short period confinement of explosive gases may lead to more noise, throw and fly rock. Therefore, a careful assessment of damage and blasting efficiency should take place to avoid undesirable damage to rock mass while utilizing the maximum potential of the explosive materials.

In near field rock damage analysis, there is a controversy as to which blast component, i.e. stress wave or high-pressure gases, contribute more to rock fragmentation. On one hand, the amount of energy in the high stress waves is calculated to be only a fraction of total blast energy that is between 10 to 18% in granite while only 2 to 4% of the total energy in salt and the remaining portion is contained in the high-pressure gases (Kutter et al., 1971). Nevertheless, the magnitude of the high stress waves is significantly higher than the dynamic strength of the rock mass and causes extensive damage to the rock mass surrounding the blasthole. On the other hand, high-pressure gases contain the greater proportion of the blast energy and are imposed on the rock mass for a longer period of time causing new and existing cracks to extend in the direction of the least resistance.

### ***A.1. Blasting Theories***

There have been a number of attempts to find out which component acts as the major contributing factor in rock fragmentation by blasting. Morhard et al. (1987) summarized some of the more common thoughts regarding rock breakage mechanisms by blasting

(Table A-1). In each case, major rock breakage mechanisms are numbered in the order of their significance and contribution to rock fragmentation.

According to Morhard et al. (1987), there are five major rock breakage mechanisms upon which various blast mechanism theories proposed by other researchers are classified (Table A-1). These mechanisms are briefly described in following.

#### A.1.1. Reflection Theory

Initially proposed by Obert et al. (1949; 1950), Hino (1956) and Duvall et al. (1957), reflection theory is one of the first theories used to explain the rock breakage mechanism by blasting. This mechanism is based on the fact that rocks have least strength against tension compared to compression. According to this theory, rock breakage happens only by tensile failure of the rock by slabbing at free surfaces as blast generated stress waves are reflected back toward the blasthole. In this theory, rock breakage happens only by high stress waves and gas pressurization has no role in fragmenting the rock mass.

#### A.1.2. Gas Expansion Theory

Gas expansion theory was proposed by Persson et al. (1970) and Johansson et al. (Johansson et al., 1970). In this theory, the effects of high stress waves and gas pressurization are combined, however, rock fragmentation is considered to happen by gas pressurization action of the blast high pressure gases. Here, high stress waves generate new cracks in the rock next to the blasthole and cracks start from a distance of approximately two radii from the blasthole and then propagate outward and inward under

Table A-1: Rock breakage theories – a historical review (Morhard et al., 1987)

Researcher(s)	Breakage Mechanisms				
	Tensile reflected waves	Compressional stress waves	Gas Pressurization	Flexural rupture	Nuclei stress/ flaw
Obert et al. (1949; 1950)	1				
Hino (1956)	1				
Duvall et al. (1957)	1				
Rinehart (1958)	1				
Langfors et al. (1963)		2	1		
Starfield (1966)	1				
Porter et al. (1970)		2	1		
Persson et al. (1970)		1			
Kutter et al. (1971)		1	1		
Field et al. (1971)		1	1		
Johansson et al. (1974)	2		1		
Lang et al. (1974)	4	2	1		3
Ash (1973)			1	1	
Hagan et al. (1974)		1			
Barker et al. (1978b; 1978a; 1979)					1
Winzer et al. (1983)					1
Margolin et al. (1983); Adams et al. (1983)					1
McHugh (1983)					1

the effect of stress waves and pressurized gases. In this theory, fragmentation will not complete and broken rock will not be mobilized until cracks around the blasthole reach the free surface. Gas pressurization is the main contributor to rock fragmentation and stress wave acts as the starting mechanism of rock breakage.

### A.1.3. Flexural Rupture

Flexural rupture theory was originally introduced by Ash (1973). In this theory, flexural rupture and fragmentation is mainly caused by high-pressure gases, which contain 90% of the total energy generated. Here, radial cracks are initiated only in planes parallel with the blasthole axis where tangential stresses are maximum adjacent to the blasthole wall and no crack is created where no explosive is in immediate contact. According to this breakage theory, rock fragmentation by reflection of strain energy at the free surface is considered to be negligible. Gas pressure initiates propagation of radial cracks through the burden to the free surface and displaces the rock by bending in the direction of least resistance. This would naturally be in the direction of existing planes of weakness.

Morhard et al. (1987), by an analogy, shows the flexural rupture theory of rock fragmentation by bending and breaking a beam. In this analogy, a rectangular rock beam loaded longitudinally by distributed load represents the case of the rock burden loaded by a column explosive. The beam is considered as a cantilever beam with fixed end to represent the toe condition of the bench and the roller at the mid-point of stemming allows rotation and longitudinal deflections but no movement is allowed in the perpendicular direction to the blasthole.

#### A.1.4. Compressional Stress Wave Theory

Kutter et al. (1971) introduced compressional stress wave theory in which they explained the rock fragmentation by combined effects of high stress waves and high-pressure gases. In this theory, high stress waves, although very large in magnitude, only contain a small proportion of the total blast energy (10-18% in granite and 2-4% in salt). High stress waves are sufficiently high to cause severe damage to the rock mass in the form of new cracks and fractures. The remaining energy is contained in the gas pressure. As the compressional stress waves rapidly decay, high-pressure gases enter the existing and newly created cracks and, if high enough, extend these cracks toward free surface.

The major difference between this theory and previous ones are:

- Rock fragmentation is induced and controlled by both high stress waves and high pressure gases.
- New radial cracks initiate from the blasthole wall and grow outward toward free surface, if exist.
- Existing cracks start to move and grow under the high stress, high-pressure gases.
- If exists, cracks grow toward the free surface with the least resistance.
- The direction of radial crack propagation is affected by the in-situ stress conditions.

### A.1.5. Combined Theory

The combined rock fragmentation theory was originally introduced by Lang et al. (1974). In this mechanism, which takes place in three consecutive stages, high stress waves reflected tensile waves and high-pressure gases, all, contribute to rock fragmentation. At stage 1, high stress waves shatter the rock mass next to the blasthole and generate a large number of cracks and fractures in the surrounding rock mass. In stage 2, as the stress wave reaches the free surface (if exists), it is reflected and transmitted through the rock mass toward the blasthole in the form of tensile waves. If the magnitude of the reflected tensile wave is larger than the tensile resistance of the rock mass, which is usually the case, tensile failure happens at the free surface in the form of slabbing. At stage 3, high-pressure gases interact with the already fractured rock mass, in which gases penetrate into the rock fractures and if the gas pressure is higher than the rock mass or joint strength, it will cause extension of the fractures. According to this theory, induced fractures propagate toward the least resistance direction; however, this direction may be affected by the state of in-situ stress.

In this mechanism, high stresses start the fragmentation process by inducing small cracks and fractures in the rock mass next to the blasthole. Then the reflected tensile waves create a number of large scale fractures near the free surface which weaken the rock mass and initiate the major fragmentation process that will be completed following the high pressure gas penetration into the existing and induced cracks and rock fractures.

### A.1.6. Nuclei or Stress Wave/Flaw Theory

Nuclei or stress wave/Flaw theory is relatively a new rock fragmentation mechanism introduced and further developed in last two decades by a number of researchers including Barker et al. (1978b; 1978a), Fournery et al. (1979), Winzer et al. (1983), Adams et al. (1983) and McHugh (1983). The theory is based on a series of laboratory tests conducted on unflawed and flawed homolite-100 models. In these tests many geologic structures including rock joints, faults, rock fractures, discontinuities and bedding planes typically present in the rock mass, which affect the outcome of the large scale blasting, were simulated. Results of these tests have shown that fragmentation is mainly caused by high stress waves and pressurized gases have a minor impact on rock fragmentation.

In this theory, as high stress waves, consist of P and S waves, travel throughout the rock mass around the blasthole, they initiate a number of small cracks around the blasthole in the absence of flaws. While in the presence of flaws and discontinuities a much greater number of cracks are nucleated at the flaws by the traveling P waves tail and are kept open by the S wave front. The effectiveness of nuclei or stress wave/flaw theory is bound to the presence of flaws and rock discontinuities upon which stress waves pass and initiate small cracks in the rock mass between the blasthole and the free surface. For this reason, the theory is called nuclei theory.

The fundamentals of the rock fragmentation by blasting via nuclei theory is demonstrated in the Figure A-2. A blasthole loaded with column explosive is located near a free

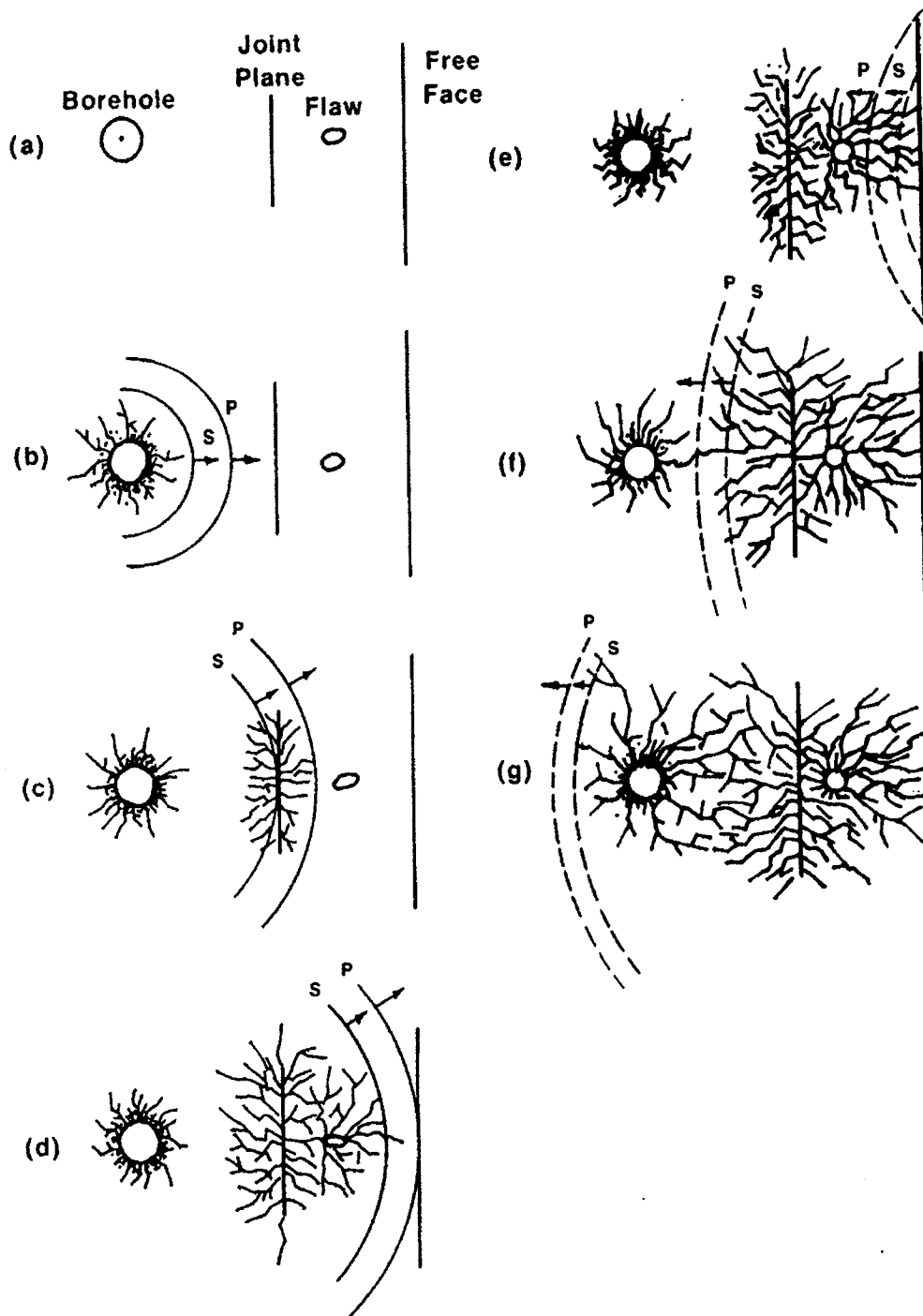


Figure A-2: Rock breakage mechanism according to nuclei theory (Morhard et al., 1987)



surface. There are two systems of rock discontinuities, a rock joint and a flaw. Following the blast, P and S waves propagate through the rock mass. In immediate vicinity of the blasthole where rock is free from rock discontinuities, only a small number of cracks will emanate from the blasthole wall. As the P wave passes over the joint plane, a great number of cracks are initiated by the P wave tail and the S wave front is high enough to keep initiated cracks from arresting Morhard (1987). Therefore, cracks are initiated at remote distances from the blasthole by the action of both P wave tail and S wave front.

Similarly, when waves travel over the flaw, a number of cracks will be nucleated at the flaw. As the waves reach the free surface, P wave is reflected and transforms to a tensile wave causing slabbing near the free surface. It is notable that immediately after P wave is reflected at the free face while S wave is not reflected yet, the two waves will interact menacing that the amplitude of the overall vibration wave will cause more fracturing and further extension of the previously formed cracks in the rock mass leading to more effective rock fragmentation. As the reflected waves travel back toward the blasthole, they interact with the newly formed and existing cracks in the rock mass causing more extension and further development of rock fragmentation. In this theory, rock fragmentation process takes place mainly by the action of the high stress waves and high-pressure gases do not contribute significantly to this process (Winzer et al., 1983).

#### A.1.7. Torque Theory

Morhard et al. (1987) introduced this rock breakage mechanism as suitable for in-situ retorting in which proper fragmentation without tight muckpile is needed. In this method,

accurate timing of initiators is of utmost importance. According to this method, two adjacent blastholes are initiated at the same time (absolutely) from the opposite ends of the explosive charges. As a result, a compressional wave is formed at each column charge traveling parallel but in opposite directions Figure A-3. The largest stress is directed perpendicular to the primary shock front. Also this stress is assumed to be the greatest near the detonation head in the explosive column and diminishes with distance away from detonation head. The stress fields generated by the simultaneously detonated charges create a stress distribution between the blastholes that tends to fracture, shake and move the fragmented rock mass in a counterclockwise direction. If explosives are fired in reversed order, the stress induced rock motions will take place in clockwise direction. The success of this rock breakage mechanism is solely dependent on the simultaneous initiation of the explosives.

The effectiveness of either of stress wave and gas pressure components is not discussed, however, it is expected that both explosion components help fragment the rock mass. This is due to the fact that this type of blasting is only used to ease the digging and loading actions of the mining equipment (dragline or shovel) and is not intended to move and/or displace the whole rock mass. Therefore, blastholes are located relatively far from the free face. As a result, tensile failure of the rock mass does not contribute to the rock breakage mechanism. High-pressure gases also are contained in the rock mass and effectively contribute to extend and further develop the cracks and fractures initiated by the high stress waves.

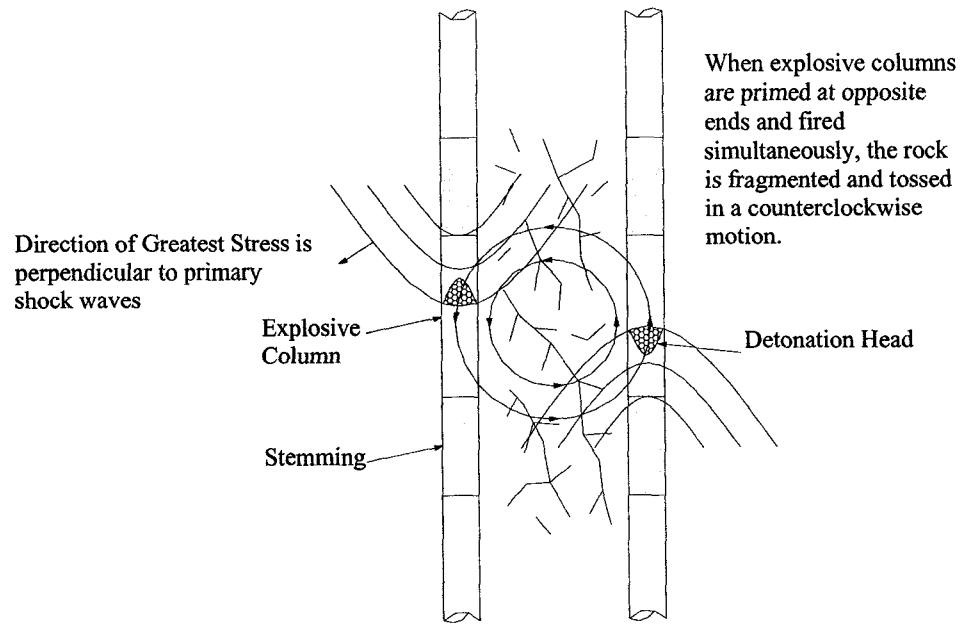


Figure A-3: Rock breakage mechanism based on Torque theory

## *A.2. Conventional approach to blast design and related damage*

Determination of the arrangement of blastholes, quantity of the explosive and sequence of detonation and breakage are the main problems of practical rock blasting (Langefors et al., 1963). A large number of excavations and blast design formulae have been proposed in the mining literature to address problems associated with blasting operations in underground and open pit mining operations. The problems mainly relate to impact of blasting on excavation performance and general stability of the mine structure. These are partly due to improper blast design and configuration, improper delay timing between blastholes and rows, and over-reliance on the empirical blast design and experimental approaches rather than applying sound theoretical approaches to investigate rock mass behavior subject to blast shock waves, vibrations and high-pressure gases. Other blast-induced problems include ore dilution, improper rock fragmentation, improper ground support system that is incapable of resisting blast induced stresses in addition to in-situ stresses, and additional costs associated with clean up activities and installation of new ground support system, etc.

While a number of the conventional approaches have been applied with success in practice, the general feedback from the mine operators and engineers is that the current methods tend to i) be simplistic and limited in their application, ii) be site specific and therefore unable to deal with changes in geological and mining conditions, iii) fail to incorporate parameters viewed by operators as critical to the mechanisms at work, and iv)

provide wide ranges for design parameters and exhibit large and unacceptable errors in their predictions (Szymanski et al., 1997).

Consequently, even though practicing engineers and mine managers recognize the intended value of the conventional methods, they continue to rely on their own and other people's judgment and experience rather than depend on any systematic engineering approach. The conventional methods are simply not providing the guidelines required by mine operators. In following, some of the more popular blast design approaches in the mining literature are described highlighting some of their limitations in terms of design and applications.

#### A.2.1. Surface and Underground Blast Design Methods

Designing an effective and successful mine blast requires one to select optimum blast design parameters including blasthole spacing  $S$ , burden  $B$ , charge weight  $W$  or powder factor  $PF$ , top-hole stemming length  $T$  and sub-grade drilling depth  $J$ . Design parameters are shown in Figure A-5. As shown blastholes are drilled either square ( $S/B=1$ ), rectangular ( $S/B \geq 1$ ) or staggered. The  $S/B$  ratio, sequence of blasthole initiation, actual timing between charge detonations, and number of blastholes rows determine the shape of the broken rock pile as well as the degree of rock fragmentation.

Among other factors, initiation sequence has the most important effect on the  $S/B$  ratio (Hagan, 1986) and essentially on the outcome of the blast in terms of rock fragmentation, ore dilution and induced damage to the rock mass. In addition to  $S/B$  ratio, in another

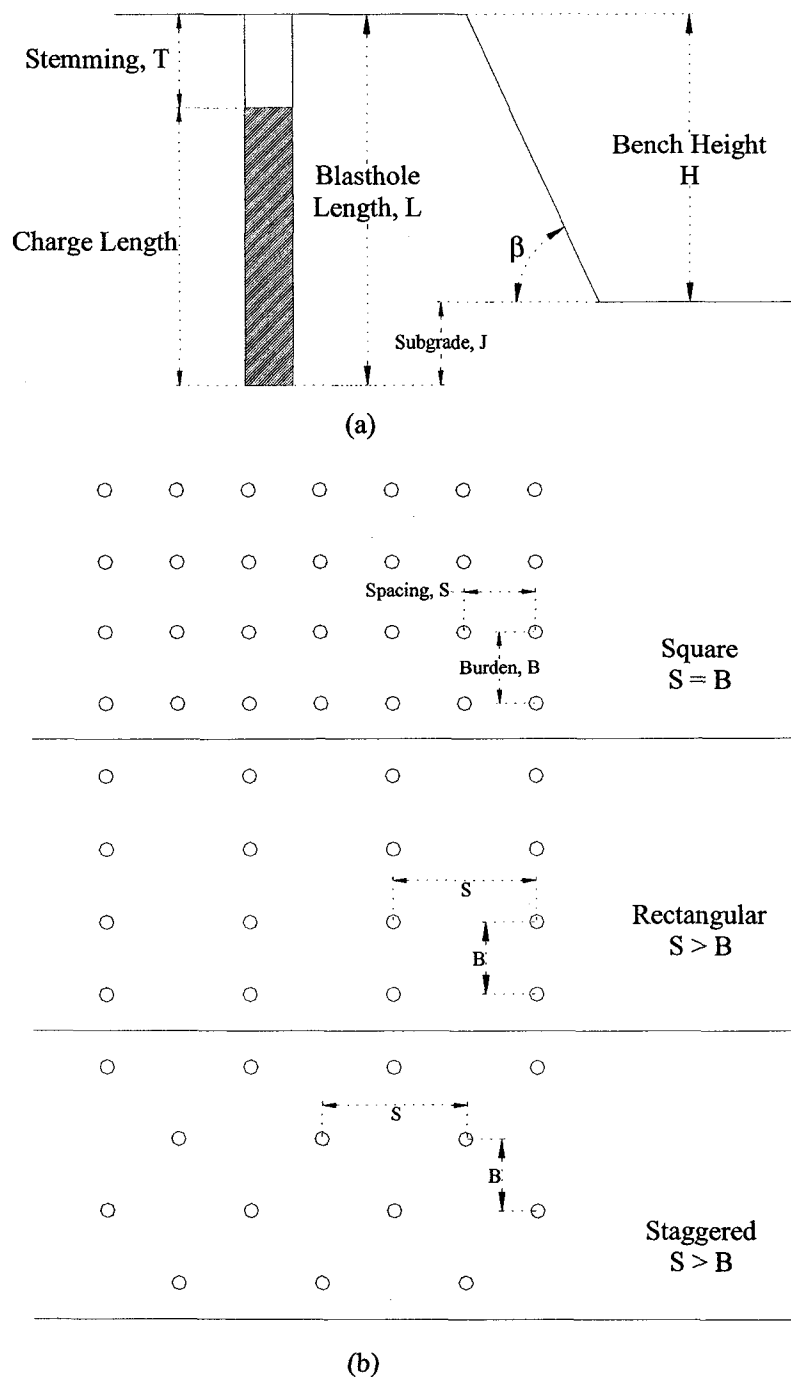


Figure A-5: Blasthole section view (A) showing terminology used in design and (B) pattern array for layout of holes

study, Hagan (1979) predicted that a very large burden distance (B) (Figure A-5) causes explosion gases bottle up within the blastholes for excessive period of time and therefore, are more likely to stream into, wedge open and extend both pre-existing fractures and strain-wave generated cracks all around the blastholes. As B increases beyond its optimum value, the preferential extension of forward looking fractures and cracks becomes less. Where B is much too large, the explosion gases act as though they are working only toward the horizontal free face (i.e. the top of the bench) and in effect blast becomes a cratering blast. Such cratering could cause over-break. It is clear then that over-break increases with B, especially when explosion gases fail to heave the burden rock forward significantly. Therefore the selected value of B must limit this damage yet achieve the required fragmentation, displacement, muckpile looseness for an efficient digging operation.

The common surface and underground blast design approaches fall into three categories and are mainly defined based on the geometry of the blast, the blast pattern and rock mass properties, namely:

1. Methods that utilize optimum blasthole spacing to burden ratios ( $S/B$ ) to calculate blast pattern geometry,
2. Methods that start with a design powder factor to derive subsequent design parameters,
3. Methods that apply a “blastability index” to determine the required powder factor and blast design parameters.

### *A.2.1.1. Spacing/Burden (S/B) ratio*

Several empirical relationships have been proposed for surface mining blast design including Ash (1963), Pugliese (1973), Van Ormer (1973), Hagan (1981), Dick et al. (1983) and others. Blasthole diameter and burden are the most important parameters in blast design and are selected based on geology and explosive energy output. Blasthole diameter is usually set by the drill rig capacity, which is matched to the range of hole depths anticipated for the job (Dowding et al., 1993). A proper diameter needs to be selected to provide an adequate powder factor for breakage while distributing the explosive evenly throughout the blasthole depth. Fragmentation and particle size are also a function of blasthole diameter and burden.

Ash (1963) provides simple empirical formulas to compute burden, spacing, sub-grade and stemming lengths using “K factors” shown in Table A-2. The parameter K itself is site specific and is found empirically for every mine separately through trial and error. For surface blast design, Hagan (1986) suggests that S/B ratio has to be higher than 3.5 for V staggered blast patterns having effective bi-planar faces as compared to S/B ratio of 2.0 for square V blast pattern shooting to a planar face (Hagan, 1979).

A number of empirical rules and formulae have been proposed for use in underground ring, bench and development blast designs. Most notable in the last decades are formulae by Myers et al. (1990), Hagan (1979), Langefors et al. (1963), Holmberg et al. (1980), Holmberg (1979), Lilly (1986), Rustan (1992), and Kou et al. (1992).



Table A-2: Selected factors for first approximation surface blast designs

Using ANFO:		
Burden	$B = K_B$	$K_B = 22$ for rock density $< 2.7 \text{ g/cm}^3$ $= 30$ for rock density $> 2.7 \text{ g/cm}^3$
Using slurry, dynamite or other high explosive:		
		$= 27$ for rock density $< 2.7 \text{ g/cm}^3$ $= 35$ for rock density $> 2.7 \text{ g/cm}^3$
Spacing	$S = K_S B$	$K_S = 1$ to $2$ , depending on initiation
Subgrade	$J = K_J B$	$K_J = 0.2$ to $0.5$ (average $0.3$ )
Stemming	$T = K_T B$	$K_T = 0.5$ to $1.3$ (average $0.7$ )

Several ratios are proposed by different authors for underground blast design practices, which should give the best energy distribution for a given blasthole diameter, blasthole length and explosive type. For instance, Hagan (1979) suggested an empirical optimum S/B range of 1.0-3.0. Myers et al. (1990) suggested an optimum range of S/B of 1.4 for delayed blasthole firing and 2.0 for cluster (non-delayed) blasting. This approach generally requires calculation of a practical burden first and then selection of a suitable spacing by applying the appropriate ratio.

#### ***A.2.1.2. Powder Factor***

Underground blasts are also designed based on powder factor. An initial design powder factor ( $P_f$ ) is selected, generally given in kilograms of explosives per tone of rock (kg/t).  $P_f$  is the mass of explosive used to break a cubic meter or tone of rock in situ. This is the most common approach used by mine operators. The design powder factor is generally

selected based on satisfactory experience in similar geological conditions. In underground ring blasting the powder factor can vary between 0.2 and 0.5 kg/t and in development blasting it can vary from 1 to 2 kg/t (Szymanski et al., 1997). Dowding et al. (1993) suggest that powder factor ranges from 0.9 to 6 Kg/m<sup>3</sup>. The lower values are then used in large open rooms in soft weak rock while the higher values are used in confined raises and shafts for hard competent rock.

#### ***A.2.1.3. Blastability index***

One of the more commonly used engineering approaches to design an underground blast is through a blastability index. This index is defined by a number of parameters related to geological, structural and mechanical properties of the rock mass and the changes in them that occur due to blasting. A blastability index was proposed by Lilly (1986), which is the sum of a number of rock parameters describing rock structure, joint spacing, joint orientation, rock mass specific gravity and hardness. The Lilly's blastability index is given by:

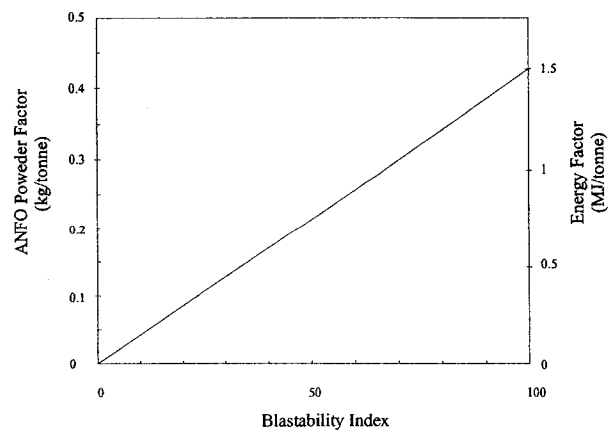
$$BI = 0.5(RMD + JPS + JPO + SGI + H)$$

where RMD is the rock mass description, JPS is the joint plane spacing, JPO is the joint plane orientation, SGI is the specific gravity influence and H is the hardness. The parameters and their associated ratings are given in Table A-3. The form of Lilly's blastability index is shown in Figure A-6. It results in a recommended powder factor for use in subsequent blast design. This approach determines the optimum powder factor in

Table A-3: Ratings for blastability index parameters (Lilly, 1986)

Parameter	Rating
<i>Rock Mass Description (RMD)</i>	
• Powdery/Friable	10
• Blocky	20
• Totally Massive	50
<i>Joint Plane Spacing (JPS)</i>	
• Close (<0.1m)	10
• Intermediate (0.1 to 1.0m)	20
• Wide (>1.0m)	50
<i>Joint Plane Orientation (JPO)</i>	
• Horizontal	10
• Dip out of face	20
• Strike normal to face	30
• Dip into face	40
<i>Specific Gravity Influence (SGI)</i>	
SGI = 25 SG – 50 (where SG is in tones/cubic meters)	
<i>Hardness (H)</i>	1 to 10

Figure A-6: Lilly's blastability index vs. Powder factor and Energy Factor (Lilly, 1986)



kilogram per tone of ore or in terms of an energy factor (MJ per tone of ore) to suit a rock mass with a pre-calculated blastability index.

### A.2.2. Limitations of the Conventional Blast Design Approaches

The blast design approaches described above are used in one form or another at most mines. However, they have several important limitations. In general, all these approaches are site specific and have limited applications to certain geological conditions using a particular type of explosive(s) used in mine blasting operations. In addition, each blast design criterion has its own limitation as briefly described in following.

*S/B ratio:* S/B ratio, although is commonly used in surface and underground blast design, it has some serious deficiencies in that it does not take into account:

- structural properties and rock mass parameters other than specific gravity and some so-called rock constants,
- dynamic characteristics of the rock mass, i.e. ability of a rock to absorb or transmit energy,
- the stiffness or inherent breakage characteristics of the rock i.e. whether the rock behaves plastically or is brittle,
- the effect of blasthole timing (delay detonation) which is now recognized as having a strong influence on rock breakage and therefore fragmentation.

*Powder Factor and Blastability Criteria:* The aspects of powder factor-based designs or those driven by the current blastability indices require further development.

In design, the term powder factor is ambiguous. A different combination of blasthole diameter, burden, spacing and explosive type can give the same powder factor but with significantly different blasting results.

In ring blasting, the concept of average powder factor has no meaning because of the geometry of holes in a ring. The powder factor at the toe is not the same as that in the mid-ring region or the collar.

The blastability index of Lilly (1986) is vague and not clear as to how it accounts for the different factors affected by the blasting operations.

The blastability index is also empirical and is obtained based on a limited number of case studies, therefore, it is only applicable to similar geological conditions and for certain rock properties. Any attempt to apply this approach to new geological and mining environment would require verification of the application of the empirical approach to new geological conditions.

The blastability indices do not take into account the dynamic characteristics of the rock mass, the behavior of the rock mass under transient cyclic loading, the dynamic nature of the applied load, its damping characteristics, the orientation of the applied cyclic load and the orientation of the dominant rock joints.

The blastability indices do not take into account the effect of blast timing, the inter-hole delay timing, delay timing between blastholes in a row and delay timing between rows of blastholes in surface and underground mining operations.

More importantly, the two approaches do not provide a logical path or methodology to optimize the blast design if the results from the initial parameters are unacceptable. It is also important to note that most of the design formulae discussed above were originally developed for parallel-hole blasts in open pit mines rather than for ring configurations.

### ***A.3. Engineering Models of Rock Fragmentation***

It is well recognized that fragmentation of rock depends on its properties, distribution of faults, geometry of the opening, the type, amount and the distribution of explosives used (Valliappan et al., 1983). When a confined explosive charge detonates, it creates a radially expanding stress wave in the surrounding rock mass. The blast energy is responsible for fragmentation by crack initiation in the immediate vicinity of the explosive column. The remaining component of the explosive energy, high pressure gases also called heave energy, is responsible for extending some of the induced cracks generated by the stress wave, creating fragmentation and very importantly, providing displacement and hence looseness of the broken rock.

Hagan (1983) investigated the influence of controllable blast parameters on fragmentation and mining costs. He stated that fragmentation has the greatest effect upon mining costs through the shape and looseness of the muckpile. A tight muckpile, even if exhibits an excellent fragmentation, may lead to higher loading and hauling costs. Blasthole diameter,  $d$ , directly affects the resulting rock fragmentation. Where  $d$  is small, the costs of drilling, priming and initiation are high, and charging, stemming and connecting-up operations are time-consuming and/or labor intensive. Where  $d$  is too

large, the correspondingly large blasthole pattern may well lead to inadequate fragmentation, especially in rocks, which contain widely spaced open discontinuities (e.g., joints). It is however, notable that small blasthole diameter may lead to more fine material than needed and wasting of explosive and drilling material. Blasthole alignment, among other effects, often leads to increased fragmentation and muckpile looseness. Inclined blastholes are more difficult to drill, but provide better fragmentation, smoother final faces and eliminate excessive front row toe burdens. Blasthole length also affects degree of fragmentation in such a way that if blastholes are too long, both B and S will exhibit considerable variability leading to an excessive fragmentation. Where B or S is excessive, fragmentation will be sub-optimum. In open pits, bench height, H, and blasthole diameter, d, should be such that the driller has a high degree of control over blasthole deviation and, hence, over B and S. To obtain a maximum effective rock fragmentation, explosive charges should be fully coupled and should provide a peak blasthole Pressure ( $P_i$ ) that just fails to cause crushing. In addition to generating sufficiently intense stress waves, explosives must provide enough heave energy (gas pressure) to create the required displacement for a loose and, therefore, highly diggable muckpile. Charge distribution also affects the blasting costs. The charge within each blasthole should be distributed such that its cost-effectiveness in fragmenting and loosening the strata is maximized. Where blastholes are short, continuous charges should be used, as these are more practical and cost-effective than deck charges. However, in long blastholes, highest technical efficiency (but not necessarily cost-effectiveness) is achieved with deck charges. The length of stemming decks should increase with decreases in the effective strength of the rock. The effect of initiation sequence is also

reflected in the burden (B) and blasthole spacing (S). According to Hagan (1983), the S/B ratio should remain in between 3.3 to 4.0 to produce a good fragmentation. Finally, blast geometry affects rock fragmentation through the shape and condition of the face, the available expansion volume, the blasthole pattern, effects of burden and spacing, stemming, subdrilling and backfill and size and shape of the blast.

A number of engineering models of rock fragmentation have been proposed over the last two decades. The most notable is the KUZ-RAM model that is an empirical fragmentation model and was developed by Cunningham (1983). He further modified his initial model to adapt to actual rock fragmentation observed in the mines (Cunningham, 1987). In this model, Kuznetsov's (1973) approach to find the mean fragment size ( $K_{50}$ ) is combined with Rosin-Rammler curve (Rosin et al., 1933; Just, 1979) to obtain the distribution of fragmented rock. Kuznetsov made measurements of fragment size from a large number of blasts and found that the following equation gave a reasonably valid estimation of the mean fragment size:

$$\bar{x} = A \left( \frac{V_0}{Q} \right)^{0.8} Q^{0.167} \quad (\text{A-1})$$

where  $\bar{x}$  is the mean fragment size, also called  $K_{50}$ , that is the mesh size through which 50% of the rock fragments will pass. A is the rock factor and is proposed to be 7 for medium rocks, 10 for hard, highly fissured rocks, and 13 for very hard, weakly fissured rocks (Cunningham, 1983). Q is the mass of explosive charge equivalent in energy to TNT in one blasthole, and  $V_0$  is volume of rock defined by the burden times spacing



times bench height. It has been found that in practice KUZ-RAM model gives realistic results under a variety of conditions. Further experience with this equation has shown that it is particularly good when comparing the effect of different blasting techniques in the same rock type (Barron, 1997). However, in these cases, the difficulty is posed by selecting the parameter A. In these circumstances, a rough guess of A is made and if the results differ significantly from the field results, then A can be adjusted to fit the field results and the revised value will be used in any ensuing calculations for this same rock type.

Equation (A-1) is based on the TNT based explosives and has been modified for ANFO based products. The mean fragment size,  $\bar{x}$  or  $K_{50}$ , in this form is given by:

$$\bar{x} = A \left( \frac{V_0}{Q} \right)^{0.8} Q^{0.167} \left( \frac{E}{115} \right)^{-19/30} \quad (\text{A-2})$$

where E is the relative weight strength of the explosive.

Rosin et al. (1933) proposed an empirical mathematical relationship to predict fragment size distribution for a given blast. This formula is given by:

$$R = e^{-\left(\frac{x}{x_c}\right)^n}$$

where R is the mass fraction larger than 'x' ('1-R' indicates the proportion of broken rock that passes through mesh). 'x' is the diameter of the fragment, 'x<sub>c</sub>' is the characteristic

size and 'n' is the Rosin-Rammler exponent of uniformity. The characteristic size,  $x_c$ , is a mathematical point of no significance, it merely fixes the point on the curve where  $x = x_c$  (Barron, 1997). It is the point on the Rosin-Rammler curve where 37% of the rock is larger than  $x_c$ , or 63% of the rock passes the mesh size. The exponent 'n', gives the shape of the curve through  $x_c$ . The higher the value of 'n', the less widely spread are the fragment sizes. Figure A-7 shows the two typical Rosin-Rammler curves for blasting, in which characteristic size,  $x_c$ , is the same but each has a different exponent 'n' (Barron, 1997). The difficulty in using this technique has been how to find the characteristic size, ' $x_c$ ', and the exponent of uniformity 'n'.

Cunningham (1983) combined the Kuznetsov's (1973) equation with Rosin-Rammler (1933) curve to find the characteristic size,  $x_c$ . According to Cunningham (1987), Kuznetsov's mean fragment size,  $K_{50}$ , would be a point on the Rosin-Rammler's fragmentation distribution curve. Having mean fragment size for particular blasting from either Equation (A-1) or (A-2), one could find the characteristic size for R equal 50% in terms of exponent of uniformity, as following:

$$0.50 = e^{-\left(\frac{\bar{x}}{x_c}\right)^n}$$

$$x_c = \frac{\bar{x}}{(0.693)^{1/n}}$$

Cunningham (1983) further developed an algorithm, which derives the exponent of uniformity, 'n', in Rosin-Rammler equation from blasting parameters. The initial algorithm developed is given by:

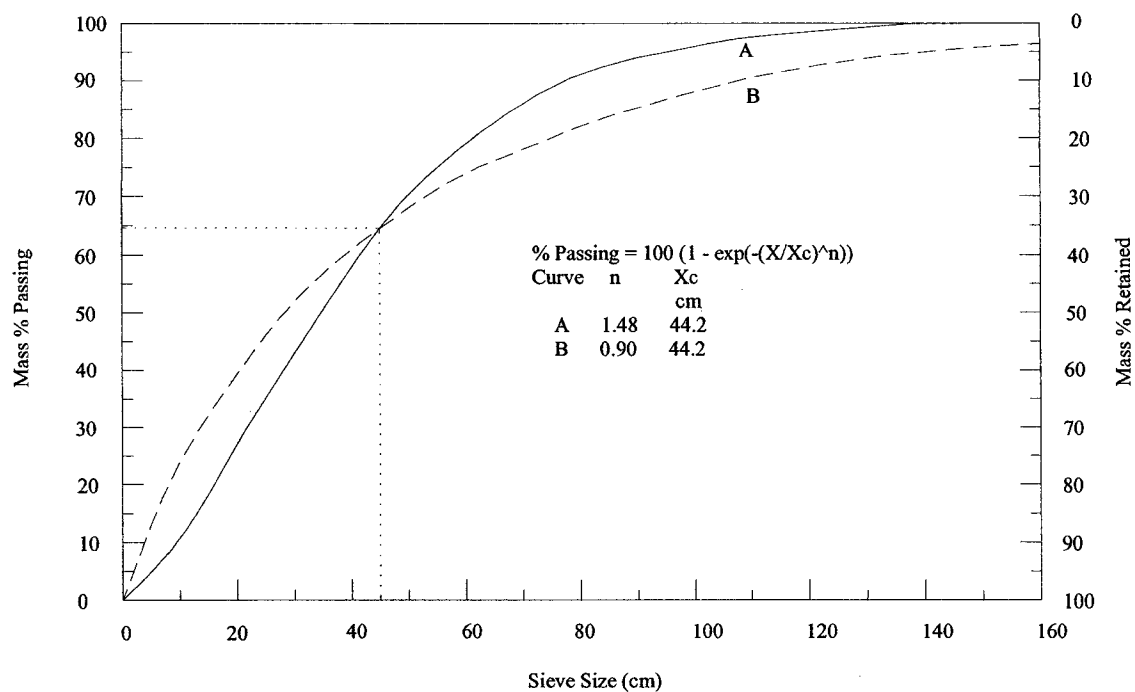


Figure A-7: Two typical Rosin-Rammler curves for blasting (Barron, 1997)

$$n = \left( 2.2 - \frac{14B}{d} \right) \left( 1 - \frac{S_d}{B} \right) \left( \frac{1 + S/B}{2} \right) \left( \frac{L}{H} \right)$$

where B is burden (m), d is the blasthole diameter (mm),  $S_d$  is the standard deviation of drilling accuracy (m), S is the blasthole spacing, L is the charge length above grade level (m), and H is the bench height. Drilling accuracy is normally taken to have a standard deviation between 0.3m to 1.0m depending on the blasthole length, angle of drilling and local conditions (Barron, 1997). Cunningham (1987) further adjusted his initial expression for exponent of uniformity, 'n', for bench height, different explosives in the blasthole, and spacing to burden ratio (S/B). The new equation for 'n' is given by:

$$n = \left( 2.2 - \frac{14B}{d} \right) \left( 1 - \frac{S_d}{B} \right) \left( \frac{1 + S/B}{2} \right)^{0.5} \left( \frac{\text{abs}(BCL - CCL)}{L} + 0.1 \right)^{0.1} \left( \frac{L}{H} \right)$$

where BCL is the bottom charge (explosive No. 1) length (m), and CCL is the column charge (explosive No. 2) length (m).

Cunningham (1983) further added that the exponent of uniformity, n:

- increases, as burden to blasthole diameter ratio (B/d) decreases;
- decreases, as drilling accuracy increases. Drilling accuracy is expressed as the ratio of the standard deviation of the blasthole position at the grade level to the burden.
- increases, as the ratio of the charge length to bench height increases;

- increases, as spacing to burden ratio (S/B) increases;
- increases by 10% if blastholes are laid out in a staggered pattern as opposed to a rectangular pattern.

Knowing blast geometry, and explosive types used and having determined Rosin-Rammler's characteristic size, ' $x_c$ ', and exponent of uniformity, ' $n$ ', one can readily find the fragment size distribution that would produce a particular mean fragment size in a given blasting operation.

Cunningham (1987) applied the concept of blastability index developed by Lilly (1986) to the KUZ-RAM model. He modified and applied Lilly's rock mass rating system, which makes use of both rock strength and jointing factors, into his model to develop an algorithm to determine rock factor,  $A$ , used in Kuznetsov's equation, as following:

$$A = 0.06(RMD + JF + RDI + HF)$$

where,  $A$  is the rock factor to be determined. Other parameters are given in Table A-4.

Fragmentation analyses, photographically obtained, were carried out by Lean et al. (1981) in an Australian coal mine and the results were compared with KUZ-RAM model. Their results showed that KUZ-RAM model gives extremely good correlation in predicting coarse proportion of fragmented rock, but predicts rather more fines that are given by the photographic analysis. They, however, pointed out that the proportions of the fines might be underestimated by the photographic method, so the KUZ-RAM model may be nearer to the truth. Cunningham (1983) reported that KUZ-RAM model has been

Table A-4: Parameter values used to evaluate Factor A (Cunningham, 1987)

Parameter	Score
A = Rock Factor	
RMD = Rock Mass Description	
▪ Powdery/Friable	10
▪ Vertically Jointed	JF
▪ Massive	50
JF = JPS + JPA	
JPS = Vertical Joint Spacing	
▪ 0.1 m	10
▪ 0.1 to MS	20
▪ MS to DP	50
MS: Oversize (m), DP: Drilling Pattern (m) Assuming DP > MS	
JPA = Joint Plain Angle	
▪ Dip out of face	20
▪ Strike perpendicular to face	30
▪ Dip into face	40
RDI = Density Influence: $RDI = 25 \times RD - 50$ (RD = Density, t/m <sup>3</sup> )	
HF = Hardness Factor: $If Y < 50 \text{ GPa}, HF = Y / 3$ $If Y > 50 \text{ GPa}, HF = UCS / 5$ (UCS in MPa)	

predicting coarse proportion of fragmented rock, but predicts rather more fines that are given by the photographic analysis. They, however, pointed out that the proportions of the fines might be underestimated by the photographic method, so the KUZ-RAM model

may be nearer to the truth. Cunningham (1983) reported that KUZ-RAM model has been used extensively in South African mining conditions with much success and has given designs and analyses which have proved realistic over the complete range of blasthole diameters and explosive types.

Despite its successful application in practice, Cunningham (1983) reported a number of limitations on the KUZ-RAM model. These are i) the S/B ratio applies to the drilling and blast pattern only, and do not consider the blasting sequence and delayed detonation timing, and should not exceed 2, ii) the explosive should yield energy close to its calculated Relative Weight Strength, iii) the jointing and homogeneity of the ground require careful assessment, as fragmentation is often built into the rock structure, especially when loose jointing is more closely spaced than the drilling pattern, iv) initiation and timing must be arranged so as to reasonably enhance fragmentation and avoid misfires or cut-offs. According to Persson et al. (1993), short delay blasting would improve rock fragmentation. This is due to, on one hand, the short delay time between firing of consecutive rows is long enough to allow the rock of one row to move away, and the free face of the following row to be uncovered, prior to the detonation of its charges. On the other hand, the short delay time is short enough for the rock from the previous rows to still be hanging in the air at the detonation of the second row, creating an effective curtain to stop rock fragments from the second row from moving with a speed above the average. In addition, collisions between rock fragments moving with different velocities will considerably increase the fragmentation. Rollins et al. (1989) attempted to mimic timing by looking at the contribution of individual blastholes to overall

fragmentation. They reported, however, that the results showed that the effects are not the same as incorporating actual blasthole timing. Results of the experimental investigations by Grant et al. (1991) confirmed the effects of delay timing on rock fragmentation. Significant difference in fragmentation results has been reported in field studies, which is believed to be due to changes in inter-hole delay timing. This is particularly true in massive rocks. For instance, for a given rock type and geological structure there is an optimum inter-hole timing  $\Delta t$  which produces the best fragmentation. The optimal delay time  $\tau$ , i.e., the delay time at which the best fragmentation is achieved, is a function of the burden  $B$  (Persson et al., 1993). According to Langefors et al. (1963), for burden between 0.5 and 8 m,

$$\tau = \kappa B$$

where  $\kappa$  varies between 3 to 5 msec/m of burden. The inclusion of timing effects into existing engineering models of fragmentation would be a significant improvement which should render these models more applicable to practical design problems in mines.

#### ***A.4. Design Stability Charts***

In a study commissioned by the Canadian Department of Energy, Mines and Resources (CANMET) to establish the information required to predict stable spans for open stopes at mining depths below 1000m, Mathews et al. (1981) developed an empirical relation between NGI rock mass rating (Barton et al., 1974), mining depth and stope dimensions. An empirical stability formula was developed based on the analysis of more than 350



case histories collected from Canadian underground mines. In this study, information about the rock mass strength and structure, the stresses around the opening and the size, shape and orientation of the opening is used to determine whether the stope will be stable without support, stable with support, or unstable even if supported. The method also suggests ranges of cable bolt density when design is in the realm of 'stable with support'.

The design procedure is based upon the calculation of two factors,  $N'$ , the modified stability number which represents the ability of the rock mass to stand up under given condition, and  $S$ , the shape factor or hydraulic radius which accounts for the stope size and shape. The stability number,  $N'$ , is defined as

$$N' = Q' \cdot A \cdot B \cdot C$$

where,

- $Q'$  modified Q Tunneling Quality Index
- $A$  rock stress factor,
- $B$  joint orientation adjustment factor
- $C$  design surface orientation factor

The modified Tunneling Quality Index,  $Q'$ , is calculated from the results of structural mapping of the rock mass in exactly the same way as the standard NGI rock mass classification, except that the stress reduction factor SRF is set to 1.00. The rock stress factor,  $A$ , reflects the stresses acting on the free surfaces of open stopes at depth. The

factor is determined from the ratio of unconfined compressive strength of the intact rock over the stress acting parallel to the exposed face of the stope under consideration,  $\sigma_c/\sigma_1$ . The intact rock strength can be determined from laboratory testing of the rock or from estimates such as Hoek-Brown strength criterion (Hoek et al., 1980b; Hoek et al., 1988) or Mohr-Columb criterion (Brady et al., 1993). The induced compressive stress is found from numerical modeling or estimated from published stress distributions such as those in Hoek et al. (1980a), using measured or assumed in-situ stress values. The rock stress factor,  $A$ , is then determined from  $\sigma_c/\sigma_1$  as:

- for  $\sigma_c/\sigma_1 < 2$ :  $A = 0.1$
- for  $2 < \sigma_c/\sigma_1 < 10$ :  $A = 0.1125 (\sigma_c/\sigma_1) - 0.125$
- and for  $\sigma_c/\sigma_1 > 10$ :  $A = 1.0$

The joint orientation adjustment factor,  $B$ , accounts for the influence of joints on the stability of the stope faces. Most cases of structurally controlled failures occur along critical joints, which will form a shallow angle with the free surface ( $\theta$ ). The shallower the angle between the discontinuities and the surface, the easier it is for the bridge of intact rock to be broken by blasting, stress or by another joint set (Hoek et al., 1995). When the angle  $\theta$  approaches zero, a slight strength increase occurs since the jointed rock blocks act as a beam. The influence of the critical joint on the stability of the excavation surface is highest when the strike is parallel to the free surface and smallest when the planes are at right angles to one another.

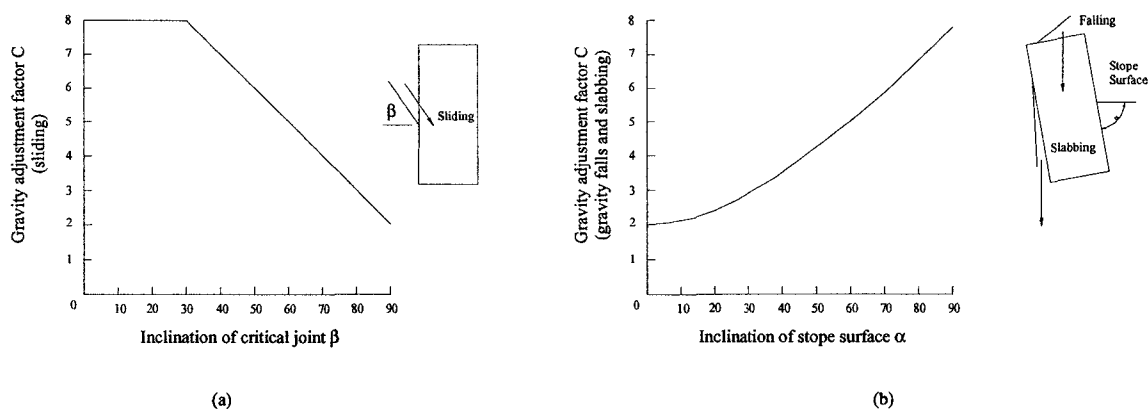


Figure A-8: Gravity adjustment factor C for (a) sliding failure mode, (b) gravity falls and slabbing (Potvin, 1988)

The factor C is an adjustment for the effects of gravity. Failure can occur from roof by gravity induced falls or from the stope walls by slabbing or sliding. According to Potvin (1988) both gravity-induced failure and slabbing failure depend on the inclination of the stope surface,  $\alpha$ . The factor C can be calculated from the relationship,  $C = 8 - 6 \cos\alpha$ . The sliding failure depends on the inclination  $\beta$  of the critical joint, and the adjustment factor C is found from Figure A-8.

*The Shape Factor:* The hydraulic radius, or the shape factor, for the stope surface under consideration, is calculated as follows:

$$S = \text{Cross sectional area of surface analyzed} / \text{Perimeter of surface analyzed}$$

Values of  $N'$  are plotted on a logarithmic scale against the shape factor S, for the surfaces of a number of open stopes in 350 case histories collected from Canadian mines. According to the available data from these mines, the permitted approximate boundaries

between stable, potentially unstable and potentially caving zones are defined on the N-S plot as shown in Figure A-9 (Potvin, 1988; Nickson, 1992).

This approach has found widespread use in practice (Potvin et al., 1992; Potvin et al., 1989; Potvin, 1988; Bawden et al., 1987; Nickson, 1992), as a result of which the original charts have been calibrated based on further experience. Bawden et al. (1987) has shown a modified stability chart specifically developed and calibrated for Noranda Minerals Inc, Canada.

An alternate stability chart was also developed by Diering et al. (1987). It plots Laubscher's (1977; 1984) adjusted rock mass rating against the hydraulic radius or shape factor of the stope surface being considered. The presence of blast-induced damage can be expected to lower the quality of the rock mass as measured by either the NGI Q factor (Barton et al., 1974) or Laubscher's adjusted rock mass rating.

Currently neither of the above empirical methods used in the design of stopes explicitly takes blast damage into account. Laubscher method applies what could effectively be classed as an arbitrary adjustment factor to account for damage via the process described on Table A-5. Under blast dynamic loading in near field region (immediate vicinity of the blasthole) and cyclic loading in mid- to far-field region from the blast location, the resulting applied stress could exceed the resistance of the rock joints or the intact rock

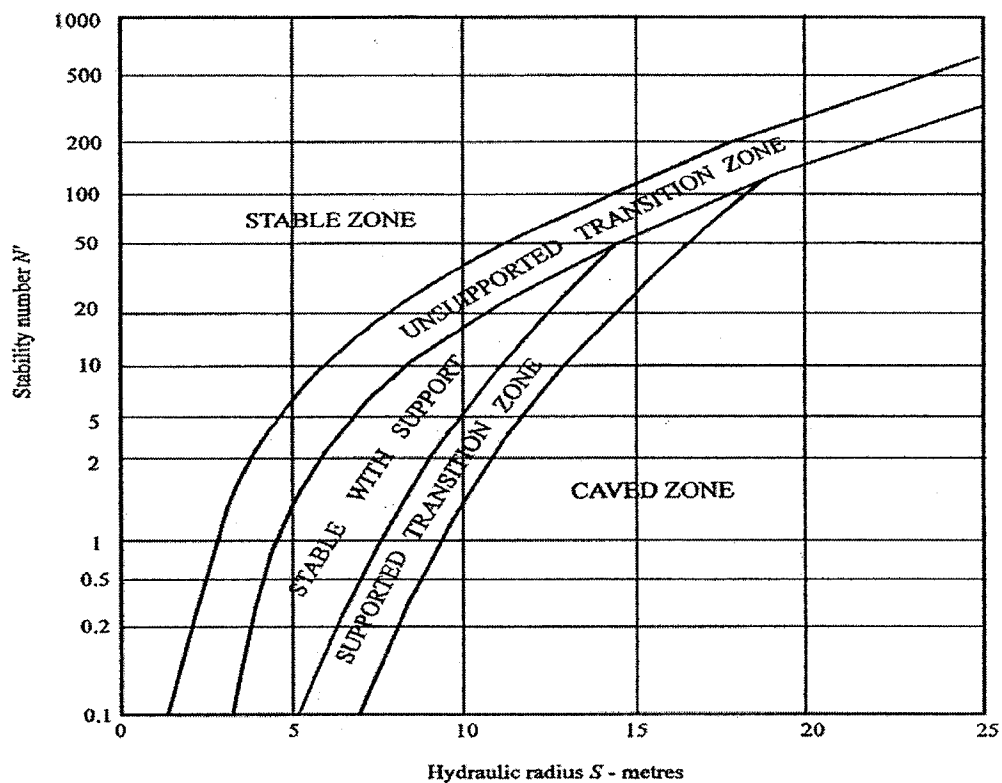


Figure A-9: Stability graph showing zones of stable ground, caving ground and ground requiring support (Potvin, 1988; Nickson, 1992).

Table A-5: Blasting adjustment developed by Laubscher (1984)

Technique	Adjustment, %
Boring	100
Smooth wall blasting	97
Good conventional blasting	94
Poor conventional blasting	80

leading to failure of the rock blocks either by falling, sliding or slabbing. The latter will happen under tensile failure of the rock mass either at joint locations or through the rock mass. If the extent of damage and its effect on excavation performance can be predicted, potential instability or excessive dilution may be prevented by modification to blast design, i.e. blast pattern, type of explosive, delay detonators, etc., excavation and/or support designs.

The approaches described above, generally use a number of rock constants or parameters which infer the characteristics of the rock mass, the geometry between the explosive charge and the point of interest and the amount of explosive.

## Appendix B: Inversion of Cauchy Integral Equation

Muskhelishvili (1953) have investigated singular integral equations of the form:

$$\frac{1}{\pi i} \int_L \frac{\varphi(t) dt}{t - t_0} = f(t_0) \quad (\text{B-1})$$

where  $\varphi(t)$  is the unknown function of the point  $t$  on  $L$  and  $f(t)$  is a known function.  $L$  is the union of smooth, non-intersecting arcs,  $L_1, L_2, \dots, L_p$ , with definite positive directions. For Cauchy integral equation (B-1) to have solution, the functions  $\varphi(t)$  and  $f(t)$  must satisfy Hölder conditions on  $L$ , i.e. they must belong to  $H$  and  $H^*$  classes<sup>1</sup>, respectively.

---

<sup>1</sup> Hölder condition: Function  $\sigma(t)$  satisfies Hölder condition on  $L$  if

$$|\sigma(t_2) - \sigma(t_1)| \leq C |t_2 - t_1|^\alpha$$

where  $t_1$  and  $t_2$  are any two arbitrary points along the smooth arc  $L=ab$  except the end points,  $\alpha$ , called the Hölder index and  $C$ , called Hölder constant, are positive constants. Provided that the function  $\sigma(t)$  satisfies this condition, it is said to belong to Class  $H$ .

Near the end points  $a$  and  $b$  on  $L$ , if the function  $\varphi(t)$  can be defined in the form of (Muskhelishvili, 1953):

$$\varphi(t) = \frac{\varphi^*(t)}{(t-c)^\gamma}, \quad \gamma = \alpha + i\beta, \quad 0 \leq \alpha < 1$$

The inversion of the Cauchy integral to find the unknown function  $\varphi(t)$ , according to Muskhelishvili (1953, p. 249), is as follows.

Consider a sectionally (piecewise) analytic function  $\Phi(z)$ , vanishing at infinity, defined by:

$$\Phi(z) = \frac{1}{2\pi i} \int_L \frac{\varphi(t) dt}{t - z}$$

By Plemelj formula (Muskhelishvili, 1953, p. 43)

$$\Phi^+(t_0) = \frac{1}{2} \varphi(t_0) + \frac{1}{2\pi i} \int_L \frac{\varphi(t) dt}{t - t_0} \quad (a)$$

$$\Phi^-(t_0) = \frac{-1}{2} \varphi(t_0) + \frac{1}{2\pi i} \int_L \frac{\varphi(t) dt}{t - t_0} \quad (b) \quad (B-2)$$

By adding Equations (B-2a) and (B-2b) one obtains:

$$\Phi^+(t_0) + \Phi^-(t_0) = \frac{1}{\pi i} \int_L \frac{\varphi(t) dt}{t - t_0}$$

---

where  $c$  is either of the end points  $a$  or  $b$ ,  $\alpha$  and  $\beta$  are real constants and  $\varphi^*(t)$  satisfies the  $H$  condition near and at  $c$ . Then,  $\varphi(t)$  satisfies the Hölder condition and belongs to class  $H^*$ .



Therefore, the original integral equation (B-1) is equivalent to the problem

$$\Phi^+(t_0) + \Phi^-(t_0) = f(t_0) \quad \text{on } L \quad (\text{B-3})$$

with the additional boundary condition,  $\Phi(\infty) = 0$ . Equation (B-3) is known as the Hilbert problem for the case of arcs whose general solution consists of a homogeneous solution and a particular solution.

By subtracting Equation (B-2b) from Equation (B-2a), one finds:

$$\Phi^+(t_0) - \Phi^-(t_0) = \varphi(t_0) \quad (\text{B-4})$$

Having  $\Phi(z)$  from the solution of Equation (B-3),  $\varphi(t)$  can be found from Equation (B-4).

Considering Hilbert problem of Equation (B-3), Muskhelishvili (1953, section 84, p. 239) showed that homogeneous solution of Hilbert problem of the form:

$$\Phi^+(t_0) + \Phi^-(t_0) = 0$$

is given by:

$$X(z) = C \frac{\sqrt{R_1(z)}}{\sqrt{R_2(z)}} = C \sqrt{\frac{R_1(z)}{R_2(z)}}$$

for 'class  $h^2$ ', where  $C$  is an arbitrary non-zero constant and  $R_i(z)$ ,  $i=1,2$  is given by:

$$R_1(z) = \prod_{j=1}^q (z - c_j), \quad R_2(z) = \prod_{j=q+1}^{2p} (z - c_j)$$

where  $q$  is the number of end points at which density function  $\varphi(x)$  remain bounded and  $p$  is the number of segments that form the integration domain  $L$  ( $2p-q$  is the remaining number of end points at which  $\varphi(x)$  may be unbounded).  $c_j$  are the end points of each arc (segment). The general solution of the class  $h$  of the non-homogenous Hilbert problem (Equation B-3) is therefore given by Muskhelishvili (1953):

$$\Phi(z) = \frac{1}{2\pi i} \sqrt{\frac{R_1(z)}{R_2(z)}} \int_L \sqrt{\frac{R_2(t)}{R_1(t)}} \frac{f(t)dt}{(t-z)} + \sqrt{\frac{R_1(z)}{R_2(z)}} Q_{p-q-1}(z) \quad (\text{B-5})$$

---

<sup>2</sup> A problem is called of class  $h(c_1, c_2, \dots, c_q)$ , where  $c_i$  could be either ends of each arc, if the unknown solution is bounded at non-special ends, i.e.,  $c_1, c_2, \dots, c_q$ . Note that special ends are those at which solution is NOT bounded. The class corresponding to  $q=0$  is called  $h_0$  which contains all other classes. If the class contains 'm' non-special ends i.e.,  $c_1, c_2, \dots, c_m$ , it is called class  $h_m$ . Such class  $h_m$  is a subclass of all other classes (Muskhelishvili, 1953, p.239). In short, a problem that has bounded solutions at  $c_i$ , is called of class  $h_i$ .

where  $Q_{p-q-1}(z)$  is an arbitrary polynomial of degree not greater than  $(p-q-1)$ . Now having  $\Phi(z)$ , using Equation (B-4), one can find  $\varphi(t_0)$ .

By using Plemelj formula again:

$$\Phi^+(t_0) = \frac{1}{2\pi i} \left[ \sqrt{\frac{R_1(t_0)}{R_2(t_0)}} \right]^+ \int_L \sqrt{\frac{R_2(t)}{R_1(t)}} \frac{f(t)dt}{(t-z)} + \frac{1}{2} \left[ \sqrt{\frac{R_1(t_0)}{R_2(t_0)}} \right]^+ Q_{p-q-1}(t_0) \quad (a)$$

$$\Phi^-(t_0) = \frac{1}{2\pi i} \left[ \sqrt{\frac{R_1(t_0)}{R_2(t_0)}} \right]^- \int_L \sqrt{\frac{R_2(t)}{R_1(t)}} \frac{f(t)dt}{(t-t_0)} + \frac{1}{2} \left[ \sqrt{\frac{R_1(t_0)}{R_2(t_0)}} \right]^- Q_{p-q-1}(t_0) \quad (B-6)$$

$$= \frac{-1}{2\pi i} \left[ \sqrt{\frac{R_1(t_0)}{R_2(t_0)}} \right]^+ \int_L \sqrt{\frac{R_2(t)}{R_1(t)}} \frac{f(t)dt}{(t-t_0)} - \frac{1}{2} \left[ \sqrt{\frac{R_1(t_0)}{R_2(t_0)}} \right]^+ Q_{p-q-1}(t_0) \quad (b)$$

By subtracting Equation (B-6b) from Equation (B-6a), one obtains:

$$\Phi^+(t_0) - \Phi^-(t_0) = \frac{1}{\pi i} \sqrt{\frac{R_1(t_0)}{R_2(t_0)}} \int_L \sqrt{\frac{R_2(t)}{R_1(t)}} \frac{f(t)dt}{(t-t_0)} + \sqrt{\frac{R_1(t_0)}{R_2(t_0)}} Q_{p-q-1}(t_0) \quad (B-7)$$

Comparing Equation (B-7) with Equation (B-4), the unknown function  $\varphi(t)$  is determined as:

$$\varphi(t_0) = \frac{-1}{\pi^2} \sqrt{\frac{R_1(t_0)}{R_2(t_0)}} \int_L \sqrt{\frac{R_2(t)}{R_1(t)}} \frac{f(t)dt}{(t-t_0)} + \sqrt{\frac{R_1(t_0)}{R_2(t_0)}} Q_{p-q-1}(t_0) \quad (B-8)$$

RHS of the Equation (B-8) is already multiplied by  $\left(\frac{1}{\pi i}\right)$  to account for the corresponding term in the LHS of the Cauchy integral equation (B-1).

Equation (B-8) is the inversion of the Cauchy integral equation (B-1) in general form. For  $q=2p$ , which corresponds to having the density function  $\varphi(t)$ , bounded at all end points, we get:

$$Q_{p-q-1}(t_0) \equiv 0 \quad \text{since } p - q < 0$$

Since  $p-q < 0$ , a unique solution bounded at the end points exists if and only if the known function  $f(t)$  satisfies the condition (Muskhelishvili, 1953, Head et al., 1955):

$$\int_L \sqrt{\frac{R_2(t)}{R_1(t)}} t^n f(t) dt = 0, \quad \text{for } n = 0, 1, \dots, (q - p - 1), \dots \quad (\text{B-9})$$

This condition forms the boundary condition at the end of plastic zone and is further simplified as follows. For  $q=2p$ , we also get:

$$R_1(z) = \prod_{j=1}^{q=2p} (z - c_j) = R(z), \quad R_2(z) = \prod_{j=q+1}^{2p} (z - c_j) = 1$$

if  $p=1$ , meaning  $L$  consists of only one segment (arc), then

$$R_1(z) = R(z) = (z - a)(z - b), \quad R_2(z) = 1$$

where  $a$  and  $b$  are the end points of the segment over which integral is taken. Substituting  $Q_{p-q-1}(t_0)$ ,  $R_1(z)$  and  $R_2(z)$  into Equation (B-8), we get:

$$\varphi(t_0) = \frac{-1}{\pi^2} \frac{\sqrt{R(t_0)}}{C} \int_L \frac{C}{\sqrt{R(t)}} \frac{f(t) dt}{(t - t_0)} \quad (\text{B-10})$$

Equation (B-10) is the inversion of the Cauchy integral equation where domain of the integral is defined over a single segment (arc) provided that  $f(t)$  satisfies the conditions of Equation (B-9).

To make notations more convenient and correspondent to notations in Equation (B-1), the Equation (B-10) is re-written, after re-arrangement, as given below:

$$\varphi(t) = \frac{-\sqrt{R(t)}}{\pi^2} \int_L \frac{f(t_0) dt_0}{\sqrt{R(t_0)}(t_0 - t)} \quad (\text{B-11})$$

For this case, since  $p=1$  and  $q=2p$ , then  $n=0$ , the boundary condition (B-9) is reduced to:

$$\int_L \frac{f(t) dt}{\sqrt{R(t)}} = 0, \quad (\text{B-12})$$

Cauchy integral equation (B-1) has also been inverted by Bilby et al. (1968, p.173-175) in a less rigorous method using real variable analysis. This derivation is only applicable to the case where a series of cracks lined up along  $x$ -axis at equal intervals from one another. This solution is based on the BCS solution (Bilby et al., 1963) where for a single crack and is derived using a certain change of variables. For more information on this method refer the original work.

## **Appendix C: Monotonic Loading Solutions**

In this appendix the results of simulation of monotonically loading shear cracks of various sizes are presented. The simulation is carried out for the rock type given in Chapter 6 for the initial crack lengths of 20, 50, 100, 200 and 400 mm. As mentioned in Chapter 6, rock response to various applied loads is investigated using the dislocation model. For each crack length, the dislocation model is run. The effect of applying loads of up to  $0.65\tau_y$  is investigated, where  $\tau_y$  is the yield strength (stress) of the rock. For each given initial crack length, two diagrams are presented, the first one is the plastic displacement distribution ahead of the crack tip and the second one is the shear stress field in the plastic zone.

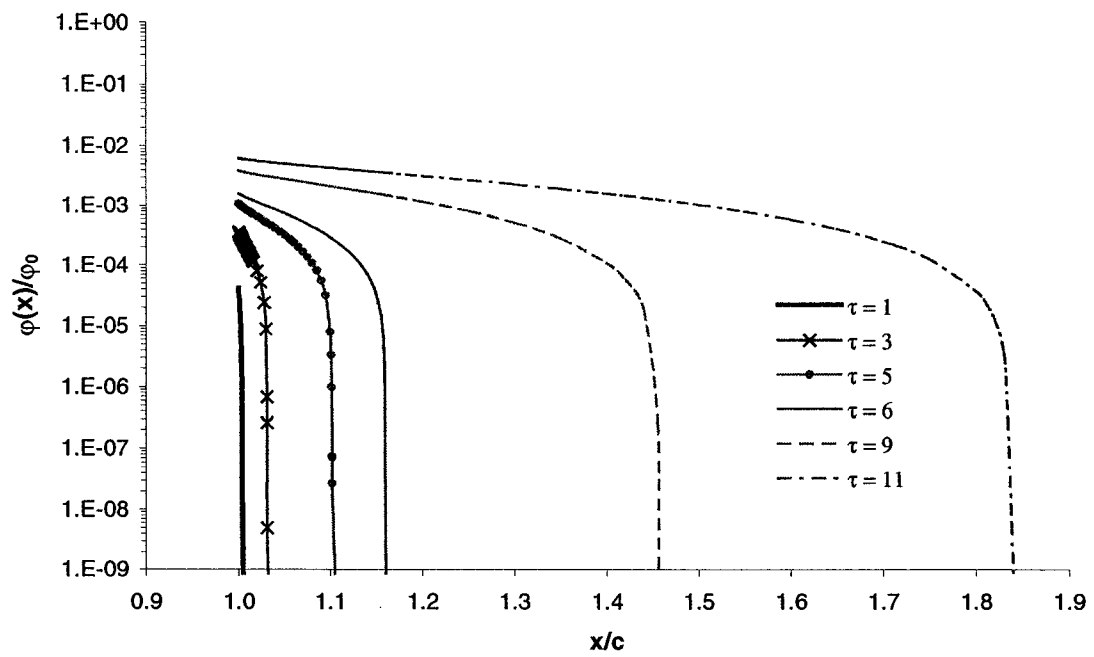


Figure C-1: Non-dimensionalized plastic displacement ahead of crack tip of a 20 mm crack subject to given monotonic loads as given.

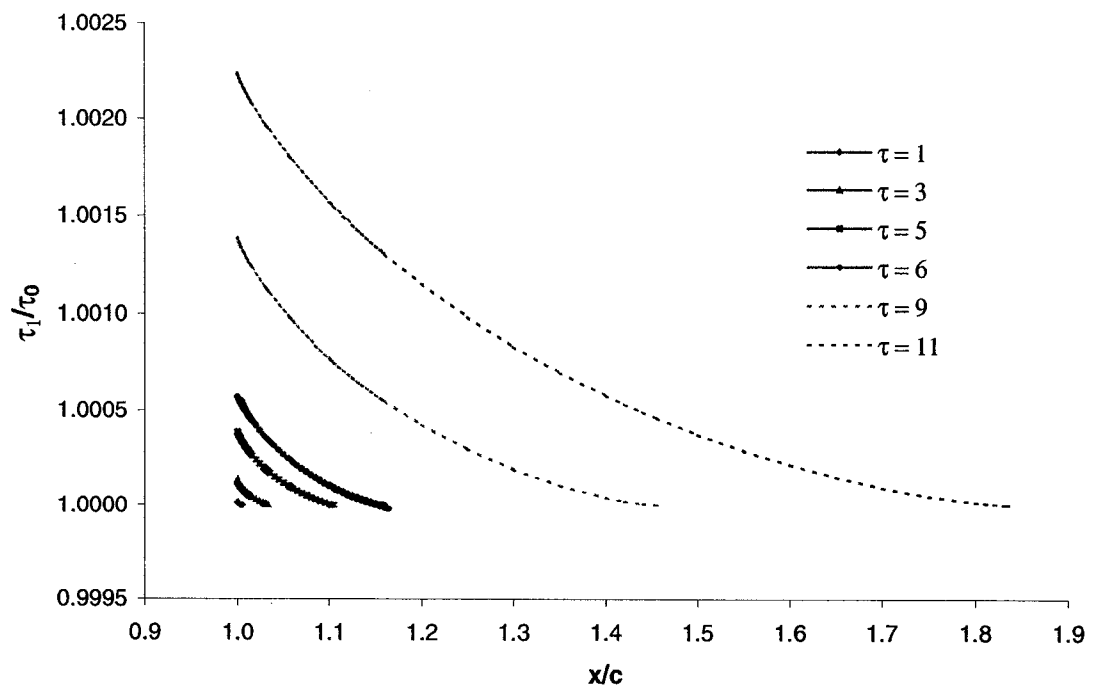


Figure C-2: Non-dimensionalized shear stress field ahead of crack tip of a 20 mm crack subject to given monotonic loads as given.



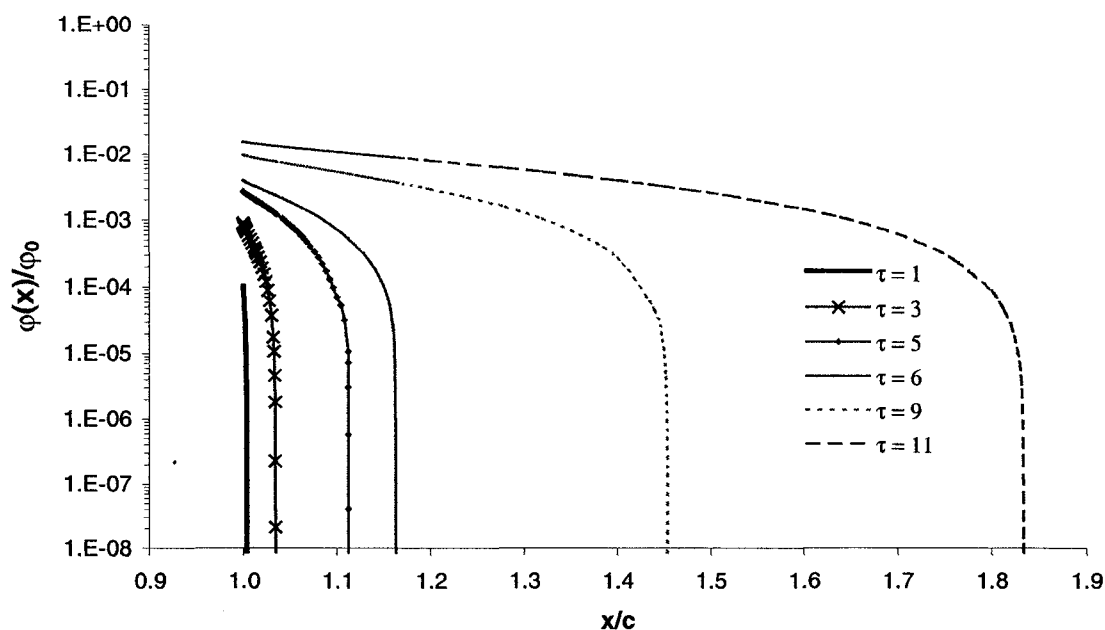


Figure C-3: Non-dimensionalized plastic displacement ahead of crack tip of a 50 mm crack subject to given monotonic loads as given

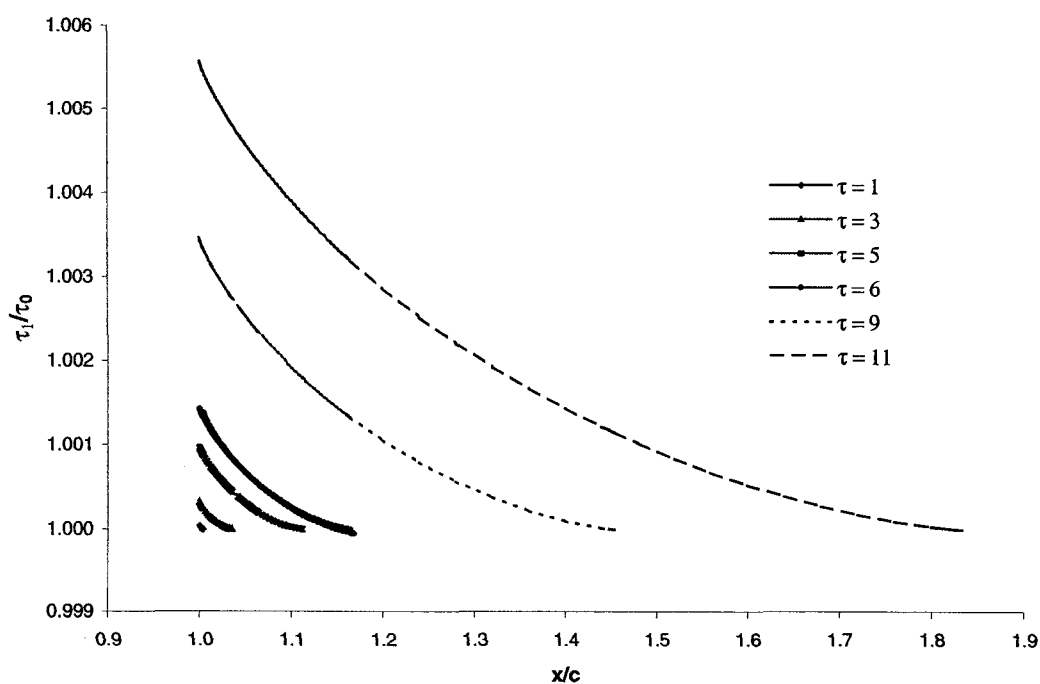


Figure C-4: Non-dimensionalized shear stress field ahead of crack tip of a 50 mm crack subject to given monotonic loads as given

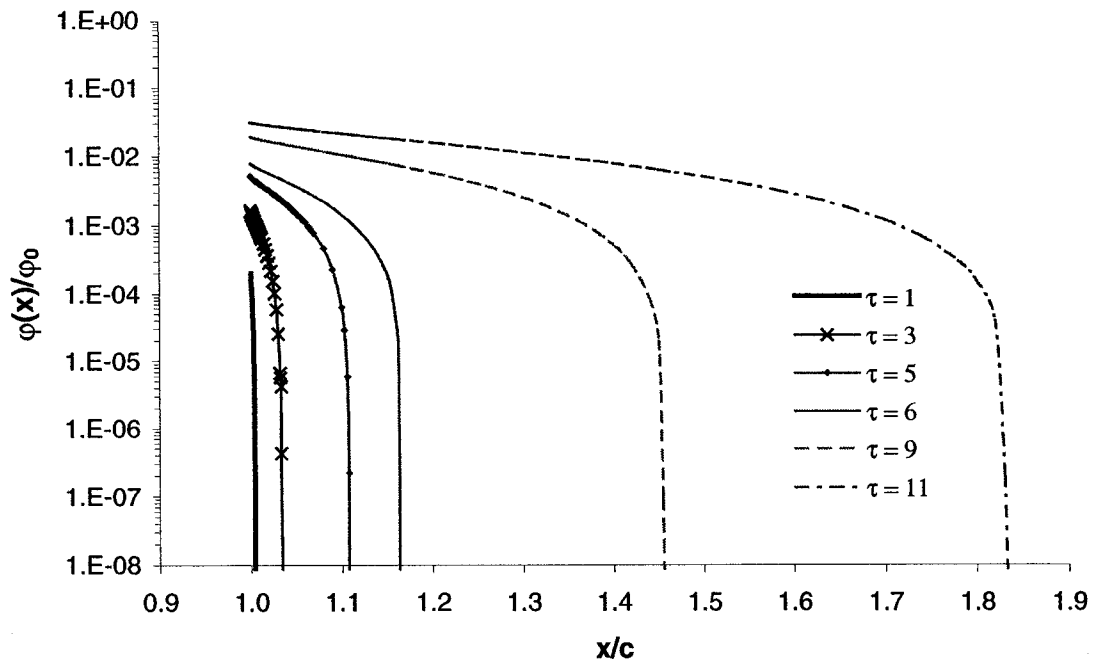


Figure C-5: Non-dimensionalized plastic displacement ahead of crack tip of a 100 mm crack subject to given monotonic loads as given

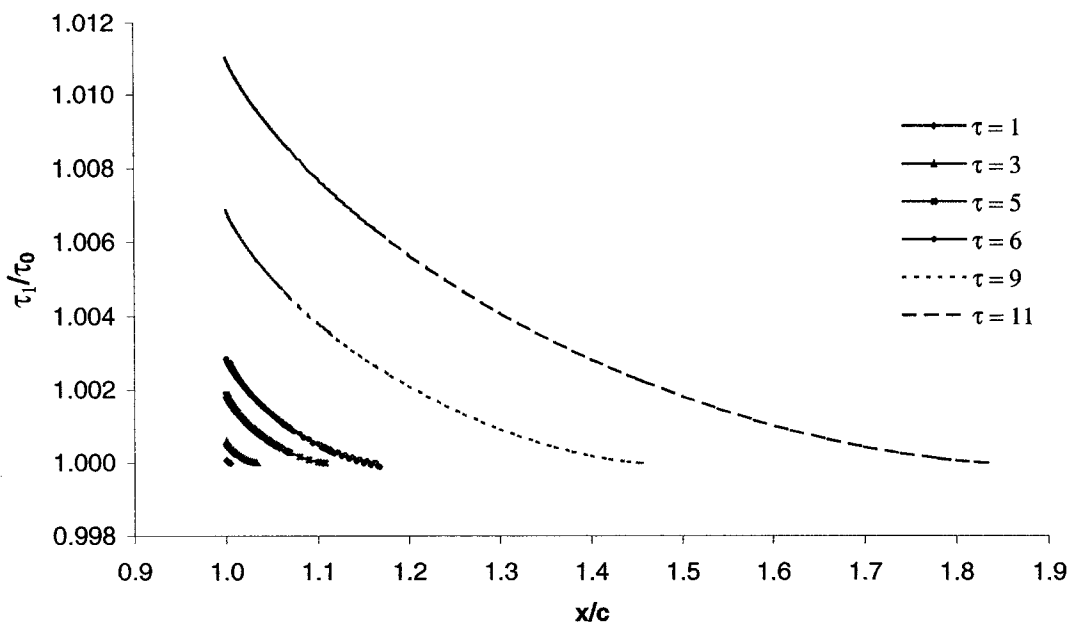


Figure C-6: Non-dimensionalized shear stress field ahead of crack tip of a 100 mm crack subject to given monotonic loads as given

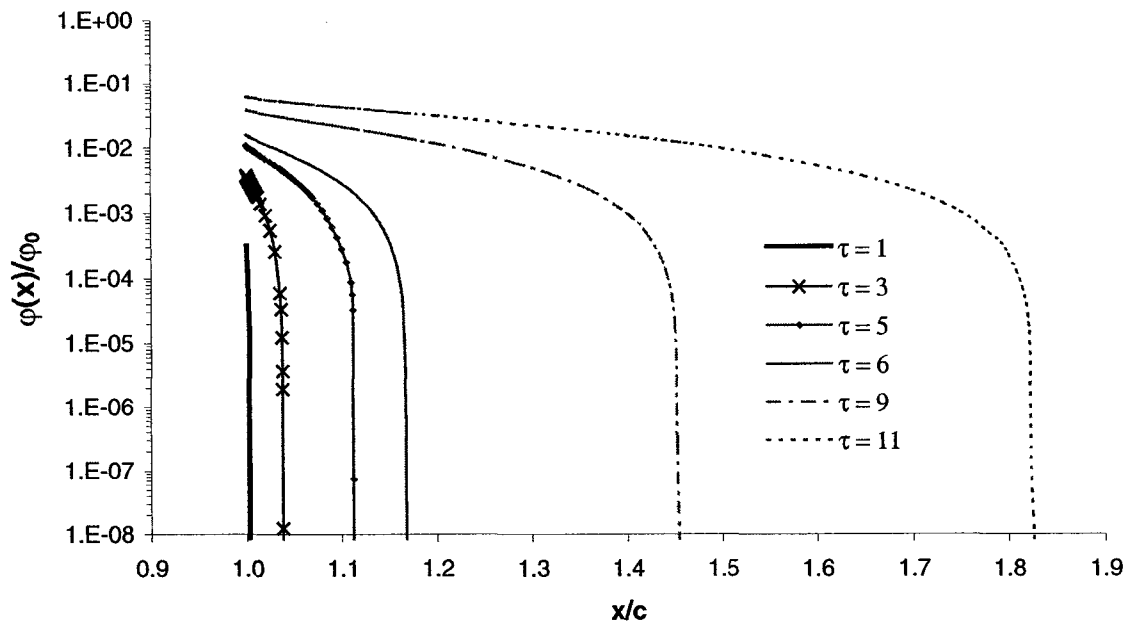


Figure C-7: Non-dimensionalized plastic displacement ahead of crack tip of a 200 mm crack subject to given monotonic loads as given

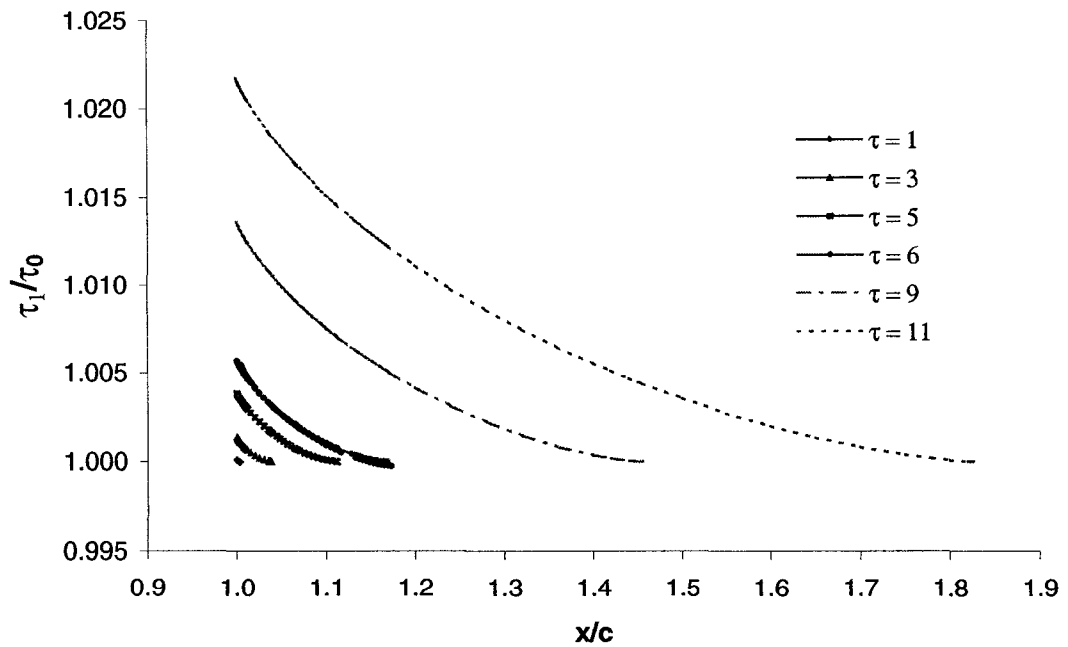


Figure C-8: Non-dimensionalized shear stress field ahead of crack tip of a 200 mm crack subject to given monotonic loads as given

## Appendix D: Unloading Solutions

The results of the simulation of monotonically loading shear cracks of various sizes were presented in Appendix C. In this appendix, the results of the simulation of cyclically loading shear cracks in the rock of the same type given in Chapter 5 are reported. The results of simulation of a 10 mm and a 400 mm crack were reported in Chapter 5. Similar results obtained for cracks of initial lengths of 20 to 1000 mm are presented in this appendix. As mentioned in Chapter 5, rock response to various applied loads is investigated using the dislocation model. The effect of applying loads of up to  $0.65\tau_y$  is investigated, where  $\tau_y$  is the yield strength (stress) of the rock. Then the unloading model is run and rock damage in terms of crack tip plastic displacement is estimated using the dislocation model. The unloading solution is found for five different unloading ratios of  $0.2\tau$ ,  $0.4\tau$ ,  $0.6\tau$ ,  $0.8\tau$  and  $1.0\tau$  (fully reversed loading) where  $\tau$  is the applied monotonic load. The unloading problem is solved for two commonly used plasticity rules, i.e. kinematic hardening and isotropic hardening rules. For each given initial crack length, four diagrams are presented, the first two are the reversed plastic displacement ahead of the crack tip and the reversed shear stress field in the reversed plastic zone, respectively for kinematic hardening rule and the last two diagrams show similar results under isotropic hardening rule.

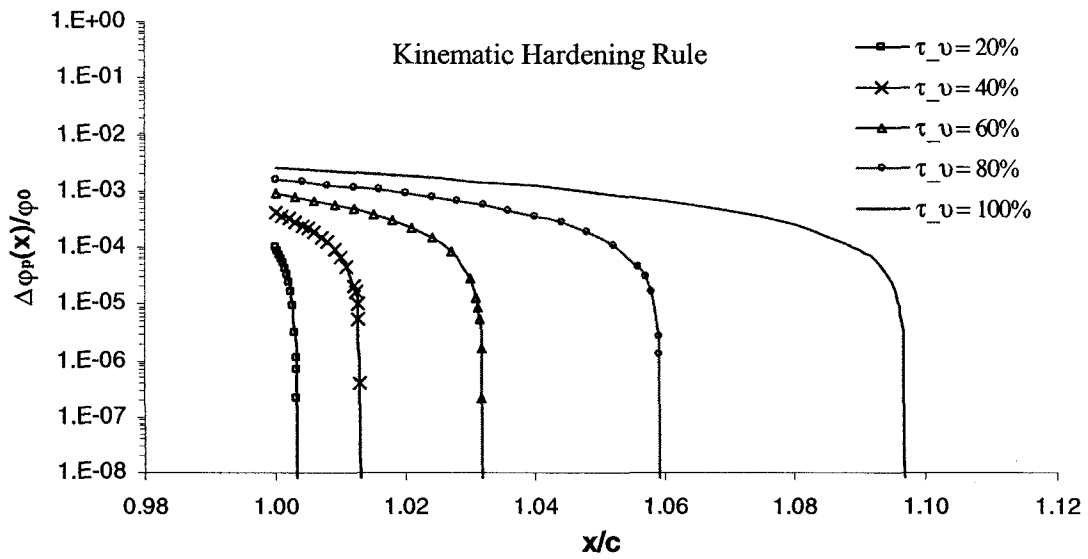


Figure D-1: Reversed plastic displacement versus distance from the crack tip for a loading stress of 11 MPa and unloading stress ratios as shown ahead of a 20 mm crack under kinematic hardening rule

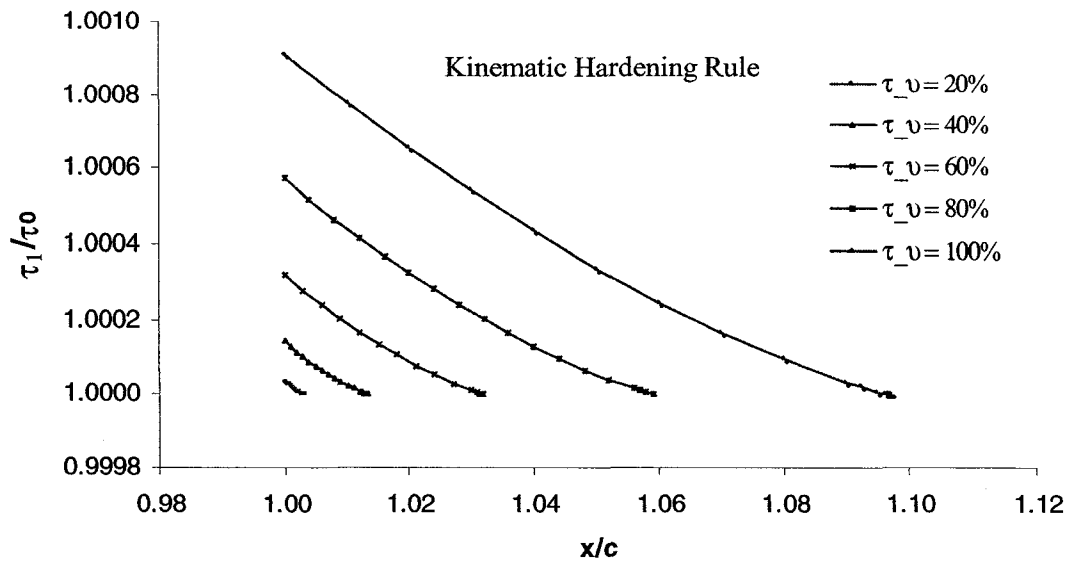


Figure D-2: Reversed crack tip stress field versus distance from the crack tip for a loading stress of 11 MPa and unloading stress ratios as shown ahead of a 20 mm crack under kinematic hardening rule

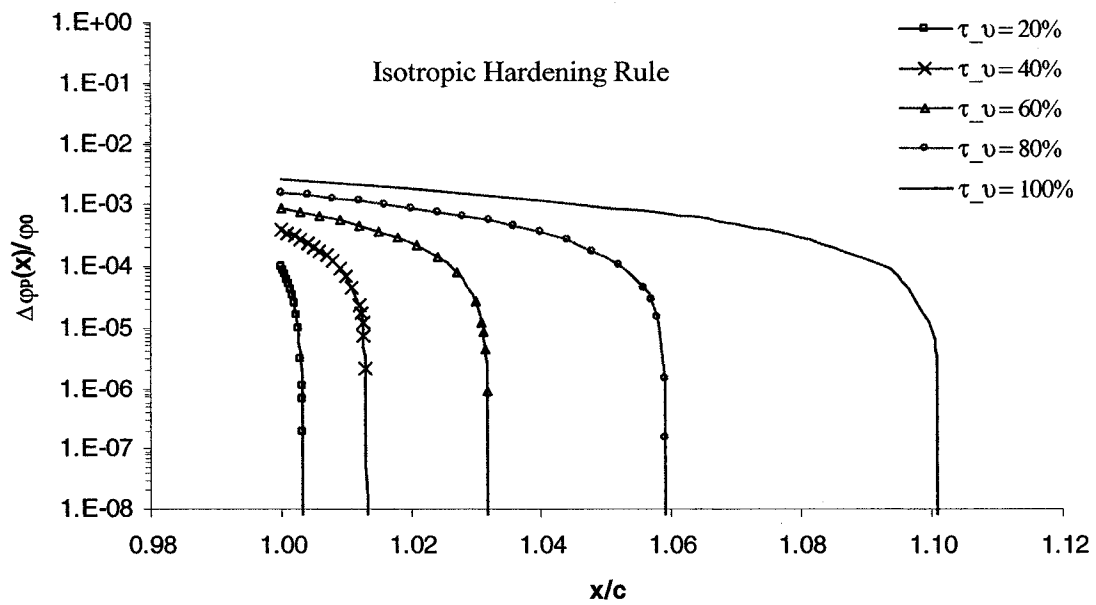


Figure D-3: Reversed plastic displacement versus distance from the crack tip for a loading stress of 11 MPa and unloading stress ratios as shown ahead of a 20 mm crack under isotropic hardening rule

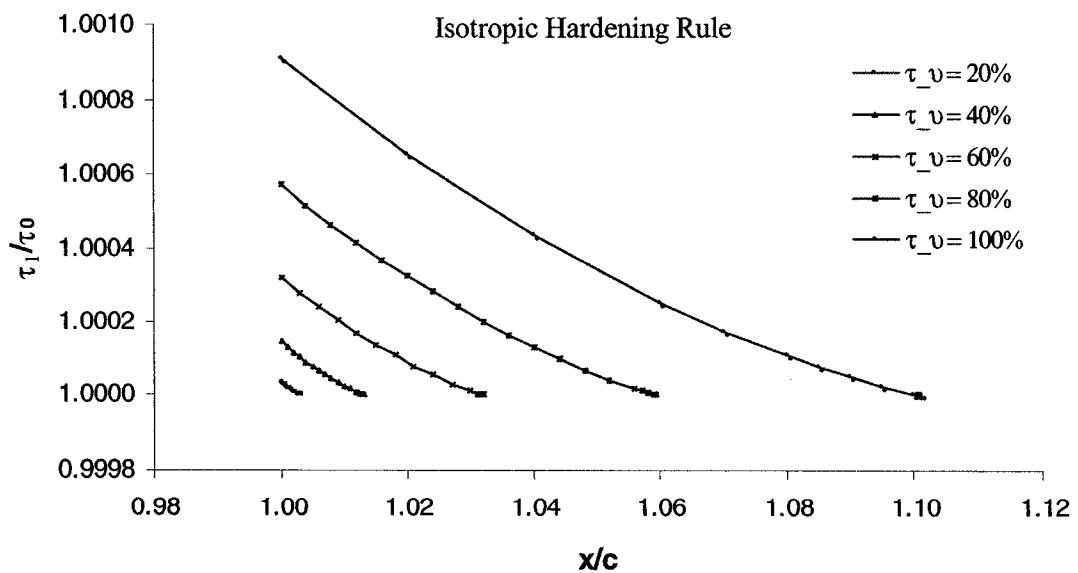


Figure D-4: Reversed crack tip stress field versus distance from the crack tip for a loading stress of 11 MPa and unloading stress ratios as shown ahead of a 20 mm crack under isotropic hardening rule

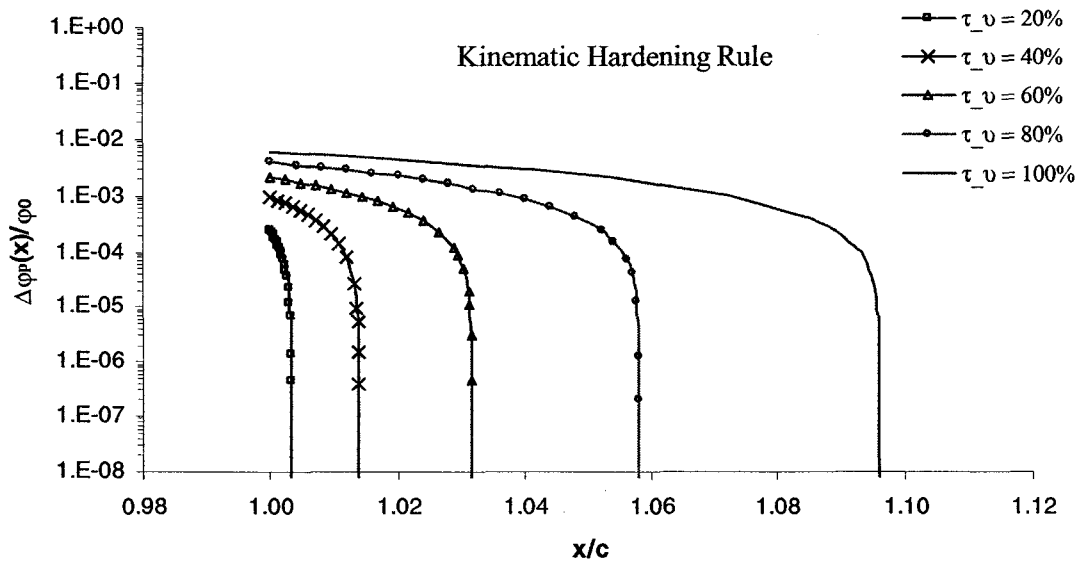


Figure D-5: Reversed plastic displacement versus distance from the crack tip for a loading stress of 11 MPa and unloading stress ratios as shown ahead of a 50 mm crack under kinematic hardening rule

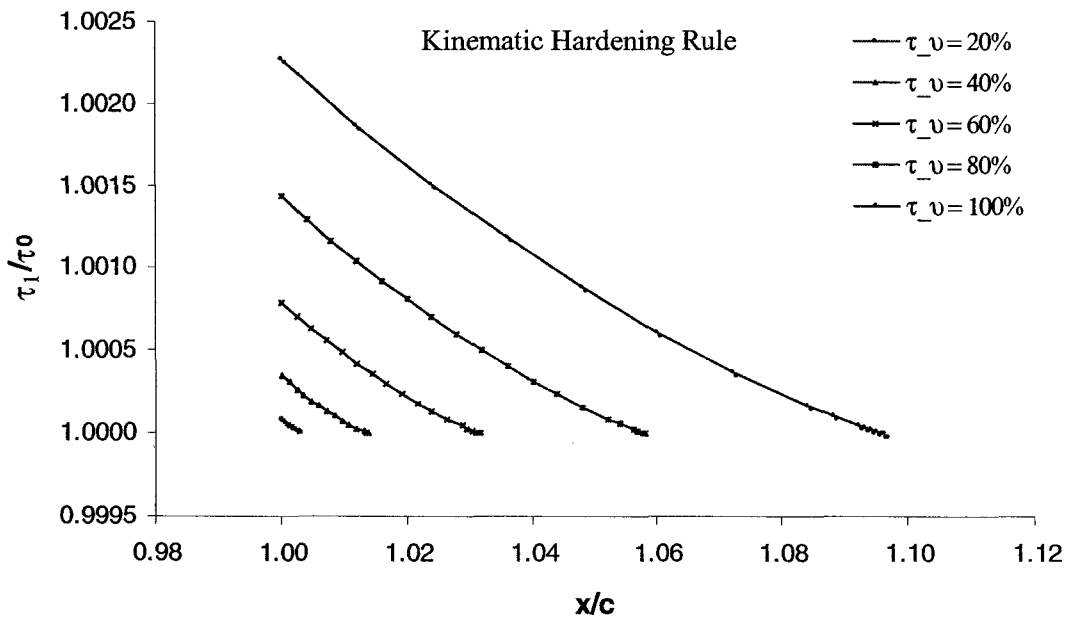


Figure D-6: Reversed crack tip stress field versus distance from the crack tip for a loading stress of 11 MPa and unloading stress ratios as shown ahead of a 50 mm crack under kinematic hardening rule

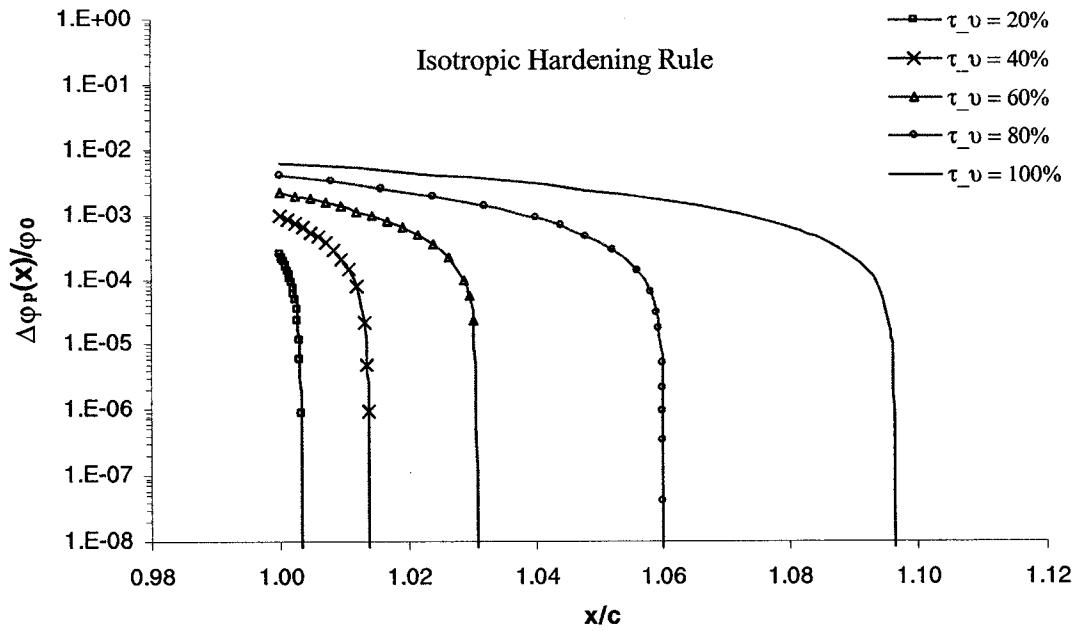


Figure D-7: Reversed plastic displacement versus distance from the crack tip for a loading stress of 11 MPa and unloading stress ratios as shown ahead of a 50 mm crack under isotropic hardening rule

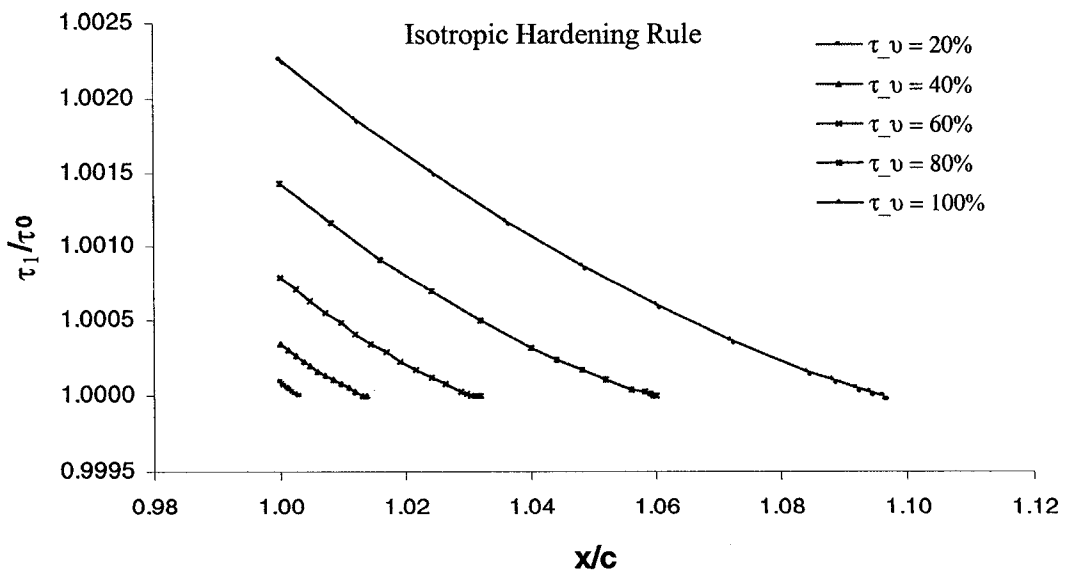


Figure D-8: Reversed crack tip stress field versus distance from the crack tip for a loading stress of 11 MPa and unloading stress ratios as shown ahead of a 50 mm crack under isotropic hardening rule



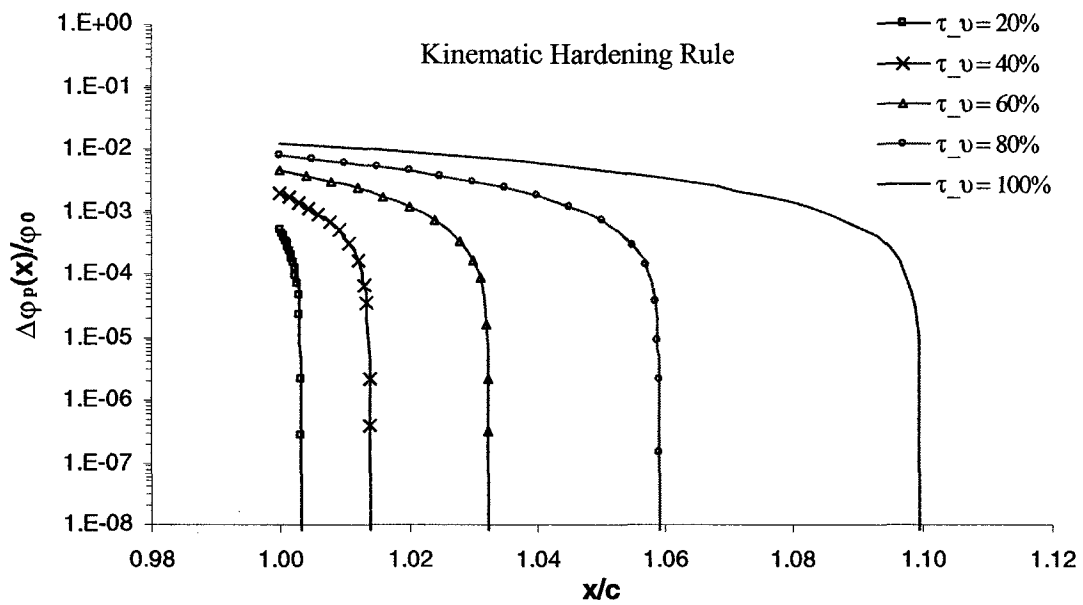


Figure D-9: Reversed plastic displacement versus distance from the crack tip for a loading stress of 11 MPa and unloading stress ratios as shown ahead of a 100 mm crack under kinematic hardening rule

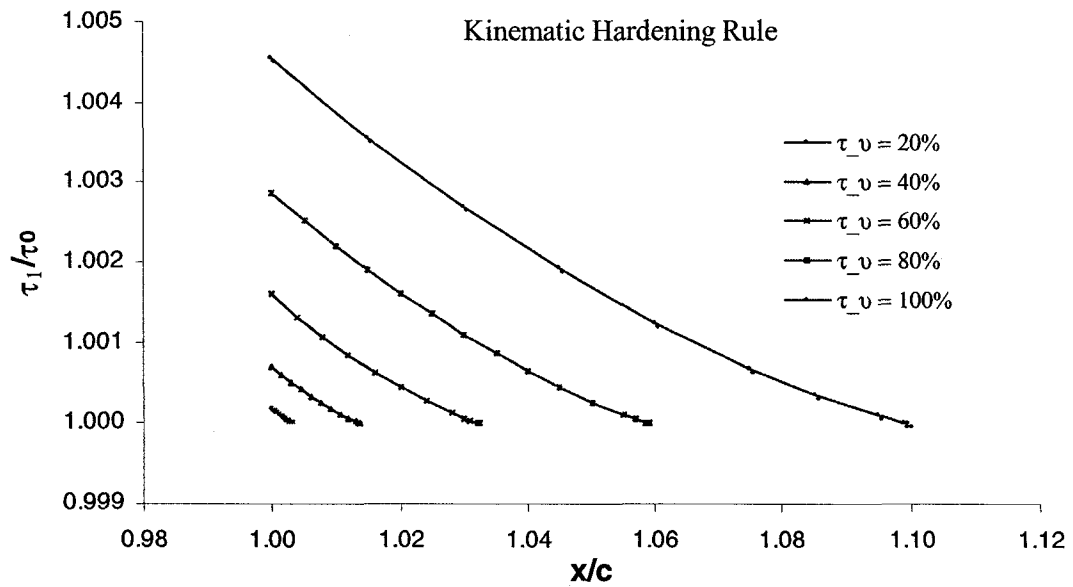


Figure D-10: Reversed crack tip stress field versus distance from the crack tip for a loading stress of 11 MPa and unloading stress ratios as shown ahead of a 100 mm crack under kinematic hardening rule

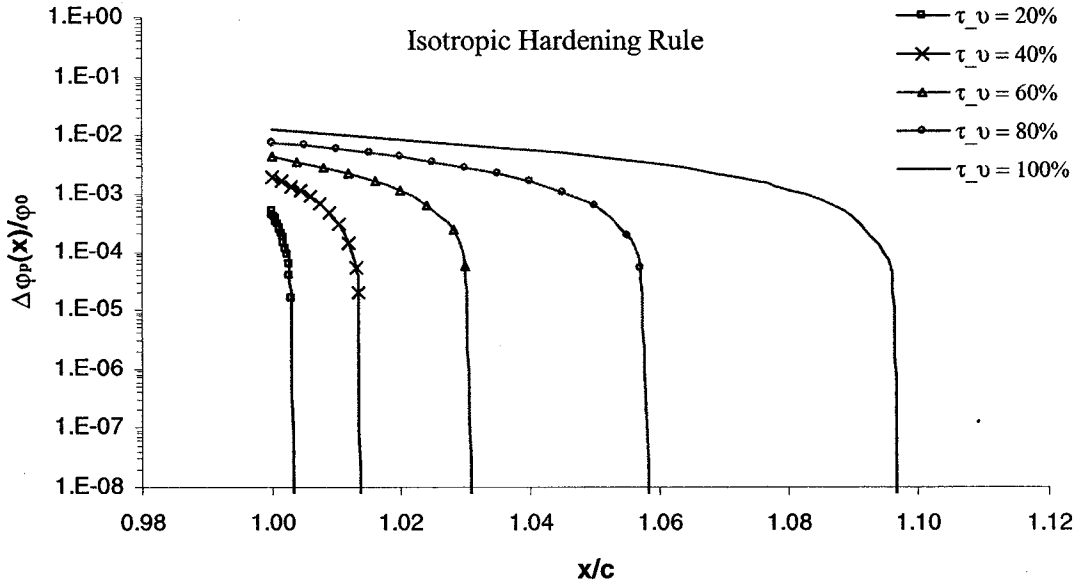


Figure D-11: Reversed plastic displacement versus distance from the crack tip for a loading stress of 11 MPa and unloading stress ratios as shown ahead of a 100 mm crack under isotropic hardening rule

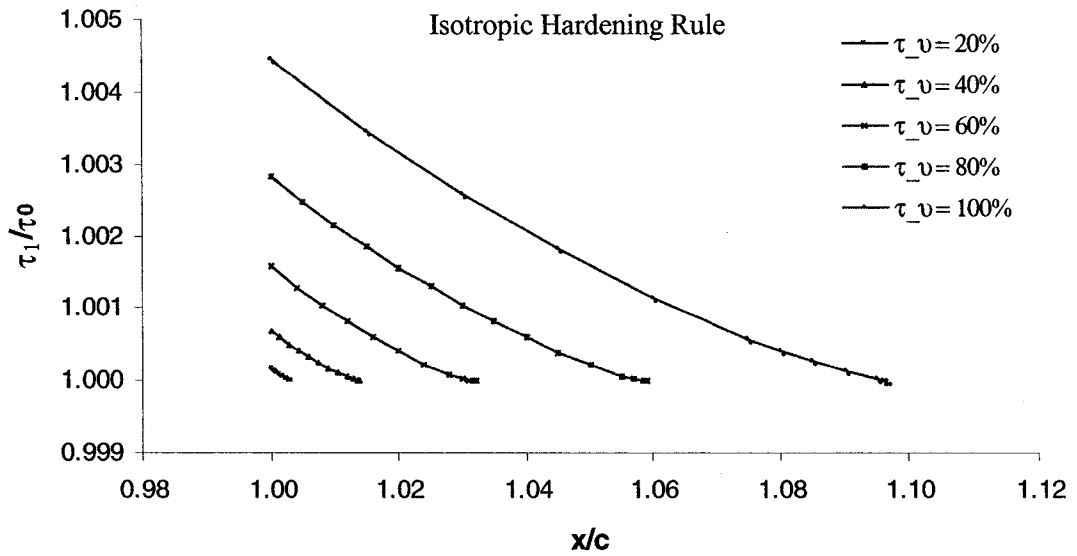


Figure D-12: Reversed crack tip stress field versus distance from the crack tip for a loading stress of 11 MPa and unloading stress ratios as shown ahead of a 100 mm crack under isotropic hardening rule

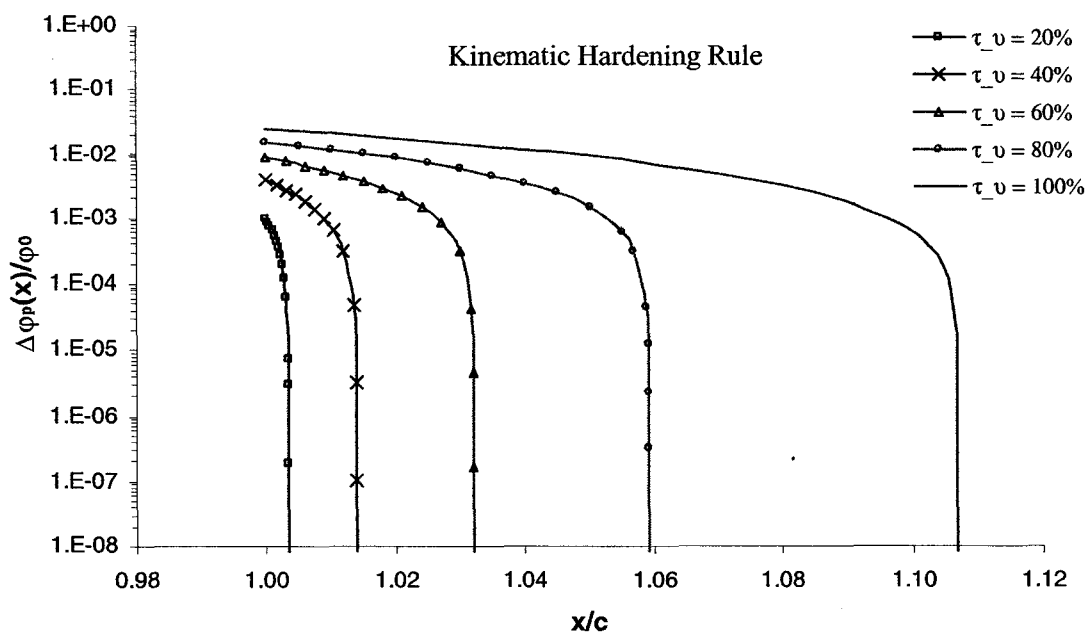


Figure D-13: Reversed plastic displacement versus distance from the crack tip for a loading stress of 11 MPa and unloading stress ratios as shown ahead of a 200 mm crack under kinematic hardening rule

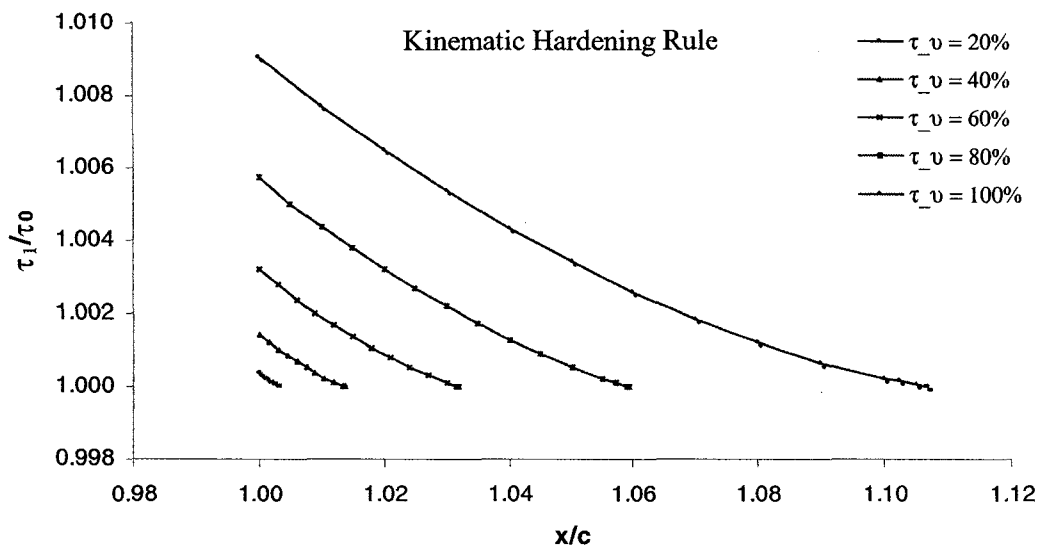


Figure D-14: Reversed crack tip stress field versus distance from the crack tip for a loading stress of 11 MPa and unloading stress ratios as shown ahead of a 200 mm crack under kinematic hardening rule

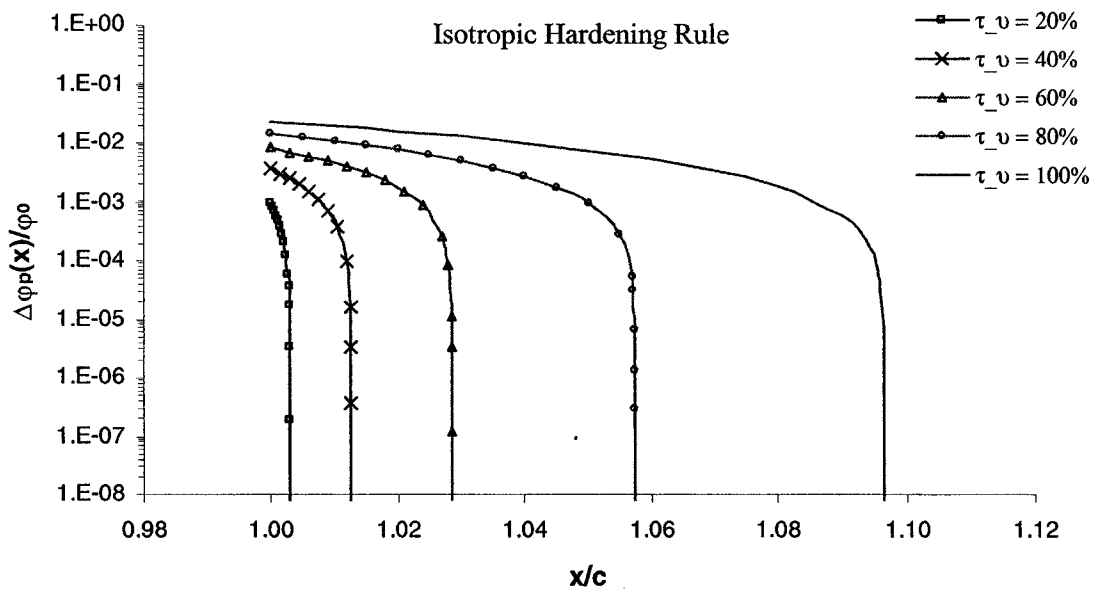


Figure D-15: Reversed plastic displacement versus distance from the crack tip for a loading stress of 11 MPa and unloading stress ratios as shown ahead of a 200 mm crack under isotropic hardening rule

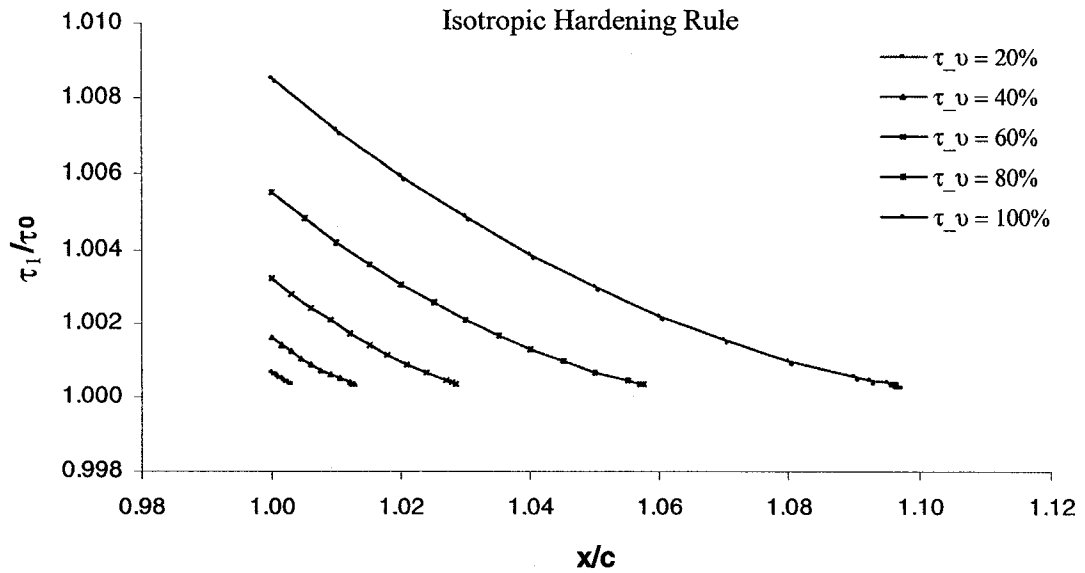


Figure D-16: Reversed crack tip stress field versus distance from the crack tip for a loading stress of 11 MPa and unloading stress ratios as shown ahead of a 200 mm crack under isotropic hardening rule

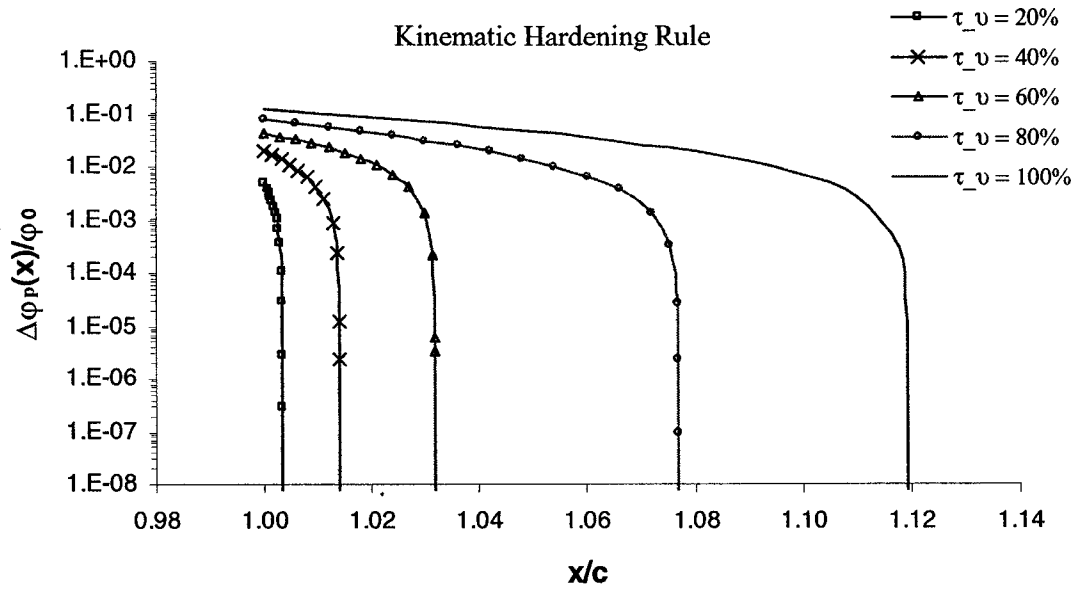


Figure D-17: Reversed plastic displacement versus distance from the crack tip for a loading stress of 11 MPa and unloading stress ratios as shown ahead of a 1000 mm crack under kinematic hardening rule

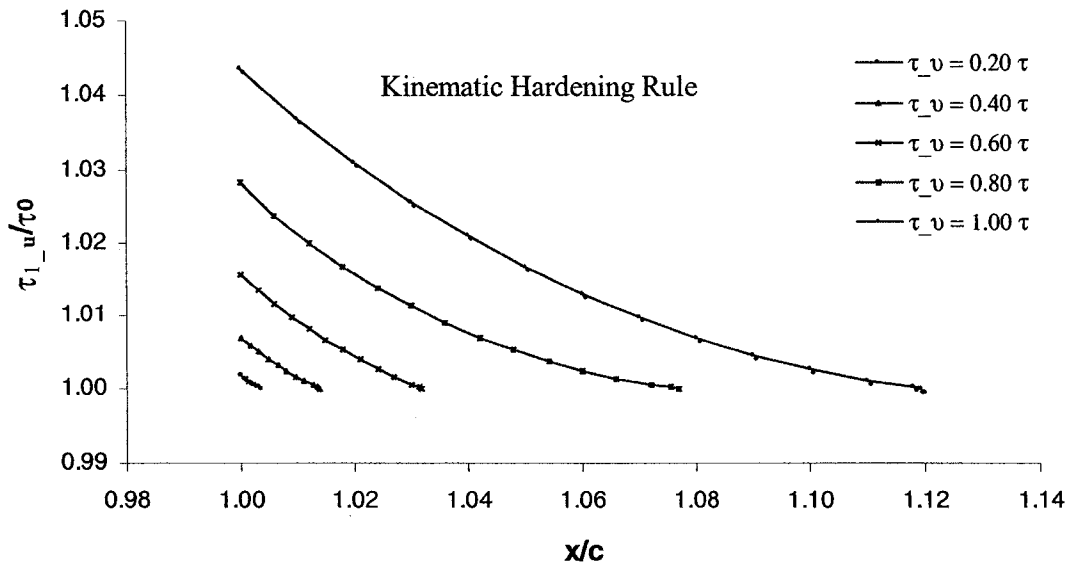


Figure D-18: Reversed crack tip stress field versus distance from the crack tip for a loading stress of 11 MPa and unloading stress ratios as shown ahead of a 1000 mm crack under kinematic hardening rule

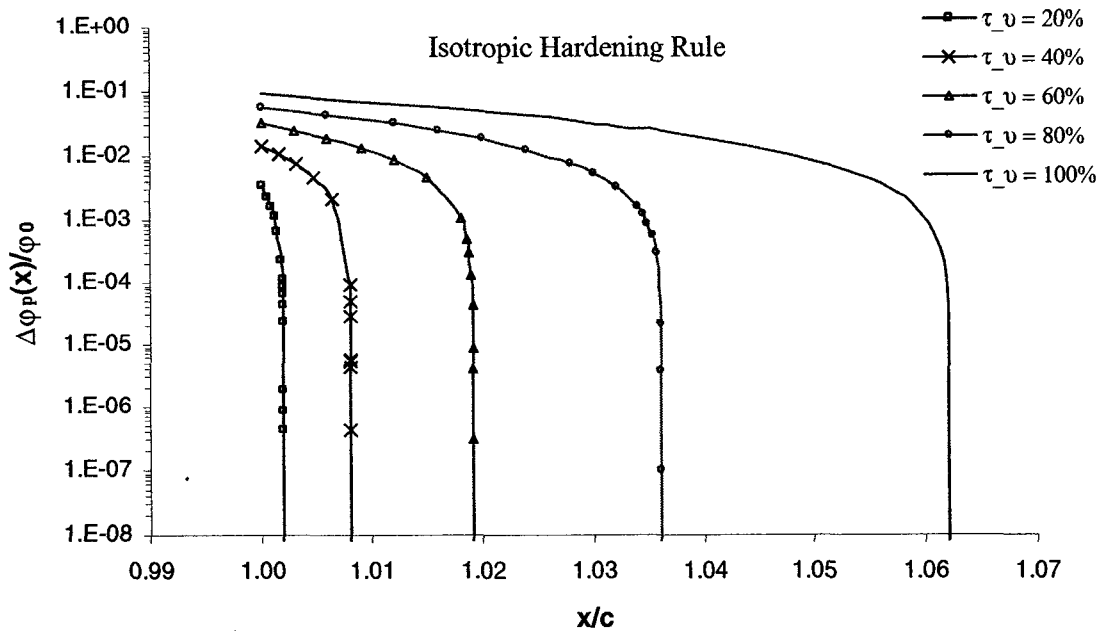


Figure D-19: Reversed plastic displacement versus distance from the crack tip for a loading stress of 11 MPa and unloading stress ratios as shown ahead of a 1000 mm crack under isotropic hardening rule

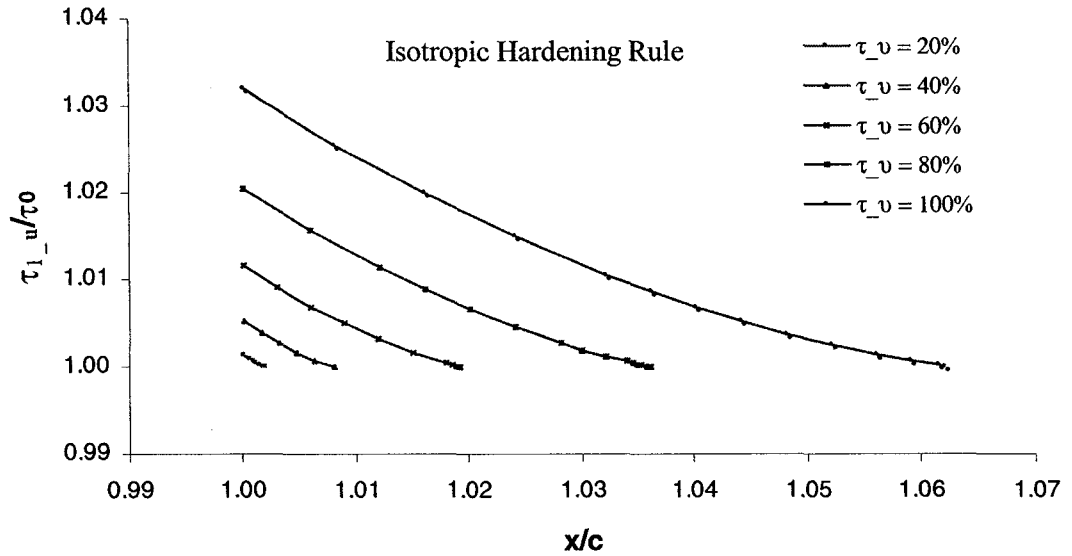


Figure D-20: Reversed crack tip stress field versus distance from the crack tip for a loading stress of 11 MPa and unloading stress ratios as shown ahead of a 1000 mm crack under isotropic hardening rule